A SYSTEMATIC CHARACTERIZATION OF THE TISSUE RESPONSE IN THE BRAIN TO IMPLANTED ELECTRODE ARRAYS

By

Cort Hausserman Thompson

A DISSERTATION

Submitted to
Michigan State University
in partial fulfillment of the requirements
for the degree of

Biomedical Engineering – Doctor of Philosophy

2023

ABSTRACT

Neural prosthetics are an emerging technology which has great potential to treat neurological conditions in the clinic and advance neuroscience research at the bench. By stimulating or recording from local neuronal populations using implantable electrode arrays, neural prostheses can interact with the nervous system to treat disease and injury. However, detectable neuronal signals required for the function of neural prostheses can become inconsistent and even progressively decline in chronically implanted devices to the point of failure. The tissue response to implanted electrode arrays is believed to play a significant role in generating the progressive loss of signal fidelity in implanted electrode arrays. The tissue response was initially characterized by the progressive encapsulation of the implant by reactive microglia and astrocytes and the loss of neuronal cell bodies and processes. Further studies suggested that the severity of the tissue response could be attenuated or circumvented by altering the design of electrode arrays by reducing feature size and functional bending stiffness. Many ‘next-generation’ electrode arrays have been fabricated that feature softer biomaterials and smaller feature sizes. In many cases these next-generation devices were successful in reducing gliosis and neuronal death. However, signal fidelity can still become unstable in apparently normal tissue where implanted devices remain undamaged and tissue response is minimal. Therefore, it is essential that we find new understandings into the complexity of the tissue response to inform and guide the design of cortical implanted with greater biocompatibility. The studies in this dissertation present a systematic analysis of the tissue response by (1) reviewing the need for guiding principles in device design, (2) identifying the spatiotemporal patterns of

gene expression through RNA-sequencing, (3) exploring protein expression of RNA-seq identified genes, and (4) utilizing novel in-situ methods to evaluate the transcriptional tissue response as the single-cell level in response to implanted devices. The results of these studies expand current understandings of the tissue response and may help guide the design of new generations of biocompatible implanted electrode arrays.

This dissertation is dedicated to my family, friends, colleagues and all the people who have supported me and shaped my experiences throughout the duration of my academic pursuits. I would like to specifically thank my parents, Steve and Linda Thompson, who gave me the opportunities and privilege to be scientifically curious and pursue my academic passions. I also dedicate this dissertation to my wonderful partner, Lisa Yun, who has supported me throughout my academic and professional pursuits.

ACKNOWLEDGEMENTS

I would like to sincerely thank my advisor and mentor, Dr. Erin K. Purcell for her excellent mentorship. As the first student in her lab back in 2015, she taught me nearly every skill that I know. At every opportunity she has supported my personal, professional, and academic growth. I can say with absolute certainty that I consider myself to be exceptionally fortunate for the gift of her mentorship and I would not be where I am today without her. I also thank Dr. Chris Contag, Dr. John Seymour, and Dr. Wen Li for serving on my graduate committee and providing their expertise, insight, time, and effort. I would like to sincerely thank Dr. Erin Purcell again, as well as Dr. Chris Contag, and the Michigan State Biomedical Engineering department for giving me the opportunity to become a capable scientist and academic. I would also like to sincerely thank my mentors and friends, Dr. Steve Suhr and Dr. Marie-Claude Senut, who taught me essential skills in the practices of cell culture and molecular biology, which I have utilized thoroughly in my graduate career. I would also like to thank all of my lab members, past and present, with who I have shared ideas, frustrations, and celebrations.

In 2020, colleagues and I published an invited review manuscript titled “Toward guiding principles for the design of biologically integrated electrodes for the central nervous system” which was published in the Journal of Neural Engineering (doi: 10.1088/1741-2552/ab7030). For this work I thank Dr. John Seymour for his helpful feedback, Nick Heelan and Kathleen Williams for their helpful review of table references, and Bailey Winter and Shardul Deolekar for early discussions regarding the article concept. I would also like to thank the co-author Dr. Ti’Air Riggins for her

assistance in preparing the manuscript as well as critical figures.

In 2021, we published the first RNA-sequencing study in the context of implanted electrode arrays titled “Spatiotemporal patterns of gene expression around implanted silicon electrode arrays” in the Journal of Neural Engineering (doi: 10.1088/1741-2552/ab7030). I would like to sincerely thank Rebecca Tagett and the Bioinformatics Core of the University of Michigan Medical School’s Biomedical Research Core Facilities for analysis support. Steven Suhr of BiomiLab, LLC provided helpful feedback and discussions. Kaleb Howard assisted with initial study planning. I also thank Akash Saxena for assistance in preparing essential figures for this manuscript.

In 2023, we published a manuscript titled “Spatiotemporal expression of RNA-seq identified proteins at the device interface” (doi: 10.1016/j.actbio.2023.04.028) in the journal Acta Biomaterialia. I would like to sincerely thank the Nick Heelan for assistance in the initial histological optimization efforts of this study. I would also like to thank Andrew Pratt and Dorothy Zhao for their assistance in generating cell counting data for the methodology of this paper. I would also like to acknowledge the excellent work of Blake Evans, who generated the MATLAB scripts that were essential for the analysis in this study. We also thank Dr. Melinda Frame and the Michigan State University Center for Advanced Microscopy (CAM) for their assistance in tissue imaging.

Currently, I am working on a study which provides the first use of novel in-situ hybridization methods to observe the transcriptional response of tissues around implanted electrodes in the brain at single-cell resolution. I sincerely thank Dr. John Seymour and Dr. Wen Li for their assistance and fabrication of the devices used in this study. I thank

Dr. Melinda Frame and the Michigan State University Center for Advanced Microscopy (CAM) for their assistance in tissue imaging.

TABLE OF CONTENTS

CHAPTER 1 | TOWARD GUIDING PRINCIPLES FOR THE DESIGN OF BIOLOGICALLY INTEGRATED ELECTRODES FOR THE CENTRAL NERVOUS SYSTEM

1. INTRODUCTION

Electrode arrays implanted in the brain have created a renaissance in the study of normal and pathological brain function. These devices are being developed to treat a growing number of medical conditions, including Parkinson's disease, paralysis, Alzheimer's disease, depression, Tourette's syndrome, deafness, blindness, stroke or tinnitus[1], [2], [11]–[20], [3]–[10]. Many of these conditions are treated through electrical stimulation, where closed-loop systems can provide added therapeutic and performance benefits by conditioning stimulation based on a recorded 'trigger' signal[21]. Recorded signals are also used to drive the decoding algorithms used to restore function for paralysis patients through brain-machine interfaces. While many successes in chronic recordings have been reported, these devices are characterized by an often variable ability to sense or stimulate activity over time[22]–[25]. This variability burdens decoding strategies and compromises the fidelity of closed-loop systems. The foreign body response to the implant is widely believed to be a key underlying source of signal instability and loss, where local neuronal loss and encapsulation by a glial "scar" progressively isolate devices from signal-generating neural circuitry[26], [27]. Likewise, newer observations suggest that indwelling devices impact the function of the remaining neurons at the implanted interface[28]–[30], and implantation in motor cortex has produced behavioral deficits in rodents[31].

Despite these observations, direct, mechanistic links between specific cellular responses in the brain, device design features, and chronic performance remain to be established. Two central issues impede progress: (1) the relationship between the biological response to electrodes, and the impact on signal quality, is unclear, and (2) the surge in new electrode designs, which simultaneously alter multiple attributes of the array (materials, feature size, architecture), complicates the ability to assimilate observations across studies into guiding principles for electrode design. On the first issue, it remains unknown as to which aspects of the tissue response determine effective chronic performance. Local neuronal and glial densities are commonly used as metrics for assessing biocompatibility, but given the complexity of the system, these broad-based assessments may not provide the level of granularity necessary to identify key biomarkers of device performance. Brain cells are highly heterogeneous, where neurons can be distinguished based on unique structural and functional properties[32], [33]. Likewise, non-neuronal cells are more complex than previously appreciated, and may respond to implanted electrode arrays in unexpected ways. For instance, recent evidence suggests that neuron glial antigen-2 (NG2)-glia react to device implantation within the initial days following insertion, exhibiting altered morphology and migration toward the interface[34]. Likewise, reactive astrocytes can be delineated into unique subclasses of phenotypes, with the potential to influence the structure and function of neural circuitry in distinct ways[35]. These cells can exert either positive or negative effects on surrounding neurons following injury[36], and a recent report distinguishes a pro-inflammatory, *neurotoxic* astroglial subtype from a hypoxia-induced, *neuroprotective*

subtype[37]. Injury surrounding an electrode can produce differential effects on subtypes of neurons as well: shifts in the expression of excitatory and inhibitory synaptic transporters reportedly occur proximally to devices, indicating a progression toward increased inhibitory tone in the tissue surrounding chronically implanted electrodes[29]. Likewise, observations of sustained calcium influx and changes in the expression of voltage-gated ion channels indicate that implanted electrodes may alter the intrinsic excitability of the neurons they are designed to interface with[28], [30], illustrating the potential for devices to not only affect cellular densities, but also the *function* of residual cells at the interface.

Regarding the second issue, recent years have seen a veritable explosion in the design strategies that characterize implanted electrode arrays. New devices can feature a variety of architectures, dimensions, insertion strategies, materials, and modifications as they push the boundaries of neural interface design. However, the relationship between complex biological effects and the design attributes of the implanted electrode array remains undefined, even for relatively traditional designs and metrics of tissue response. Studies which directly and systematically test the effect of new design features *in isolation* on the biological response to implants are generally scarce, which is a problem compounded by the differing materials, bending stiffnesses, and feature sizes of recent "next-generation" devices at the forefront of neural engineering research. As such, many of these devices utilize a wholly unique blend of characteristics that make it difficult to empirically determine which of the chosen features contribute to the observed tissue response. Furthermore, it is generally unclear whether or not any observed improvements

in biocompatibility translate to improved chronic performance. Here, we review the state-of-the-art in electrode design, as well as the knowns and unknowns related to the biological response to key design features, to frame a discussion on the necessary next steps to formalize guiding principles for biologically-integrated electrode design.

2. ELECTRODE DESIGN PARAMETERS: STATE-OF-THE-ART

It is well documented that traditional metal- and silicon-based probes often elicit an undesirable immune response, typified by local neuronal loss and glial reactivity[26], [27], [38]. These observations have motivated the design of "next-generation" devices which utilize sizes and materials that are smaller and more flexible than the standard approaches, and generally depart from more traditional designs in a variety of aspects, including unique architectures and insertion methods[39]. The novel approaches represented in next-generation devices seek, in part, to remedy the inconsistencies in the chronic performance of traditional probes. The current state-of-the-art encompasses a wide range of device attributes which are coupled to a relatively limited subset of biological assessments. Some of these next-generation devices have the potential to be commercialized and made accessible to the general public in the future. For ethical reasons, it is important that the biological impacts of new designs be better understood before next-generation devices are implanted long-term in human patients[40]. We have assimilated a description of design components of a variety of devices in Table 1.1 and Figure 1.1, and describe their features and reported effects on tissue response.

2.1 METAL BASED ELECTRODE ARRAYS

2.1.1 MICROWIRES

Microwires are traditionally fabricated from insulated stainless steel or tungsten wires, with diameters typically ranging from 50-100μm. As an early recording technology, detailed histological assessments of these devices were initially reported in the 1950's[41]. Collias and Manuelidis reported observations of marked hemorrhagic necrosis surrounding stainless steel microwires (~130μm diameter) implanted in the cat brain at 24 hours post-insertion, followed by neovascularization, microglial activation, demyelination, and astrocyte encapsulation in the following weeks. The tissue response became stable between the two- and six-month time points, and changes in glial and myelin appearance surrounding the device were generally unremarkable following the first month. A similarly stable chronic tissue-microwire interface was reported in the late 1990's, when Liu and McCreery described the response to Epoxylite-insulated, 50μm diameter platinum-iridium lead wires with iridium electrodes following implantation into the cat brain[42]. Based on the stability of the detected waveform shape, the authors reported that, "after implantation, the electrode-tissue interface may change from day-to-day over the first 1–2 weeks, week-to-week for 1–2 months, and become quite stable thereafter."[42] Post-mortem histology displayed minimal gliosis, thin fibrous encapsulation (~2-8μm thick), and typically good proximity of electrode tips to local neurons (often within ~30-50μm of the recording site). A more recent histological study of single stainless steel microwires insulated with Epoxylite (75μm diameter tapered to a 1μm tip) implanted in rat cortex revealed persistent blood brain barrier leakage and

inflammation throughout a twelve week time course[43]. Interestingly, neuronal loss and glial reactivity were relatively stable throughout the study, although the glial fibrillary acidic protein (GFAP)-positive region surrounding devices became more compacted and localized over time. This latter result deviates from the pronounced, progressive neuronal loss and glial encapsulation that are often observed surrounding silicon-based micromachined arrays.

2.1.2 SILICON-BASED SHANK ARRAYS

'Michigan'-style arrays (Figure 1.2A) are micromachined planar devices with a tapered shape terminating in an apex with variable shank dimensions (commonly ~120μm maximum width x ~15-50μm thickness, with length determined based on the target structure of interest). These devices consist primarily of silicon with either iridium or platinum recording sites, where metal sites are deposited onto conductive traces (typically polysilicon, insulated with silicon dioxide and silicon nitride) embedded in the silicon shank[44], [45]. A key advantage of the technology is that the fabrication approach enables devices to be readily customizable into a wide variety of configurations (multi-shank, multi-modal, unique site configurations, etc). In an initial study which characterized the recording quality of these devices, unit activity was detected with subject-dependent longevity up to a >4 month period[45], where over 90% of individual sites registered detectable unit activity. Nevertheless, results can be variable, and these electrodes are associated with an observable tissue response. A seminal study by Biran *et al.* reported ~40% loss of neurons within the estimated recordable radius of the device and persistent microglial activation present over a four week implantation period[38],

[46].

More recently, high-density silicon-based shank arrays have been developed by Masmanidis and colleagues, using newer fabrication techniques to achieve a minimum feature size of 0.4μm (the minimum width of the conducting gold wires)[47]. The silicon shank had a geometry similar to more traditional 'Michigan'-style arrays, with dimensions measuring 7mm x 86μm x 23μm. The silicon shank supported 0.1μm thick gold traces insulated by 0.5μm thick layers of silicon nitride, and gold recording sites measuring 10μm x 10μm in area. Individual shanks were separated by ~300μm patterned with 37μm site spacing, allowing dense sampling of neural activity of various brain

Device	Components	Material	Dimension (width um)	Thickness (nm)	Young's Modulus (gPa)	Bending Modulus (N/M)	Reference
3D Macroporous Probe	Longitudinal interconnects	**SU-8**	7	800	2	6.64E-08	[72] Xie et al. 2015
		Cr	5	1.5	140		
		Au	5	100	79		
	Transverse Scrolling	**SU-8**	10	400	2	9.48E-08	
		Cr	3	10-20 , 1.5	140		
		Pd	3	80	16		
	Device Bend Arms	**SU-8**	6	800	2	5.69E-08	
		Cr	4	1.5 / 30 - 50	140		
		Pd	4	80	16		
	Sensor Metal Contact	**SU-8**	5	800	2	5.93E-09	
		Cr	4	1.5	140		
		Pd	4	50 - 80	16		
		Pt	4	100	168		
Syringe Injectable Probe	Polymer Ribbons	**SU-8**	5 - 20um	350-400	2	2.37E-08	[73] Liu et al. 2015, [74,75]Schuhmann et al. 2018, [76] Zhou et al. 2017
		Au	2 - 10um	100	79		
		Cr	2 - 10um	5	140		
Flexible Parylene Based Multi Electrode Array	Planar Shank (150um)	**Parylene**	150	20000	3.2	3.56E-02	[79,80] Xu et al., 2015
		Pt	45	200	168		
	Planar Shank (100um)	**Parylene**	100	20000	3.2	2.37E-02	
		Pt	45	200	168		
Polyimide	Planar Shank	**Polyimide**	80	12000	2.5	2.44E-03	[87] Chung et al. 2019; Dimensions: [85,86]Tooker et al. 2012
		Ti / Au / **Pt**	6	300	168		
		Polyimide	61	12000	2.5		
		Pt	6	300	168		
Carbon Nanowire	Nanowire	**C**	7	7000	234	3.06E-03	[92, 93] Patel et al. 2016
All Diamond Ultramicroelectrode	Polycrystalline Diamond	**(PCD) C**	25	6000	1000	5.00E-02	[95] Rusinek et al. 2018
	Boron-Doped Diamond	(BDD) C	19	3700	1000		
Michigan Probe	Planar Shank (Thick)	**Si**	123	15000	179	6.88E-01	[38] Biran et al. 2005
	Planar Shank (Tapered)	**Si**	33	15000	179	1.85E-01	
Nanoelectronic Thread (NET-e-i)	Subcellular Thread (Min)	**SU-8**	8	800	2	1.48E-07	[100] Luan et al. 2017, [87]Xiaoling et al. 2018
		Au	0.2	16	79		
		Cr	0.2	4	140		
	Subcelular Thread (Max)	**SU-8**	8	1000	2		
		Au	0.2	200	79		
		Cr	0.2	6	140		
Sewing Machine Thread Electrode	Subcellular Thread	**Polyimide**	16	4000	2.5	2.37E-05	[89] Hanson et al. 2019
		Pt	4	130	168		
		SiO2	16	200	75		
NeuroPixels	Planar Shank	**Si**	70	20000	179	9.28E-01	[48] Jun et al. 2017, [49] Lopez et. Al. 2017
		TiN	12	120	~200		

Table 1.1: Overview of device design features and calculated bending stiffnesses. Bending stiffness was evaluated as previously described in [97].

regions in mice (1,024 sites implanted in total)[47]. While chronic recording performance and tissue response have yet to be fully characterized, and the biocompatibility of this device has yet to be characterized *in vivo*, the technology is promising for its ability to sample neuronal activity with high spatial resolution.

The Neuropixels probe (Figure 1.1C) is another example of a high-density, silicon-based array and features >900 multiplexed channels on each individual shank[48]. The device physically resembles the Michigan array and has been developed to further improve the recording capabilities of current designs. The device is 70µm wide by 20µm

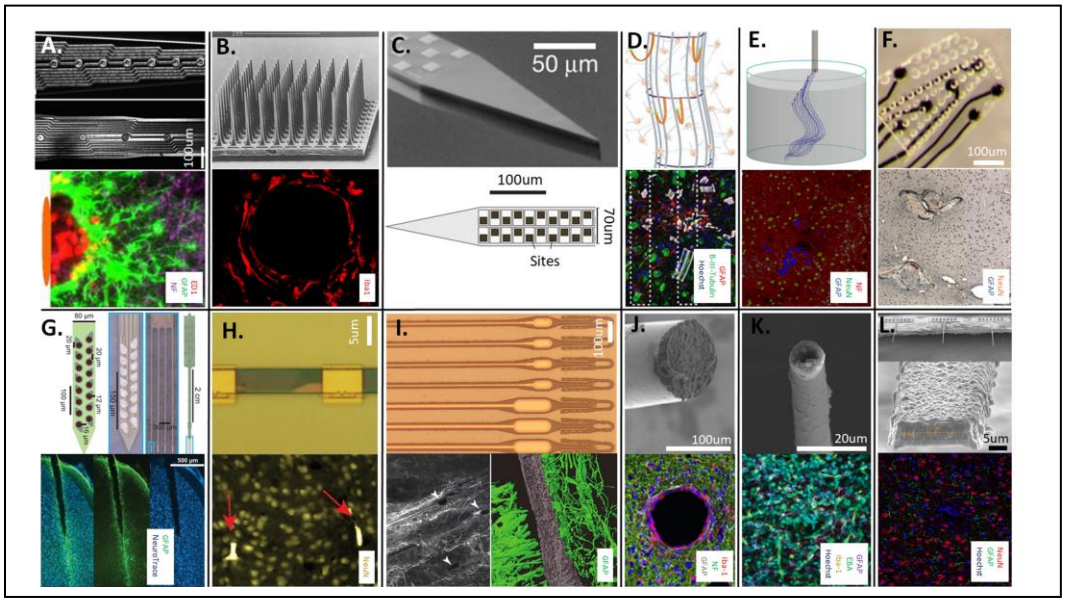

Figure 1.1: Device designs and histological metrics used in the field vary widely. Device materials, architectures, and dimensions encompass a broad design space, including "traditional" and high-density silicon- and metal-based arrays (A-C), mesh arrays (D-E), polymer (F-I), and carbon-based (J-L) electrodes. Accompanying histological images, located below device images, typically include, but are not limited to assessments of neuronal and glial densities surrounding implant sites, however, the choice of histology often varies by research group. Detailed commentary and associated references on the devices represented in this figure can be found in section 2. NF: Neurofilament, Iba-1: Microglia, EBA: Endothelial Barrier Antigen (Blood Brain Barrier), Hoechst: Nuclei, NeuN: Neuronal Nuclei, NeuroTrace: Neurons, B-Tubulin-III: Neuronal Microtubules. A.[38] B.[50, 53] C.[48] D.[72] E.[76] F.[81] G.[87] H.[88] I.[89] J.[90] K.[91, 93] L.[95]

thick with 960 titanium nitride (TiN) semiconductor recording sites located along the length of the array. Each TiN recording site is approximately 12μm x 12μm with a thickness of 120nm. The Neuropixels probe has significant recording advantages over the more traditional silicon-based Michigan array with respect to the unprecedented number of recording sites[49]. Preliminary data suggest that the recording capability of the device remains stable out to 60 days *in vivo*, and viable signals were obtained for 153 days in an exemplary animal[48]. Histological and other biocompatible metrics have yet to be utilized to evaluate the Neuropixels probe, so the precise measure of biocompatibility has yet to be determined.

2.1.3 UTAH ARRAYS

The Utah microelectrode array was developed by Normann and colleagues at the University of Utah (Figure 1.1B[50]–[53]). The body of the device is doped (i.e. conductive) silicon, etched into 100 microneedles with SiO_2 insulating channels between them. They have an insulating layer of Parylene-C along most of the length. The base of each needle is approximately 80μm in diameter and a common geometry has needles 1-1.5 mm long at 400μm pitch, though other geometries are possible. Tip metallization can be platinum or iridium based. The flat top of the device with a flexible wire bundle at a right angle to the needles enables it to "float" with a brain that moves with respect to the skull, which made it well suited for use in primate brains[54], [55]. This device was brought under a quality management system throughout the early 2000s[56] for use in the Braingate clinical trial[57]. It has since become the most widespread implant used in humans. A recent literature search reveals 48 human implants as of 2018[58], primarily

in epilepsy or intraoperative studies, with 18 chronic implants done for a mean number of 578 days under an investigational device exemption (e.g.[7]–[9], [59]–[61]). However, due to predominant use in large animals and humans, very little is known about the long-term immune response of these devices. Early studies in cat visual cortex suggested that scarring was limited to <10 μm from the electrode[51], [62]. Also, both human and monkey experiments are typically conducted across years, long after the 6-8 week period of scar formation, sometimes for as many as 5-7[63]–[65]. This suggests that at least a subset of neurons survive the scarring process. However, based on rodent studies[66]–[68], we know that the scarring and even long term remodelling may be substantial[53]. This has likely been limiting the neuronal yield of these devices from the beginning. Gradual degradation after 8 weeks may be dominated by materials failures[69], [70] due to a warm, salty environment across many years[71].

2.2 POLYMER & NEXT GENERATION ELECTRODE ARRAYS

2.2.1 3D MACROPOROUS PROBE

A common goal in the design of "next-generation" devices is to employ flexible substrates with small feature sizes to close the gap in the mechanical mismatch between devices and host tissue. The Three-Dimensional (3D) Macroporous Probe developed by Charles Lieber's group is a two-dimensional mesh that has been folded into a semi-cylindrical shape with a blunted end. This device has a greater structural complexity when compared to standard shank devices. The bulk of these devices is composed of an insulating SU-8 photoresist layer. For added structural integrity and flexibility, multiple aspects of this design also include palladium and chromium within non-recording, global

‘scrolling’ elements. This electrode is complex, and consists of multiple components including the ‘longitudinal interconnects’, ‘transverse scrolling’ elements, ‘device bend arms’, and the sensor contacts (see Figure 1.1D). The longitudinal interconnects of the device comprise the majority of the device. The longitudinal component consists of an 800nm thick by 7μm wide ribbon of SU-8 photoresist with a 100nm gold metal trace with a width of 5μm. The transverse element is a ribbon of SU-8 photoresist of the same thickness but a greater width (10μm). The transverse element maintains the structure and flexibility of the device and contains a palladium/chromium core with a thickness of 80nm and width of 3μm. The device bend arms house the recording elements (100nm thick platinum sites which are 4μm wide), which extend outward from the main structure following implantation. The bend arms provide the unique feature of allowing the recording elements to drift away from the body of the device, potentially escaping downstream immune response. . Insertion of this device was facilitated by flash-freezing in liquid nitrogen to temporarily maintain structural stability during implantation. Following implantation, the macroporous probe shows an initial void of tissue following injury at acute timepoints. This void appears to regenerate after five weeks with a sustained, but modest level of gliosis surrounding the device. Histological analysis suggests that neuronal cell bodies and glia are present in close proximity to the device both within and outside the structure of the mesh. The results presented by this device design appear to be markedly better than traditional planar device architectures[39], [72].

2.2.2 SYRINGE INJECTABLE PROBE

In addition to the macroporous probe, syringe-injectable electronics have been

developed by Lieber's group (Figure 1.1E). Much like the 3D macroporous probe, the syringe injectable probe is a two-dimensional mesh made from planar ribbons of polymer and metal with incorporated recording elements. The bulk material of the syringe injectable mesh is SU-8 photoresist with internal metal components that include trace chromium, gold interconnects, and platinum recording sites. The SU-8 ribbon has a total thickness of 800nm and ranges from 5μm to 20μm wide. The metal traces of chromium and gold have a cumulative thickness of 105nm and a width that ranges from 2-10μm[39], [73]–[76]. Histological evaluation shows that the syringe injectable mesh has improved biocompatibility in comparison to planar polymer thin-film probes. Over a three-month time period, the injectable mesh has a smaller footprint than planar polymers. Syringe injection of the electrode mesh has a noticeable footprint at the 2-week time-point that is represented by loss of neuronal nuclei, disruption of neuronal processes, and an increase in proximal astrocytes. However, the footprint of the mesh is relatively much smaller than the polymer thin-film that was used as a comparison. The improved tissue integration becomes more apparent at the 4-week and 3-month timepoints. The planar polymer control exhibits a stereotypical chronic immune response with an increased loss of neuronal cell types and a much larger accumulation of astrocytic scar tissue by the 3-month time-point. The mesh probe, however, at 4-weeks and beyond shows a regeneration of neuronal processes into and around the electronic mesh and a disappearance of GFAP positive cells. The 4-week timepoint suggests that neuronal density is still diminished near the device, but histology at the 3-month time-point shows that neuronal cell bodies are present proximally and within the structure of the mesh[39].

This concept of creating finely featured devices that mimic the structure of neuronal morphology has also been expanded on in the form of the ‘neuron-like electronics’ (NeuE) probe.[77]

In a unique approach, Trevathan *et al.* have developed a new strategy for an ‘injectable electrode’[78]. This novel electrode uses an uncured solution containing conductive elements which polymerizes into a functional neural interface following injection into the body. The cured polymer interface is highly compliant and can encapsulate target nerves. These devices were evaluated using a battery of tests to characterize the electrical and mechanical performance characteristics. Sufficiently percolated material with a silver content level of at least 65% w/v was found to have an impedance of less than 10MΩ, whereas ‘injectrodes’ with silver content below 65% maintain much higher impedances. The estimated Young’s modulus of a cured injectable electrode is 65kPa, which is orders of magnitude lower than traditional electrode materials such as silicon. Injection of this device could theoretically be altered to form specifically sized features to enhance biocompatibility. Histological results are limited and no observations have been reported to-date outside of the peripheral nervous system. Additional characterization is needed to fully assess the biocompatibility of this device, particularly for future applications in the brain.

2.2.3 FLEXIBLE PARYLENE-C

Ellis Meng’s research group has reported a flexible Parylene-based array (Figure 1.1F) to chronically record from the rat hippocampus. The recording sites of the hippocampal array are precisely laid out to match the unique shape of hippocampal

projections. This array consists of tapered planar shanks with embedded platinum traces and recording sites. The proximal area of the Parylene probe is approximately 20μm thick and 150μm wide. The 150μm shank tapers down to an approximate 100μm width. The platinum recording sites are 200nm thick and approximately 45μm wide. The changes in bending stiffness (the measured material resistance towards deformation) along the taper are considered to be negligible[79]. Parylene devices successfully recorded single unit activity throughout the entirety of a 1-month period, and some observations suggest that Parylene devices can remain viable *in vivo* out to one year. While the chronic histological evaluation of these devices has yet to be fully characterized, Parylene-C has been designated as a class VI United States Pharmacopeia biocompatible material[79], [80]. Histological analysis was performed on implanted brains at time points up to 1-month post implantation. Initial histological results and cresyl violet stains suggest that properly implanted Parylene devices display minimal tissue reactivity aside from a suspected microglia sheath at 1-week post implantation.

Meng's group has also developed a Parylene sheath electrode that can be implanted with the aid of an assistive microwire. This device is approximately 7-10μm thick with a width that tapers from 300μm to 50μm. Each sheath contains 8 platinum electrodes with a 45μm diameter. The sheath structure also contains perforations that allow tissue to invade the structure of the device and to facilitate cellular signalling across the Parylene structure. This device can be coated with a variety of bioactive components such as Matrigel to potentially further enhance biocompatibility. This electrode has been reported to detect activity *in vivo* for up to 50 weeks[81].

Histological evaluations from alternate Parylene-based devices have shown generally good tissue integration and biocompatibility. Seymour and Kipke published a seminal report which explored the impact of feature size on tissue response using a Parylene-coated, 'Michigan'-style device using an SU-8 backbone[82]. Here, electrodes are displaced from the main shank using support arms with varying dimensions; importantly, neuronal loss and gliosis were mitigated surrounding the subcellular features of the device. Purcell and Seymour explored the idea of a hollowed-out, planar, Parylene-coated probe designed to incorporate a neural stem cell-seeded scaffold[83]. The two main arms of the device are bulk SU-8 with a 5μm thick Parylene-C coating on each face. The total of the support arms are 42μm thick and 45μm wide. The hollow structure that houses the alginate scaffold has a 110μm width and variable thickness. When seeded with stem cells, the devices resulted in an initially decreased acute immune response and an increase in neuronal densities following implantation. The mode of influence may be a "bystander" effect (providing trophic support) rather than direct differentiation and integration into surrounding tissue[84]. However, these effects were transient, and the increase in neuronal density declines beyond 6-weeks, at which point neuronal densities more closely match control conditions and glial encapsulation becomes present around all devices.

2.2.4 FLEXIBLE POLYIMIDE

Intracortical polyimide-based devices were described roughly two decades ago by Rousche and colleagues, who initially reported successful, short-term recording capabilities of devices fabricated with standard photolithographic techniques[85].

Characterization of the devices was relatively limited, but a variety of architectures were presented, including devices presenting embedded wells for delivery of bioactive substances. Recently, the flexible polyimide probe designed by Loren Frank's group has advanced the use of polyimide based devices as previously described (Figure 1.1G)[84-86], demonstrating efficacy in recording unit activity over a ~5 month time frame. The device is a 16-channel planar shank device with a total width and thickness of 80μm and 14μm, respectively. The bulk material used in this approach is polyimide with a total thickness of 12μm and a width of 80μm. The trace metals used consist of titanium on gold with either platinum or iridium recording sites. The trace metals share a thickness of approximately 300nm at 6μm wide. Additionally, polyimide is a compatible material surface for the utilization of bioactive surface modification[86]. The polyimide device was capable of recording single units over a period of 283 days post-implantation, albeit with a decline over time. This device has yet to be fully characterized by histology *in vivo*, but available coronal histology shows an apparent lack of astrocyte encapsulation of the device after 160 days post-implantation. The extent of the glial encapsulation has yet to be directly compared to standard technologies[86].

2.2.5 SU-8 NANOELECTRONIC THREAD ELECTRODES

The Xie lab has created an SU-8 based electrode by utilizing both photolithography and electron beam lithography (EBL) (Figure 1.1H). These 'nanoelectronic thread' (NET) electrodes can be fabricated with dimensions as small as 0.8μm x 8μm[88]. This device is also inserted with the aid of a shuttle device that interacts with the implanted electrode in a similar way that a sewing needle interacts with

thread. The shuttle device is made from a <10μm diameter carbon fiber with a smaller 3μm diameter tip that has a length of 4μm. The shuttle device engages with a micro-hole at the apex of the NET electrode and disengages from the electrode as the shuttle is retracted after the target depth is reached. This device was inspired in an effort to expand on the capabilities of devices such as the Utah array. The NET electrode consists of two insulating 300-500nm layers of SU-8 fabricated with photolithography, as well as EBL-defined 100nm gold interconnects and a 2-3nm chromium adhesion layer. Histological evaluations were performed at two- and four-months post-implantation. 3D reconstruction of vasculature surrounding implanted NET electrodes suggest that there is no significant leakage of capillary networks at chronic timepoints. Other histological evaluations of neuronal morphology show that the subcellular NET electrodes can form tight interfaces with neuronal populations without any apparent disruptions to neuronal morphology. At four months post-implantation, any reduction in neuronal cell density is likely recovered as observed by neuronal nuclei stains. Insertional trauma has yet to be reported, but chronic histology does suggest that damage to the tissues surrounding implanted devices recovers in a promising way. Histological evaluation of gliosis has yet to be reported using these devices.

2.2.6 'SEWING MACHINE' POLYMER PROBE

This approach uses small thread electrodes made from polyimide (Figure 1.1I), similar to the NET probe, and utilizes an automated insertional shuttle in the form of a

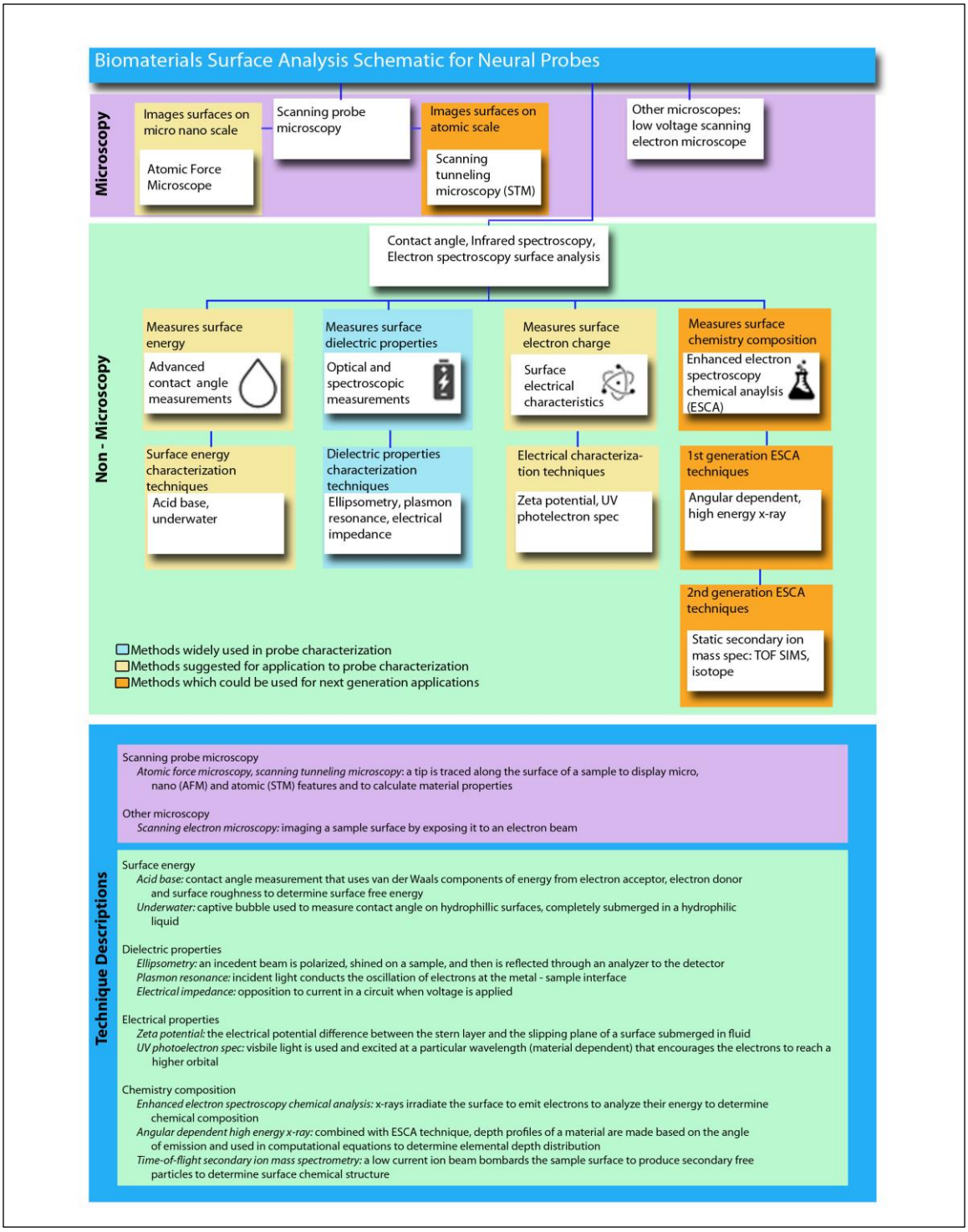

Figure 1.2: A systematic approach to choosing surface characterization techniques for neural probe biocompatibility, based on desired properties to be measured. [94], [120], [154], [155], [123], [125], [143], [144], [150]–[153].

'sewing machine' style device[89]. The robotic sewing machine device is designed with the goal to reliably implant devices with minimal vasculature damage through the aid of an Erythrosin-B saline stain of the dura. The ability of these devices to be robotically implanted with high levels of fidelity is highly attractive in biomedical and research applications. The device is fabricated from two separate layers of 2μm x 16μm polyimide, platinum or gold traces 130nm x 4μm, 400nm copper, 5-6μm Parylene, and a hard mask of 200nm silicon dioxide on the basal side of the electrode. The total width of the shank is 16μm with a total thickness of approximately 10μm. Preliminary histology conducted on slices surrounding these devices suggest that astrogliosis is also present near the implanted sewing machine devices. However, detailed analysis of biocompatibility at chronic timepoints has yet to be reported using the devices.

2.2.7 POLYMER MICROWIRE

Tracy Cui's ultra-soft polymer wire electrode (Figure 1.1J) is a combination of poly(fumaric acid-co-1,7-octadiene diepoxide-co-terephthalic acid) polyethylene glycol (PFOT-PEG) and polydimethysiloxane (PDMS). The ultra-soft microwire was designed largely due to the historical mechanical mismatch between neural tissues and traditional devices. The ultra-soft microwire electrode array has a diameter of 125μm and is fabricated via extrusion of poly(3,4-ethylenedioxythiophene) polyethylene glycol (PEDOT-PEG) conducting polymer and PDMS through a 29-gauge syringe needle. The resulting Young's modulus for these soft microwires is 974kPa. Following extrusion, electrodes are coated in fluorosilicone. The device was implanted via a stainless steel shuttle and evaluated in the brain for either 1 or 8 weeks[90]. Results were compared to

relatively stiff tungsten devices of identical size and shape. The soft electrodes facilitated neuronal adherence to the outer surface without any apparent deleterious effects. *In situ* imaging of sectioned microwire electrodes showed that neurons surrounding the device underwent significantly less deformation when compared to stiff metal electrodes. Over the course of 8 weeks, tissue surrounding the microwire electrodes displayed fewer microglia and macrophages (Iba-1), reactive astrocytes (GFAP), and less evidence of cleaved caspase-3 (a marker of neuronal apoptosis) or distortion of mature axons (NF200). Blood brain barrier (BBB) leakage also was reduced around the soft electrodes compared to stiff electrodes. Devices were explanted at each timepoint and histologically stained to characterize cellular adhesion to the device. In general, soft devices showed a greater level of adherent cells after explant compared to stiff devices. Of the cell types analysed, beta-tubulin positive neural cells appear to make up the bulk of adherent cells[90].

2.2.8 CARBON MICROTHREAD ELECTRODE (MTE)

In 2012, Kozai and colleagues reported the chronic recording performance of a novel, carbon fiber-based recording electrode with subcellular dimensions[91]. The device was an ultra-small 7μm diameter carbon fiber with a conductive poly(3,4-ethylenedioxythiophene) (PEDOT) coating at the distal end for recording and an insulating bulk coating of 800nm poly(p-xylylene) and 50nm poly((p-xylylene-4-methyl-2-bromoisobutyrate)-co-(p-xylylene)). While carbon has a Young's modulus of ~200GPa, it has a competitive composite bending stiffness at a 7μm diameter (Table 1.1). As such, this microelectrode is relatively flexible, but it can be implanted into the cortex

with the aid of an assistive insertion device[91]. Chronically implanted MTEs show a markedly improved tissue response compared to implanted silicon-based 'Michigan' probes, with greater interfacial neuronal densities and lower accumulation of proximal astrocytes, microglia, and endothelial cells. Such improvements in biocompatibility may be due, in part, to the relatively small footprint of this device. The MTE is one of the smallest freestanding implantable devices, and therefore, it is able to "stealthily" interface with the brain by minimizing BBB disruption and tissue displacement. In addition to being relatively biocompatible, MTEs have been shown to provide stable recordings out to 5 weeks *in vivo* and are also capable of single unit recordings[91].

More recently, Paras Patel and Cynthia Chestek have further developed this technology through the testing of different tip coatings (Figure 1.1K), fabricating MTEs into an array configuration, and evaluating the array *in vivo*. First, MTEs were coated in poly(3,4-ethylenedioxythiophene):p-toluene sulfonate (PEDOT:pTS) as opposed to poly(3,4-ethylenedioxythiophene)-poly(styrenesulfonate) (PEDOT:PSS) and were aged at an accelerated rate in a heated bath. Overall, the PEDOT:pTS devices were found to have more extended longevity than the PEDOT:PSS probes and were selected for chronic *in vivo* characterization[92]. The new arrays consisted of 16 MTEs in a 2 x 8 configuration with a pitch of 152.4μm. Insertion of the arrays was accomplished with a sacrificial layer of polyethylene glycol (PEG) that encapsulated the MTEs during insertion, but was dissolved just as the fibers penetrated the brain[93]. Chronic implantation of the arrays showed similar neuronal survivability around the device interface and reduced foreign body response as seen in Kozai et al.[94]. While the devices maintained recording

fidelity out to 112 days[93], there is still a disconnect between the nearly non-existent immune response and the overall recording yield/longevity. These results indicate that while mitigating tissue response plays an important role in long-term recording yield, other factors such as tip coating preparation and the stability/degradation thereof, may also be critical to chronic electrode performance.

2.2.9 DIAMOND ULTRAMICROELECTRODE

Diamond is an emergent electrode material owing to its biocompatibility and suitability for both electrophysiological and neurochemical measurements. On the latter point, the wide potential window, low capacitance, and low background current of conductive, boron-doped polycrystalline diamond (BDD) are attractive features for fast scan cyclic voltammetry for neurotransmitter detection[95]. Li and colleagues have fabricated an all-diamond electrode array featuring a BDD core that is insulated by a thin layer of polycrystalline diamond (PCD) (Figure 1.1L). The internal BDD core is 3.7μm in thickness and 19μm wide, and including PCD insulation, shank dimensions are approximately 6μm thick by 25μm wide (although, devices can be fabricated in a range of feature sizes). PCD is a mechanically robust material with a Young's modulus of approximately 1000GPa. Despite the exceptionally high Young's modulus, the ability to fabricate devices with subcellular dimensions (<10μm) allows for these devices to maintain a reasonable bending stiffness[95]. Histological characterization of these devices *in vivo* is ongoing.

3. THE RELATIONSHIP BETWEEN ELECTRODE FEATURES AND BIOCOMPATIBILITY

Assimilating the impacts of electrode features on biointegration is challenging due to the wide assortment of next-generation electrodes under development and the lack of standardized testing regimens across laboratories. Here, we review reported observations linking electrode features to histological outcomes and describe strategies to modify probes to improve tissue integration.

3.1 STIFFNESS AND FEATURE SIZE

Studies suggest that the architecture and flexibility of devices play important roles in determining effective tissue integration: device cross-sectional dimensions, Young's modulus, and bending stiffness have all been identified as key features of design. An early study by Szarowski *et al.* indicated that initial insertion damage and reactivity within the first week of implantation is proportional to the cross-sectional area of the device, but that responses were insensitive to device geometry in the chronic assessment period (>4 weeks)[96]. The authors concluded that they had observed, "an early response that is proportional to device size and a sustained response that is independent of device size, geometry, and surface roughness." However, in support of the importance of device dimensions in determining tissue response, later studies revealed that gliosis and neuronal loss were mitigated when device features were reduced to a subcellular scale (~5μm thickness)[82]. Likewise, 7μm diameter insulated carbon fibers with PEDOT-functionalized electrode tips display a negligible tissue response, which may be attributable to their minimal footprint[91]. In combination, these observations suggest

that electrodes with subcellular dimensions (<~10μm) result in improved tissue response. Reduced Young's modulus has also been credited with improved tissue integration, based on studies that have examined the response of BBB leakage, as well as microglia/macrophage, astrocyte, and neuronal densities proximal to various planar probes of differing stiffnesses. In experiments in which devices ranging from 6MPa to 150GPa were evaluated, the foreign body response appeared to plateau at stiffnesses of 1.5GPa and below[97]. Nevertheless, a recent meta-analysis indicated that it was not feature size or Young's modulus that most strongly determined the degree of tissue response, but rather bending stiffness[98], which incorporates feature dimensions, 'softness'/Young's modulus, and cross-sectional shape into its calculation. In summary, combining observations across these initial studies indicates that smaller, softer devices

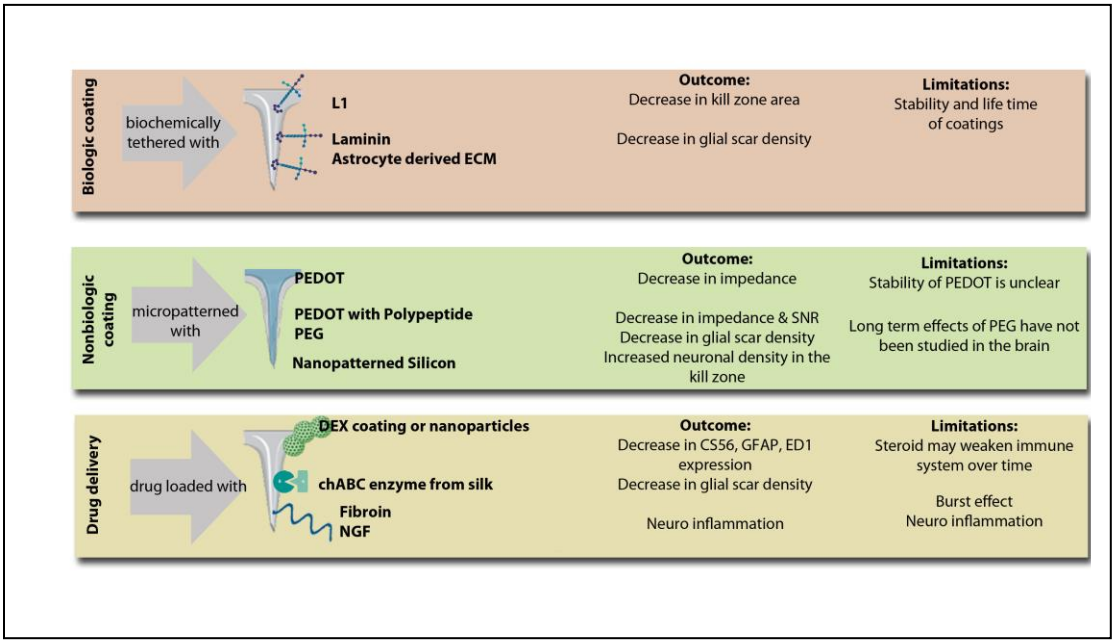

Figure 1.3: Next generation surface modification strategies with experimental outcomes and limitations. [94], [119], [143]–[145], [150], [151], [156]–[160], [124], [125], [133], [137]–[139], [141], [142].

favor improved tissue integration. However, studies which directly assess the impact of device features on biocompatibility are relatively scarce and disparate in methodology, and questions remain regarding the generalizability of observations and underlying mechanisms.

For instance, the primary motivator for the movement toward softer, more flexible electrodes is to remove the mismatch in mechanical properties between brain tissue and devices, thus creating a more seamless interface. However, a first question pertains to what, exactly, are the mechanical properties of brain tissue? Since it is difficult to quantify the mechanical properties of human brain tissue *in vivo* and *in situ*, literature characterizing brain tissue mechanical properties are widely varying. A myriad of tissue preparation methods[99],[100],[101],[102], temperature[103],[104],[105], post-mortem times[102],[105],[106], and testing such as rheometry[107],[108],[109], magnetic resonance elastography (MRE)[107],[108],[110], shear wave elastography,[111] and atomic force microscopy (AFM)[111],[109],[106], are used, resulting in a range of values, 35-422, 100,000Pa[112], that vary by eight orders of magnitude (summarized in Supplementary Table 1**)**. Many characterization studies occur not in the human brain, but in animal models such as rats and mice, which further complicates this view since murine models have fewer striations, surface area, different pharmacokinetic profiles, and distinct structural organization in comparison to human brains[113],[114]. These uncertainties make it challenging to accurately predict the desired elastic modulus to minimize micromotion at the implantation site and adequately "match" the properties of brain tissue. Furthermore, neurosurgeons have reported regional variation in stiffness in

the brain[115], which suggests that, depending on the function of the probe and the area in which it is implanted, that each probe may require a different design. Nevertheless, polymer, hydrogel, and nanocomposite-based materials have been introduced as possible solutions to create softer devices and facilitate tissue integration[116]. The use of Parylene-C and polyimide is primarily motivated by the improvement in Young's modulus in comparison to metal- and silicon-based electrodes (Table 1.1). Likewise, hydrogel coatings have been implemented to create a softer, more tissue-friendly interface[117]. Newer approaches utilize materials that are initially rigid (facilitating insertion), but transition to more compliant materials following contact with the *in vivo* environment. Hybrids and composites, such as nanocomposites based off of the architecture and structure of sea cucumber dermis[118], allow for mechanical tuning *in vivo*[119]. Polyvinyl acetate structures enable changes in electrode compliancy to minimize the foreign body response[120],[118] via this mechanism. The biomimetic nanocomposite is comprised of a low modulus polymer and cellulose-based nanowhiskers that swell when hydrated or inserted in the brain, resulting in a decreased modulus due to increased water content by volume, on a timescale of 5 minutes. The tissue response was characterized by a 50μm neuronal "kill zone" and a decrease in glial reactivity[121],[122]. Similarly, thio-ene/acrylate substrates, polymerized via click chemistry reactions on the surface of the probe decrease shear modulus from 460 MPa to 2.3MPa. Softening of the substrate upon hydration, a week after implantation, facilitates neural function[123]. Substrates were an order of magnitude stiffer than tissue, but the modulus mismatch was reduced in comparison to stiffer substrates. Bioresorbable

interfaces, termed “live electrodes”, improve acute and short term foreign body response by utilizing biocompatible mesh/microporous structures that integrate with environment, minimize electrode-neuron distance, and support the mechanical and biochemical environment of the neurons[116]. Other biologically active compounds such as silk[124] and the fibroin derived enzyme, chondroitinase (chABC),[125] have been used to address the issue of mechanical mismatch by using the enzyme to dissolve the chondroitin layers of the scar tissue that encapsulates the probe.

3.2 DEVICE TETHERING

Tethering forces exerted by the connector configuration can also influence the tissue response. Traditional devices are generally either free-floating in the brain tissue (untethered), mounted to a connector fixed to skull-mounted bone screws (skull-fixed), or semi-floating (e.g. flexibly tethered to a connector via a ribbon cable encased in elastomer). Skull-fixed devices lack the ability to compensate for natural micromotion and swelling of the brain, which may lead to increased irritation and damage in interfacial tissue. In 2005, the mechanical effects of implanted CNS electrodes on surrounding tissue were investigated using finite element modelling. Device analogues for silicon, polyimide, and a hypothetical ‘soft’ material were evaluated *in silico,* and simulation results suggested that devices made from stiffer materials exacerbate shear strain along the device-tissue interface. Shear strain from skull-fixed devices can impact tissues out to 100um from the interface and result in delamination of tissue from the device. In turn, these effects may further aggravate the chronic immune response associated with implanted electrodes. The model produced in this paper suggested that interfacial strain

on host tissue could be mitigated by 65-94% by adopting more flexible materials such as polyimide[126]. These results were corroborated by *in vivo* results collected by different groups during evaluations of free floating and tethered cortical silicon devices[127], [128]. Histology showed that, in comparison to untethered counterparts, tethered devices elicit greater levels of immune response at the tissue interface. The depletion of local neurons, increase in GFAP positive astrocytes, and upregulation of ED1 positive microglia and macrophages were all notably worse surrounding tethered devices. Next-generation devices often adopt materials and architectures that may better accommodate micromotion and mitigate device-tissue strain, offsetting the relative impact of tethering on the tissue response. Nonetheless, it is still essential to consider device fixation as an additional design variable that can significantly impact the biocompatibility of implanted electrodes.

3.3 SURFACE FEATURES AND MODIFICATION STRATEGIES

Surface chemistry and topographical cues have received relatively lesser attention from the device design community than architecture and flexibility/softness; nonetheless, their impacts are inextricably intertwined with the incorporation of new materials in next-generation designs (Figure 1.1). The surface variables that can be measured and controlled are: hydrophilicity, chemistry, and surface topography. Contact angle/wettability measures surface energy, spectroscopy determines chemical composition, and scanning probe technique characterizes micro-level topography (Figure 1.2). While there are no field-standard guidelines, contact angles measured ideally should be low, indicating high surface energy in the range of 40-80dynes/cm. This is the range at

which materials are hydrophilic enough to favor hydrogen bonding between the biomaterial surface and surrounding fluid over the hydrophobic interactions which favor protein adsorption[129]. Foundational studies have reported the fundamental physical characteristics of the surfaces presented by materials commonly used in electrode design. Polyimide is a hydrophobic material (contact angle reported between 80-100°) with an associated high adsorption of proteins[130]. Nonetheless, it exhibits low cytotoxicity and hemolysis, in alignment with biocompatible materials that served as a benchmark in the study (Teflon® and Silastic®). Parylene-C is similarly hydrophobic and biocompatible, although plasma treatment can be used to render the surface hydrophilic[131]. Silicon has been shown to be comparatively less biocompatible (in terms of thrombogenicity) than its polymeric counterparts, Parylene and polyurethane[132]. SU-8, while generally regarded as a highly biocompatible polymer, reportedly displays similar hemocompatibility to silicon, with similar platelet reactivity and thrombogenicity[132].

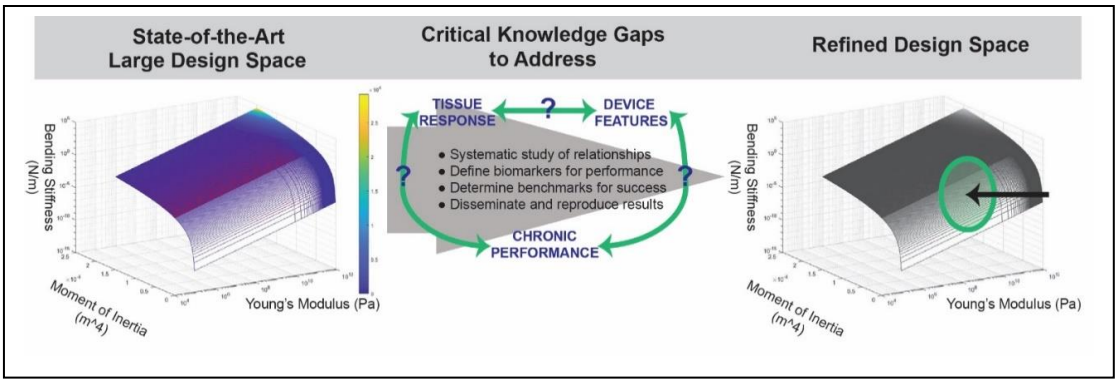

Figure 1.4: Toward the rational design of biologically-integrated electrodes. Currently, the relationships between device features, tissue response, and chronic performance are ill-defined, and the field has produced a wide variety of device designs encompassing a large parameter space (left panel). The systematic study of those relationships, identification of appropriate biomarkers for functional performance, and standardization of approaches (middle panel) may enable the definition of a refined parameter space, expediting the design process and increasing the likelihood of success (right panel).

Specific surface cues have been observed to be especially amenable to neuronal growth and responsiveness[133],[134],[135], and the dimensions of topographical features are known to influence effects: optimal promotion of neuronal growth occurs when the spatial pattern for controlled directionality matches the dimensions of neuronal growth cones[136]. Preliminary reports from Ereifej and colleagues in the Capadona lab suggest that nuanced topographical and architectural changes can impact the expression of pro-inflammatory factors surrounding neural implants. In an experiment where traditional planar probes were etched to form small, 200nm high grooves across the length of the probe, tumor necrosis factor alpha (TNFα), nitric oxide synthase (NOS2), and a chromatin protein, high mobility group box 1 (HMGB1), were upregulated in the un-etched devices. The patterned probes showed a downregulation of the lipopolysaccharide binding receptor CD14 expression over a 2-4-week time-period which may suggest a trend towards increased regeneration as microglia and monocyte populations return to baseline. These results suggest that smooth planar shanks may create a more continuous expression of interleukin 1 beta (IL1B), resulting in prolonged BBB leakage, and potentially upregulated TNFα and NOS2 as a downstream consequence[137].

Given the rationale for surface-mediated control of biocompatibility, numerous strategies have emerged in the field to influence biocompatibility through modifications to implanted electrode surface features (Figure 1.3). Biomimicry—making the device invisible to brain tissue by imitating its key features—is one strategy to address device failure and improve long term function and “mask” the device from its surroundings.

Biologically active materials such as L1 (neural adhesion molecule) have been coated on Parylene-C microwires and shown to decrease markers of apoptosis and astrogliosis at the injury site[138] and improve neuronal growth and survival around the implant[139]. Alpha melanocyte stimulating hormone (Alpha-MSH) [140] has also been proven to lower expression of markers of gliosis while chABC delivery likewise has been reported to reduce ionized calcium binding adaptor molecule (IBA1) and chondroitin sulfate (CS) expression[141]. Recently, Oakes *et al.* used a decellularized bovine astrocyte derived extracellular matrix (ECM), traditionally used in emergency rooms to promote wound healing, to coat Michigan-style arrays. The coating reduced the amount of astrogliosis, hemostatic activity, and macrophage activation *in vitro* [142]. However, the short life time of the coating limits an effective response to chronic or long-term foreign body response.

Drug-eluting or drug-presenting surfaces are another avenue to modulate device-tissue integration. Dexamethasone (DEX) coated[141] and DEX loaded probes[143] have been shown to decrease anti-chondroitin sulfate antibody (CS56), GFAP, and ED1 expression in surrounding tissue as well as reduce impedance by up to 25% for 9 days. However, there are also limitations surrounding long term tethering of biologically active molecules on these probes with reports of cracks in DEX film coatings at 4 weeks [144], and observations of the “burst effect”[145]. Future improvements may include prolonged drug release, better drug adherence to the surface, and increased drug loading/release for enhanced efficacy[144].

4. OUTLOOK: PERSPECTIVE ON CRITICAL KNOWLEDGE GAPS IN THE FIELD

While many of these approaches to improve tissue compatibility have delivered evidence of positive results, they also have saturated the field with a multitude of designs that change multiple variables simultaneously. Furthermore, foundational understanding of benchmarks for success, clear goals for longevity and integration, and standardization of approaches across users are lacking in the field. Here, we make recommendations for studies to be pursued to reconcile current barriers to progress to achieve a seamless, chronic electrode interface (Figure 1.4): *(1) A systematic study of the relationship between device design features (materials, architecture, flexibility), biointegration, and signal quality needs to be performed, and interaction effects between different features of design need to be parsed apart to reduce confounds in data interpretation.*

As reviewed above, several design aspects may influence the biocompatibility and signal detection of implanted electrode arrays in the brain. However, studies which explore these effects in a systematic way are scarce, and it is extremely challenging to truly parse apart individual effects. For instance, the effects of Young's modulus on tissue response may require the use of multiple material types to produce the desired range of flexibilities (e.g., silicon, polyimide, and off-stoichiometry thiol-enes-epoxy (OSTE+) polymer)[97]. While it is possible that the effects of surface chemistry could be negligible, there remains the potential for differences in topology, hydrophobicity, and cytotoxicity to affect results (Figure 1.2, 1.3). Furthermore, the surface charge, topography, size and geometry could all synergistically affect biocompatibility of the

device as a whole. A study published by Capadona and colleagues effectively decouples the impact of surface chemistry and substrate stiffness (in terms of Young's modulus) on the biocompatibility of implanted electrodes by coating all substrates with the identical polymer[146]. Nevertheless, bending stiffness and geometry remain important considerations to integrate into such analyses. If such effects could be studied in a more broadly systematic way, the value and interpretation of the data collected from these, and other studies, would be greatly enhanced. A central challenge is that the parameter space would be expansive, requiring a large sample size and an extensive observation set for each sample. However, prioritizing testing of selected high-value features of the greatest relevance for current designs could make this seemingly intractable study achievable.

(2) Benchmarks for success need to be determined (biological integration, recording performance, longevity, stability).

What makes a "good" chronic electrode? In terms of biocompatibility, what tests are the most relevant for predicting safety and performance? According to ISO 10993-1, because electrodes are permanent implant devices with external communication capabilities that come in contact with blood and brain tissue, probes should be subjected to cytotoxicity, sensitization, irritation, acute and subchronic toxicity, implantation, hemocompatibility, and carcinogenicity testing (ISO 10993) (**Supplementary Table 2**). However, relatively limited controlled biocompatibility testing occurs in pre-clinical reports, and read-outs heavily depend on metrics of neuronal and glial densities. Based on these metrics, it has been suggested that critical 'thresholds' of device flexibility and feature size can be identified for optimal device-tissue integration[82],[96] . Likewise, a

recent meta-analysis suggests that bending stiffness is the strongest design-related predictor of neuronal and glial responses[98]. However, available observations suggest that there is not a simple relationship between the traditional metrics of tissue response and chronic function[147], underscoring the need to better understand which aspects of the biological response to electrodes most profoundly and predictably affect their function. If those markers of the tissue response were identified, it may simplify and standardize assessment of the biological response to electrodes. For instance, are changes in cellular densities (neuronal and glial) most strongly predictive of device function, or are particular markers related to certain functional signalling pathways, or sub-cellular structural remodelling (as a few possibilities) the most important? While assessments of new electrode design almost invariably test their impact on local neuronal and glial densities, these metrics have not been validated as effective benchmarks for success in terms of recording quality: it may be the case that some other aspect of the biological response is more directly deterministic of functional outcomes.

Recent evidence suggests that chronic implantation of neural interfaces results in changes in intrinsic neuronal excitability at the protein level[28], [29]. The proteins that have been currently explored outside of cell type specific markers are ion channels and transporters that may influence cellular excitability. These data suggest that there may be effective biomarkers for biocompatibility of implanted devices that investigate mechanisms beyond cellular density. In order to drive the field forward in a more constructive way, it is imperative that future research includes a more thorough evaluation of biocompatibility at the cellular and molecular level. This would ideally

include traditional histological analyses as well as acute and chronic genetic changes at the transcriptional level[137]. In doing so, there is a possibility to define biocompatibility at a deeper level that results in identifying key bio-integrative electrode features and potential targets for intervention following implantation.

(3) User results and methods, particularly those that champion a specific design or electrode modification, need to be replicated across laboratories.

A related challenge is centered on the approach needed to unmask 'master' biological signalling pathways that influence performance: there is a need to identify more effective and reproducible testbeds to refine electrode design and benchmark results between technologies. Correlation between device functional metrics and histological outcomes may be a reasonable point of departure to assess device-tissue integration within individual labs, but ultimately, direct methods to determine the most relevant mechanisms with improved specificity and control will be required. Likewise, given the expansive set of potential pathways at play, the identification of the most important changes in protein or gene expression amongst the many available possibilities is a major challenge. Developing a high-throughput testbed to assess the impacts of design features on tissue response would be extremely valuable to the field. Likewise, incorporating broad-based assessment strategies which avoid pre-selecting targets of interest could reveal that the expression of unexpected targets which bear a stronger relationship with recording quality than previously-studied metrics. Accounting for inter-areal and inter-species differences will be important in these analyses, given the potential for brain microenvironment heterogeneity to influence results. Likewise, insertion methods vary

between users, and the relationship between chronic histology and the initial surgical approach should be studied. As an example, the presence of reactive astrogliosis surrounding “sewing machine devices” is notable, since the electrodes are designed with subcellular dimensions and are fabricated using materials that are regarded as highly biocompatible. It is also possible that unanticipated reactivity results due to the novel insertion method. Finally, since alterations in electrode design characteristics have the potential to influence not only the tissue response to implants, but also the electrical and mechanical performance of the devices, it will be critical to move towards standardization of electrophysiological metrics of success (longevity, signal-to-noise ratio, the number of units, site impedance, etc.) in the context of biocompatibility studies.

The combination of new federal funding initiatives, commercial ventures, and explosive growth in the number of medical applications for implanted electrode arrays has produced a groundswell of innovation in neurotechnology in recent years. However, many of these technologies have not achieved broad-based dissemination in the field, confining their impact to a few selected laboratories. A notable exception to this rule is the “Neuropixels” array, which has become more broadly available recently[48]. However, many laboratories may not have the capabilities, funding, or motivation to support the broad-based dissemination of their novel device designs to the field. Likewise, modifying electrodes with polymer coatings, biologics, topographical cues[137], [148] and related approaches often remains within the purview of the specific lab originating the technique. With respect to surface coatings, rapid degradation calls for the long-term characterization of the *in vivo* effects of these materials in the

brain[140],[144],[149],[141]. Corroborating results across laboratories should be a central focus of efforts in the field, in order to more systematically validate which designs produce improved tissue integration reproducibly. The need to standardize benchmarks for success goes hand-in-hand with identifying appropriate biomarkers for effective device-tissue integration.

5. CONCLUDING REMARKS

Devices implanted in the brain often simultaneously adopt different biomaterials, unique device architectures, and varying feature sizes within each design. As each lab adopts their own strategies and approaches, the field begins to fragment in a way that makes it difficult to empirically determine which device elements generate the most stable and biocompatible chronic interfaces. Additionally, the analysis of biocompatibility is often limited to neuronal density and glial scar analyses, and in some cases, neglected almost entirely. Neural interfaces have recently gained popularity in private industries, potentially broadening the accessibility of neurotechnology to the public. As such, it is increasingly important to rationally design devices which maximize safety and efficacy, including a fair assessment of performance relative to user expectations. Biological boundaries intrinsically create limitations to the design space of next generation electrode arrays. It is important to understand, define, and work within these limits to create devices with an optimized combination of performance and biocompatibility. New approaches to assess biocompatibility using a broader arsenal of technologies, including the analysis of gene expression, will create new avenues to assess biocompatibility in neurons and glia at the tissue interface. Likewise, standardizing

approaches, repeating results across laboratories, and performing systematic studies of the effects of device attributes on tissue response will be essential to move the field toward the rational design of seamlessly-integrated electrodes.

REFERENCES

[1] A. W. Laxton *et al.*, “A phase i trial of deep brain stimulation of memory circuits in Alzheimer’s disease,” *Ann. Neurol.*, vol. 68, no. 4, pp. 521–534, Oct. 2010, doi: 10.1002/ana.22089.

[2] J. Kuhn *et al.*, “Deep brain stimulation of the nucleus basalis of Meynert in Alzheimer’s dementia,” *Mol. Psychiatry*, vol. 20, no. 3, pp. 353–360, Mar. 2015, doi: 10.1038/mp.2014.32.

[3] J. V. Smit *et al.*, “Deep brain stimulation in tinnitus: Current and future perspectives,” *Brain Res.*, vol. 1608, pp. 51–65, 2015, doi: 10.1016/j.brainres.2015.02.050.

[4] G. S. Shekhawat *et al.*, “Intensity, duration, and location of high-definition transcranial direct current stimulation for tinnitus relief,” *Neurorehabil. Neural Repair*, vol. 30, no. 4, pp. 349–359, May 2016, doi: 10.1177/1545968315595286.

[5] L. R. Hochberg *et al.*, “Neuronal ensemble control of prosthetic devices by a human with tetraplegia,” *Nature*, vol. 442, no. 7099, pp. 164–171, Jul. 2006, doi: 10.1038/nature04970.

[6] B. MICROSYSTEMS, “US FDA 2005 NeuroPortTM Cortical Microelectrode Array System K042384”.

[7] J. L. Collinger *et al.*, “High-performance neuroprosthetic control by an individual with tetraplegia,” *Lancet*, vol. 381, no. 9866, pp. 557–564, Feb. 2013, doi: 10.1016/S0140-6736(12)61816-9.

[8] T. Aflalo *et al.*, “Decoding motor imagery from the posterior parietal cortex of a tetraplegic human,” *Science (80-.).*, vol. 348, no. 6237, pp. 906–910, May 2015, doi: 10.1126/science.aaa5417.

[9] C. E. Bouton *et al.*, “Restoring cortical control of functional movement in a human with quadriplegia,” *Nature*, vol. 533, no. 7602, pp. 247–250, May 2016, doi: 10.1038/nature17435.

[10] F. T. Sun, M. J. Morrell, and R. E. Wharen, “Responsive Cortical Stimulation for

the Treatment of Epilepsy," *Neurotherapeutics*, vol. 5, no. 1, pp. 68–74, Jan. 2008, doi: 10.1016/j.nurt.2007.10.069.

[11] E. J. Quinn *et al.*, "Beta oscillations in freely moving Parkinson's subjects are attenuated during deep brain stimulation," *Mov. Disord.*, vol. 30, no. 13, pp. 1750–1758, Nov. 2015, doi: 10.1002/mds.26376.

[12] P. J. Grahn *et al.*, "A neurochemical closed-loop controller for deep brain stimulation: Toward individualized smart neuromodulation therapies," *Front. Neurosci.*, vol. 8, no. 8 JUN, p. 169, Jun. 2014, doi: 10.3389/fnins.2014.00169.

[13] A. L. Crowell, P. Riva-Posse, S. J. Garlow, and H. S. Mayberg, "Toward an Understanding of the Neural Circuitry of Major Depressive Disorder Through the Clinical Response to Deep Brain Stimulation of Different Anatomical Targets," *Curr. Behav. Neurosci. Reports*, vol. 1, no. 2, pp. 55–63, Jun. 2014, doi: 10.1007/s40473-014-0008-z.

[14] D. M. Whiting *et al.*, "Lateral hypothalamic area deep brain stimulation for refractory obesity: A pilot study with preliminary data on safety, body weight, and energy metabolism: Clinical article," *J. Neurosurg.*, vol. 119, no. 1, pp. 56–63, Jul. 2013, doi: 10.3171/2013.2.JNS12903.

[15] A. L. Ho, E. S. Sussman, A. V. Pendharkar, D. E. Azagury, C. Bohon, and C. H. Halpern, "Deep brain stimulation for obesity: Rationale and approach to trial design," *Neurosurg. Focus*, vol. 38, no. 6, p. E8, Jun. 2015, doi: 10.3171/2015.3.FOCUS1538.

[16] J. Rotsides and A. Mammis, "The use of deep brain stimulation in Tourette's syndrome," *Neurosurg. Focus*, vol. 35, no. 5, p. E4, Nov. 2013, doi: 10.3171/2013.8.FOCUS13292.

[17] D. R. Moore and R. V. Shannon, "Beyond cochlear implants: Awakening the deafened brain," *Nat. Neurosci.*, vol. 12, no. 6, pp. 686–691, Jun. 2009, doi: 10.1038/nn.2326.

[18] H. H. Lim and T. Lenarz, "Auditory midbrain implant: Research and development towards a second clinical trial," *Hear. Res.*, vol. 322, no. 1, pp. 212–223, Apr. 2015, doi: 10.1016/j.heares.2015.01.006.

[19] P. M. Lewis, H. M. Ackland, A. J. Lowery, and J. V. Rosenfeld, “Restoration of vision in blind individuals using bionic devices: A review with a focus on cortical visual prostheses,” *Brain Res.*, vol. 1595, pp. 51–73, Jan. 2015, doi: 10.1016/j.brainres.2014.11.020.

[20] H. T. Peters, D. J. Edwards, S. Wortman-Jutt, and S. J. Page, “Moving forward by stimulating the brain: Transcranial direct current stimulation in post-stroke hemiparesis,” *Front. Hum. Neurosci.*, vol. 10, p. 8, Aug. 2016, doi: 10.3389/fnhum.2016.00394.

[21] B. Rosin *et al.*, “Closed-loop deep brain stimulation is superior in ameliorating parkinsonism,” *Neuron*, vol. 72, no. 2, pp. 370–384, Oct. 2011, doi: 10.1016/j.neuron.2011.08.023.

[22] J. A. Perge *et al.*, “Intra-day signal instabilities affect decoding performance in an intracortical neural interface system,” *J. Neural Eng.*, vol. 10, no. 3, p. 036004, Jun. 2013, doi: 10.1088/1741-2560/10/3/036004.

[23] A. Prasad and J. C. Sanchez, “Quantifying long-term microelectrode array functionality using chronic in vivo impedance testing,” *J. Neural Eng.*, vol. 9, no. 2, p. 026028, Apr. 2012, doi: 10.1088/1741-2560/9/2/026028.

[24] D. B. McCreery, T. G. H. Yuen, W. F. Agnew, and L. A. Bullara, “A characterization of the effects on neuronal excitability due to prolonged microstimulation with chronically implanted microelectrodes,” *IEEE Trans. Biomed. Eng.*, vol. 44, no. 10, pp. 931–939, 1997, doi: 10.1109/10.634645.

[25] D. B. McCreery, W. F. Agnew, and L. A. Bullara, “The effects of prolonged intracortical microstimulation on the excitability of pyramidal tract neurons in the cat,” *Ann. Biomed. Eng.*, vol. 30, no. 1, pp. 107–119, Jan. 2002, doi: 10.1114/1.1430748.

[26] V. S. Polikov, P. A. Tresco, and W. M. Reichert, “Response of brain tissue to chronically implanted neural electrodes,” *J. Neurosci. Methods*, vol. 148, no. 1, pp. 1–18, 2005, doi: 10.1016/j.jneumeth.2005.08.015.

[27] J. W. Salatino, K. A. Ludwig, T. D. Y. Kozai, and E. K. Purcell, “Erratum:

Publisher Correction: Glial responses to implanted electrodes in the brain (Nature biomedical engineering (2017) 1 11 (862-877)),” *Nat. Biomed. Eng.*, vol. 2, no. 1, p. 52, Jan. 2018, doi: 10.1038/s41551-017-0177-7.

[28] J. W. Salatino, A. P. Kale, and E. K. Purcell, “Alterations in Ion Channel Expression Surrounding Implanted Microelectrode Arrays in the Brain,” *bioRxiv*, p. 518811, 2019, doi: 10.1101/518811.

[29] J. W. Salatino, B. M. Winter, M. H. Drazin, and E. K. Purcell, “Functional remodeling of subtype-specific markers surrounding implanted neuroprostheses,” *J. Neurophysiol.*, vol. 118, no. 1, pp. 194–202, Jul. 2017, doi: 10.1152/jn.00162.2017.

[30] J. R. Eles, A. L. Vazquez, T. D. Y. Kozai, and X. T. Cui, “In vivo imaging of neuronal calcium during electrode implantation: Spatial and temporal mapping of damage and recovery,” *Biomaterials*, vol. 174, pp. 79–94, Aug. 2018, doi: 10.1016/j.biomaterials.2018.04.043.

[31] M. Goss-Varley *et al.*, “Microelectrode implantation in motor cortex causes fine motor deficit: Implications on potential considerations to Brain Computer Interfacing and Human Augmentation,” *Sci. Rep.*, vol. 7, no. 1, p. 15254, Dec. 2017, doi: 10.1038/s41598-017-15623-y.

[32] M. Oberlaender, Z. S. R. M. Boudewijns, T. Kleele, H. D. Mansvelder, B. Sakmann, and C. P. J. De Kock, “Three-dimensional axon morphologies of individual layer 5 neurons indicate cell type-specific intracortical pathways for whisker motion and touch,” *Proc. Natl. Acad. Sci. U. S. A.*, vol. 108, no. 10, pp. 4188–4193, Mar. 2011, doi: 10.1073/pnas.1100647108.

[33] Y. Kubota, “Untangling GABAergic wiring in the cortical microcircuit,” *Curr. Opin. Neurobiol.*, vol. 26, pp. 7–14, Jun. 2014, doi: 10.1016/j.conb.2013.10.003.

[34] S. M. Wellman and T. D. Y. Kozai, “In vivo spatiotemporal dynamics of NG2 glia activity caused by neural electrode implantation,” *Biomaterials*, vol. 164, pp. 121–133, May 2018, doi: 10.1016/j.biomaterials.2018.02.037.

[35] Y. Zhang and B. A. Barres, “Astrocyte heterogeneity: An underappreciated topic in neurobiology,” *Curr. Opin. Neurobiol.*, vol. 20, no. 5, pp. 588–594, Oct. 2010,

doi: 10.1016/j.conb.2010.06.005.

[36] A. Buffo, C. Rolando, and S. Ceruti, “Astrocytes in the damaged brain: Molecular and cellular insights into their reactive response and healing potential,” *Biochem. Pharmacol.*, vol. 79, no. 2, pp. 77–89, Jan. 2010, doi: 10.1016/j.bcp.2009.09.014.

[37] S. A. Liddelow *et al.*, “Neurotoxic reactive astrocytes are induced by activated microglia,” *Nature*, vol. 541, no. 7638, pp. 481–487, 2017, doi: 10.1038/nature21029.

[38] R. Biran, D. C. Martin, and P. A. Tresco, “Neuronal cell loss accompanies the brain tissue response to chronically implanted silicon microelectrode arrays,” *Exp. Neurol.*, vol. 195, no. 1, pp. 115–126, Sep. 2005, doi: 10.1016/j.expneurol.2005.04.020.

[39] G. Hong and C. M. Lieber, “Novel electrode technologies for neural recordings,” *Nat. Rev. Neurosci.*, vol. 20, no. 6, pp. 330–345, Jun. 2019, doi: 10.1038/s41583-019-0140-6.

[40] L. Cabrera, C. Sadle, and E. Purcell, “Neuroethical considerations of high-density electrode arrays,” *Nat. Biomed. Eng.*, vol. 3, no. 8, pp. 586–589, Aug. 2019, doi: 10.1038/s41551-019-0407-2.

[41] J. C. COLLIAS and E. E. MANUELIDIS, “Histopathological changes produced by implanted electrodes in cat brains; comparison with histopathological changes in human and experimental puncture wounds,” *J. Neurosurg.*, vol. 14, no. 3, pp. 302–328, May 1957, doi: 10.3171/jns.1957.14.3.0302.

[42] X. Liu, D. B. McCreery, R. R. Carter, L. A. Bullara, T. G. H. Yuen, and W. F. Agnew, “Stability of the interface between neural tissue and chronically implanted intracortical microelectrodes,” *IEEE Trans. Rehabil. Eng.*, vol. 7, no. 3, pp. 315–326, 1999, doi: 10.1109/86.788468.

[43] B. D. Winslow and P. A. Tresco, “Quantitative analysis of the tissue response to chronically implanted microwire electrodes in rat cortex,” *Biomaterials*, vol. 31, no. 7, pp. 1558–1567, 2010, doi: 10.1016/j.biomaterials.2009.11.049.

[44] K. L. Drake, K. D. Wise, J. Farraye, D. J. Anderson, and S. L. BeMent,

"Performance of Planar Multisite Microprobes in Recording Extracellular Single-Unit Intracortical Activity," *IEEE Trans. Biomed. Eng.*, vol. 35, no. 9, pp. 719–732, 1988, doi: 10.1109/10.7273.

[45] R. J. Vetter, J. C. Williams, J. F. Hetke, E. A. Nunamaker, and D. R. Kipke, "Chronic neural recording using silicon-substrate microelectrode arrays implanted in cerebral cortex," *IEEE Trans. Biomed. Eng.*, vol. 51, no. 6, pp. 896–904, Jun. 2004, doi: 10.1109/TBME.2004.826680.

[46] D. A. Henze, Z. Borhegyi, J. Csicsvari, A. Mamiya, K. D. Harris, and G. Buzsáki, "Intracellular features predicted by extracellular recordings in the hippocampus in vivo," *J. Neurophysiol.*, vol. 84, no. 1, pp. 390–400, Jul. 2000, doi: 10.1152/jn.2000.84.1.390.

[47] J. L. Shobe, L. D. Claar, S. Parhami, K. I. Bakhurin, and S. C. Masmanidis, "Brain activity mapping at multiple scales with silicon microprobes containing 1,024 electrodes," *J. Neurophysiol.*, vol. 114, no. 3, pp. 2043–2052, Sep. 2015, doi: 10.1152/jn.00464.2015.

[48] J. J. Jun *et al.*, "Fully integrated silicon probes for high-density recording of neural activity," *Nature*, vol. 551, no. 7679, pp. 232–236, Nov. 2017, doi: 10.1038/nature24636.

[49] C. Mora Lopez *et al.*, "A Neural Probe with Up to 966 Electrodes and Up to 384 Configurable Channels in 0.13 μm SOI CMOS," *IEEE Trans. Biomed. Circuits Syst.*, vol. 11, no. 3, pp. 510–522, 2017, doi: 10.1109/TBCAS.2016.2646901.

[50] C. T. Nordhausen, E. M. Maynard, and R. A. Normann, "Single unit recording capabilities of a 100 microelectrode array," *Brain Res.*, vol. 726, no. 1–2, pp. 129–140, Jul. 1996, doi: 10.1016/0006-8993(96)00321-6.

[51] R. A. Normann, E. M. Maynard, P. J. Rousche, and D. J. Warren, "A neural interface for a cortical vision prosthesis," *Vision Res.*, vol. 39, no. 15, pp. 2577–2587, Jul. 1999, doi: 10.1016/S0042-6989(99)00040-1.

[52] R. Bhandari, S. Negi, L. Rieth, R. A. Normann, and F. Solzbacher, "A novel masking method for high aspect ratio penetrating microelectrode arrays," *J. Micromechanics Microengineering*, vol. 19, no. 3, p. 035004, Mar. 2009, doi:

10.1088/0960-1317/19/3/035004.

[53] K. A. Malaga *et al.*, “Data-driven model comparing the effects of glial scarring and interface interactions on chronic neural recordings in non-human primates,” *J. Neural Eng.*, vol. 13, no. 1, p. 016010, Feb. 2015, doi: 10.1088/1741-2560/13/1/016010.

[54] M. D. Serruya, N. G. Hatsopoulos, L. Paninski, M. R. Fellows, and J. P. Donoghue, “Instant neural control of a movement signal,” *Nature*, vol. 416, no. 6877, pp. 141–142, Mar. 2002, doi: 10.1038/416141a.

[55] G. Santhanam, S. I. Ryu, B. M. Yu, A. Afshar, and K. V. Shenoy, “A high-performance brain-computer interface,” *Nature*, vol. 442, no. 7099, pp. 195–198, 2006, doi: 10.1038/nature04968.

[56] J. C. Barrese *et al.*, “Failure mode analysis of silicon-based intracortical microelectrode arrays in non-human primates,” *J. Neural Eng.*, vol. 10, no. 6, p. 066014, Dec. 2013, doi: 10.1088/1741-2560/10/6/066014.

[57] S. P. Kim, J. D. Simeral, L. R. Hochberg, J. P. Donoghue, and M. J. Black, “Neural control of computer cursor velocity by decoding motor cortical spiking activity in humans with tetraplegia,” *J. Neural Eng.*, vol. 5, no. 4, pp. 455–476, Dec. 2008, doi: 10.1088/1741-2560/5/4/010.

[58] A. Bullard, “Feasibility of Using the Utah Array for Long-Term Fully Implantable Neuroprosthesis Systems,” University of Michigan, 2019. doi: .1037//0033-2909.I26.1.78.

[59] L. R. Hochberg *et al.*, “Reach and grasp by people with tetraplegia using a neurally controlled robotic arm,” *Nature*, vol. 485, no. 7398, pp. 372–375, May 2012, doi: 10.1038/nature11076.

[60] V. Gilja *et al.*, “Clinical translation of a high-performance neural prosthesis,” *Nat. Med.*, vol. 21, no. 10, pp. 1142–1145, Oct. 2015, doi: 10.1038/nm.3953.

[61] A. B. Ajiboye *et al.*, “Restoration of reaching and grasping movements through brain-controlled muscle stimulation in a person with tetraplegia: a proof-of-concept demonstration,” *Lancet*, vol. 389, no. 10081, pp. 1821–1830, May 2017,

doi: 10.1016/S0140-6736(17)30601-3.

[62] E. M. Maynard, E. Fernandez, and R. A. Normann, “A technique to prevent dural adhesions to chronically implanted microelectrode arrays,” *J. Neurosci. Methods*, vol. 97, no. 2, pp. 93–101, Apr. 2000, doi: 10.1016/S0165-0270(00)00159-X.

[63] J. D. Simeral, S. P. Kim, M. J. Black, J. P. Donoghue, and L. R. Hochberg, “Neural control of cursor trajectory and click by a human with tetraplegia 1000 days after implant of an intracortical microelectrode array,” *J. Neural Eng.*, vol. 8, no. 2, p. 025027, Apr. 2011, doi: 10.1088/1741-2560/8/2/025027.

[64] J. C. Kao, P. Nuyujukian, S. I. Ryu, and K. V. Shenoy, “A High-Performance Neural Prosthesis Incorporating Discrete State Selection with Hidden Markov Models,” *IEEE Trans. Biomed. Eng.*, vol. 64, no. 4, pp. 935–945, Apr. 2017, doi: 10.1109/TBME.2016.2582691.

[65] C. A. Chestek *et al.*, “Long-term stability of neural prosthetic control signals from silicon cortical arrays in rhesus macaque motor cortex,” *J. Neural Eng.*, vol. 8, no. 4, p. 045005, Aug. 2011, doi: 10.1088/1741-2560/8/4/045005.

[66] N. F. Nolta, M. B. Christensen, P. D. Crane, J. L. Skousen, and P. A. Tresco, “BBB leakage, astrogliosis, and tissue loss correlate with silicon microelectrode array recording performance,” *Biomaterials*, vol. 53, pp. 753–762, Jun. 2015, doi: 10.1016/j.biomaterials.2015.02.081.

[67] P. A. Cody, J. R. Eles, C. F. Lagenaur, T. D. Y. Kozai, and X. T. Cui, “Unique electrophysiological and impedance signatures between encapsulation types: An analysis of biological Utah array failure and benefit of a biomimetic coating in a rat model,” *Biomaterials*, vol. 161, pp. 117–128, Apr. 2018, doi: 10.1016/j.biomaterials.2018.01.025.

[68] K. T. Wachrathit *et al.*, “Biotic response to long-term implantation of neural electrodes in the mouse motor cortex,” in *2013 6th International IEEE/EMBS Conference on Neural Engineering*, 2013.

[69] R. Caldwell *et al.*, “Neural electrode resilience against dielectric damage may be improved by use of highly doped silicon as a conductive material,” *J. Neurosci. Methods*, vol. 293, pp. 210–225, Jan. 2018, doi: 10.1016/j.jneumeth.2017.10.002.

[70] R. Caldwell, M. G. Street, R. Sharma, P. Takmakov, B. Baker, and L. Rieth, "Characterization of Parylene-C degradation mechanisms: In vitro reactive accelerated aging model compared to multiyear in vivo implantation," *Biomaterials*, vol. 232, 2020, doi: 10.1016/j.biomaterials.2019.119731.

[71] P. Takmakov, K. Ruda, K. Scott Phillips, I. S. Isayeva, V. Krauthamer, and C. G. Welle, "Rapid evaluation of the durability of cortical neural implants using accelerated aging with reactive oxygen species," *J. Neural Eng.*, vol. 12, no. 2, p. 026003, Apr. 2015, doi: 10.1088/1741-2560/12/2/026003.

[72] C. Xie, J. Liu, T. M. Fu, X. Dai, W. Zhou, and C. M. Lieber, "Three-dimensional macroporous nanoelectronic networks as minimally invasive brain probes," *Nat. Mater.*, vol. 14, no. 12, pp. 1286–1292, Dec. 2015, doi: 10.1038/nmat4427.

[73] J. Liu *et al.*, "Syringe-injectable electronics," *Nat. Nanotechnol.*, vol. 10, no. 7, pp. 629–635, 2015, doi: 10.1038/nnano.2015.115.

[74] T. G. Schuhmann *et al.*, "Syringe-injectable mesh electronics for stable chronic rodent electrophysiology," *J. Vis. Exp.*, vol. 2018, no. 137, pp. 1–15, Jul. 2018, doi: 10.3791/58003.

[75] T. G. Schuhmann, J. Yao, G. Hong, T. M. Fu, and C. M. Lieber, "Syringe-Injectable Electronics with a Plug-and-Play Input/Output Interface," *Nano Lett.*, vol. 17, no. 9, pp. 5836–5842, Sep. 2017, doi: 10.1021/acs.nanolett.7b03081.

[76] T. Zhou *et al.*, "Syringe-injectable mesh electronics integrate seamlessly with minimal chronic immune response in the brain," *Proc. Natl. Acad. Sci. U. S. A.*, vol. 114, no. 23, pp. 5894–5899, Jun. 2017, doi: 10.1073/pnas.1705509114.

[77] X. Yang *et al.*, "Bioinspired neuron-like electronics," *Nat. Mater.*, vol. 18, no. 5, pp. 510–517, May 2019, doi: 10.1038/s41563-019-0292-9.

[78] J. K. Trevathan *et al.*, "An Injectable Neural Stimulation Electrode Made from an In-Body Curing Polymer/Metal Composite," *Adv. Healthc. Mater.*, vol. 8, no. 23, p. 1900892, Dec. 2019, doi: 10.1002/adhm.201900892.

[79] H. Xu *et al.*, "Design of a flexible parylene-based multi-electrode array for multi-

region recording from the rat hippocampus," in *Proceedings of the Annual International Conference of the IEEE Engineering in Medicine and Biology Society, EMBS*, Aug. 2015, vol. 2015-Novem, no. August, pp. 7139–7142. doi: 10.1109/EMBC.2015.7320038.

[80] H. Xu, A. Weltman, K. Scholten, E. Meng, T. W. Berger, and D. Song, "Chronic multi-region recording from the rat hippocampus in vivo with a flexible Parylene-based multi-electrode array," in *Proceedings of the Annual International Conference of the IEEE Engineering in Medicine and Biology Society, EMBS*, Jul. 2017, pp. 1716–1719. doi: 10.1109/EMBC.2017.8037173.

[81] S. A. Hara, B. J. Kim, J. T. W. Kuo, C. D. Lee, E. Meng, and V. Pikov, "Long-term stability of intracortical recordings using perforated and arrayed Parylene sheath electrodes," *J. Neural Eng.*, vol. 13, no. 6, p. 066020, Dec. 2016, doi: 10.1088/1741-2560/13/6/066020.

[82] J. P. Seymour and D. R. Kipke, "Neural probe design for reduced tissue encapsulation in CNS," *Biomaterials*, vol. 28, no. 25, pp. 3594–3607, Sep. 2007, doi: 10.1016/j.biomaterials.2007.03.024.

[83] E. K. Purcell, J. P. Seymour, S. Yandamuri, and D. R. Kipke, "In vivo evaluation of a neural stem cell-seeded prosthesis.," *J. Neural Eng.*, vol. 6, no. 2, p. 026005, Apr. 2009, doi: 10.1088/1741-2560/6/2/026005.

[84] E. K. Purcell, A. Singh, and D. R. Kipke, "Alginate composition effects on a neural stem cell-seeded scaffold," *Tissue Eng. - Part C Methods*, vol. 15, no. 4, pp. 541–550, Dec. 2009, doi: 10.1089/ten.tec.2008.0302.

[85] P. J. Rousche, D. S. Pellinen, D. P. Pivin, J. C. Williams, R. J. Vetter, and D. R. Kipke, "Flexible polyimide-based intracortical electrode arrays with bioactive capability," *IEEE Trans. Biomed. Eng.*, vol. 48, no. 3, pp. 361–370, Mar. 2001, doi: 10.1109/10.914800.

[86] A. Tooker *et al.*, "Optimization of multi-layer metal neural probe design," in *Proceedings of the Annual International Conference of the IEEE Engineering in Medicine and Biology Society, EMBS*, Aug. 2012, pp. 5995–5998. doi: 10.1109/EMBC.2012.6347360.

[87] J. E. Chung *et al.*, “High-Density, Long-Lasting, and Multi-region Electrophysiological Recordings Using Polymer Electrode Arrays,” *Neuron*, vol. 101, no. 1, pp. 21-31.e5, Jan. 2019, doi: 10.1016/j.neuron.2018.11.002.

[88] X. Wei *et al.*, “Nanofabricated Ultraflexible Electrode Arrays for High-Density Intracortical Recording,” *Adv. Sci.*, vol. 5, no. 6, p. 1700625, Jun. 2018, doi: 10.1002/advs.201700625.

[89] T. L. Hanson, C. A. Diaz-Botia, V. Kharazia, M. M. Maharbiz, and P. N. Sabes, “The ‘sewing machine’ for minimally invasive neural recording,” *bioRxiv*, no. 1, p. 578542, 2019, doi: 10.1101/578542.

[90] Z. J. Du *et al.*, “Ultrasoft microwire neural electrodes improve chronic tissue integration,” *Acta Biomater.*, vol. 53, pp. 46–58, 2017, doi: 10.1016/j.actbio.2017.02.010.

[91] T. D. Yoshida Kozai *et al.*, “Ultrasmall implantable composite microelectrodes with bioactive surfaces for chronic neural interfaces,” *Nat. Mater.*, vol. 11, no. 12, pp. 1065–1073, 2012, doi: 10.1038/nmat3468.

[92] P. R. Patel *et al.*, “Insertion of linear 8.4 μm diameter 16 channel carbon fiber electrode arrays for single unit recordings,” *J. Neural Eng.*, vol. 12, no. 4, p. 046009, Aug. 2015, doi: 10.1088/1741-2560/12/4/046009.

[93] P. R. Patel *et al.*, “Chronic in vivo stability assessment of carbon fiber microelectrode arrays,” *J. Neural Eng.*, vol. 13, no. 6, p. 066002, Dec. 2016, doi: 10.1088/1741-2560/13/6/066002.

[94] T. D. Y. Kozai, A. S. Jaquins-Gerstl, A. L. Vazquez, A. C. Michael, and X. T. Cui, “Brain tissue responses to neural implants impact signal sensitivity and intervention strategies,” *ACS Chem. Neurosci.*, vol. 6, no. 1, pp. 48–67, Jan. 2015, doi: 10.1021/cn500256e.

[95] C. A. Rusinek *et al.*, “All-Diamond Microfiber Electrodes for Neurochemical Analysis,” *J. Electrochem. Soc.*, vol. 165, no. 12, pp. G3087–G3092, Jul. 2018, doi: 10.1149/2.0141812jes.

[96] D. H. Szarowski *et al.*, “Brain responses to micro-machined silicon devices,”

Brain Res., vol. 983, no. 1–2, pp. 23–35, Sep. 2003, doi: 10.1016/S0006-8993(03)03023-3.

[97] H. C. Lee *et al.*, "Histological evaluation of flexible neural implants; Flexibility limit for reducing the tissue response?," *J. Neural Eng.*, vol. 14, no. 3, p. 036026, Jun. 2017, doi: 10.1088/1741-2552/aa68f0.

[98] A. M. Stiller *et al.*, "A meta-analysis of intracortical device stiffness and its correlation with histological outcomes," *Micromachines*, vol. 9, no. 9, p. 443, Sep. 2018, doi: 10.3390/mi9090443.

[99] F. Shen, T. E. Tay, J. Z. Li, S. Nigen, P. V. S. Lee, and H. K. Chan, "Modified Bilston nonlinear viscoelastic model for finite element head injury studies," *J. Biomech. Eng.*, vol. 128, no. 5, pp. 797–801, Oct. 2006, doi: 10.1115/1.2264393.

[100] L. Luan *et al.*, "Ultraflexible nanoelectronic probes form reliable, glial scar–free neural integration," *Sci. Adv.*, vol. 3, no. 2, p. e1601966, Feb. 2017, doi: 10.1126/sciadv.1601966.

[101] D. C. Stewart, A. Rubiano, K. Dyson, and C. S. Simmons, "Mechanical characterization of human brain tumors from patients and comparison to potential surgical phantoms," *PLoS One*, vol. 12, no. 6, p. e0177561, Jun. 2017, doi: 10.1371/journal.pone.0177561.

[102] S. A. Lippert, E. M. Rang, and M. J. Grimm, "The high frequency properties of brain tissue," *Biorheology*, vol. 41, no. 6, pp. 681–691, 2004.

[103] B. Rashid, M. Destrade, and M. D. Gilchrist, "Mechanical characterization of brain tissue in tension at dynamic strain rates," *J. Mech. Behav. Biomed. Mater.*, vol. 33, no. 1, pp. 43–54, May 2014, doi: 10.1016/j.jmbbm.2012.07.015.

[104] A. TAMURA, S. HAYASHI, I. WATANABE, K. NAGAYAMA, and T. MATSUMOTO, "Mechanical Characterization of Brain Tissue in High-Rate Compression," *J. Biomech. Sci. Eng.*, vol. 2, no. 3, pp. 115–126, 2007, doi: 10.1299/jbse.2.115.

[105] X. Jin, F. Zhu, H. Mao, M. Shen, and K. H. Yang, "A comprehensive experimental study on material properties of human brain tissue," *J. Biomech.*,

vol. 46, no. 16, pp. 2795–2801, Nov. 2013, doi: 10.1016/j.jbiomech.2013.09.001.

[106] T. Luque, M. S. Kang, D. V. Schaffer, and S. Kumar, “Microelastic mapping of the rat dentate gyrus,” *R. Soc. Open Sci.*, vol. 3, no. 4, p. 150702, Apr. 2016, doi: 10.1098/rsos.150702.

[107] P. G. Carlier, D. Bertoldi, C. Baligand, C. Wary, and Y. Fromes, “Muscle blood flow and oxygenation measured by NMR,” *NMR Biomed.*, vol. 21, pp. 954–967, 2006, doi: 10.1002/nbm.

[108] J. Vappou, E. Breton, P. Choquet, C. Goetz, R. Willinger, and A. Constantinesco, “Magnetic resonance elastography compared with rotational rheometry for in vitro brain tissue viscoelasticity measurement,” *Magn. Reson. Mater. Physics, Biol. Med.*, vol. 20, no. 5–6, pp. 273–278, Dec. 2007, doi: 10.1007/s10334-007-0098-7.

[109] K. Pogoda *et al.*, “Compression stiffening of brain and its effect on mechanosensing by glioma cells,” *New J. Phys.*, vol. 16, no. 7, p. 075002, Jul. 2014, doi: 10.1088/1367-2630/16/7/075002.

[110] S. M. Atay, C. D. Kroenke, A. Sabet, and P. V. Bayly, “Measurement of the dynamic shear modulus of mouse brain tissue in vivo by magnetic resonance elastography,” *J. Biomech. Eng.*, vol. 130, no. 2, p. 021013, 2008, doi: 10.1115/1.2899575.

[111] D. Chauvet *et al.*, “In Vivo Measurement of Brain Tumor Elasticity Using Intraoperative Shear Wave Elastography,” *Ultraschall der Medizin - Eur. J. Ultrasound*, vol. 37, no. 06, pp. 584–590, Apr. 2015, doi: 10.1055/s-0034-1399152.

[112] Z. Taylor and K. Miller, “Reassessment of brain elasticity for analysis of biomechanisms of hydrocephalus,” *J. Biomech.*, vol. 37, no. 8, pp. 1263–1269, Aug. 2004, doi: 10.1016/j.jbiomech.2003.11.027.

[113] P. S. Nakod, Y. Kim, and S. S. Rao, “Biomimetic models to examine microenvironmental regulation of glioblastoma stem cells,” *Cancer Lett.*, vol. 429, no. February, pp. 41–53, Aug. 2018, doi: 10.1016/j.canlet.2018.05.007.

[114] E. I. Fomchenko and E. C. Holland, “Mouse models of brain tumors and their applications in preclinical trials,” *Clin. Cancer Res.*, vol. 12, no. 18, pp. 5288–5297, Sep. 2006, doi: 10.1158/1078-0432.CCR-06-0438.

[115] S. Budday *et al.*, “Mechanical characterization of human brain tissue,” *Acta Biomater.*, vol. 48, pp. 319–340, Jan. 2017, doi: 10.1016/j.actbio.2016.10.036.

[116] S. P. Lacour, G. Courtine, and J. Guck, “Materials and technologies for soft implantable neuroprostheses,” *Nat. Rev. Mater.*, vol. 1, no. 10, p. 16063, Oct. 2016, doi: 10.1038/natrevmats.2016.63.

[117] D. H. Kim, M. Abidian, and D. C. Martin, “Conducting polymers grown in hydrogel scaffolds coated on neural prosthetic devices,” *J. Biomed. Mater. Res. - Part A*, vol. 71, no. 4, pp. 577–585, Dec. 2004, doi: 10.1002/jbm.a.30124.

[118] J. R. Capadona, D. J. Tyler, C. A. Zorman, S. J. Rowan, and C. Weder, “Mechanically adaptive nanocomposites for neural interfacing,” *MRS Bull.*, vol. 37, no. 6, pp. 581–589, Jun. 2012, doi: 10.1557/mrs.2012.97.

[119] R. Green and M. R. Abidian, “Conducting Polymers for Neural Prosthetic and Neural Interface Applications,” *Adv. Mater.*, vol. 27, no. 46, pp. 7620–7637, Dec. 2015, doi: 10.1002/adma.201501810.

[120] A. E. Hess *et al.*, “Development of a stimuli-responsive polymer nanocomposite toward biologically optimized, MEMS-based neural probes,” *J. Micromechanics Microengineering*, vol. 21, no. 5, p. 054009, May 2011, doi: 10.1088/0960-1317/21/5/054009.

[121] J. K. Nguyen *et al.*, “Mechanically-compliant intracortical implants reduce the neuroinflammatory response,” *J. Neural Eng.*, vol. 11, no. 5, p. 056014, Oct. 2014, doi: 10.1088/1741-2560/11/5/056014.

[122] J. R. Capadona, K. Shanmuganathan, D. J. Tyler, S. J. Rowan, and C. Weder, “Stimuli-responsive polymer nanocomposites inspired by the sea cucumber dermis,” *Science (80-.).*, vol. 319, no. 5868, pp. 1370–1374, Mar. 2008, doi: 10.1126/science.1153307.

[123] T. Ware *et al.*, “Thiol-ene/acrylate substrates for softening intracortical

electrodes," *J. Biomed. Mater. Res. - Part B Appl. Biomater.*, vol. 102, no. 1, pp. 1–11, Jan. 2014, doi: 10.1002/jbmb.32946.

[124] L. W. Tien, F. Wu, M. D. Tang-Schomer, E. Yoon, F. G. Omenetto, and D. L. Kaplan, "Silk as a multifunctional biomaterial substrate for reduced glial scarring around brain-penetrating electrodes," *Adv. Funct. Mater.*, vol. 23, no. 25, pp. 3185–3193, Jul. 2013, doi: 10.1002/adfm.201203716.

[125] D. H. Kim *et al.*, "Dissolvable films of silk fibroin for ultrathin conformal bio-integrated electronics," *Nat. Mater.*, vol. 9, no. 6, pp. 511–517, Jun. 2010, doi: 10.1038/nmat2745.

[126] J. Subbaroyan, D. C. Martin, and D. R. Kipke, "A finite-element model of the mechanical effects of implantable microelectrodes in the cerebral cortex," *J. Neural Eng.*, vol. 2, no. 4, pp. 103–113, Dec. 2005, doi: 10.1088/1741-2560/2/4/006.

[127] R. Biran, D. C. Martin, and P. A. Tresco, "The brain tissue response to implanted silicon microelectrode arrays is increased when the device is tethered to the skull," *J. Biomed. Mater. Res. - Part A*, vol. 82, no. 1, pp. 169–178, Jul. 2007, doi: 10.1002/jbm.a.31138.

[128] J. Thelin *et al.*, "Implant size and fixation mode strongly influence tissue reactions in the CNS," *PLoS One*, vol. 6, no. 1, p. e16267, Jan. 2011, doi: 10.1371/journal.pone.0016267.

[129] E. M. Harnett, J. Alderman, and T. Wood, "The surface energy of various biomaterials coated with adhesion molecules used in cell culture," *Colloids Surfaces B Biointerfaces*, vol. 55, no. 1, pp. 90–97, Mar. 2007, doi: 10.1016/j.colsurfb.2006.11.021.

[130] R. R. Richardson, J. A. Miller, and W. M. Reichert, "Polyimides as biomaterials: preliminary biocompatibility testing," *Biomaterials*, vol. 14, no. 8, pp. 627–635, Jan. 1993, doi: 10.1016/0142-9612(93)90183-3.

[131] T. Y. Chang *et al.*, "Cell and protein compatibility of parylene-C surfaces," *Langmuir*, vol. 23, no. 23, pp. 11718–11725, Nov. 2007, doi: 10.1021/la7017049.

[132] B. A. Weisenberg and D. L. Mooradian, “Hemocompatibility of materials used in microelectromechanical systems: Platelet adhesion and morphology in vitro,” *J. Biomed. Mater. Res.*, vol. 60, no. 2, pp. 283–291, May 2002, doi: 10.1002/jbm.10076.

[133] B. Mammadov, M. Sever, M. O. Guler, and A. B. Tekinay, “Neural differentiation on synthetic scaffold materials,” *Biomater. Sci.*, vol. 1, no. 11, pp. 1119–1137, 2013, doi: 10.1039/c3bm60150a.

[134] K. H. Yang and R. J. Narayan, “Biocompatibility and functionalization of diamond for neural applications,” *Curr. Opin. Biomed. Eng.*, vol. 10, pp. 60–68, Jun. 2019, doi: 10.1016/j.cobme.2019.03.002.

[135] A. Farrukh, S. Zhao, and A. del Campo, “Microenvironments designed to support growth and function of neuronal cells,” *Front. Mater.*, vol. 5, no. November, pp. 1–22, 2018, doi: 10.3389/fmats.2018.00062.

[136] J. M. V. Basso, I. Yurchenko, M. Simon, D. J. Rizzo, and C. Staii, “Role of geometrical cues in neuronal growth,” *Phys. Rev. E*, vol. 99, no. 2, p. 022408, Feb. 2019, doi: 10.1103/PhysRevE.99.022408.

[137] E. S. Ereifej, C. S. Smith, S. M. Meade, K. Chen, H. Feng, and J. R. Capadona, “The Neuroinflammatory Response to Nanopatterning Parallel Grooves into the Surface Structure of Intracortical Microelectrodes,” *Adv. Funct. Mater.*, vol. 28, no. 12, pp. 1–13, Mar. 2018, doi: 10.1002/adfm.201704420.

[138] C. L. Kolarcik *et al.*, “In vivo effects of L1 coating on inflammation and neuronal health at the electrode-tissue interface in rat spinal cord and dorsal root ganglion,” *Acta Biomater.*, vol. 8, no. 10, pp. 3561–3575, Oct. 2012, doi: 10.1016/j.actbio.2012.06.034.

[139] E. Azemi, C. F. Lagenaur, and X. T. Cui, “The surface immobilization of the neural adhesion molecule L1 on neural probes and its effect on neuronal density and gliosis at the probe/tissue interface,” *Biomaterials*, vol. 32, no. 3, pp. 681–692, Jan. 2011, doi: 10.1016/j.biomaterials.2010.09.033.

[140] W. He, G. C. McConnell, T. M. Schneider, and R. V. Bellamkonda, “A novel anti-inflammatory surface for neural electrodes,” *Adv. Mater.*, vol. 19, no. 21, pp.

3529–3533, Nov. 2007, doi: 10.1002/adma.200700943.

[141] A. Mercanzini *et al.*, “Controlled release nanoparticle-embedded coatings reduce the tissue reaction to neuroprostheses,” *J. Control. Release*, vol. 145, no. 3, pp. 196–202, Aug. 2010, doi: 10.1016/j.jconrel.2010.04.025.

[142] R. S. Oakes, M. D. Polei, J. L. Skousen, and P. A. Tresco, “An astrocyte derived extracellular matrix coating reduces astrogliosis surrounding chronically implanted microelectrode arrays in rat cortex,” *Biomaterials*, vol. 154, pp. 1–11, Feb. 2018, doi: 10.1016/j.biomaterials.2017.10.001.

[143] Y. Zhong and R. V. Bellamkonda, “Dexamethasone-coated neural probes elicit attenuated inflammatory response and neuronal loss compared to uncoated neural probes,” *Brain Res.*, vol. 1148, no. 1, pp. 15–27, May 2007, doi: 10.1016/j.brainres.2007.02.024.

[144] R. Wadhwa, C. F. Lagenaur, and X. T. Cui, “Electrochemically controlled release of dexamethasone from conducting polymer polypyrrole coated electrode,” *J. Control. Release*, vol. 110, no. 3, pp. 531–541, Feb. 2006, doi: 10.1016/j.jconrel.2005.10.027.

[145] M. R. Abidian and D. C. Martin, “Multifunctional nanobiomaterials for neural interfaces,” *Adv. Funct. Mater.*, vol. 19, no. 4, pp. 573–585, Feb. 2009, doi: 10.1002/adfm.200801473.

[146] J. P. Harris *et al.*, “Mechanically adaptive intracortical implants improve the proximity of neuronal cell bodies,” *J. Neural Eng.*, vol. 8, no. 6, p. 066011, Oct. 2011, doi: 10.1088/1741-2560/8/6/066011.

[147] N. J. Michelson *et al.*, “Multi-scale, multi-modal analysis uncovers complex relationship at the brain tissue-implant neural interface: New emphasis on the biological interface,” *J. Neural Eng.*, vol. 15, no. 3, p. 033001, Jun. 2018, doi: 10.1088/1741-2552/aa9dae.

[148] C. H. Thompson, M. J. Zoratti, N. B. Langhals, and E. K. Purcell, “Regenerative Electrode Interfaces for Neural Prostheses,” *Tissue Eng. - Part B Rev.*, vol. 22, no. 2, pp. 125–135, Apr. 2016, doi: 10.1089/ten.teb.2015.0279.

[149] T. Guo *et al.*, “Three dimensional extrusion printing induces polymer molecule alignment and cell organization within engineered cartilage,” *J. Biomed. Mater. Res. - Part A*, vol. 106, no. 8, pp. 2190–2199, Aug. 2018, doi: 10.1002/jbm.a.36426.

[150] G. Kook, S. W. Lee, H. C. Lee, I. J. Cho, and H. J. Lee, “Neural probes for chronic applications,” *Micromachines*, vol. 7, no. 10, p. 179, Oct. 2016, doi: 10.3390/mi7100179.

[151] J. P. Seymour, N. B. Langhals, D. J. Anderson, and D. R. Kipke, “Novel multi-sided, microelectrode arrays for implantable neural applications,” *Biomed. Microdevices*, vol. 13, no. 3, pp. 441–451, 2011, doi: 10.1007/s10544-011-9512-z.

[152] J. S. Brinen and A. Melera, “Electron spectroscopy for chemical analysis (ESCA) studies on catalysts. Rhodium on charcoal,” *J. Phys. Chem.*, vol. 76, no. 18, pp. 2525–2526, Aug. 1972, doi: 10.1021/j100662a007.

[153] M. Pijolat and G. Hollinger, “New depth-profiling method by angular-dependent x-ray photoelectron spectroscopy,” *Surf. Sci.*, vol. 105, no. 1, pp. 114–128, Apr. 1981, doi: 10.1016/0039-6028(81)90151-5.

[154] J. A. Gardella and D. M. Hercules, “Static Secondary Ion Mass Spectrometry of Polymer Systems,” *Anal. Chem.*, vol. 52, no. 2, pp. 226–232, Feb. 1980, doi: 10.1021/ac50052a003.

[155] H. Wang and P. K. Chu, “Surface Characterization of Biomaterials,” in *Characterization of Biomaterials*, Elsevier, 2013, pp. 105–174. doi: 10.1016/B978-0-12-415800-9.00004-8.

[156] J. R. Eles *et al.*, “Neuroadhesive L1 coating attenuates acute microglial attachment to neural electrodes as revealed by live two-photon microscopy,” *Biomaterials*, vol. 113, pp. 279–292, 2017, doi: 10.1016/j.biomaterials.2016.10.054.

[157] K. A. Ludwig, J. D. Uram, J. Yang, D. C. Martin, and D. R. Kipke, “Chronic neural recordings using silicon microelectrode arrays electrochemically deposited with a poly(3,4-ethylenedioxythiophene) (PEDOT) film,” *J. Neural Eng.*, vol. 3,

no. 1, pp. 59–70, Mar. 2006, doi: 10.1088/1741-2560/3/1/007.

[158] X. Cui and D. C. Martin, “Electrochemical deposition and characterization of poly(3,4-ethylenedioxythiophene) on neural microelectrode arrays,” *Sensors Actuators, B Chem.*, vol. 89, no. 1–2, pp. 92–102, Mar. 2003, doi: 10.1016/S0925-4005(02)00448-3.

[159] D. Bezuidenhout *et al.*, “Covalent incorporation and controlled release of active dexamethasone from injectable polyethylene glycol hydrogels,” *J. Biomed. Mater. Res. - Part A*, vol. 101 A, no. 5, pp. 1311–1318, May 2013, doi: 10.1002/jbm.a.34438.

[160] Y. Kato, I. Saito, T. Hoshino, T. Suzuki, and K. Mabuchi, “Preliminary study of multichannel flexible neural probes coated with hybrid biodegradable polymer,” in *Annual International Conference of the IEEE Engineering in Medicine and Biology - Proceedings*, Aug. 2006, pp. 660–663. doi: 10.1109/IEMBS.2006.259978.

CHAPTER 2 | SPATIOTEMPORAL PATTERNS OF GENE AND PROTEIN EXPRESSION AROUND IMPLANTED SILICON ELECTRODES

1. INTRODUCTION

Microelectrodes implanted in the nervous system are rapidly evolving technologies with ever-increasing applications in clinical and research settings. By recording from, and/or stimulating neuronal populations, it is possible to interface the nervous system with assistive devices or modulate neuronal activity to treat neurological disease and injury. Re-animation of a patient's limbs following spinal cord injury, treatment of the medication-resistant motor symptoms of Parkinson's disease, and interruption of seizure activity in intractable epilepsy are examples of the potential clinical applications of implantable neurotechnologies[1]–[15]. Likewise, the commercial value of neural prosthetics has been highlighted by the recent investment of private companies in "next-generation" electrode designs and the development of novel closed-loop neural interface systems[16], [17].

As advances in neurotechnology continue, the biological response to implanted electrodes in the brain is an on-going challenge to progress in the field[18]–[21]. Vascular disruption and microglial activation are early responses to implantation, where the extension of microglial processes toward the device has been observed within minutes of insertion[22]. An astroglial scar subsequently encapsulates the interface and further separates the electrode from nearby neuronal populations. The glial response is reportedly accompanied by a ~40% loss of neuronal somata within the first 100 microns of the electrode surface in comparison to a stab wound control[23], [24]. These observations, in

combination with other early reports[21], [25], [26], provided motivation for the design of next-generation neural interfaces with improved biological integration[18], [27], [28]. However, questions remain regarding the relationship between the biological impacts of electrodes, design, and their long-term performance[18]. Reports of poor signal fidelity and loss of neuronal signals in tissue with no apparent neuronal loss or glial scarring suggest additional complexity in the underlying relationship between the tissue response and device performance[29].

In recent years, new factors have been identified as potential contributors to the biological response to implanted devices. Insertion of electrode arrays damages cellular populations and the extracellular matrix, and disruption of the
blood brain barrier (BBB) generates disruptive debris and initiates downstream cytokine signaling cascades[30]. Both *in vivo* imaging and gene expression studies have confirmed vascular damage and BBB disruption resulting from implanted electrodes, where insertional trauma is evident in the downregulation of genes associated with tight junctions and adherens junctions[31]–[34]. New research also implicates oligodendrocytes and NG2 cells as dynamic players in the response to an indwelling foreign body. Literature has shown that much like other cell types, oligodendrocytes and NG2 cells are affected by BBB disruption, inflammation, and the traumatic injury caused by device insertion[22], [35]. Device insertion causes direct mechanical damage to oligodendroglia and myelin structure as well as secondary damage through inflammatory mechanisms. Increased permeability of the BBB following insertion exposes the cortical environment to inflammatory plasma proteins and debris which can recruit myelin-

targeting immune cells which create further damage [35]. Likewise, Bedell et al. have identified numerous differentially expressed (DE) genes at the device interface involved in neuroinflammatory cascades known to contribute to glial scarring and cell death [33], [36]. These recent reports indicate that the biological response to implanted electrode arrays remains incompletely understood, motivating the search for additional biomarkers of device-tissue interaction.

Here, we report the results of sequencing the transcriptome of tissue collected both within 100 microns ("near", or "interfacial") and ~500 microns ("far", or "distal") from Michigan-style electrode arrays implanted into rat motor cortex. We compared their profiles to the transcriptome of naïve, unimplanted animals. Tissue was collected at time points designed to capture the initial insertion injury (24 hours), early reactivity (1 week), and chronic responses (6 weeks). We detected the expression of >1,000 genes per condition, where >100 were significantly differentially expressed in near-device versus naïve tissue and >90 genes were DE in near-device versus far tissue. Interestingly, >20 genes were DE in tissue 500 μm from the device versus naïve tissue. A description of symbols and reported roles for DE genes are found in Table 2.1. A selected subset of detected and DE genes identified in this study are discussed which either validate existing understandings of tissue response in the brain or expand upon contemporary reports with additional mechanisms in the context of implanted devices. Complete raw results from the data analysis can be found in supplementary files (1-15). By reporting RNA-sequencing on tissue samples captured at multiple distances and time points, we extend current understanding of the spatiotemporal profile of gene expression surrounding

Gene Symbol	Gene name	Role	Reference
Ap2a1	Adaptor Related Protein Complex 2 Alpha 1 Subunit	Blood brain barrier integrity	[32]
Aqp4	Aquaporin 4	Water movement, cell adhesion, synaptic plasticity, and cellular migration	[39], [40]
Arc	Activity Regulated Cytoskeleton Associated Protein	Synaptic plasticity and dendritic spine maintenance	[41], [42]
Aox1	Aldehyde Oxidase 1	Oxidative stress	[32]
Apoe	Apolipoprotein E	Construction of lipoprotein and lipid transport	[43]–[45]
Bcl2	B-cell lymphoma 2	Apoptosis inhibition. NFκB pathway	[46]
Best1	Bestrophin 1	GABA / glutamate permissible channel dependent on astrocyte identity. Astrocyte enriched	[47]
Bsn	Bassoon Presynaptic Cytomatrix Protein	Presynaptic vesicle release	[48], [49]
C1qa	Complement C1q A chain	Innate immune response, promotes phagocytosis and synapse pruning	[50], [51]
C1qb	Complement C1q B chain	Innate immune response, promotes phagocytosis and synapse pruning	[50], [51]
C1qc	Complement C1q C chain	Innate immune response and promoter of phagocytosis and synapse pruning	[50], [51]
C3	Complement C3	Innate immune response and promoter of phagocytosis and synapse pruning	[33], [50], [52], [53]
Cacna1i	Calcium Voltage-Gated Channel Subunit Alpha1	Voltage gated calcium activity and plasticity	[54], [55]
Cacng3	Calcium Voltage-Gated Channel Auxiliary Subunit Gamma 3	Voltage gated calcium activity and plasticity	[56]
Camk2a	Calcium/calmodulin-dependent protein kinase II alpha	Calcium signaling intermediate protein. Essential for neuronal function	[57], [58]
Ccl3	C-C Motif Chemokine Ligand 3	Immune response chemotaxis and regulation of cellular BBB transmigration	[31], [59]
Cd68	CD antigen	Microglial immune response activation molecule	[60], [61]
Cdh5	Cadherin 5	BBB stability and barrier transmigration	[62]
Cldn5	Claudin 5	BBB stability and barrier transmigration	[63]
Clint1	Clathrin Interactor 1	Synaptic vesicle formation and neurotransmitter recycling	[64], [65]
Cltb	Clathrin Light Chain B	Synaptic vesicle formation and neurotransmitter recycling	[64], [65]
Cnksr2	Connector enhancer of kinase suppressor of Ras 2	Synaptic protein assembly	[66]
Cnp	2',3'-Cyclic Nucleotide 3' Phosphodiesterase	Oligodendrocyte surface protein	[67]
Col4a1	Collagen alpha-1(IV)	Fibrosis. Glial scar component	[68]
Csf1r	Colony stimulating factor 1 receptor	Cytokine response. Macrophage, microglia, and phagocyte differentiation and survival.	[69], [70]
Ctsb	Cathepsin B	Cysteine protease. EMC degradation, apoptosis, clathautophagy, and glia induced cell death	[71]
Ctsl	Cathepsin L	Cysteine protease. EMC degradation, apoptosis, autophagy, and glia induced cell death	[72]
Cx3cr1	CX3C chemokine receptor 1	Cytokine signaling	[33], [73]
Cxcl1	C-X-C Motif Chemokine Ligand 1	Cytokine signaling	[33], [74]
Cxcl2	C-X-C Motif Chemokine Ligand 2	Cytokine signaling, inflammation, and BBB transmigration	[75]
Cyfip2	Cytoplasmic FMR1 Interacting Protein 2	Regulations of mRNA translation at the synapse. Synapse maintenance	[76], [77]
Dctn1	Dynactin subunit 1	Microtubule motor and axonal transport protein	[78], [79]
Dock8	Dedicator of cytokinesis 8	Microglial immune response activation molecule	[80]
Dusp1	Dual Specificity Phosphatase 1	Inflammation	[32]
Gabbr1	Gamma-Aminobutyric Acid Type B Receptor Subunit 1	Inhibits post synaptic potentials	[80]
Gabbr2	Gamma-Aminobutyric Acid Type B Receptor Subunit 2	Inhibits post synaptic potentials	[35], [81]
Galc	Galactosylceramidase	Myelin component. Enriched in oligodendrocytes	[82]
Gfap	Glial fibrillary acidic protein	Intermediate filament protein. Enriched in reactive astrocytes	[83], [84]
Gpnmb	Transmembrane glycoprotein NMB	Immune response regulation	[83], [84]

Table 2.1: Genes detected in this study through RNA-sequencing that are associated with tissue response to implanted devices as well as neurodegenerative disease.

Table 2.1: (cont'd)

Gene Symbol	Gene name	Role	Reference
Gpx1	Glutathione Peroxidase 1	Oxidative stress	[32]
Gpx4	Glutathione Peroxidase 4	Oxidative stress	[32]
Hmox1	Heme Oxygenase 1	Oxidative stress	[32]
IL1a	Interleukin 1 Alpha	Cytokine signalling in immune response	[85]
Il1b	Interleukin 1 beta	NF-kB effector in immune response	[85]
Il1ra	Interleukin 1 Receptor Antagonist	Il1a and Il1b inhibition	[85]
Il6r	Interleukin 6 Receptor	NF-kB effector in immune response	[33], [85]
IL1a	Interleukin 1 Alpha	Cytokine signalling. Immune response	[85]
Kif5a	Kinesin Family Member 5A	Anterograde transport	[86]–[88]
Kif5b	Kinesin Family Member 5B	Anterograde transport	[86], [89]–[91]
Kif5c	Kinesin Family Member 5C	Anterograde transport	[92], [93]
Lcn2	Lipocalin 2	Inflammatory response. Secretion via astrocytes promote neuron death	[32], [94]
Map2	Microtubule Associated Protein 2	Neuronal Cytoskeleton	[95], [96]
Map4	Microtubule Associated Protein 4	Neuronal Cytoskeleton	[95]
Mapt	Microtubule Associated Protein Tau	Neurogenesis microtubule assembly protein; essential for neurodevelopment and recovery	[95], [97]
Mbp	Myelin basic protein	Myelin sheath adhesion protein enriched in oligodendrocytes	[98]
Mfsd2a	Major Facilitator Superfamily Domain Containing 2a	Causes BBB instability and barrier diffusion for lipids	[99]
Mmp2	Matrix Metallopeptidase 2	Extracellular matrix lattice protein; may negatively impact myelination	[31], [100]
Mmp9	Matrix Metallopeptidase 9	Extracellular matrix protein degrader; plays role in neural tissue structuring	[31], [101]
Mpv17	Mitochondrial Inner Membrane Protein	Oxidative stress	[32]
Ncan	Neurocan, CSPG3(Chondroitan sulfate proteoglycan 3)	Reactive astrocyte adhesion molecule. Inhibits neurite outgrowth	[102]
Ncf1	Neutrophil Cytosol Factor 1	Oxidative stress	[32]
Nefh	Neurofilament heavy	Neuronal cytoskeleton intermediate filament protein	[103]
Nefl	Neurofilament light	Neuronal cytoskeleton intermediate filament protein	[103]
Nefm	Neurofilament medium	Neuronal cytoskeleton intermediate filament protein	[103]
Nes	Nestin	Neuroepithelial intermediate filament protein. Type IV intermediate filament	[104]
Nos1	Neuronal Nitric-Oxide Synthase 1	Oxidative stress	[32]
Nos2	Inducible Nitric-Oxide Synthase	Oxidative stress	[32]
Nptxr	Neuronal Pentraxin Receptor	Synaptic regulation and plasticity	[105], [106]
Nrgn	Neurogranin	Dendritic spine maintenance and plasticity	[55], [107], [108]
Ocln	Occludin	Regulator of BBB stability and barrier diffusion	[31], [109]
Olig2	Oligodendrocyte Transcription Factor 2	Regulates CNS development via multiple pathways. Oligodendrocyte marker	[35], [110]
Plp1	Proteolipid protein 1	Myelin sheath adhesion and maintenance	[111]
Ptbp1	Polypyrimidine Tract-Binding Protein 1	Alternative splicing of genes involved with multiple cellular processes	[112]–[114]
Ptprz1	Protein Tyrosine Phosphatase Receptor Type Z1	PI3K-AKT pathway. Oligodendrocyte differentiation	[43], [115], [116]
Prdx1	Peroxiredoxin 1	Oxidative stress	[32]
Prdx2	Peroxiredoxin 2	Oxidative stress	[32]
Prdx3	Peroxiredoxin 3	Oxidative stress	[32]
Rgs5	Regulator of G-protein signalling 5	Marker of activated pericytes	[31], [117]
Rbfox3	RNA Binding Fox 3	Mature Neuron Marker (NeuN). Neuronal differentiation	[118], [119]
Rtn1	Reticulon 1	Neuron enriched. Cellular trafficking	[120], [121]
S100b	S100 calcium binding protein B	Calcium binding protein; Reactive astrocyte marker	[33]
Scara3	Scavenger Receptor Class A Member 3	Oxidative stress	[32]
Shh	Sonic Hedgehog	Astrocyte-endothelium gliovascular subunit maintenance	[32]
Snap25	Synaptosome Associated Protein 25	Presynaptic terminal regulation	[122]
Sod1	Superoxide Dismutase 1	Oxidative stress. Superoxide radical degradation	[32]
Sod2	Superoxide Dismutase 2	Oxidative stress. Superoxide radical degradation	[32]
Sod3	Superoxide Dismutase 3	Oxidative stress. Superoxide radical degradation	[32]
Sox2	SRY-Box Transcription Factor 2	Stem cell maintenance and differentiation	[123]
Stxbp1	Syntaxin Binding Protein 1	Synaptic vesicle regulation	[124], [125]
Syn1	Synapsin 1	Neurotransmitter release	[126], [127]
Tf	Transferrin	Iron transport and sequestration	[43], [128]
Tjp1	Tight Junction Protein 1	Regulator of BBB barrier transmigration	[31], [109]
Tjp2	Tight Junction Protein 2	Regulator of BBB barrier transmigration	[31], [62]
Tlr2	Toll-Like Receptor 2	Inflammation. TLR pathway	[32], [33]
Tlr4	Toll-Like Receptor 4	Inflammation. TLR pathway	[32], [33]
Tmem119	Transmembrane Protein 119	Inflammation. Microglial biomarker	[129]
Tnfrsf1a	Tumor necrosis factor receptor superfamily member 1A	Inflammation. TNF pathway	[33], [130]
Tnfrsf1b	Tumor necrosis factor receptor superfamily member 1B	Inflammation. TNF pathway	[33], [130]
Trem2	Triggering Receptor Expressed on Myeloid Cells 2	Encourages microglia survival via apoptosis inhibition and proliferation	[131], [132]
Tfrc	Transferrin Receptor	Transferrin uptake	[32]
Vim	Vimentin	Intermediate filament protein found in mesenchymal cells; plays a role in migration, attachment, and signalling	[104], [133]

implanted electrode arrays in the brain. The data reinforce observations and hypotheses described in literature while unmasking previously-unreported effects of implanted devices on gene expression.

2. METHODS

2.1 SURGICAL IMPLANTATION OF SILICON ELECTRODES

Single shank "Michigan"-style probes (16-channel A1x16-3mm, 15µm wide, 703µm^2 site size, 100µm site spacing, Neuronexus Technologies) were stereotaxically implanted in the motor cortex (M1) of male Sprague-Dawley rats (aged 12-14 weeks)[37]. Animals were isoflurane-anesthetized and a craniotomy was performed over M1 (+3.0mm AP, 2.5ML from Bregma), dura was resected, and the probe was stereotaxically inserted to a depth of 2mm from the cortical surface[38]. A dental cement headcap was used to secure bilateral implants to two stainless steel bone screws. Bupivacaine and Neosporin were applied topically to the area around the incision to minimize discomfort and infection risk, and meloxicam was administered via injection for post- operative pain management. Devices remained implanted in M1 for the duration of designated time points (1 day, 1 week, and 6 weeks). All surgical procedures described were approved by the Michigan State University Animal Care and Use Committee.

2.2 TISSUE EXTRACTION AND SLIDE PREPARATION

At the terminal time point, animals were deeply anesthetized with sodium pentobarbital, perfused with 4% paraformaldehyde transcardially, and the brains were extracted. Following graded sucrose protection (5-20%) and cryo-embedding, the brains were sliced via cryostat (Leica) as 20µm thick sections and mounted on Superfrost™

Plus slides (Fisher Scientific). Six tissue sections (n = 6) were collected for analysis at each timepoint (24 hours, n = 3 rats; 1 week, n = 5 rats; 6 weeks, n = 4 rats) in addition to six samples collected from naïve, unimplanted rats. Depth of collection spanned the implant shank (~600-1700 µm from cortical surface). The nature of the tissue collection along the implantation depth did not allow for analysis of the full volume of tissue or tissue proximity to different electrode materials (e.g. recording sites versus bulk material).

2.3 LASER CAPTURE MICROSCOPY (LCM) FOR TISSUE COLLECTION

Tissue near the implant injury, or 'interfacial' (within 100µm) was extracted using laser capture microscopy (LCM) (Zeiss Palm MicroBeam IV). Distal tissue of an approximately equivalent total surface area was extracted from ~500µm away from the implant site to assess distance-dependent effects. These
samples were collected and pooled from four smaller sections obtained at locations equidistant from the implant site. Using similar collection methods, control tissue from naïve brains was used to compare implanted tissue to unimplanted tissue. Settings were optimized by using excess tissue to calibrate laser strength and focus, allowing for efficient collection of tissue while avoiding any apparent heat damage to either the slide or the tissue. This process was repeated for each laser capture session.

2.4 RNA EXTRACTION AND SEQUENCING

RNA was extracted from LCM-collected tissue using a specialized RNAstorm extraction kit (Cell Data Sciences). cDNA library preparation and RNA sequencing was carried out by the University of Michigan Advanced Genomics Core. cDNA libraries

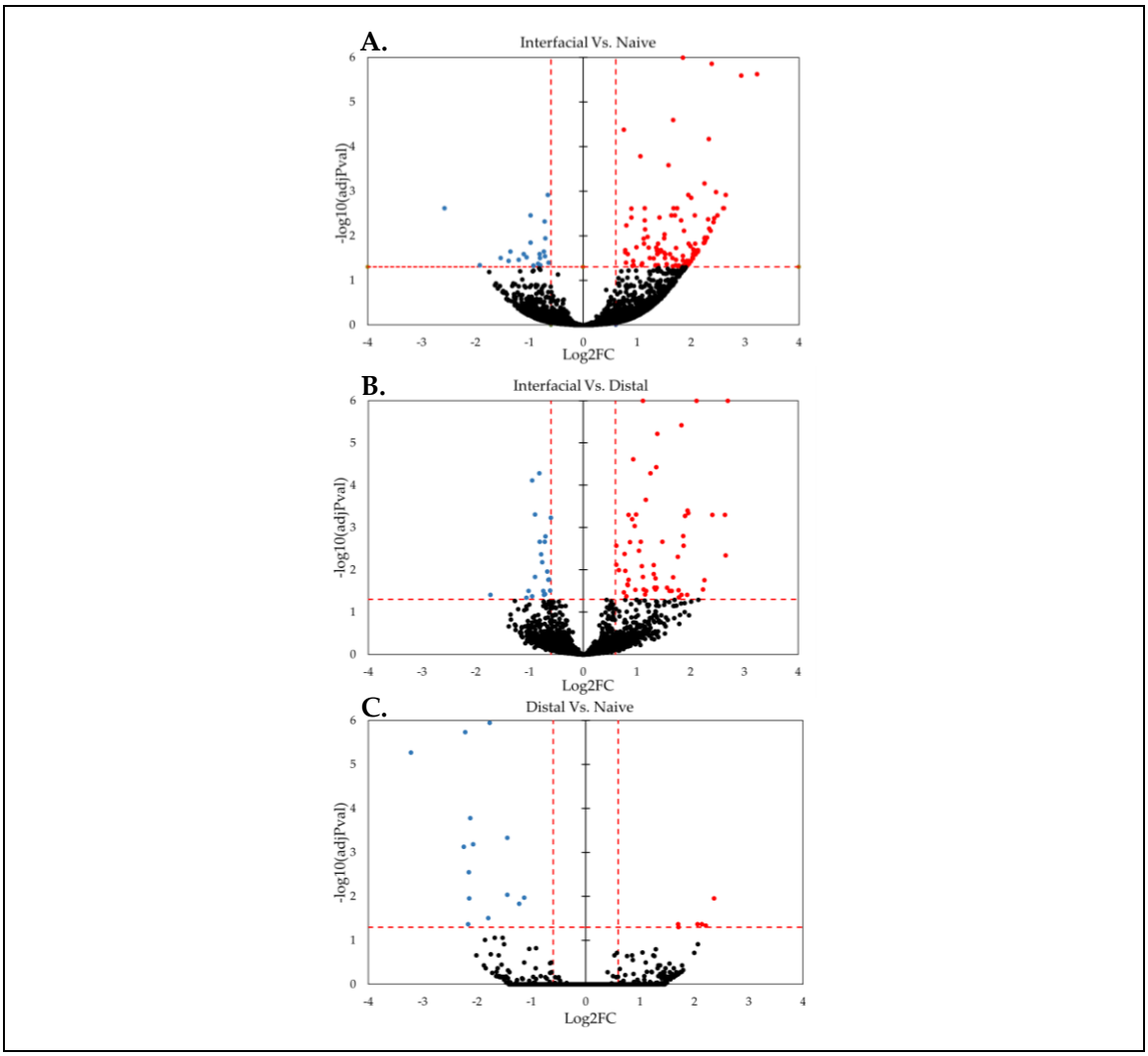

Figure 2.1: RNA-sequencing of cortical tissue reveals spatiotemporal gene expression at the device interface. Volcano plots illustrate overall DE of genes at near-device relative to naïve tissue ((A) 157 DE genes), near relative to far tissue ((B) 94 DE genes), and far relative to naïve tissue ((C) 21 DE genes). "Overall" expression represents the group comparisons of samples pooled across time points. Significance was thresholded at Log2FC $\geq$ 0.6 and P $\leq$ 0.05 (dashed red lines). (Red: Upregulated DE, Blue: Downregulated DE, Black: Detected not DE).

were prepped using a Takara SMART-stranded kit and subsequently subjected to 150 paired-end cycles on the NovaSeq-6000 platform (Illumina). Sequencing adapters were trimmed using Cutadapt (v2.3). FastQC[134] (v0.11.8) was used to ensure the quality of

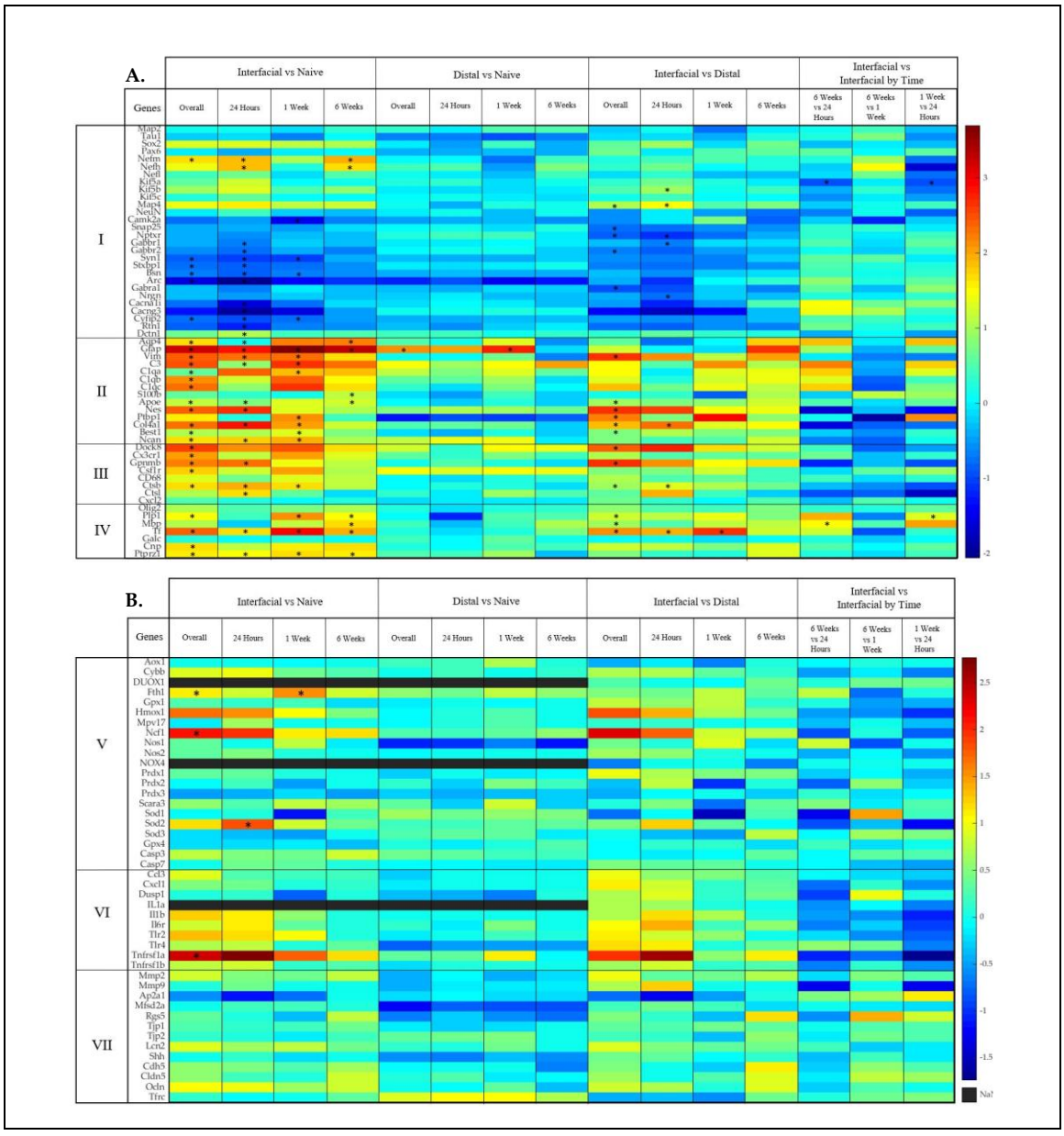

Figure 2.2: Transcriptomic analysis of interfacial and distal tissue at the device interface. (A) Representative heatmap of differential gene expression for each contrast for previously characterized cell types and their known roles in tissue response to implanted devices. (I) neurons, (II) astrocytes, (III) microglia, and (IV) oligodendrocytes. (B) Representative heatmap showing differential gene expression of each contrast in our analysis for (V) oxidative stress, (VI) inflammation, and (VII) blood-brain barrier. Color bar indicates Log2FC. "NaN" indicates non-detection. Significance was thresholded at Log2FC ≥ 0.6 and $P \leq 0.05$. Asterisks* denote statistically significant differentially expressed genes.

Synapse Associated Differentially Expressed Genes: Interface vs. Naive (Log2FC)

Gene	Overall	24 Hours	1 Week	6 Weeks
Camk2a	-0.798	*-0.4757	-1.4428	-0.6257
Snap25	-0.3500	-0.4063	-0.4831	-0.1431
Nptxr	-0.4123	-0.6035	-0.2819	-0.3471
Gabbr1	-0.3697	*-0.7078	-0.1774	-0.2745
Gabbr2	-0.6064	*-0.7965	-0.3641	-0.6683
Syn1	*-0.8032	*-0.9886	*-1.0270	-0.4388
Stxbp1	*-0.7174	*-0.8486	-0.7287	-0.5602
Bsn	*-0.6639	*-0.8206	*-0.6235	-0.5514
Arc	*-1.5350	*-2.0594	-1.4092	-1.1265
Gabra1	-0.3383	-0.6787	-0.0099	-0.3297
Nrgn	-0.3230	-0.4703	-0.2234	-0.2732
Cacna1i	-0.7170	*-1.5979	-0.7974	-0.1296
Cacng3	-1.2571	*-1.9495	-1.5899	-0.4666

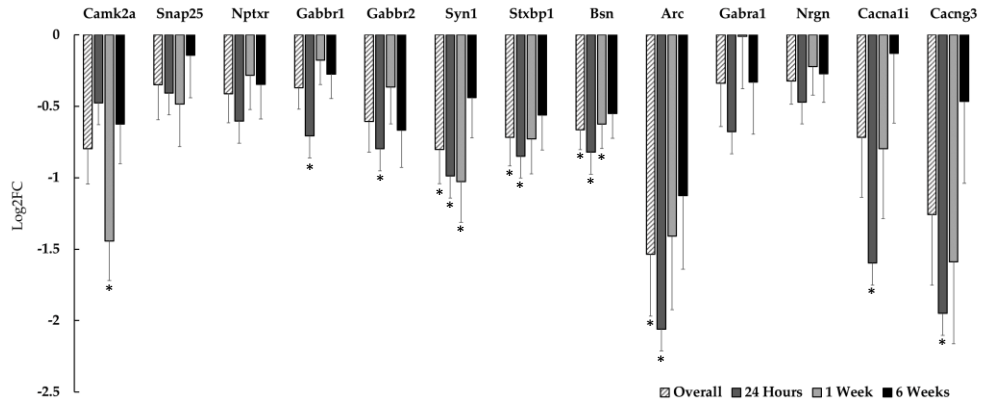

Figure 2.3: Differential expression of genes associated with the neuronal synaptic architecture at the device interface relative to naïve tissue. The table and representative graphs that illustrate the downregulation of synaptic associated genes at 24 hours, 1-week and 6-weeks post-implantation. "Overall" expression represents the group comparisons of samples pooled across time points. Significance was thresholded at Log2FC $\geq$ 0.6 and P $\leq$ 0.05. Asterisks (*) denote statistically significant differentially expressed genes.

data. Reads are mapped to the reference genome Rattus_norvegicus.Rnor_6.0.9, using STAR[135] (v2.6.1b) and assigned count estimates to genes with RSEM[136] (v1.3.1). Alignment options follow ENCODE standards for RNA-seq[137]. FastQC is used in an additional post-alignment step to ensure that only high-quality data gets used for

expression quantitation and differential expression.

2.5 DIFFERENTIAL EXPRESSION OF RNA

Data was pre-filtered to remove genes with 0 counts in all samples. Differential gene expression analysis is performed using DESeq2[138], using a negative binomial generalized linear model (thresholds: linear fold change >1.5 or <-1.5, Benjamini-Hochberg FDR (Padj) <0.05). Functional analysis, including candidate pathways activated or inhibited in comparison(s) and GO-term enrichments[139], are performed using iPathway Guide (Advaita)[140], [141]. While the nature of our tissue preparation and retrieval is prone to degradation, duplication, and low yield, these conditions were consistent across samples and were not expected to influence any sample cohort preferentially. Likewise, a review of data via principal component analysis did not reveal outliers associated with specific section depths. As such, genes identified as DE are expected to represent effects related to the presence of the device.

3. RESULTS & DISCUSSION

3.1 DIFFERENTIAL GENE EXPRESSION IN INTERFACIAL, DISTAL, AND NAÏVE TISSUES

In comparison to traditional immunohistochemistry or analysis of gene expression through quantitative polymerase chain reaction (qPCR), RNA-sequencing simultaneously assesses thousands of genes while obviating the need to pre-select a limited number of biomarkers of interest [142], [143]. Traditionally, device-tissue interaction has been assessed through quantitative immunohistochemistry or qPCR, while a more recent approach by Bedell *et. al.* profiled a broader set of genes associated specifically with

neuroinflammatory cascades[33]. To the best of our knowledge, our data is the first to report sequencing analysis of the whole transcriptome of tissue collected surrounding implanted Michigan-style electrode arrays in rat motor cortex. The data revealed differential gene expression as a function of time and distance from implanted devices (Figures (2.1) and (2.2)). Overall, 157 genes were detected as significantly DE in

Neuron Cytoskeleton Associated Differentially Expressed Genes: Interface Vs. Naive (Log2FC)

Gene	Overall	24 Hours	1 Week	6 Weeks
Nefm	*1.6971	*1.8663	1.0142	*1.9825
Nefh	1.3712	*1.8663	0.2738	*1.651
Kif5a	0.5684	*1.1868	0.1003	0.1186
Kif5b	*0.9207	*1.3001	0.4657	0.8255
Kif5c	0.2672	*0.6234	0.0649	0.0271
Map2	0.1482	0.165	-0.1105	0.3485
Mapt	-0.2271	-0.1198	-0.7067	0.0704
Map4	*1.3841	*1.5798	1.1079	1.2485
Cyfip2	*-0.7208	*-0.9416	*-0.7985	-0.4494
Rtn1	-0.8201	*-1.2194	-0.6958	-0.5795
Dctn1	0.7040	*1.0238	0.4336	0.5475

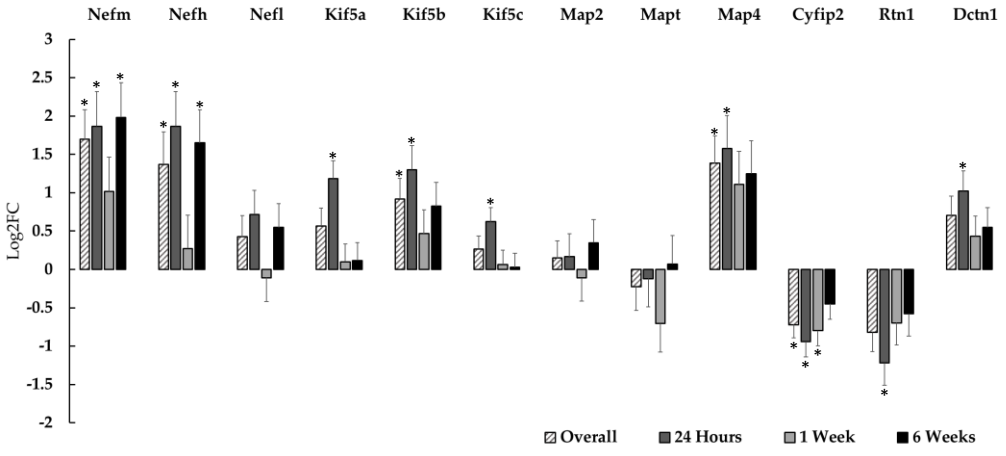

Figure 2.4: Differential expression of genes associated with the cytoskeletal architecture of neurons at the device interface relative to naïve tissue. The table and representative graphs above show fluctuations in neuronal genes associated with cytoskeleton and motor proteins at 24 hours, 1-week and 6-weeks post-implantation. "Overall" expression represents the group comparisons of samples pooled across time points. Significance was thresholded at Log2FC ≥ 0.6 and $P \leq 0.05$. Asterisks* denote significantly differentially expressed genes.

interface versus naïve, 94 genes were detected as significantly DE in near versus far, and 21 genes were detected as significantly DE in far versus naïve (Figure 2.1). The majority of DE genes were upregulated in near versus naïve and near versus far tissue, while a shift toward downregulation was observed in far versus naïve tissue (Figure 2.1). We observed the highest number of DE genes at the interface relative to naïve tissue following implantation (157 DE genes at 24 hours) and fewer DE genes over time post-implantation (62 DE genes at 1-week, 26 DE genes at 6-weeks), likely reflecting a pronounced impact of insertional trauma. Contrasts in distal versus naïve tissue followed an opposite time course, with 1 DE gene at 24-hours, 5 DE genes at 1-week, and 5 DE genes 6-weeks post implantation. The identification of DE genes in distal tissue collected 500 microns from the device versus naïve control tissue suggests that implanted electrode arrays affect tissue beyond the proximal device interface.

As described in following sections, our results validate foundational and contemporary literature while also providing new observations of patterns of spatiotemporal gene expression surrounding devices. The DE genes discussed in this study have been grouped into known associations of cellular expression and interactions. We observed DE of glial and neuronal genes that have not been characterized in the context of implanted electrode arrays. While the majority of these genes reinforce mechanisms of neuronal loss, synaptic pruning, and reactive gliosis, our data also revealed a minority of genes which are associated with protective and regenerative effects, suggesting novel therapeutic targets.

3.2 DIFFERENTIAL EXPRESSION OF NEURON-ASSOCIATED GENES

Foundational literature has described a “kill-zone” at the device interface where neuronal density declines over time, as evidenced by a loss of neuronal cell bodies and neurofilaments in interfacial tissue. Our data did not reveal a statistically significant reduction in the neuronal nuclear marker NeuN (Rbfox3) near the device, but we did observe decreases in the expression of several genes associated with neuronal structure and synaptic function in excitatory pyramidal neurons (e.g., CaMKIIa) (Figures (2.3) and (4)), which may reflect a simple loss of neurons from the local population. An alternative explanation is that altered gene expression occurs within individual neurons, potentially as a result of structural or functional remodeling in the neuronal network. Our recent observations have revealed significant loss of dendritic arbors and spine density locally to implanted electrodes [144], supporting an at-least partial role for plasticity to contribute to the observed gene expression results. The data also showed increased expression of neuronal cytoskeleton-associated genes (Figure 2.3), which is not explainable by broad-based neuronal loss. Potential reasons for the apparent decoupling of synapse and cytoskeleton-associated genes include: (1) a separation of damage-associated effects on local neurons and dendritic arbors versus long-range connections from axons of passage, and/or (2) cycles of persistent repair and damage within individual neurons at the interface, potentially related to pulsatile micromotion of brain tissue relative to the device. Review of the data set revealed novel observations of neuronal genes associated with cytoskeletal remodeling, intracellular signaling, synaptic structure and intrinsic excitability surrounding implanted electrodes, revealing new mechanisms and potential

targets to improve integration.

3.2.1 NEURONAL STRUCTURE: CYTOSKELETAL GENES

Previous descriptions of the tissue response to indwelling electrodes have been characterized by a loss of neurofilament protein at the device interface[24]. We did not observe significant reductions in expression in any of the isoforms of neurofilament protein, but rather an apparent upregulation of *Nefh*, *Nefm*, and *Map4* throughout the duration of device implantation out to 6-week timepoint (Figure 2.4). This observation has been corroborated by recent histological studies where neurofilament protein was found to be elevated above control tissue over time [145], [146]. Accumulation of neurofilament at sites of injury is known to be associated with neuronal pathology as well as the dysfunction of axonal transport mechanisms[103]. In accordance with altered axonal transport, we detected DE of kinesins at the device interface. The kinesin superfamily and dynein transport proteins play an essential role in axo-dendritic transport of synaptic vesicles, cytoskeletal proteins, and mitochondria[147]. These motor proteins have also been shown to play a role in the transport of post-synaptic density (PSD) proteins such as Snap-25, Syntaxin-1, and Bsn, which were also DE at the device interface[148]. Upregulation of *Kif5a*, *Kif5b*, and *Kif5c* at the device interface relative to naïve tissue was significant at 24-hours post-implantation. Kif5a and Kif5c are neuron-specific kinesins. *Kif5b* is expressed ubiquitously in many cell types and is known to play a role in ion channel and mitochondrial transport in neurons, which can be disrupted in states of injury[89], [149]. Upregulation of neuronal kinesins is associated with changes in mitochondrial trafficking during injury, but it is unclear if this response is

adaptive and neuroprotective or a driver of neurodegeneration [150]. Dctn1, a microtubule motor component of the dynein complex, was also upregulated coincidentally with the observed kinesins at the 24-hour timepoint. It is currently unknown whether upregulation of axonal transport proteins is adaptive for neuronal survival or results in axonopathy[87], but dysfunction of Dctn1, kinesins, and related proteins are known to be highly associated with neurodegenerative disease [87], [88].

3.2.2 NEURONAL FUNCTION: SYNAPSE-ASSOCIATED GENES

In addition to neuronal cytoskeletal perturbations, we observed significant downregulation of several synapse-associated genes in interfacial tissue, particularly during the first week post-implantation (including *CaMKIIa*, *Syn1*, *Stxbp1*, *Bsn*, *Arc*, *Gabbr1/2*, *Cacna1i* and *Cacng3*) (Figure 2.3)[75]. Several of these genes are associated with regulating vesicular release. For example, synapsins are known to play key functions in synaptic formation and plasticity through their role in chaperoning synaptic vesicles during cytoskeletal transport[126]. *Syn1*, which is downregulated in our analysis at 24 hours and 1 week post-implantation, has been reported to play roles in neurite outgrowth, synapse formation, and synapse maturation[126]. Bsn is a protein component of the presynaptic skeleton that is well-known for its role in vesicle loading at synaptic ribbons in the auditory system [48], and it was also downregulated during the first week post-implantation in our data. *Bsn* has been reported to be expressed in the cortex, although its function in that location has yet to be fully characterized[151]. Bsn has been reported to play a role in inflammatory pathologies such as multiple sclerosis, where it has been reported to contribute to neurodegeneration via upregulation and somatic Bsn

accumulation[49]. The observed downregulation of *Bsn* and other genes associated with synaptic release is potentially another indicator of neuronal loss, or perhaps an indirect adaptive mechanism to preserve neuronal health.

We also observed acute and overall downregulation of *Stxbp1* at the interface

Astrocyte Associated Differentially Expressed Genes: Interface vs. Naive (Log2FC)

Gene	Overall	24 Hours	1 Week	6 Weeks
Aqp4	*1.7187	0.1247	*2.2469	*2.198
Gfap	*3.22	*2.8546	*3.7008	*3.3191
Vim	*2.4244	*2.3249	*2.2921	1.6884
Ncan	*1.6711	*1.7799	*1.9459	1.0628
C3	*2.4849	0.8646	*2.6327	*2.3193
C1qa	*2.2323	0.6351	*2.4304	1.8738
C1qb	*2.1229	1.2435	2.4242	1.5113
C1qc	*2.2609	0.8542	2.6312	1.6603
S100b	0.6156	0.3096	0.1307	*1.178
Apoe	*1.144	0.7737	*1.3558	*1.2061
Best1	*1.0896	1.0244	*1.318	0.7784
Nes	*2.4125	*2.6963	1.3054	1.0781
Ptbp1	1.5937	0.2001	*2.1559	0.3708
Col4a1	*2.3265	*2.8574	*2.0388	1.2493

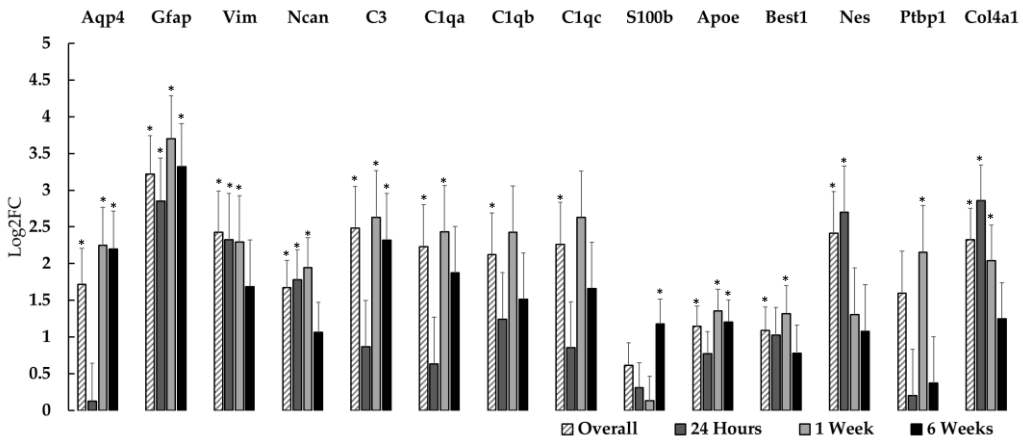

Figure 2.5: Differential expression of genes associated with astrocyte activity at the device interface relative to naïve tissue. The table and representative graphs that outline the general upregulation of astrocyte associated genes at 24 hours, 1-week and 6-weeks post-implantation. "Overall" expression represents the group comparisons of samples pooled across time points. Significance was thresholded at Log2FC ≥ 0.6 and $P \leq 0.05$. Asterisks (*) denote statistically significant differentially expressed genes.

relative to both naïve and distal tissue. Stxbp1 binds synaptic vesicle at the pre-synapse and is a protein that has been reported to be essential for the exocytosis of neurotransmitter release[152], [153]. Studies where Stxbp1 is dysfunctional has been shown to eliminate neurotransmitter release in affected neurons[152]. Likewise, while not statistically significant, we observed consistent downregulation of *Snap-25* at the device interface relative to distal tissue. Snap-25 is known to interact with Stxbp1 in their roles for docking pre-synaptic vesicles, regulation of Ca^{2+} channels, and in some cases, post-synaptic spine development and neuronal survival[122], [154]. Taken together, the decreased expression of these genes indicates a decline in synaptic transmission surrounding the device, likely due to neuronal loss and/or loss of local dendrites and spines[144] on residual neurons, both of which have been observed at the device interface[96].

Genes associated with dendritic spine formation, function, and maintenance also were significantly DE at the device interface. We found that *Cyfip2* is downregulated overall, at 24-hours, and 1-week post implantation at the interface relative to naïve tissue. Cyfip2 is enriched in neurons and has been reported to play roles in mRNA translation at the synapse as well as the structural maintenance of the pre-synapse, and the maturity of dendritic spines[77]. Reduced Cyfip2 has been implicated in the progression of Alzheimer's disease but has yet to be investigated in the context of implanted electrodes[77]. Arc is a highly regulated neuronal specific protein and its mRNA levels are directly controlled by neuronal activity, specifically via NMDA receptors[41], [42]. The *Arc* gene is widely expressed in the brain and has been directly implicated in its role

in synaptic plasticity at the post-synapse by modulating the formation of dendritic spines and the recruitment and maintenance of AMPAr[41]. Arc is best characterized as a player in behavior and learning, but has also been identified in M1 following motor learning tasks[155]. Arc is also suspected to bind dynamin in its role as an intermediate-early gene which we also found to be downregulated at the interface[41]. We have observed downregulation of *Arc* expression overall and at 24 hours post-implantation. Loss of Arc at the post-synapse in the event of injury has been shown to exacerbate neuronal injury and even lead to neuronal death through endoplasmic reticulum stress and necroptosis[156]. Because loss of Arc has been implicated in the decline of neuronal health, this gene may find use as a novel biomarker for evaluating device-tissue integration.

Many of the DE synapse-associated genes identified in this study are known to be driven by calcium-based mechanisms. Gabbr1 is the primary component of the metabotropic G-protein coupled receptor for $GABA_{B1}$. Gabbr2 (gpr51) combines with GABA-B1 as a heterodimer to form functional GABA-B receptors and inhibits high voltage activated Ca^{2+} channels as a driver of inhibitory post-synaptic potentials [80]. We have observed downregulation of both *Gabbr1* and *Gabbr2* 24-hours post-implantation. If these downregulations are not solely a product of neuronal loss at the interface, downregulation of *Gabbr1* and *Gabbr2* could potentially be indicators of neuronal excitotoxicity and increased calcium influx at early stages in the tissue response. We observed later downregulation of the calcium/calmodulin-dependent protein kinase *CaMKIIa* which was significant one week following insertion. *CaMKIIa* is a gene that

has been found to be necessary for neuronal function and long-term potentiation through its interaction with post-synaptic proteins in response to calcium influx[57], [157]. Nrgn has been reported to bind calmodulin (CaM) at the post-synapse and facilitate the generation of active CamKII required for long-term potentiation (LTP)[107]. We observed overall downregulation in *Nrgn* in interfacial vs. distal contrasts with pronounced changes at 24-hours post-implantation. *Ngrn* knockout studies have shown a marked decline in intracellular Ca^{2+} and increased incidence of long-term depression (LTD) of neuronal synapses[55], [107], [108]. Nrgn is a neuronal protein that is highly expressed in cortex, specifically in the post-synapse in dendritic spines[55], [108]. Cacna1i and Cacng3 are both neuronal low voltage-activated calcium channel components which are downregulated at the device interface 24 hours post-implantation. *Cacna1i* encodes the pore forming subunit of the CaV 3.3 ion channel in subsets of neurons such as GABAergic neurons in the thalamic reticular nucleus (TRN). In TRN neurons, the *Cav3.3* ion channel is activated by transient membrane hyperpolarization as a mediator of rebound burst firing in oscillatory neuronal activity [54]. *Cacng3* codes for a calcium channel γ3 auxiliary subunit that is also known as a transmembrane AMPA regulatory protein (TARP)[158], [159]. Both Cacna1i and Cacng3 have been reported to play roles in neuronal plasticity and in the development of epilepsy[54], [158]. Previous work by Eles et al. reports increased calcium-based activity as a direct result of device implantation-based trauma, which appeared to normalize by 1-month post-insertion. Insertion-driven Ca^{2+} influx can activate cellular mechanisms that contribute to axonal blebbing, axon transport disruption, neurite degeneration, synaptic degradation,

Microglial & Inflammation Associated Differentially Expressed Genes: Interface vs. Naive (Log2FC)

Gene	Overall	24 Hours	1 Week	6 Weeks
Dock8	*2.5891	2.1065	2.4511	1.6915
CD68	1.2724	0.6460	1.2973	1.1036
Ctsb	*1.6618	*1.9773	*1.6677	1.1016
Ctsl	1.0131	*1.6556	0.6290	-0.1168
Cxcl2	0.4632	0.2765	0.0138	0.2684
Cx3cr1	*1.9929	1.1117	2.0143	1.3144
Csf1r	*1.7965	1.1842	2.0085	1.0604
Gpnmb	*2.2418	*2.2822	1.4343	1.1483
Casp3	0.7371	0.5135	0.4415	0.8005
Casp7	-0.0155	0.4449	0.3739	0.0226
Cxcl1	0.4784	0.4131	0.0510	0.1153
Dusp1	0.0517	0.1498	-0.7974	0.0582
Il6r	0.8318	1.1257	0.3354	0.0811
Il1b	1.2772	1.0951	0.5676	0.0651
Tlr2	1.2922	1.1838	1.0659	0.0719
Tlr4	0.6741	0.7751	0.0437	0.3122
Tnfrsf1a	*2.361	2.7704	1.7396	1.1832
Tnfrsf1b	0.7698	0.8272	0.1285	0.2509

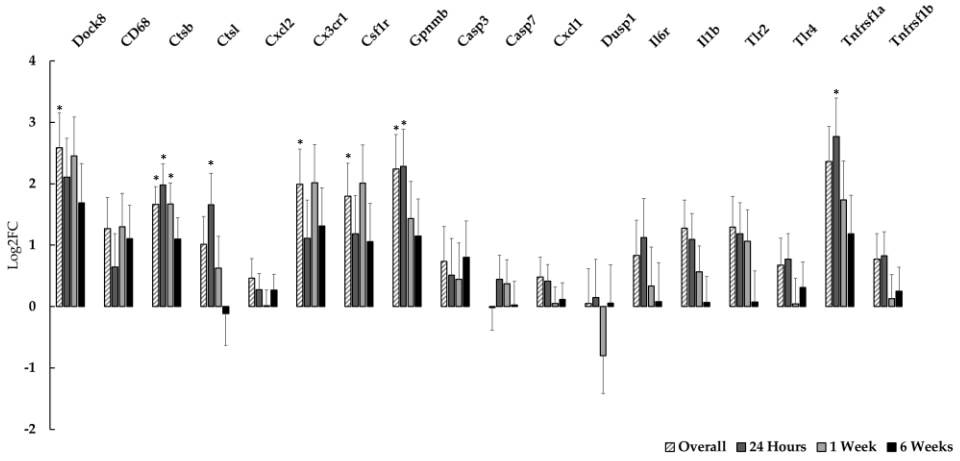

Figure 2.6: Differential expression of genes associated with inflammation and microglial activity at the device interface relative to naïve tissue. The table and representative graphs that show the generalized upregulation of microglial and inflammation associated genes at 24 hours, 1-week and 6-weeks post-implantation. "Overall" expression represents the group comparisons of samples pooled across time points. Significance was thresholded at Log2FC ≥ 0.6 and P ≤ 0.05. Asterisks (*) denote statistically significant differentially expressed genes.

and neuron death[160]. Early downregulation of *Gabbr1* and *Gabbr2* may facilitate early calcium influx and promote excitotoxicity. Decreased expression of a cluster of calcium-related genes at the one-week time point potentially could be an adaptive response following electrode insertion-driven Ca^{2+} influx to reduce Ca^{2+} driven activity. Future work will need to explore these mechanisms.

It is possible that monitoring synaptic-associated genes could serve as useful indicators of neuronal health and function in surviving populations. Downregulation of *Syn1* may point to potential synaptic dysfunction and axonal disruptions in local neurons. For example, the significant downregulation of *Bsn* at 24 hours and 1 week post implantation could indicate a decline of neuronal populations or possibly indicate early synaptic dysfunction or neuronal loss at the device interface [151]. The observed downregulation of *Stxbp1* overall and at 24 hours post-implantation may reflect early neuronal damage and loss of neuronal processes. Further investigation is required to determine whether these genes are related to adaptive mechanisms in individual neurons and/or neuronal loss, and assess their suitability as novel biomarkers for neuronal responses to implanted electrodes.

3.3 DIFFERENTIAL EXPRESSION OF ASTROCYTE RELATED GENES

3.3.1 ASTROGLIAL SCAR-ASSOCIATED GENES

Astrogliosis is considered to be a significant component of the fibrotic glial "scar" that forms over time around indwelling devices. This scar is believed to impede signal acquisition, segregate neuronal populations from insertion insult, and interfere with the exchange of ions and soluble factors[161]. We detected multiple DE genes associated

with astrocytic activity around implanted devices (Figure 2.5). Activated astrocytes at the device interface are commonly characterized through the progressive increase of GFAP and vimentin[23], [24], [30], [133], [162]. Our analysis confirmed a significant upregulation of these genes near the device interface and, in the case of *Gfap*, radiating out to tissue ~500 microns distal to the device (far versus naïve, log2FC = 2.219, padj= 0.042). Complementary to these previously-reported effects, we detected DE of additional genes potentially associated with glial scar formation. Col4a1, which astrocytes are known to secrete at sites of injury and inflammation, was significantly upregulated at the device interface overall and specifically at 24-hours and 1-week post-implantation[68], [163]. *Ncan* (chondroitin sulfate proteoglycan 3, CSPG3) was also upregulated through 1-week post-implantation at the device interface and is reportedly expressed by activated astrocytes in the fibrotic scar following traumatic brain injury[164]. Similarly to other reported CSPGs, *Ncan* is implicated in the failure of neural regeneration in the CNS via interference of neuronal adhesion molecules and cadherins. At the device interface, the intermediate filament nestin (*Nes*) is upregulated overall and at 24-hours. Nestin is commonly associated with multiple cell types such as neural progenitors[165], but because *Nes* is strongly upregulated in proliferating reactive astrocytes[104], at the device interface this may indicate the transition of local astrocytes to reactive states.

3.3.2 HOMEOSTATIC SUPPORT AND REPAIR

Astrocytes are also well known for their ability to communicate with neurons in the cortex and provide homeostatic support[161]. As such, open questions remain

regarding the beneficial versus detrimental impacts of reactive astrocytes surrounding devices[166]. Our data unmasked modulation of genes potentially associated with a neuroprotective or reparative role. For example, we observed significant upregulation of Apolipoprotein E (*Apoe*), which has been associated with reactive astrocytes as well as neurons in inflammatory states[44], [45], [167]. Apoe plays a key role in positive cellular processes, but increased presence of Apoe is most commonly reported as a constituent of inflammatory tissue response which is common during neurodegeneration[44], [45], [167]. We also observed upregulation of Bestrophin-1 (*Best1*), which is an ion channel that is highly expressed in astrocytes in the brain and is permeable to both glutamate and GABA[47]. Under normal conditions, *Best1* is localized to astrocytic processes where it favors glutamate release to maintain neuronal synapses. Under pathological conditions, *Best1* is redistributed to the astrocytic soma and takes on the role of GABAergic release, which is known to suppress synaptic transmission and neuronal excitability[47]. At the device interface, this mechanism could potentially work to counteract neuronal excitotoxicity during the initial inflammatory phase of the tissue response created by BBB breach, microglial activation, and insertion-driven calcium influx. Modifying the excitatory/inhibitory tone of surrounding brain tissue has been previously proposed as a candidate protective mechanism to preserve neuronal tissue surrounding devices, albeit at the likely expense of signal generation[37], [146]. We observed significant upregulation of *Aqp4* overall and at 1- and 6-weeks post-implantation. *Aqp4* is essential for cellular water homeostasis in the brain and is abundantly expressed in astrocytic end-feed; its upregulation in astrocytes has been proposed to be involved in cell swelling during injury

and ischemia. Aqp4 can also influence astrocyte-neuron communication as an adhesion molecule that is involved during cellular migration, neuromodulation, and neuronal plasticity. The complete extent to which Aqp4 is involved in the tissue response to brain injury is still unclear, but increased expression is strongly correlated with glial scar formation and inflammation[39].

Ptbp1 was strongly upregulated at the device interface relative to distal tissue and

Oligodendrocyte Associated Differentially Expressed Genes: Interface Vs. Naive (Log2FC)

Gene	Overall	24 Hours	1 Week	6 Weeks
Olig2	1.0043	0.474	0.7407	1.0247
Plp1	*1.5097	0.4326	*2.1238	*1.5106
Mbp	1.0893	-0.1962	1.1049	*1.6471
Tf	*2.3807	*1.6836	*2.9283	*1.9431
Galc	0.2046	0.0654	0.2632	0.0408
Cnp	*1.6503	1.1674	1.6281	1.6476
Ptprz1	*1.6299	*1.4541	*1.7138	*1.6104

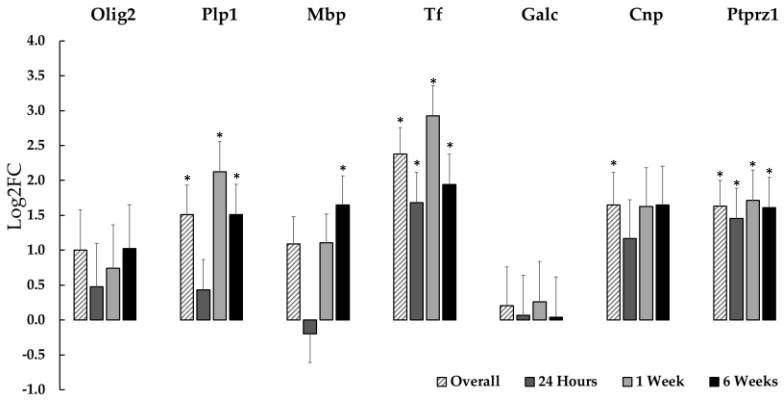

Figure 2.7: Differential expression of genes associated with oligodendrocytes at the device interface relative to naïve tissue. The table and representative graphs illustrate the upregulation of key genes associated with oligodendrocytes at 24 hours, 1-week and 6-weeks post-implantation. "Overall" expression represents the group comparisons of samples pooled across time points. Significance was thresholded at Log2FC ≥ 0.6 and $P \leq 0.05$. Asterisks (*) denote statistically significant differentially expressed genes.

at 1-week post-implantation relative to naïve tissue. *Ptbp1* is an RNA-binding protein which has been implicated in alternative splicing and the regulation of numerous cellular processes in the brain[113], [114], [168]. Recently, *Ptbp1* has been shown to suppress pro-neural genes, and shRNA knockdown of *Ptbp*1 in midbrain converted astrocytes into functional dopaminergic neurons within the nigrostriatal region of the mouse brain[112]. It is still unclear if *Ptbp1* upregulation at the interface correlates with increased astrocyte density, but due to the recently demonstrated potential for repair, this gene is a promising target for future investigation.

3.4 DIFFERENTIAL EXPRESSION OF GENES ASSOCIATED WITH MICROGLIA AND INFLAMMATION

Microglia have long been implicated in the tissue response to implanted electrode arrays as well as in neurodegenerative disease[169], [170]. In healthy cortical tissue, microglia play a supportive role in a variety of cellular processes such as synapse formation and maintenance, disposal of cellular debris, pruning of nonfunctional synapses, and promotion of oligodendrocyte precursor cell (OPC) survival and differentiation. Following insult to cortical tissue, microglia become activated, causing them to proliferate, migrate to sites of injury, produce inflammatory cytokines, upregulate lytic enzymes and assume a pathological phenotype[50], [171]–[176]. Activated microglia are documented to lose the ability to support healthy processes such as maintaining functioning synapses. Cytokines secreted by activated microglia can drive neurons into a state of excitotoxicity and neurodegeneration, potentially exacerbating an environment that is already unfriendly for neurons at the interface. In our data, we

observed expected upregulation of genes typically associated with microglial reactivity (Figure 2.6), particularly at early time points (e.g., *Cx3cr1*, *Csf1r*).

The upregulation of lysosomal *Ctsl* also appears to validate microglial-driven inflammation at the interface. Knockdown studies have provided evidence that Cstl is associated with phagocytotic microglia and contributes to neuronal cell death[71]. We observed acute upregulation of *Ctsl* at 24-hours post-implantation. In the context of indwelling devices, upregulation of *Ctsl* could act as a marker for microglial activation and may contribute to inflammatory neuronal damage. Similarly to *Ctsl*, *Ctsb* is highly expressed in pro-inflammatory microglia and plays a role in degradation of extracellular matrix proteins and can contribute to neuronal damage[69], [70], [177]. Tnfrsf1a, as a known activator of inflammatory microglial pathways *NF–κB* and MAPK, is also modestly upregulated at the device interface. *Ptprc* (CD45) is associated with infiltrating leukocytes and is known to be expressed in microglia as well, so it is possible that upregulation of this gene suggests the presence of general macrophage-like activity. However, it is likely that *Ptprc* expression is being driven by the local microglial population. In general, our data confirms the expected presence of activated microglia at the device interface, while identifying the perturbation of previously unreported genes related to these cells.

We also observed a cluster of gene expression associated with the complement cascade relevant to microglial function, which is well documented in pathological states where cellular debris and apoptotic cell bodies are present[50]–[52], [169]. C3 and C1q bind the membrane of apoptotic cell bodies and synapses as a marker for pruning by local

microglia[169], [174]. The upregulation of *C1q* and *C3* have been reported to destabilize functional synapses[50]. Additionally, the secretion of C1q from microglia is associated with the induction neurotoxic 'A1' reactive astrocytes, which in turn stimulates *C3* expression as a key biomarker of A1-astrocytes[173]. High complement levels during

Blood Brain Barrier & Vasculature: Interface Vs. Naïve (Log2FC)

Gene	Overall	24 Hours	1 week	6 weeks
Mmp2	0.8172	0.4547	0.3841	0.7350
Mmp9	0.0764	0.4429	-0.0219	-0.0245
Ap2a1	-0.5787	-1.1393	-0.7051	-0.0186
Mfsd2a	-0.0169	0.2335	0.1767	0.0252
Rgs5	0.3217	0.0715	-0.3440	0.7420
Tjp1	0.2514	0.1276	0.1771	0.3850
Tjp2	0.1324	0.0717	-0.1218	0.2199
Lcn2	0.9222	0.5981	0.7713	0.4258
Shh	-0.0298	0.1385	-0.2085	-0.0162
Cdh5	0.5639	0.4949	0.2358	0.6367
Cldn5	0.5678	0.1882	0.0329	0.8498
Ocln	1.0568	0.9550	0.6044	0.8449
Tfrc	0.1385	-0.0594	0.0076	0.3406

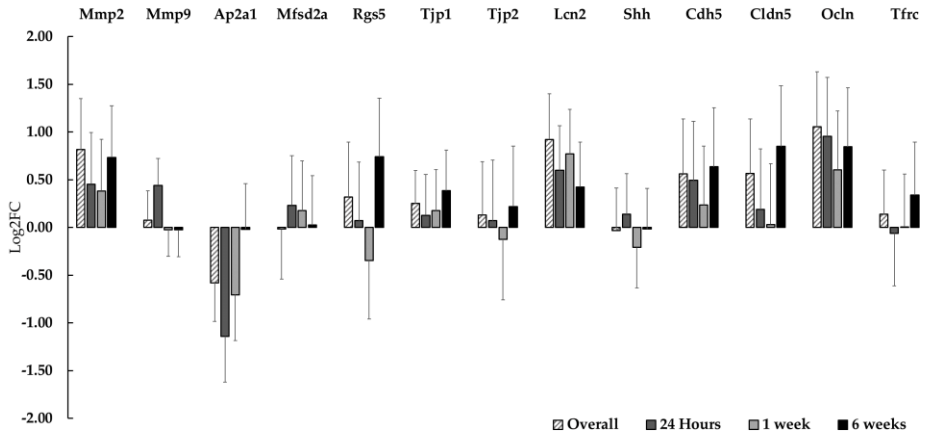

Figure 2.8: Differential expression of genes associated with blood brain barrier integrity at the device interface relative to naïve tissue. The table and representative graphs illustrate fluctuations of blood brain barrier associated genes at 24 hours, 1-week and 6-weeks post-implantation. "Overall" expression represents the group comparisons of samples pooled across time points. Significance was thresholded at Log2FC ≥ 0.6 and $P \leq 0.05$. No genes were identified as significantly DE in this group.

pathological states can lead to ‘over-pruning’ of synapses and myelin which can, in turn, lead to excessive loss of neuronal connectivity [131], [176]. Thus, genes associated with microglial-mediated inflammation and the complement cascade are candidate targets for restoration of lost neuronal network connectivity surrounding devices.

While the majority of our observations of microglial-associated genes suggest mechanisms associated with synaptic pruning, neurotoxicity and inflammation, upregulation of *Gpnmb* overall and at the 24-hour timepoint may suggest a more complex interplay of protective and detrimental effects. Gpnmb, which has been discussed in the context of Alzheimer’s disease, may suggest that there are microglia- mediated mechanisms which work to attenuate the inflammatory response of reactive astrocytes through CD44 receptor action[83]. Gpnmb is a transmembrane glycoprotein that has been reported to be expressed in microglia and macrophages in the brain and are reported to play roles in neurodegenerative states. Gpnmb has been shown to bind astrocytic CD44 to attenuate astrocyte driven inflammation and provide neuroprotection in neurodegenerative disease. As such, it has been suggested as a potential therapeutic target against neuroinflammation[83].

3.5 DIFFERENTIAL EXPRESSION OF OLIGODENDROCYTES ASSOCIATED GENES

Oligodendrocytes are well-known for their role in myelination of axonal fibers in the brain, but they also provide metabolic and trophic support directly to neurons. While previous studies have often focused on microglia and astrocytes as the primary glial players in the tissue response to implanted electrode arrays, more recent studies have

explored the role of oligodendrocytes and their progenitors (OPCs) in device-tissue interaction. Our data identified several DE genes associated with oligodendrocytes and OPCs (Figure 2.7). Interestingly, *Ptprz1* was found to be upregulated overall and at every

Oxidative Stress Associated Genes: Interface vs. Naive (Log2FC)

Gene	Overall	24 Hours	1 week	6 weeks
Aox1	0.0051	0.0116	-0.0617	0.0145
Cybb	0.9291	0.9808	0.4447	0.2723
Fth1	*1.1365	0.8291	*1.5545	0.8543
Gpx1	0.2648	0.1398	0.1951	-0.1906
Hmox1	*1.6734	1.5363	1.0245	0.4523
Mpv17	-0.1570	0.6083	-0.0306	-0.0329
Ncf1	*2.1043	1.9382	1.1138	1.1745
Nos1	0.3243	0.0162	0.7967	-0.1327
Nos2	0.3730	0.4565	0.0833	0.0011
Prdx1	0.3684	0.3306	0.0640	-0.0217
Prdx2	-0.0802	0.1878	-0.4819	-0.0388
Prdx3	-0.5358	-0.4153	-0.2343	-0.5403
Scara3	0.5797	0.2901	0.7731	0.5998
Sod1	-0.1098	0.0916	-1.1097	0.2313
Sod2	1.2157	*1.8175	0.8200	0.4346
Sod3	-0.2561	-0.3586	-0.5213	-0.0072
Gpx4	-0.2537	-0.2537	-0.1442	-0.3914

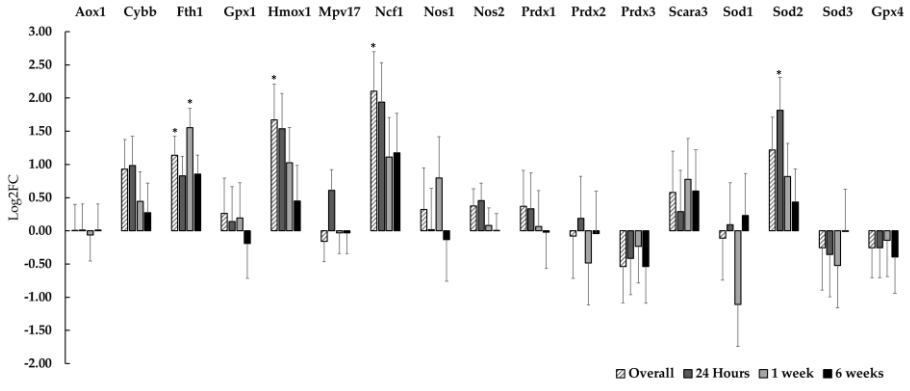

Figure 2.9: Differential expression of genes associated with oxidative stress at the device interface relative to naïve tissue. The table and representative graphs illustrate fluctuations of oxidative stress associated genes at 24 hours, 1-week and 6-weeks post-implantation. "Overall" expression represents the group comparisons of samples pooled across time points. Significance was thresholded at Log2FC ≥ 0.6 and $P \leq 0.05$. Asterisks (*) denote significant differentially expressed genes.

timepoint out to 6-weeks post-implantation. Ptprz1 is enriched in OPCs and is believed to play a role in the maintenance OPCs in an undifferentiated state[115]. Upregulation of *Ptprz1* by itself doesn't necessary imply that OPCs are being locked into an undifferentiated state, but it would allow for more binding sites for associated substrate molecules which have been shown to directly inhibit OPC differentiation into mature oligodendrocytes.

Oligodendrocytes are one of the few cell types in the brain to express transferrin (*Tf*) post developmentally[43], [128], and it is notable that *Tf* is upregulated at all timepoints throughout the six week implantation period in comparison to naïve tissue. It is possible that the chronic upregulation of iron sequestering proteins such as Tf and possibly Fth1 reflect the increased metabolic demands of oligodendrocytes, which may result from chronic cycles of damage and repair presented by a fixed, indwelling microelectrode array. Oligodendrocytes are known to be susceptible to oxidative damage due to their relatively high basal metabolic requirements to produce and maintain myelination while providing trophic support to nearby cellular populations. These demands may be further exacerbated in the injury zone of the device interface. As with other reactive glia, there may be a combination of reparative and degenerative effects of these cells at the interface.

Myelin is largely comprised of structural proteins Plp1 and Mbp, and the expression of these genes is directly linked to axonal myelin construction[98], [178]. It is possible that upregulation of these genes reflects a need for myelin regeneration and repair, or alternatively, the formation of damage-associated "myelinosomes."

Myelinosomes have been recently reported to be frequently targeted by microglia and invasive macrophages for phagocytosis[179], likely via the complement system. It has been reported that high prevalence and upregulation of *Plp1* is directly linked to microglial activation and inflammation, and myelinosomes may contribute to persistent microglial inflammation at the interface[175]. The need for remyelination after myelinosome pruning may be one explanation for the upregulation of *Plp1* and *Mbp* at the device interface over the duration of implantation. *Plp1* overexpression also has been reported to directly influence activation of inflammatory microglia, so there is some uncertainty as to whether the upregulation of *Plp1* at the device interface is regenerative or inflammatory[172], [175]. In the context of Alzheimer's disease, states of chronic inflammation can drive OPCs into a proinflammatory state over long periods of time (out to 18 months)[180], [181], but we have not seen evidence in this 6-week dataset of that particular phenotype of oligodendrocyte. The chronic upregulation of oligodendrocyte and myelin specific genes such as *Plp1* and *Mbp* at the device interface in our data supports the need to further understand the role of oligodendrocytes in device-tissue integration, which is an emerging line of inquiry recently pursued by Kozai and colleagues[22], [179], [182].

3.6 DIFFERENTIAL EXPRESSION OF GENES ASSOCIATED WITH BBB AND OXIDATIVE STRESS

Recent literature has begun to explore the role of BBB integrity as a component of the tissue response to indwelling electrodes. Insertion of devices in most cases causes ischemic insult through direct contact with vasculature. Transient rupture of the BBB

causes an influx of circulatory cell types, plasma proteins, and extracellular iron, thus exacerbating the existing immune response[31]. Increased permeability of the BBB disrupts cortical homeostasis and is known to result in the upregulation of matrix metalloproteases, antioxidant activity, and genes that control regeneration of the neurovascular unit[31], [32]. BBB disruption and the associated oxidative stress that follows has been typically observed at 48 and 72 hours post implantation, with one report suggesting no significant upregulation of these genes within 24 hours of device insertion[32]. We detected numerous genes associated with blood brain barrier (Figure 2.8) and oxidative stress (Figure 2.9), but few of them were flagged as statistically significant DE. It is possible that we did not observe significant DE in genes associated with vascular trauma and associated pathways because the 24-hour time point was not a sufficient duration to reveal effects. While we did detect many genes associated with oxidative stress, neurovascular unit and inflammation, most of these effects were not statistically significant. However, we detected significant upregulation of the antioxidant *Sod2* at the 24-hour timepoint, which may be related to acute oxidative stress following device insertion. *Ncf1* was also found to be generally upregulated overall at the device interface. *Ncf1* is enriched in phagocytic cells such as microglia and is upregulated as a part of the innate immune response. Upregulation of *Ncf1* may also be a signifier of infiltrating neutrophils following BBB breach caused by device insertion. *Ncf1* upregulation is known to directly increase the levels of reactive oxygen species (ROS) in the extracellular environment and may contribute to cellular damage at the device interface[32]. In addition to generators of oxidative stress, we observed upregulation of

protective mechanisms which are responsive to oxidative stress in the brain. *Fth1* has recently been characterized as a protectant against oxidative stress following device insertion[32]. We observed upregulation of *Fth1* overall and also at 1-week post-implantation. *Fth1* upregulation could be a sign of increased extracellular heme degradation due to increased BBB permeability related to device insertion and micromotion. Likewise, *Rtn1* downregulation is notable since the reticulon protein family has been reported to play involvement in neuronal apoptotic pathways in injury and disease[120], [121]. *Rtn1* upregulation following injury has been implicated in activation of apoptosis in neurons as a result of ER stress through the Bcl2 pathway[120]. Neuronal oxidative stress and cell death has been suggested at the device interface, but we have observed a marked downregulation of *Rtn1* at the device interface, which could imply potentially compensatory activation of neuroprotective mechanisms in surviving neurons.

4. CONCLUSION AND PERSPECTIVES

This study has expanded current understanding of the complexity of the biological impacts of electrodes implanted in the brain. The data validate previous observations while identifying novel genes associated with the tissue response to implanted cortical devices. While we present and discuss selected genes in this initial report, we have provided the comprehensive raw data set, which includes many additional statistically significant DE genes, as supplementary files (1-15).

In addition to expected DE of genes associated with astrocytic fibrosis, inflammation, and glial activation, our transcriptional analysis has highlighted new DE genes at the device interface which may be contributing to performance outcomes. The observed

upregulation of neuronal cytoskeletal genes in parallel with downregulation of synapse associated genes leads to new questions regarding the neuronal response at the device interface (i.e., plasticity versus loss). Changes in neuronal kinesins, pre- and post-synaptic proteins, and myelin structural proteins are all implicated in injury and neurogenerative disease, and the impact that these effects have in surviving neuronal populations at the device interface is the subject of future work. The coincident and persistent upregulation of *Tf*, *Plp1*, and *Mbp* support evidence that oligodendrocytes play a role in the tissue response. It is possible that neuronal injury and inflammation leads to increased generation of myelin associated proteins and a subsequent increase in oligodendrocyte metabolism required to maintain myelinated axons at the electrode interface. We also observed the expression of multiple genes which may contribute to a positive, adaptive function. For instance, potential astrocyte-driven neuronal hypo-excitability via *Best1* may provide neuroprotective benefits immediately post-implantation, but prolonged neuronal inhibition may contribute to signal loss or instability over time. It is likely that the DE of genes at the device interface represent a spectrum of tissue response effects, both protective as well as detrimental to local interfacial tissue. The fibrotic scar that forms around the device is essential to re-establish the BBB and cortical homeostasis, but prolonged presence of an *Ncan* rich glial scar may prove to be detrimental for long-term device integration. Many of the DE genes are expressed in multiple cell types and may play multi-functional roles in the tissue response, which warrants additional investigations to determine cell-type specificity and downstream outcomes of gene expression effects.

We have also identified a small number (21) of DE genes in distal tissue to implanted devices relative to naïve tissue. We observed downregulation of the cholesterol synthesis intermediate lanosterol synthase (*Lss*) and 7SK RNA. Additionally, we observed upregulation of *Gfap, Tensin3,* collagen type IV, neural precursor cell expressed, neural precursor expressed developmentally down-regulated 9 (*Nedd9*), and the Hsp70 co-chaperone *Hsp40* in distal tissue. Upregulation of *Gfap* is expected, but the DE of *Lss* and *Nedd9* lead to questions regarding a novel role of these genes in the context of implanted electrode arrays and brain injury. The presence of DE genes in distal tissue suggests that future work should explore distal gene expression, as it raises new questions about an influence of the tissue response on the broader network generating the local field potential.

Many of the DE neuronal genes discussed in this study have been previously implicated in neurodegenerative diseases such as multiple sclerosis, Alzheimer's disease, and Parkinson's disease. The possibility that mechanisms are conserved between device-based tissue response and neurodegenerative disease may allow for insights to be shared between these fields of research. Future work will explore gene ontology and pathway analysis to contextualize newly identified DE genes surrounding devices.

Significant questions for further investigation remain, such as: (1) how do the changes in gene expression influence the interplay between affected cell types at the device interface and their contribution to the overall tissue response, (2) to what extent is this observed DE being driven by fluctuations in individual cells versus changes in cell populations at the device interface, (3) do the observed fluctuations in gene expression

drive significant alterations in protein expression, and (4) which, if any, of these genes are useful biomarkers of signal quality? Finally, the observation that genes are DE in tissue 500 microns away from the device relative to unimplanted tissue indicates that the tissue response to the implanted electrode array may extend further than previously thought.

Future work may extend on the current observations by assessing chronic time-points beyond 6-weeks and performing focused analysis of gene expression localized to electrode sites. Likewise, assessing the relationship between recording quality and gene expression remains an important area of future work. Nonetheless, identification of genes associated with multiple cell types and processes at the device interface provides an expanded toolkit for evaluation of the tissue-device interface. This study has opened new avenues to investigate how the DE genes identified contribute to tissue response, creating opportunities for intervention and improved chronic performance.

REFERENCES

[1] A. W. Laxton *et al.*, "A phase I trial of deep brain stimulation of memory circuits in Alzheimer's disease," *Ann. Neurol.*, vol. 68, no. 4, pp. 521–534, Oct. 2010.

[2] J. Kuhn *et al.*, "Deep brain stimulation of the nucleus basalis of Meynert in Alzheimer's dementia," *Mol. Psychiatry*, vol. 20, no. 3, pp. 353–360, Mar. 2015.

[3] D. M. Whiting *et al.*, "Lateral hypothalamic area deep brain stimulation for refractory obesity: a pilot study with preliminary data on safety, body weight, and energy metabolism," *J. Neurosurg.*, vol. 119, no. 1, pp. 56–63, Jul. 2013.

[4] A. L. Ho, E. S. Sussman, A. V. Pendharkar, D. E. Azagury, C. Bohon, and C. H. Halpern, "Deep brain stimulation for obesity: rationale and approach to trial design," *Neurosurg. Focus*, vol. 38, no. 6, p. E8, Jun. 2015.

[5] D. R. Moore and R. V. Shannon, "Beyond cochlear implants: awakening the deafened brain," *Nat. Neurosci.*, vol. 12, no. 6, pp. 686–691, Jun. 2009.

[6] H. H. Lim and T. Lenarz, "Auditory midbrain implant: Research and development towards a second clinical trial," *Hear. Res.*, vol. 322, no. 1, pp. 212–223, Apr. 2015.

[7] P. M. Lewis, H. M. Ackland, A. J. Lowery, and J. V. Rosenfeld, "Restoration of vision in blind individuals using bionic devices: A review with a focus on cortical visual prostheses," *Brain Res.*, vol. 1595, pp. 51–73, Jan. 2015.

[8] J. V. Smit *et al.*, "Deep brain stimulation in tinnitus: Current and future perspectives," *Brain Res.*, vol. 1608, pp. 51–65, 2015.

[9] J. L. Collinger *et al.*, "High-performance neuroprosthetic control by an individual with tetraplegia," *Lancet*, vol. 381, no. 9866, pp. 557–564, Feb. 2013.

[10] T. Aflalo *et al.*, "Decoding motor imagery from the posterior parietal cortex of a tetraplegic human," *Science (80-.).*, vol. 348, no. 6237, pp. 906–910, May 2015.

[11] C. E. Bouton *et al.*, "Restoring cortical control of functional movement in a human with quadriplegia," *Nature*, vol. 533, no. 7602, pp. 247–250, May 2016.

[12] F. T. Sun, M. J. Morrell, and R. E. Wharen, "Responsive cortical stimulation for the treatment of epilepsy," *Neurotherapeutics*, vol. 5, no. 1, pp. 68–74, Jan. 2008.

[13] E. J. Quinn *et al.*, "Beta oscillations in freely moving Parkinson's subjects are attenuated during deep brain stimulation," *Mov. Disord.*, vol. 30, no. 13, pp.

1750–1758, Nov. 2015.

[14] P. J. Grahn *et al.*, “A neurochemical closed-loop controller for deep brain stimulation: toward individualized smart neuromodulation therapies,” *Front. Neurosci.*, vol. 8, no. 8 JUN, p. 169, Jun. 2014.

[15] A. L. Crowell, P. Riva-Posse, S. J. Garlow, and H. S. Mayberg, “Toward an Understanding of the Neural Circuitry of Major Depressive Disorder Through the Clinical Response to Deep Brain Stimulation of Different Anatomical Targets,” *Curr. Behav. Neurosci. Reports*, vol. 1, no. 2, pp. 55–63, Jun. 2014.

[16] T. L. Hanson, C. A. Diaz-Botia, V. Kharazia, M. M. Maharbiz, and P. N. Sabes, “The ‘sewing machine’ for minimally invasive neural recording,” *bioRxiv*, no. 1, p. 578542, 2019.

[17] E. Musk, “An integrated brain-machine interface platform with thousands of channels,” *J. Med. Internet Res.*, vol. 21, no. 10, p. e16194, Oct. 2019.

[18] C. H. Thompson, T. E. Riggins, P. R. Patel, C. A. Chestek, W. Li, and E. Purcell, “Toward guiding principles for the design of biologically-integrated electrodes for the central nervous system,” *J. Neural Eng.*, vol. 17, no. 2, p. 021001, Mar. 2020.

[19] N. J. Michelson *et al.*, “Multi-scale, multi-modal analysis uncovers complex relationship at the brain tissue-implant neural interface: New emphasis on the biological interface,” *J. Neural Eng.*, vol. 15, no. 3, 2018.

[20] S. M. Wellman *et al.*, “A Materials Roadmap to Functional Neural Interface Design,” *Adv. Funct. Mater.*, vol. 28, no. 12, pp. 1–38, 2018.

[21] T. D. Y. Kozai, A. S. Jaquins-Gerstl, A. L. Vazquez, A. C. Michael, and X. T. Cui, “Brain tissue responses to neural implants impact signal sensitivity and intervention strategies,” *ACS Chem. Neurosci.*, vol. 6, no. 1, pp. 48–67, Jan. 2015.

[22] S. M. Wellman and T. D. Y. Kozai, “In vivo spatiotemporal dynamics of NG2 glia activity caused by neural electrode implantation,” *Biomaterials*, vol. 164, pp. 121–133, May 2018.

[23] R. Biran, D. C. Martin, and P. A. Tresco, “The brain tissue response to implanted silicon microelectrode arrays is increased when the device is tethered to the skull,” *J. Biomed. Mater. Res. Part A*, vol. 82A, no. 1, pp. 169–178, Jul. 2007.

[24] R. Biran, D. C. Martin, and P. A. Tresco, “Neuronal cell loss accompanies the brain tissue response to chronically implanted silicon microelectrode arrays,” *Exp. Neurol.*, vol. 195, no. 1, pp. 115–126, Sep. 2005.

[25] B. Ghane-Motlagh and M. Sawan, “Design and Implementation Challenges of Microelectrode Arrays: A Review,” *Mater. Sci. Appl.*, vol. 04, no. 08, pp. 483–495, 2013.

[26] J. P. Seymour and D. R. Kipke, “Neural probe design for reduced tissue encapsulation in CNS,” *Biomaterials*, vol. 28, no. 25, pp. 3594–3607, Sep. 2007.

[27] J. Rivnay, H. Wang, L. Fenno, K. Deisseroth, and G. G. Malliaras, “Next-generation probes, particles, and proteins for neural interfacing,” *Sci. Adv.*, vol. 3, no. 6, p. e1601649, 2017.

[28] C. H. Thompson, M. J. Zoratti, N. B. Langhals, and E. K. Purcell, “Regenerative Electrode Interfaces for Neural Prostheses,” *Tissue Eng. Part B Rev.*, vol. 22, no. 2, pp. 125–135, Apr. 2016.

[29] N. J. Michelson *et al.*, “Multi-scale, multi-modal analysis uncovers complex relationship at the brain tissue-implant neural interface: new emphasis on the biological interface,” *J. Neural Eng.*, vol. 15, no. 3, p. 033001, Jun. 2018.

[30] T. D. Y. Kozai, A. S. Jaquins-Gerstl, A. L. Vazquez, A. C. Michael, and X. T. Cui, “Brain Tissue Responses to Neural Implants Impact Signal Sensitivity and Intervention Strategies,” *ACS Chem. Neurosci.*, vol. 6, no. 1, pp. 48–67, Jan. 2015.

[31] C. Bennett, M. Samikkannu, F. Mohammed, W. D. Dietrich, S. M. Rajguru, and A. Prasad, “Blood brain barrier (BBB)-disruption in intracortical silicon microelectrode implants,” *Biomaterials*, vol. 164, no. 3, pp. 1–10, May 2018.

[32] C. Bennett *et al.*, “Neuroinflammation, oxidative stress, and blood-brain barrier (BBB) disruption in acute Utah electrode array implants and the effect of deferoxamine as an iron chelator on acute foreign body response,” *Biomaterials*, vol. 188, pp. 144–159, Jan. 2019.

[33] H. W. Bedell, N. J. Schaub, J. R. Capadona, and E. S. Ereifej, “Differential expression of genes involved in the acute innate immune response to intracortical microelectrodes,” *Acta Biomater.*, vol. 102, no. xxxx, pp. 205–219, Jan. 2020.

[34] T. D. Y. Kozai *et al.*, “Reduction of neurovascular damage resulting from microelectrode insertion into the cerebral cortex using in vivo two-photon mapping,” *J. Neural Eng.*, vol. 7, no. 4, 2010.

[35] S. M. Wellman, F. Cambi, and T. D. Kozai, “The role of oligodendrocytes and their progenitors on neural interface technology: A novel perspective on tissue

regeneration and repair," *Biomaterials*, vol. 183, no. August, pp. 200–217, 2018.

[36] E. S. Ereifej *et al.*, "Implantation of neural probes in the brain elicits oxidative stress," *Front. Bioeng. Biotechnol.*, vol. 6, no. FEB, 2018.

[37] J. W. Salatino, A. P. Kale, and E. K. Purcell, "Alterations in Ion Channel Expression Surrounding Implanted Microelectrode Arrays in the Brain," *bioRxiv*, p. 518811, 2019.

[38] E. K. Purcell, D. E. Thompson, K. A. Ludwig, and D. R. Kipke, "Flavopiridol reduces the impedance of neural prostheses in vivo without affecting recording quality," *J. Neurosci. Methods*, vol. 183, no. 2, pp. 149–157, Oct. 2009.

[39] H. Ikeshima-Kataoka, "Neuroimmunological implications of AQP4 in astrocytes," *Int. J. Mol. Sci.*, vol. 17, no. 8, pp. 1–16, 2016.

[40] Y. X. Yong, Y. M. Li, J. Lian, C. M. Luo, D. X. Zhong, and K. Han, "Inhibitory role of lentivirus-mediated aquaporin-4 gene silencing in the formation of glial scar in a rat model of traumatic brain injury," *J. Cell. Biochem.*, vol. 120, no. 1, pp. 368–379, 2019.

[41] E. Korb and S. Finkbeiner, "Arc in synaptic plasticity: From gene to behavior," *Trends Neurosci.*, vol. 34, no. 11, pp. 591–598, 2011.

[42] L. Li, J. Carter, X. Gao, J. Whitehead, and W. G. Tourtellotte, "The Neuroplasticity-Associated Arc Gene Is a Direct Transcriptional Target of Early Growth Response (Egr) Transcription Factors," *Mol. Cell. Biol.*, vol. 25, no. 23, pp. 10286–10300, 2005.

[43] J. D. Cahoy *et al.*, "A transcriptome database for astrocytes, neurons, and oligodendrocytes: A new resource for understanding brain development and function," *J. Neurosci.*, vol. 28, no. 1, pp. 264–278, Jan. 2008.

[44] G. W. Rebeck, "The role of APOE on lipid homeostasis and inflammation in normal brains," *J. Lipid Res.*, vol. 58, no. 8, pp. 1493–1499, 2017.

[45] M. Tzioras, C. Davies, A. Newman, R. Jackson, and T. Spires-Jones, "Invited Review: APOE at the interface of inflammation, neurodegeneration and pathological protein spread in Alzheimer's disease," *Neuropathol. Appl. Neurobiol.*, vol. 45, no. 4, pp. 327–346, 2019.

[46] G. Lu, W. H. Kwong, Q. Li, X. Wang, Z. Feng, and D. T. Yew, "Bcl2, Bax, and Nestin in the Brains of Patients With Neurodegeneration and Those of Normal Aging," *J. Mol. Neurosci.*, vol. 27, no. 2, pp. 167–174, 2005.

[47] S. J. Oh and C. J. Lee, “Distribution and function of the Bestrophin-1 (Best1) channel in the brain,” *Exp. Neurobiol.*, vol. 26, no. 3, pp. 113–121, 2017.

[48] T. Frank *et al.*, “Bassoon and the synaptic ribbon organize Ca2+ channels and vesicles to add release sites and promote refilling,” *Neuron*, vol. 68, no. 4, pp. 724–738, 2010.

[49] B. Schattling *et al.*, “Bassoon proteinopathy drives neurodegeneration in multiple sclerosis,” *Nat. Neurosci.*, vol. 22, no. 6, pp. 887–896, 2019.

[50] M. K. Zabel and W. M. Kirsch, “From development to dysfunction: Microglia and the complement cascade in CNS homeostasis,” *Ageing Res. Rev.*, vol. 12, no. 3, pp. 749–756, Jun. 2013.

[51] A. Hammad, L. Westacott, and M. Zaben, “The role of the complement system in traumatic brain injury: A review,” *J. Neuroinflammation*, vol. 15, no. 1, pp. 1–15, 2018.

[52] B. Stevens *et al.*, “The Classical Complement Cascade Mediates CNS Synapse Elimination,” *Cell*, vol. 131, no. 6, pp. 1164–1178, 2007.

[53] H. Lian, A. Litvinchuk, A. C. A. Chiang, N. Aithmitti, J. L. Jankowsky, and H. Zheng, “Astrocyte-microglia cross talk through complement activation modulates amyloid pathology in mouse models of alzheimer’s disease,” *J. Neurosci.*, vol. 36, no. 2, pp. 577–589, 2016.

[54] A. Ghoshal *et al.*, “Effects of a patient-derived de novo coding alteration of CACNA1I in mice connect a schizophrenia risk gene with sleep spindle deficits,” *Transl. Psychiatry*, vol. 10, no. 1, pp. 1–12, 2020.

[55] A. M. Zhabotinsky, R. N. Camp, I. R. Epstein, and J. E. Lisman, “Role of the neurogranin concentrated in spines in the induction of long-term potentiation,” *J. Neurosci.*, vol. 26, no. 28, pp. 7337–7347, 2006.

[56] J. Xia *et al.*, “Identification and characterization of human neuronal voltage-gated calcium channel gamma 3 subunit gene,” *Chinese Sci. Bull.*, vol. 45, no. 23, pp. 2172–2176, Dec. 2000.

[57] M. J. Kool *et al.*, “CAMK2-dependent signaling in neurons is essential for survival,” *J. Neurosci.*, vol. 39, no. 28, pp. 5424–5439, 2019.

[58] P. H. Chia *et al.*, “A homozygous loss-of-function camk2a mutation causes growth delay, frequent seizures and severe intellectual disability,” *Elife*, vol. 7,

pp. 1–19, 2018.

[59] R. Chui and K. Dorovini-Zis, “Regulation of CCL2 and CCL3 expression in human brain endothelial cells by cytokines and lipopolysaccharide,” *J. Neuroinflammation*, vol. 7, pp. 1–12, 2010.

[60] M. E. Lopez, “Combined in situ Hybridization/Immunohistochemistry (ISH/IH) on Free-floating Vibratome Tissue Sections.,” *Bio-protocol*, vol. 4, no. 18, pp. 1–10, 2014.

[61] D. A. E. Hendrickx, C. G. van Eden, K. G. Schuurman, J. Hamann, and I. Huitinga, “Staining of HLA-DR, Iba1 and CD68 in human microglia reveals partially overlapping expression depending on cellular morphology and pathology,” *J. Neuroimmunol.*, vol. 309, no. November 2016, pp. 12–22, 2017.

[62] J. D. Gaston, L. L. Bischel, L. A. Fitzgerald, K. D. Cusick, B. R. Ringeisen, and R. K. Pirlo, “Gene Expression Changes in Long-Term in Vitro Human Blood-Brain Barrier Models and Their Dependence on a Transwell Scaffold Materia,” *J. Healthc. Eng.*, vol. 2017, 2017.

[63] H. Jiao, Z. Wang, Y. Liu, P. Wang, and Y. Xue, “Specific role of tight junction proteins claudin-5, occludin, and ZO-1 of the blood-brain barrier in a focal cerebral ischemic insult,” *J. Mol. Neurosci.*, vol. 44, no. 2, pp. 130–139, 2011.

[64] S. Stamm, D. Casper, J. Dinsmore, C. A. Kaufmann, J. Brosius, and D. M. Helfman, “Clathrin light chain B: gene structure and neuron-specific splicing.,” *Nucleic Acids Res.*, vol. 20, no. 19, pp. 5097–103, Oct. 1992.

[65] S. J. Royle and L. Lagnado, “Clathrin-Mediated Endocytosis at the Synaptic Terminal: Bridging the Gap Between Physiology and Molecules,” *Traffic*, vol. 11, no. 12, pp. 1489–1497, 2010.

[66] L. Yang, E. M. Kan, J. Lu, C. Wu, and E. A. Ling, “Expression of 2′,3′-cyclic nucleotide 3′-phosphodiesterase (CNPase) and its roles in activated microglia in vivo and in vitro,” *J. Neuroinflammation*, vol. 11, no. 1, pp. 1–17, 2014.

[67] M. A. Cannarile, M. Weisser, W. Jacob, A. M. Jegg, C. H. Ries, and D. Rüttinger, “Colony-stimulating factor 1 receptor (CSF1R) inhibitors in cancer therapy,” *J. Immunother. Cancer*, vol. 5, no. 1, pp. 1–13, 2017.

[68] P. Liesi and T. Kauppila, “Induction of type IV collagen and other basement-membrane-associated proteins after spinal cord injury of the adult rat may participate in formation of the glial scar,” *Exp. Neurol.*, vol. 173, no. 1, pp. 31–45, 2002.

[69] G. Hook, J. S. Jacobsen, K. Grabstein, M. Kindy, and V. Hook, “Cathepsin B is a new drug target for traumatic brain injury therapeutics: Evidence for E64d as a promising lead drug candidate,” *Front. Neurol.*, vol. 6, no. SEP, pp. 1–27, 2015.

[70] C. L. Luo *et al.*, “Cathepsin B contributes to traumatic brain injury-induced cell death through a mitochondria-mediated apoptotic pathway,” *J. Neurosci. Res.*, vol. 88, no. 13, pp. 2847–2858, 2010.

[71] S. Xu, H. Zhang, X. Yang, Y. Qian, and Q. Xiao, “Inhibition of cathepsin L alleviates the microglia-mediated neuroinflammatory responses through caspase-8 and NF-κB pathways,” *Neurobiol. Aging*, vol. 62, pp. 159–167, 2018.

[72] H. Hering and M. Sheng, “Activity-Dependent Redistribution and Essential Role of Cortactin in Dendritic Spine Morphogenesis,” *J. Neurosci.*, vol. 23, no. 37, pp. 11759–11769, 2003.

[73] Y. Tamura *et al.*, “Association study of the chemokine, CXC motif, ligand 1 (CXCL1) gene with sporadic Alzheimer’s disease in a Japanese population,” *Neurosci. Lett.*, vol. 379, no. 3, pp. 149–151, 2005.

[74] A. A. Babcock, W. A. Kuziel, S. Rivest, and T. Owens, “Chemokine expression by glial cells directs leukocytes to sites of axonal injury in the CNS,” *J. Neurosci.*, vol. 23, no. 21, pp. 7922–7930, 2003.

[75] R. Dutta and S. R. Sarkar, “Neurophysiology and Rehabilitation Role of Dynein and Dynactin (DCTN-1) in Neurodegenerative Diseases,” vol. 2, no. 1, pp. 53–58, 2019.

[76] I. Özer, “Analyzing the Role of CyFIP2 in the Mouse Brain,” p. 160, 2019.

[77] S. S. Tiwari *et al.*, “Alzheimer-related decrease in CYFIP2 links amyloid production to tau hyperphosphorylation and memory loss,” *Brain*, vol. 139, no. 10, pp. 2751–2765, 2016.

[78] K. Namekata, X. Guo, A. Kimura, N. Arai, C. Harada, and T. Harada, “DOCK8 is expressed in microglia, and it regulates microglial activity during neurodegeneration in murine disease models,” *J. Biol. Chem.*, vol. 294, no. 36, pp. 13421–13433, 2019.

[79] C. J. Kearney, K. L. Randall, and J. Oliaro, “DOCK8 regulates signal transduction events to control immunity,” *Cell. Mol. Immunol.*, vol. 14, no. 5, pp. 406–411, 2017.

[80] G. Zai, N. King, G. W. H. Wong, C. L. Barr, and J. L. Kennedy, “Possible association between the gamma-aminobutyric acid type B receptor 1 (GABBR1) gene and schizophrenia,” *Eur. Neuropsychopharmacol.*, vol. 15, no. 3, pp. 347–352, 2005.

[81] N. I. Weinstock *et al.*, “Brainstem development requires galactosylceramidase and is critical for pathogenesis in a model of Krabbe disease,” *Nat. Commun.*, vol. 11, no. 1, pp. 1–16, 2020.

[82] J. E. Burda, A. M. Bernstein, and M. V. Sofroniew, “Astrocyte roles in traumatic brain injury,” *Exp. Neurol.*, vol. 275, pp. 305–315, 2016.

[83] M. L. Neal, A. M. Boyle, K. M. Budge, F. F. Safadi, and J. R. Richardson, “The glycoprotein GPNMB attenuates astrocyte inflammatory responses through the CD44 receptor,” *J. Neuroinflammation*, vol. 15, no. 1, pp. 1–14, 2018.

[84] H. Tanaka *et al.*, “The potential of GPNMB as novel neuroprotective factor in amyotrophic lateral sclerosis,” *Sci. Rep.*, vol. 2, pp. 1–11, 2012.

[85] A. Helmy, M. G. De Simoni, M. R. Guilfoyle, K. L. H. Carpenter, and P. J. Hutchinson, “Cytokines and innate inflammation in the pathogenesis of human traumatic brain injury,” *Prog. Neurobiol.*, vol. 95, no. 3, pp. 352–372, 2011.

[86] K. Nakajima, X. Yin, Y. Takei, D. H. Seog, N. Homma, and N. Hirokawa, “Molecular Motor KIF5A Is Essential for GABAA Receptor Transport, and KIF5A Deletion Causes Epilepsy,” *Neuron*, vol. 76, no. 5, pp. 945–961, Dec. 2012.

[87] K. Hares *et al.*, “Overexpression of Kinesin Superfamily Motor Proteins in Alzheimer’s Disease,” *J. Alzheimer’s Dis.*, vol. 60, no. 4, pp. 1511–1524, 2017.

[88] C.-H. Xia *et al.*, “Abnormal neurofilament transport caused by targeted disruption of neuronal kinesin heavy chain KIF5A,” *J. Cell Biol.*, vol. 161, no. 1, pp. 55–66, Apr. 2003.

[89] Y. Y. Su *et al.*, “KIF5B promotes the forward transport and axonal function of the voltage-gated sodium channel Nav1.8,” *J. Neurosci.*, vol. 33, no. 45, pp. 17884–17896, Nov. 2013.

[90] J. Rivera, P. J. Chu, T. L. Lewis, and D. B. Arnold, “The role of Kif5B in axonal localization of Kv1 K+ channels,” *Eur. J. Neurosci.*, vol. 25, no. 1, pp. 136–146, Jan. 2007.

[91] H. Ma, Q. Cai, W. Lu, Z. H. Sheng, and S. Mochida, “KIF5B motor adaptor

syntabulin maintains synaptic transmission in sympathetic neurons," *J. Neurosci.*, vol. 29, no. 41, pp. 13019–13029, Oct. 2009.

[92] D. G. Iworima, B. A. Pasqualotto, and G. L. Rintoul, "Kif5 regulates mitochondrial movement, morphology, function and neuronal survival.," *Mol. Cell. Neurosci.*, vol. 72, pp. 22–33, Apr. 2016.

[93] M. H. Willemsen *et al.*, "Involvement of the kinesin family members KIF4A and KIF5C in intellectual disability and synaptic function," *J. Med. Genet.*, vol. 51, no. 7, pp. 487–494, 2014.

[94] F. Bi *et al.*, "Reactive astrocytes secrete lcn2 to promote neuron death," *Proc. Natl. Acad. Sci. U. S. A.*, vol. 110, no. 10, pp. 4069–4074, 2013.

[95] K. Tokuraku, S. Okuyama, K. Matsushima, T. Ikezu, and S. Kotani, "Distinct neuronal localization of microtubule-associated protein 4 in the mammalian brain," *Neurosci. Lett.*, vol. 484, no. 2, pp. 143–147, 2010.

[96] N. Hayashi, A. Oohira, and S. Miyata, "Synaptic localization of receptor-type protein tyrosine phosphatase ζ/β in the cerebral and hippocampal neurons of adult rats," *Brain Res.*, vol. 1050, no. 1–2, pp. 163–169, 2005.

[97] L. Dehmelt and S. Halpain, "Protein family review The MAP2 / Tau family of microtubule-associated proteins," *Genome Biol.*, vol. 6, no. 1, pp. 1–10, 2004.

[98] J. M. Boggs, "Myelin basic protein: A multifunctional protein," *Cell. Mol. Life Sci.*, vol. 63, no. 17, pp. 1945–1961, Sep. 2006.

[99] Y. R. Yang *et al.*, "Mfsd2a (major facilitator superfamily domain containing 2a) attenuates intracerebral hemorrhage-induced blood-brain barrier disruption by inhibiting vesicular transcytosis," *J. Am. Heart Assoc.*, vol. 6, no. 7, 2017.

[100] E. J. Walker and G. A. Rosenberg, "Divergent role for MMP-2 in myelin breakdown and oligodendrocyte death following transient global ischemia," *J. Neurosci. Res.*, vol. 88, no. 4, pp. 764–773, 2010.

[101] D. Leppert, S. L. Leib, C. Grygar, K. M. Miller, U. B. Schaad, and G. A. Holländer, "Matrix metalloproteinase (MMP)-8 and MMP-9 in cerebrospinal fluid during bacterial meningitis: Association with blood-brain barrier damage and neurological sequelae," *Clin. Infect. Dis.*, vol. 31, no. 1, pp. 80–84, 2000.

[102] M. Sajad, J. Zargan, R. Chawla, S. Umar, and H. A. Khan, "Upregulation of CSPG3 accompanies neuronal progenitor proliferation and migration in EAE," *J. Mol. Neurosci.*, vol. 43, no. 3, pp. 531–540, 2011.

[103] R. Perrot, R. Berges, A. Bocquet, and J. Eyer, “Review of the multiple aspects of neurofilament functions, and their possible contribution to neurodegeneration,” *Mol. Neurobiol.*, vol. 38, no. 1, pp. 27–65, 2008.

[104] I. Tamagno and D. Schiffer, “Nestin expression in reactive astrocytes of human pathology,” *J. Neurooncol.*, vol. 80, no. 3, pp. 227–233, 2006.

[105] S. J. Lee *et al.*, “Presynaptic neuronal pentraxin receptor organizes excitatory and inhibitory synapses,” *J. Neurosci.*, vol. 37, no. 5, pp. 1062–1080, 2017.

[106] J. Figueiro-Silva *et al.*, “Neuronal pentraxin 1 negatively regulates excitatory synapse density and synaptic plasticity,” *J. Neurosci.*, vol. 35, no. 14, pp. 5504–5521, 2015.

[107] K. P. Huang, F. L. Huang, T. Jäger, J. Li, K. G. Reymann, and D. Balschun, “Neurogranin/RC3 enhances long-term potentiation and learning by promoting calcium-mediated signaling,” *J. Neurosci.*, vol. 24, no. 47, pp. 10660–10669, 2004.

[108] F. J. Díez-Guerra, “Neurogranin, a link between calcium/calmodulin and protein kinase C signaling in synaptic plasticity,” *IUBMB Life*, vol. 62, no. 8, pp. 597–606, 2010.

[109] B. T. Hawkins, T. F. Lundeen, K. M. Norwood, H. L. Brooks, and R. D. Egleton, “Increased blood-brain barrier permeability and altered tight junctions in experimental diabetes in the rat: Contribution of hyperglycaemia and matrix metalloproteinases,” *Diabetologia*, vol. 50, no. 1, pp. 202–211, 2007.

[110] C. M. Sauvageot and C. D. Stiles, “Molecular mechanisms controlling cortical gliogenesis,” *Curr. Opin. Neurobiol.*, vol. 12, no. 3, pp. 244–249, 2002.

[111] I. Griffiths *et al.*, “Axonal swellings and degeneration in mice lacking the major proteolipid of myelin,” *Science (80-.).*, vol. 280, no. 5369, pp. 1610–1613, 1998.

[112] H. Qian *et al.*, “Reversing a model of Parkinson’s disease with in situ converted nigral neurons,” *Nature*, vol. 582, no. 7813, pp. 550–556, Jun. 2020.

[113] A. Georgilis *et al.*, “PTBP1-Mediated Alternative Splicing Regulates the Inflammatory Secretome and the Pro-tumorigenic Effects of Senescent Cells,” *Cancer Cell*, vol. 34, no. 1, pp. 85-102.e9, 2018.

[114] J. K. Vuong, C. H. Lin, M. Zhang, L. Chen, D. L. Black, and S. Zheng, “PTBP1 and PTBP2 Serve Both Specific and Redundant Functions in Neuronal Pre-

mRNA Splicing," *Cell Rep.*, vol. 17, no. 10, pp. 2766–2775, 2016.

[115] N. Tanga *et al.*, "The PTN-PTPRZ signal activates the AFAP1L2-dependent PI3K-AKT pathway for oligodendrocyte differentiation: Targeted inactivation of PTPRZ activity in mice," *Glia*, vol. 67, no. 5, pp. 967–984, 2019.

[116] K. Kuboyama, A. Fujikawa, M. Masumura, R. Suzuki, M. Matsumoto, and M. Noda, "Protein Tyrosine Phosphatase Receptor Type Z Negatively Regulates Oligodendrocyte Differentiation and Myelination," *PLoS One*, vol. 7, no. 11, pp. 1–11, 2012.

[117] N. Sladojevic, B. Yu, and J. K. Liao, "Regulator of G-Protein Signaling 5 Maintains Brain Endothelial Cell Function in Focal Cerebral Ischemia," *J. Am. Heart Assoc.*, vol. 9, no. 18, p. e017533, 2020.

[118] M. E. Watts, C. Wu, and L. L. Rubin, "Suppression of MAP4K4 Signaling Ameliorates Motor Neuron Degeneration in Amyotrophic Lateral Sclerosis-Molecular Studies Toward New Therapeutics," *J. Exp. Neurosci.*, vol. 13, pp. 10–13, 2019.

[119] K. K. Kim, Y. C. Kim, R. S. Adelstein, and S. Kawamoto, "Fox-3 and PSF interact to activate neural cell-specific alternative splicing," *Nucleic Acids Res.*, vol. 39, no. 8, pp. 3064–3078, 2011.

[120] L. Gong, Y. Tang, R. An, M. Lin, L. Chen, and J. Du, "RTN1-C mediates cerebral ischemia/reperfusion injury via ER stress and mitochondria-associated apoptosis pathways," *Cell Death Dis.*, vol. 8, no. 10, p. e3080, 2017.

[121] Q. Shi, Y. Ge, W. He, X. Hu, and R. Yan, "RTN1 and RTN3 protein are differentially associated with senile plaques in Alzheimer's brains," *Sci. Rep.*, vol. 7, no. 1, pp. 1–9, 2017.

[122] A. Kádková, J. Radecke, and J. B. Sørensen, "The SNAP-25 Protein Family," *Neuroscience*, vol. 420, pp. 50–71, 2019.

[123] R. B. Jaffe, "Induction of pluripotent stem cells from adult human fibroblasts by defined factors: Commentary," *Obstet. Gynecol. Surv.*, vol. 63, no. 3, p. 153, 2008.

[124] M. Irfan, K. R. Gopaul, O. Miry, T. Hökfelt, P. K. Stanton, and C. Bark, "SNAP-25 isoforms differentially regulate synaptic transmission and long-term synaptic plasticity at central synapses," *Sci. Rep.*, vol. 9, no. 1, pp. 1–14, 2019.

[125] M. Milh *et al.*, "Epileptic and nonepileptic features in patients with early onset

epileptic encephalopathy and STXBP1 mutations," *Epilepsia*, vol. 52, no. 10, pp. 1828–1834, 2011.

[126] F. Cesca, P. Baldelli, F. Valtorta, and F. Benfenati, "The synapsins: Key actors of synapse function and plasticity," *Prog. Neurobiol.*, vol. 91, no. 4, pp. 313–348, 2010.

[127] D. Gitler *et al.*, "Different presynaptic roles of synapsins at excitatory and inhibitory synapses," *J. Neurosci.*, vol. 24, no. 50, pp. 11368–11380, 2004.

[128] B. Todorich, J. M. Pasquini, C. I. Garcia, P. M. Paez, and J. R. Connor, "Oligodendrocytes and myelination: The role of iron," *Glia*, vol. 57, no. 5, pp. 467–478, Apr. 2009.

[129] T. A. Van Wageningen, E. Vlaar, G. Kooij, C. A. M. Jongenelen, J. J. G. Geurts, and A. M. Van Dam, "Regulation of microglial TMEM119 and P2RY12 immunoreactivity in multiple sclerosis white and grey matter lesions is dependent on their inflammatory environment," *Acta Neuropathol. Commun.*, vol. 7, no. 1, pp. 1–16, 2019.

[130] V. Paban *et al.*, "Molecular gene expression following blunt and rotational models of traumatic brain injury parallel injuries associated with stroke and depression," *J. Transl. Sci.*, vol. 2, no. 6, 2016.

[131] S. Hickman, S. Izzy, P. Sen, L. Morsett, and J. El Khoury, "Microglia in neurodegeneration," *Nat. Neurosci.*, vol. 21, no. 10, pp. 1359–1369, 2018.

[132] S. Carmona, K. Zahs, E. Wu, K. Dakin, J. Bras, and R. Guerreiro, "The role of TREM2 in Alzheimer's disease and other neurodegenerative disorders," *Lancet Neurol.*, vol. 17, no. 8, pp. 721–730, 2018.

[133] A. Adolf *et al.*, "Release of astroglial vimentin by extracellular vesicles: Modulation of binding and internalization of C3 transferase in astrocytes and neurons," *Glia*, vol. 67, no. 4, pp. 703–717, 2019.

[134] S. Andrews, "No Title," *FastQC: a quality control tool for high throughput sequence data*. [Online]. Available: https://www.bioinformatics.babraham.ac.uk/projects/fastqc/.

[135] A. Dobin *et al.*, "STAR: ultrafast universal RNA-seq aligner," *Bioinformatics*, vol. 29, no. 1, pp. 15–21, Jan. 2013.

[136] B. Li and C. N. Dewey, "RSEM: accurate transcript quantification from RNA-Seq data with or without a reference genome," *Bioinforma. Impact Accurate Quantif.*

Proteomic Genet. Anal. Res., Feb. 2011.

[137] A. Dobin, “No Title.” [Online]. Available: https://github.com/alexdobin/STAR/blob/master/doc/STARmanual.pdf.

[138] M. I. Love, W. Huber, and S. Anders, “Moderated estimation of fold change and dispersion for RNA-seq data with DESeq2,” *Genome Biol.*, vol. 15, no. 12, p. 550, Dec. 2014.

[139] “No Title.” [Online]. Available: http://www.geneontology.org/.

[140] S. Draghici *et al.*, “A systems biology approach for pathway level analysis,” *Genome Res.*, vol. 17, no. 10, pp. 1537–1545, Sep. 2007.

[141] Z. H. Zhang *et al.*, “A Comparative Study of Techniques for Differential Expression Analysis on RNA-Seq Data,” *PLoS One*, vol. 9, no. 8, p. e103207, Aug. 2014.

[142] Y. Zhang *et al.*, “An RNA-Sequencing Transcriptome and Splicing Database of Glia, Neurons, and Vascular Cells of the Cerebral Cortex,” *J. Neurosci.*, vol. 34, no. 36, pp. 11929–11947, 2014.

[143] S. A. Byron, K. R. Van Keuren-Jensen, D. M. Engelthaler, J. D. Carpten, and D. W. Craig, “Translating RNA sequencing into clinical diagnostics: opportunities and challenges,” *Nat. Rev. Genet.*, vol. 17, no. 5, pp. 257–271, May 2016.

[144] B. Gregory *et al.*, “Structural and Functional Changes of Pyramidal Neurons in Primary Motor Cortex at the Site of an Implanted Microelectrode Array,” *Soc. Neurosci. Present.*, 2021.

[145] T. D. Y. Kozai *et al.*, “Chronic tissue response to carboxymethyl cellulose based dissolvable insertion needle for ultra-small neural probes,” *Biomaterials*, vol. 35, no. 34, pp. 9255–9268, 2014.

[146] J. W. Salatino, B. M. Winter, M. H. Drazin, and E. K. Purcell, “Functional remodeling of subtype-specific markers surrounding implanted neuroprostheses,” *J. Neurophysiol.*, vol. 118, no. 1, pp. 194–202, Jul. 2017.

[147] S. Millecamps and J. P. Julien, “Axonal transport deficits and neurodegenerative diseases,” *Nat. Rev. Neurosci.*, vol. 14, no. 3, pp. 161–176, 2013.

[148] A. Szodorai *et al.*, “APP anterograde transport requires Rab3A GTPase activity for assembly of the transport vesicle,” *J. Neurosci.*, vol. 29, no. 46, pp. 14534–14544, 2009.

[149] M. Y. Lin and Z. H. Sheng, “Regulation of mitochondrial transport in neurons,” *Exp. Cell Res.*, vol. 334, no. 1, pp. 35–44, May 2015.

[150] D. T. W. Chang and I. J. Reynolds, “Mitochondrial trafficking and morphology in healthy and injured neurons,” *Prog. Neurobiol.*, vol. 80, no. 5, pp. 241–268, Dec. 2006.

[151] K. Richter *et al.*, “Presynaptic cytomatrix protein bassoon is localized at both excitatory and inhibitory synapses of rat brain,” *J. Comp. Neurol.*, vol. 408, no. 3, pp. 437–448, Apr. 1999.

[152] M. Verhage *et al.*, “Synaptic assembly of the brain in the absence of neurotransmitter secretion,” *Science (80-.).*, vol. 287, no. 5454, pp. 864–869, 2000.

[153] R. F. G. Toonen *et al.*, “Munc18-1 expression level control synapse recovery by regulating readily releasable pool size,” *Proc. Natl. Acad. Sci. U. S. A.*, vol. 103, no. 48, pp. 18332–18337, 2006.

[154] F. Antonucci, I. Corradini, G. Fossati, R. Tomasoni, E. Menna, and M. Matteoli, “SNAP-25, a Known presynaptic protein with emerging postsynaptic functions,” *Front. Synaptic Neurosci.*, vol. 8, no. MAR, pp. 1–9, 2016.

[155] J. A. Hosp, S. Mann, B. M. Wegenast-Braun, M. E. Calhoun, and A. R. Luft, “Region and task-specific activation of Arc in primary motor cortex of rats following motor skill learning,” *Neuroscience*, vol. 250, pp. 557–564, 2013.

[156] T. Chen, J. Zhu, Y. H. Wang, and C. H. Hang, “Arc silence aggravates traumatic neuronal injury via mGluR1-mediated ER stress and necroptosis,” *Cell Death Dis.*, vol. 11, no. 1, 2020.

[157] S. Takemoto-Kimura *et al.*, “Calmodulin kinases: essential regulators in health and disease,” *J. Neurochem.*, vol. 141, no. 6, pp. 808–818, 2017.

[158] A. S. Kato, M. B. Gill, H. Yu, E. S. Nisenbaum, and D. S. Bredt, “TARPs differentially decorate AMPA receptors to specify neuropharmacology,” *Trends Neurosci.*, vol. 33, no. 5, pp. 241–248, May 2010.

[159] J. S. Templin, S. J. Bang, M. Soiza-Reilly, C. B. Berde, and K. G. Commons, “Patterned expression of ion channel genes in mouse dorsal raphe nucleus determined with the Allen Mouse Brain Atlas,” *Brain Res.*, vol. 1457, no. 1, pp. 1–12, May 2012.

[160] J. R. Eles, A. L. Vazquez, T. D. Y. Kozai, and X. T. Cui, “In vivo imaging of neuronal calcium during electrode implantation: Spatial and temporal mapping of damage and recovery,” *Biomaterials*, vol. 174, pp. 79–94, Aug. 2018.

[161] J. W. Salatino, K. A. Ludwig, T. D. Y. Kozai, and E. K. Purcell, “Glial responses to implanted electrodes in the brain,” *Nat. Biomed. Eng.*, vol. 1, no. 11, pp. 862–877, Nov. 2017.

[162] D. H. H. Szarowski *et al.*, “Brain responses to micro-machined silicon devices.,” *Brain Res.*, vol. 983, no. 1–2, pp. 23–35, Sep. 2003.

[163] A. Skorupa *et al.*, “Angiogenin induces modifications in the astrocyte secretome: Relevance to amyotrophic lateral sclerosis,” *J. Proteomics*, vol. 91, pp. 274–285, 2013.

[164] F. Heindryckx and J. P. Li, “Role of proteoglycans in neuro-inflammation and central nervous system fibrosis,” *Matrix Biol.*, vol. 68–69, pp. 589–601, Aug. 2018.

[165] A. Bernal and L. Arranz, “Nestin-expressing progenitor cells: function, identity and therapeutic implications,” *Cell. Mol. Life Sci.*, vol. 75, no. 12, pp. 2177–2195, 2018.

[166] S. A. Liddelow *et al.*, “Neurotoxic reactive astrocytes are induced by activated microglia,” *Nature*, vol. 541, no. 7638, pp. 481–487, 2017.

[167] A. Iwata, K. D. Browne, X. H. Chen, T. Yuguchi, and D. H. Smith, “Traumatic brain injury induces biphasic upregulation of ApoE and ApoJ protein in rats,” *J. Neurosci. Res.*, vol. 82, no. 1, pp. 103–114, 2005.

[168] J. Pan, N. Ma, B. Yu, W. Zhang, and J. Wan, “Transcriptomic profiling of microglia and astrocytes throughout aging,” *J. Neuroinflammation*, vol. 17, no. 1, pp. 1–19, 2020.

[169] J. Presumey, A. R. Bialas, and M. C. Carroll, *Complement System in Neural Synapse Elimination in Development and Disease*, 1st ed., vol. 135. Elsevier Inc., 2017.

[170] Q. Li and B. A. Barres, “Microglia and macrophages in brain homeostasis and disease,” *Nat. Rev. Immunol.*, vol. 18, no. 4, pp. 225–242, 2018.

[171] S. Hong, L. Dissing-Olesen, and B. Stevens, “New insights on the role of microglia in synaptic pruning in health and disease,” *Curr. Opin. Neurobiol.*, vol. 36, pp. 128–134, 2016.

[172] T. Shimizu *et al.*, “The balance between cathepsin C and cystatin F controls remyelination in the brain of Plp1-overexpressing mouse, a chronic demyelinating disease model,” *Glia*, vol. 65, no. 6, pp. 917–930, 2017.

[173] S. A. Liddelow *et al.*, “Neurotoxic reactive astrocytes are induced by activated microglia,” *Nature*, vol. 541, no. 7638, pp. 481–487, 2017.

[174] H. Kettenmann, F. Kirchhoff, and A. Verkhratsky, “Microglia: New Roles for the Synaptic Stripper,” *Neuron*, vol. 77, no. 1, pp. 10–18, 2013.

[175] C. L. Tatar, S. Appikatla, D. A. Bessert, A. S. Paintlia, I. Singh, and R. P. Skoff, “Increased Plp1 gene expression leads to massive microglial cell activation and inflammation throughout the brain,” *ASN Neuro*, vol. 2, no. 4, pp. 219–231, Aug. 2010.

[176] H. Keren-Shaul *et al.*, “A Unique Microglia Type Associated with Restricting Development of Alzheimer’s Disease,” *Cell*, vol. 169, no. 7, pp. 1276-1290.e17, 2017.

[177] P. J. Kingham and J. M. Pocock, “Microglial secreted cathepsin B induces neuronal apoptosis,” *J. Neurochem.*, vol. 76, no. 5, pp. 1475–1484, 2001.

[178] K. A. Nave, “Myelination and support of axonal integrity by glia,” *Nature*, vol. 468, no. 7321, pp. 244–252, 2010.

[179] K. Chen, S. M. Wellman, Y. Yaxiaer, J. R. Eles, and T. D. Kozai, “In vivo spatiotemporal patterns of oligodendrocyte and myelin damage at the neural electrode interface,” *Biomaterials*, vol. 268, no. Iii, p. 120526, Nov. 2021.

[180] Y. Zhou *et al.*, “Human and mouse single-nucleus transcriptomics reveal TREM2-dependent and TREM2-independent cellular responses in Alzheimer’s disease,” *Nat. Med.*, vol. 26, no. 1, pp. 131–142, 2020.

[181] P. Zhang *et al.*, “Senolytic therapy alleviates Aβ-associated oligodendrocyte progenitor cell senescence and cognitive deficits in an Alzheimer’s disease model,” *Nat. Neurosci.*, vol. 22, no. 5, pp. 719–728, 2019.

[182] S. M. Wellman, L. Li, Y. Yaxiaer, I. McNamara, and T. D. Y. Kozai, “Revealing spatial and temporal patterns of cell death, glial proliferation, and blood-brain barrier dysfunction around implanted intracortical neural interfaces,” *Front. Neurosci.*, vol. 13, no. 493, pp. 1–17, May 2019.

CHAPTER 3 | SPATIOTEMPORAL EXPRESSION OF RNA-SEQ IDENTIFIED PROTEINS AROUND IMPLANTED SILICON ELECTRODES

1. INTRODUCTION

Microelectrode array technologies implanted in the nervous system have useful applications in the clinic and in the lab. Using these technologies gives ever-evolving avenues to treat diseases, restore essential functions, and study the nervous system[1–15]. However, implantation of microelectrodes damages cortical tissue and vasculature, initiating a highly complex tissue response which significantly limits functional longevity. Early studies characterized the tissue response to implanted devices as a progressive loss of neuronal cell bodies and neuronal processes, and formation of a glial scar consisting of activated microglia and astrocytes[16,17]. Based on these observations, it is believed that the tissue response is a significant contributor to the often-observed loss of recording quality and signal fidelity of implanted devices over time. In an effort to improve the performance of implanted devices, numerous next-generation devices with contemporary architectural approaches have been created for the purpose of attenuating or circumventing the tissue response entirely[18,19]. Many next-generation devices are reported to be successful in preserving neuronal populations and reducing astrogliosis at the device interface[18–23].

Despite evidence of a link between device performance and the tissue response, the signal quality of implanted electrodes can still decline when neuronal populations are preserved and gliosis is minimal[24]. There is a growing body of recent evidence which indicates that the complexity of the tissue response extends far beyond earlier

characterizations. It is now known that vascular disruptions, micromotion, and cellular reactions to damage and debris created by implanted devices produce a dynamic biological response[25–30]. Micromotion of implanted devices, as well as the steric blockade created by the indwelling device, may further disrupt natural tissue regeneration and prolong the tissue response [29,31]. Additional studies have provided evidence that the structural integrity of myelin and the structure of neuronal processes remain disrupted long after devices are implanted[32,33].

Recent transcriptional studies of tissue near implanted devices have added to this picture through the identification of differentially expressed genes surrounding implanted neurotechnology[34–38]. In a 2021 study, RNA-sequencing identified device-associated genes involved in multiple processes in the brain such as neuronal excitability and structure, glial modulation of neuronal activity, metabolic changes, myelination, and inflammation[38]. This previous study provided new information into the complexity of the tissue response at the device interface (out to100µm) and in distal tissue (500µm from implant), but fundamental questions remain, including: (1) whether or not gene expression will align with protein expression, (2) whether expression is driven within discrete cells or by changes in cellular population, and (3) what the cell type-specificity and the spatiotemporal distribution of these genes is within the respective regions of interest near devices. RNA-sequencing is a powerful tool which can provide insight into the broad transcriptional changes of tissues in states of injury and disease. However, generation of RNA-seq datasets are resource-intensive and produce large volumes of data which can be difficult to interpret without further validation at the protein level.

Considering known inconsistencies in the relationship between mRNA and protein expression[39,40], it is especially difficult to anticipate the effect of any differentially expressed genes on protein levels from RNA-seq data alone. We have chosen several RNA-seq identified genes with varying physiological functions and spatial expression patterns from our prior dataset to examine the feasibility of utilizing RNA-seq data to predict perturbations in proteins expression at the device interface. To accomplish this, we generated an automated, unbiased MATLAB-based method to evaluate the immunofluorescence of RNA-seq identified proteins involved in the tissue response at the electrode interface and estimate the association with cell type-specific markers.

Here, we have explored the spatiotemporal distribution of polypyrmidine tract binding protein-1 (Ptbp1), Ferritin Heavy Chain (Fth1), Transferrin (TF), Myelin Basic Protein (MBP), Proteolipid Protein-1 (Plp1), and Neurofilament Heavy Chain (Nefh) at the device interface. These markers were selected from the broader set of differentially expressed genes based their predicted involvement in phenomena relevant to the tissue response such as neuronal structure and function (Nefh, Plp1, MBP), cellular metabolism and oxidative stress (TF, Fth1), or glial proliferation and differentiation (Ptbp1). To accomplish this, we co-stained proteins of interest with cell type-specific markers and evaluated cellular densities and the fluorescence intensity of protein within discrete cell types at the device interface relative to distal and contralateral tissue. Our analysis found that the RNA-seq identified proteins in the present study share similar patterns of spatiotemporal expression, i.e., they are ‘aligned’ with the transcriptional data from our previous study. The results of this study provide evidence that RNA-seq generated

datasets can be utilized to develop new hypotheses about the biological processes involved in the tissue response to implanted electrodes that are testable at the protein level.

2. MATERIALS AND METHODS

2.1 SURGICAL IMPLANTATION AND TISSUE PROCESSING

Single Shank 'Michigan'-style non-functional probes (16-channel A1 x 16-3mm, 15µm thick, 703µm^2 site size, 100µm site spacing, Neuronexus Technologies) were stereotaxically implanted in the motor cortex (M1) of male Sprague-Dawley rats (aged 12-14 weeks). Animals were isoflurane-anesthetized and a craniotomy was performed over M1 (+3.0 mm Anterior, +/- 2.5 mm mediolateral from Bregma), dura was resected, and the electrode was stereotaxically inserted to a depth of 1.8mm from the cortical surface. A dental cement head-cap was used to secure the unilateral implant to two stainless steel bone screws. Bupivacaine and Neosporin were applied topically to the area around the incision to minimize discomfort and infection risk. Meloxicam was administered via injection for post-operative pain management. The surgical procedures for this study and the previous RNA-seq study are identical. Devices remained implanted in M1 for the duration of a designated time-point (1 Day, 1 Week, and 6 Weeks). All surgical procedures described were approved by the Michigan State University Animal Care and Use Committee. At the terminal time-point, animals were deeply anesthetized with isoflurane and sodium pentobarbital, transcardially flushed with phosphate buffered saline (PBS) and perfused with 4% paraformaldehyde, devices were removed, and the brains were extracted. After a graded sucrose protection (5%-20%) and cryo-embedding,

the brains were cryosectioned (Leica Biosystems) into 20µm thick sections and mounted on Superfrost^{tm} Plus slides (Fisher Scientific).

2.2 IMMUNOHISTOCHEMISTRY AND IMAGING

Six slides containing one to three tissue sections for each timepoint (n=6-8 animals per timepoint) were used for each antibody combination. Slides used for histology were selected in a way that each condition and antibody combination are represented equally across animal subjects (Supplementary Table 2). Tissue sections were hydrated in PBS, and blocked with 10% normal goat serum for one hour and subsequently incubated with primary antibodies ((GFAP 1:400 (Millipore Sigma G3893). CC1 1:100 (Millipore Sigma OP80). TF 1:100 (AbClonal A1148). Fth1 1:200 (Abcam ab65080). Ptbp1 1:250. (Abcam ab133734). MBP 1:500 (Antibodies.com A85322). NeuN 1:100 (Millipore Sigma MAB377). Iba1 1:200 (abcam ab283319). Plp1 1:200 (Thermo-Fisher PA5-40788). Nefh 1:1000 (Abcam ab7795)). Following primary incubation, samples were rinsed three times in PBS for 5 minutes and secondary antibodies (alexa-fluor 488 (Thermo-Fisher) 1:400, alexa-fluor 594 1:400 Thermo-Fisher) were applied for two hours. Slides were rinsed an additional two times for 10 minutes and nuclei were counterstained with 1ug/ml Hoechst. Images were acquired using an Olympus fluoview 1000 inverted confocal microscope with a x20 PlanFluor dry objective (0.5 NA) at a resolution of 1024x1024 pixels using kalman filtering to reduce background. A slide of tissue sections for each animal was used as a ‘no-primary’ control to validate the absence of autofluorescence and non-specific binding of antibodies.

2.3 CELL COUNTING AND CELL TYPE-SPECIFICITY

Fluorescent image analysis was performed using custom MATLAB software, adapted from the method introduced by Kozai et al. to quantify generalized fluorescence intensity from proteins of interest at a spatiotemporal level (Supplementary Figure 1)[41]. The mean intensity was calculated for each individual image, normalized, and averaged across all tissue sections for a given condition at each time point. To account for tissue regions such as vasculature which may influence intensity values, a background noise intensity threshold was calculated to subtract any bins with intensity values lower than one standard deviation below the threshold. We have also expanded upon Kozai et al.'s method to include new functionality which allows for identification of counterstained cell types which can be discretely quantified by evaluating cellular density and immunofluorescent intensity as a function of distance from the device interface.

Due to the wide variation in signal intensity spatially within the images, the cell type-specific markers (green channel) and Hoechst stain (blue channel) were contrast adjusted using the MATLAB command *adapthisteq* (contrast-limited adaptive histogram equalization)[42]. The resulting images were significantly more uniform, allowing for a binarization threshold that could consistently be calculated to fit the data. To determine the best threshold value, images were manually thresholded with a custom slider built in MATLAB during software development. This process consistently resulted in an optimal threshold value approximately equal to the mean intensity plus one standard deviation, which was implemented in the automated analysis program. The ensuing binary images were morphologically opened with *imopen*, incorporating a five-pixel disc structuring

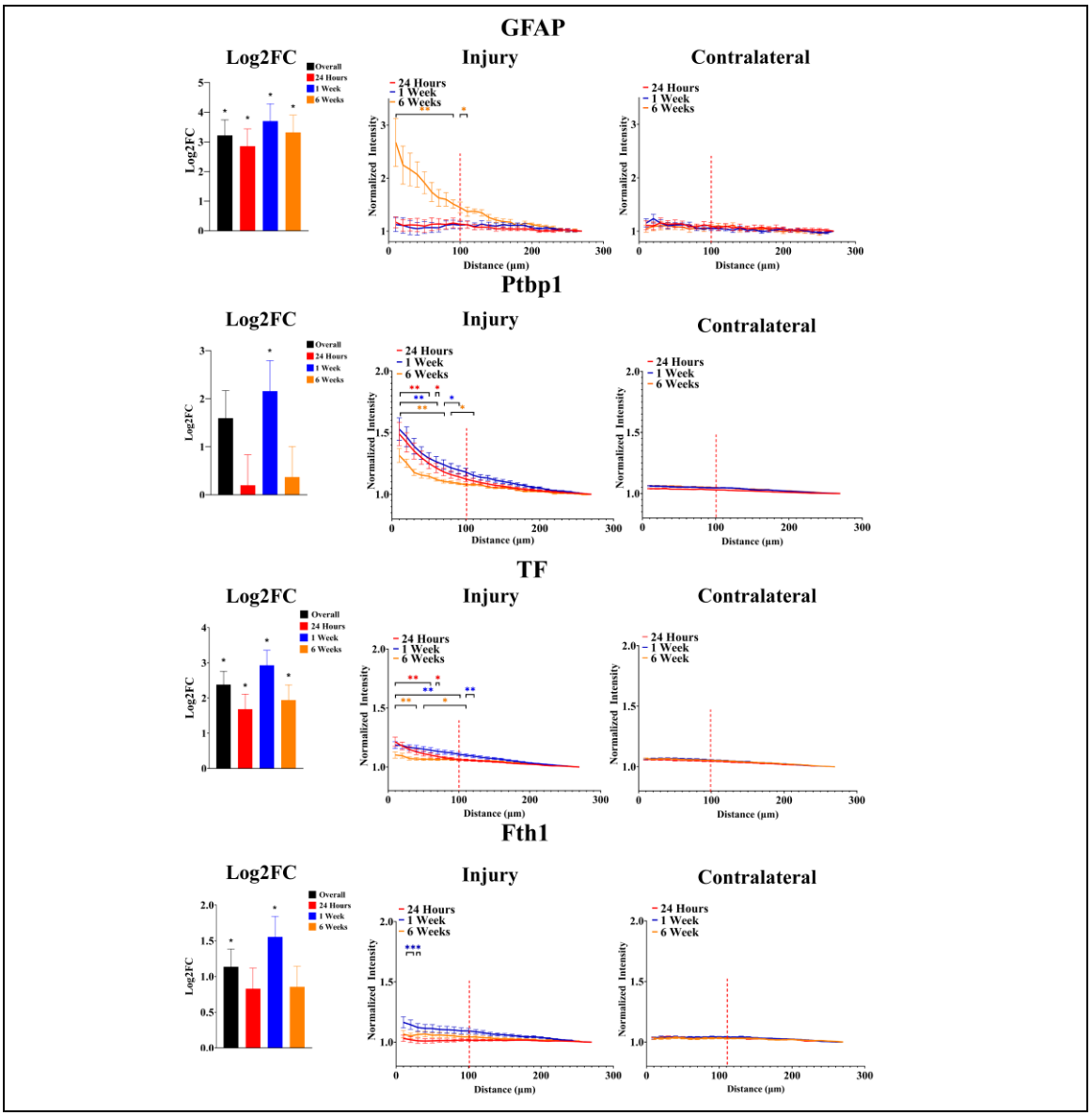

Figure 3.1: Spatiotemporal expression of RNA-seq identified proteins associated with astrogliosis and ion metabolism at the device interface. Non-cell type specific fluorescence intensity (line graph) of Glial fibrillary acidic protein (GFAP), Polypyrmidine-tract binding protein-1 (Ptbp1), Transferrin (TF), and Ferritin heavy chain-1 (Fth1) paired with the corresponding Log2FC from our previous RNA-sequencing study (Bar Graph). Dashed red line represents the area of tissue that was evaluated for RNA-sequencing. Line graphs are represented as mean intensity and error bars represent standard error. Horizontal brackets indicate significance of defined tissue regions relative to distal tissue (250µm from implant). $P \leq 0.05$* and $P \leq 0.001$**. Asterisks are color matched to the corresponding condition in each line graph. Bar graphs reproduced from reference [38] under CC BY 4.0 license.

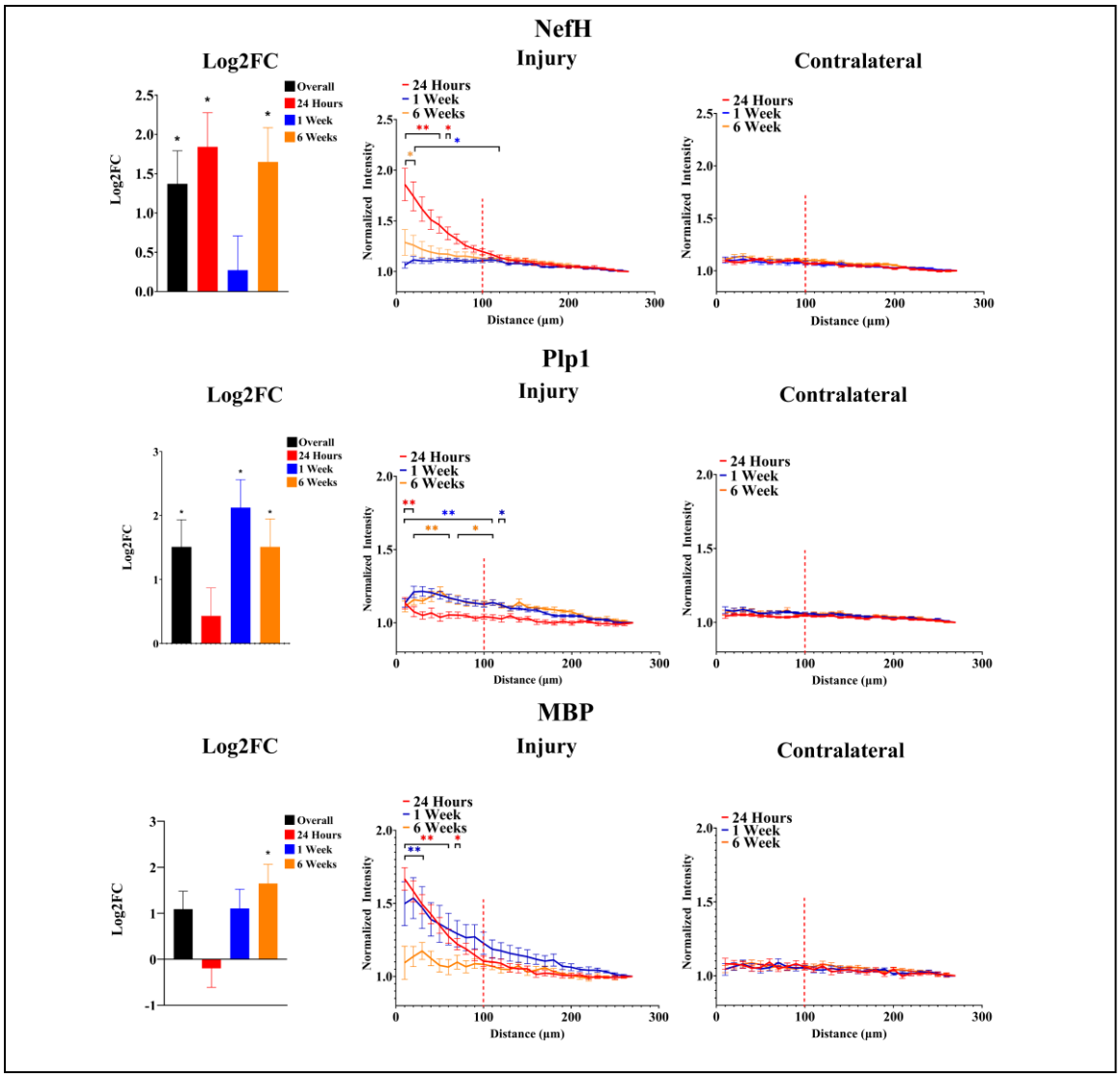

Figure 3.2: Spatiotemporal expression of RNA-seq identified proteins associated with neuronal remodeling and myelination at the device interface. Non-cell type specific fluorescence intensity (line graph) of Neurofilament heavy chain (Nefh), Myelin basic protein (MBP), and Proteolipid protein-1 (Plp1) paired with the corresponding Log2FC from our previous RNA-sequencing study (Bar Graph). Dashed red line represents the area of tissue that was evaluated for RNA-sequencing. Line graphs are represented as mean intensity and error bars represent standard error. Horizontal brackets indicate significance of defined tissue regions relative to distal tissue (250µm from implant). $P \leq 0.05$* and $P \leq 0.001$**. Asterisks are color matched to the corresponding condition in each line graph. Bar graphs reproduced from reference [38] under CC BY 4.0 license.

element, to remove cell processes and prevent cells from being overcounted and / or misidentified[43].

Finally, the binary images were window filtered based on connected pixel area to remove unwanted signals like autofluorescence and blood vessels. The remaining connected regions on both the cell-type and Hoechst stains were recorded. Cells counted with cell-type specific markers and Hoechst were sorted into “target” and “non-target” cells. A cell was considered a non-target cell if it was identified on the Hoechst stain and was not proximal to any cells counted with cell-type specific markers. If a cell counted with Hoechst was located within 20 pixels of a cell counted on the cell-type stain, the two would be merged and counted as one target cell. The centroid of the now merged target cell was taken from the center of Hoechst positive (+) nuclei. Cells counted with cell-type specific markers that did not contain Hoescht+ nuclei were counted as target cells, with the centroid unaltered from the initial green channel identification.

Cell density is calculated based on distance from the electrode implant site. Similar to Kozai et al., concentric bins are drawn radially outward from a user defined injury. MATLAB *polybuffer* command was used to generate exact concentric rings radially from the defined injury perimeter. To evaluate the spatial dynamics of cell density and localized intensity, 27 bins, each 10 microns in width, were used to capture as much of each image as possible (270μm total). The program then quantifies the total area of each bin, in addition to the number of target and non-target cells per bin. These metrics were used to calculate the target and non-target cell densities. The algorithm then extracts the localized intensity of the target protein (red channel) within both target cells

identified with cell type-specific markers (green channel) and an equal region from non-target cells. Localized intensity, in our case, is defined by the average signal intensity located within a circular region of interest (ROI), drawn about the centroid of each cell type with a radius of 10 pixels. To separate signal from background, the target protein image is thresholded with Otsu's method[44]. The algorithm then finds the average intensity located inside of each ROI for target and non-target cells. The resulting average intensity of all cells of the same type, falling within the same bin, are averaged to produce the localized intensity for each cell type spatially with respect to the electrode implant site and is subsequently normalized to the furthest bin. This methodology allows for the detection and quantification of protein which regionally overlaps with the ROIs drawn about cell bodies determined by cell-type specific markers. Regions of interest were either drawn to exclude areas of the device injury which had high levels of autofluorescence or were excluded from analysis. The accuracy of the MATLAB method described here was validated using non-biased human cell counting (Supplementary Figure 2).

2.4 STATISTICAL METHODS

To evaluate intensity of protein expression, a total of 18 animals were used across three timepoints (24 Hours, 7 Days, and 6 Weeks) and an average of six brain sections for each condition was assessed per animal. Data were compiled and analyzed using a linear mixed effects model using SPSS (IBM) to evaluate spatiotemporal effects of implanted electrode arrays relative to distal tissue as well as contralateral tissue similarly to previous work[45]. Statistical results were evaluated using the Bonferroni post-hoc

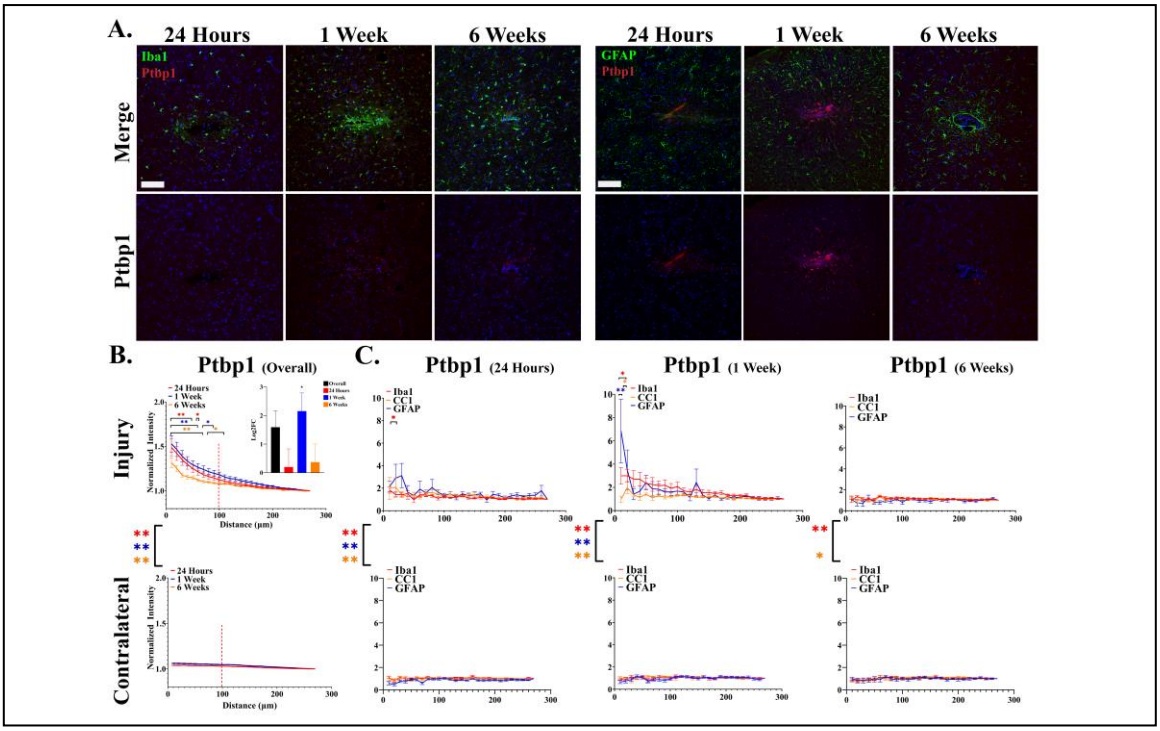

Figure 3.3: Ptbp1 is spatiotemporally expressed around implanted electrodes. A.) Representative immunohistochemistry which presents and Ptbp1 expression within microglia (Iba1), astrocytes (GFAP), and oligodendrocytes (CC1) at 24-hours, 1-week, and 6-weeks post implantation. **B.)** Line graphs which present non-cell type specific intensity analysis of pooled Fth1 data from across all histology samples at the device interface paired with RNA expression Log2FC from our previous RNA-sequencing study (Bar Graph). **C.)** Cell type specific analysis which presents the average normalized fluorescence intensity of Ptbp1 from CC1+, Iba1+, and GFAP+ cells at the device interface. Line graphs are represented as mean intensity and error bars represent standard error. Dashed red line represents the area of tissue that was evaluated for RNA-sequencing. Horizontal brackets indicate significance of defined tissue regions relative to distal tissue (250μm from implant) and vertical brackets indicate significance between tissue at the device interface relative to contralateral tissue. Scale bar = 100 μm. P≤0.05* and P≤0.001**. Asterisks are color matched to the corresponding condition in each line graph. Bar graphs reproduced from reference [38] under CC BY 4.0 license.

analysis where statistical significance was defined at P≤0.05* and P≤0.001**.

Differential expression analysis of RNAseq data from the prior study was conducted as described previously [38].

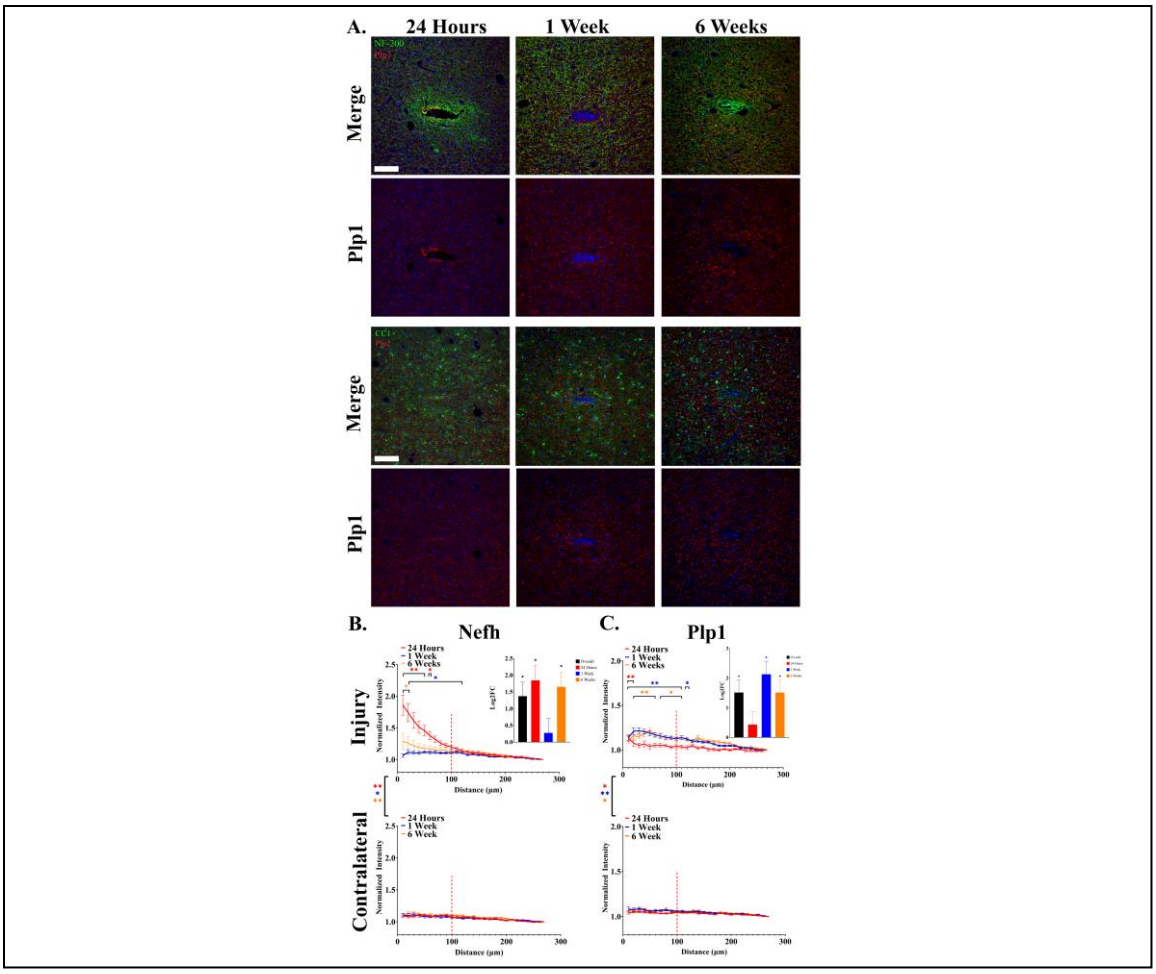

Figure 3.4: Neurofilament and proteolipid protein-1 are spatiotemporally expressed around implanted electrodes. **A.)** Representative immunohistochemistry which presents neurofilament (Nefh) and proteolipid protein-1 (Plp1) expression at 24-hours, 1-week, and 6-weeks post implantation. **B.)** Non-cell type specific fluorescence intensity analysis which shows the average normalized fluorescence intensity of Nefh at the device interface paired with RNA expression Log2FC from our previous RNA-sequencing study (Bar Graph). **C.)** Non-cell type specific fluorescence intensity analysis which shows the average normalized fluorescence intensity of Plp1 at the device interface paired with RNA expression Log2FC from our previous RNA-sequencing study (Bar Graph). Line graphs are represented as mean intensity and error bars represent standard error. Dashed red line represents the area of tissue that was evaluated for RNA-sequencing. Horizontal brackets indicate significance of defined tissue regions relative to distal tissue (250μm from implant) and vertical brackets indicate significance between tissue at the device interface relative to contralateral tissue. Scale bar = 100 μm. $P \leq 0.05$* and $P \leq 0.001$**. Asterisks are color matched to the corresponding condition in each line graph. Bar graphs reproduced from reference [38] under CC BY 4.0 license.

3. RESULTS

Our results show that the evaluated proteins of interest are locally expressed at the device interface (Figures 3.1, 3.2), and that many of these proteins are dynamically expressed within discrete cell types of the brain. In general, protein expressed at the device interface aligns with previously reported mRNA levels. GFAP is increased at the device interface by the 6-week timepoint which reflects anticipated progression of astrogliosis around standard Michigan style devices. Ptbp1 elevation at the device interface is primarily located within activated astrocyte and microglial populations at the 1-week timepoint. TF and Fth1 are elevated within 100 μm of the device and are largely present within neurons at the device interface. Elevation of TF and Fth1 may signify neuronal iron sequestration as a response to metabolic demand or iron influx at key timepoints during the tissue response. Localized changes in Nefh, Plp1, and MBP identify axonal damage and subsequent remodeling at the device interface. These RNA-seq identified proteins suggest changes in discrete local cellular populations relative to distal and contralateral tissue.

3.1 PTBP1 IS DETECTED IN GLIAL POPULATIONS AT EARLY TIMEPOINTS

At the device interface, we observed significantly elevated Ptbp1protein intensity at all timepoints (Figure 3.3). At 24 hours post-implantation, overall Ptbp1 expression is elevated out to 90μm from the device interface. Cell type-specific analysis of Ptbp1 showed that at 24 hours, Ptbp1 is significantly elevated in astrocytes and microglia at the device interface. In particular, elevated Ptbp1 expression was determined to be within astrocytes which are 20-30 μm from the device injury and in microglia 10-20 μm from

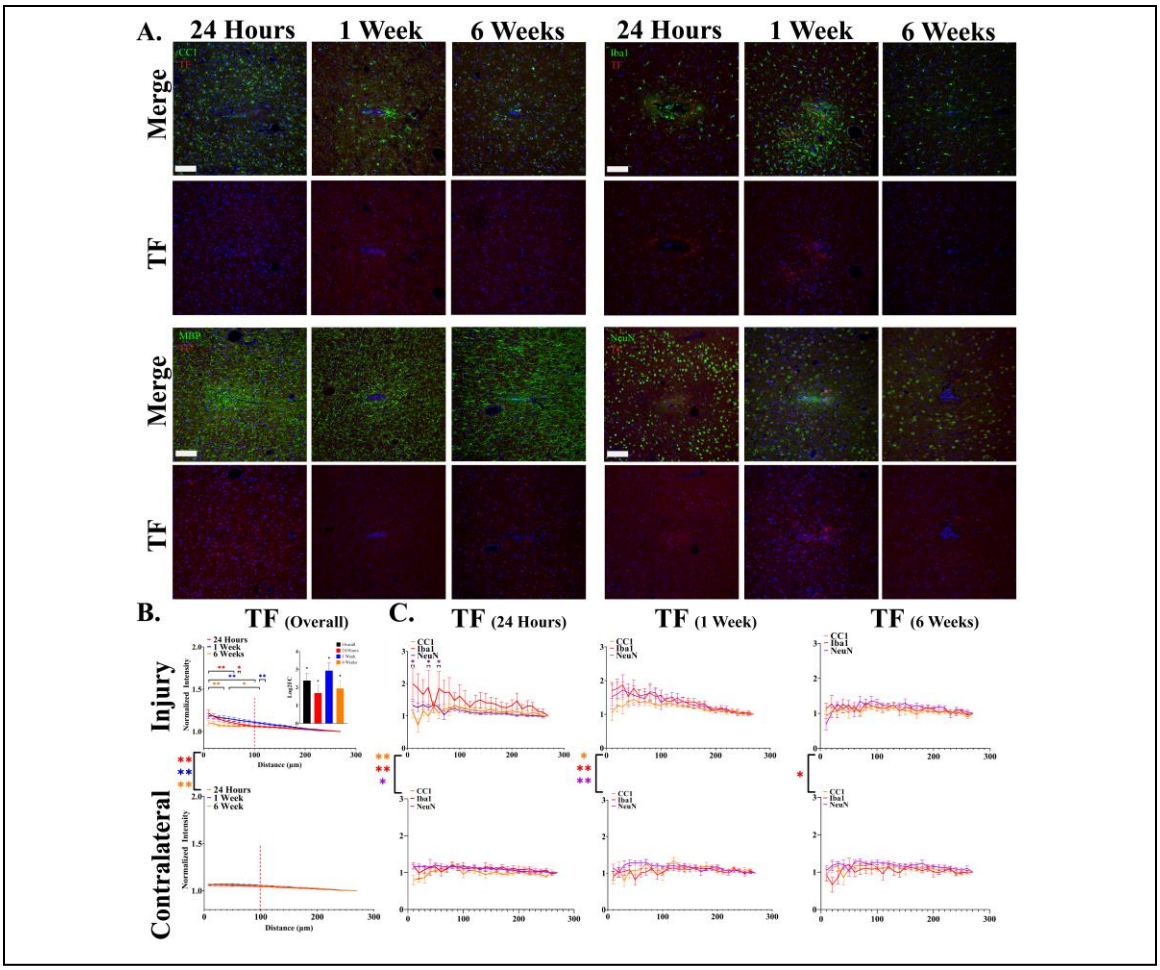

Figure 3.5: Transferrin (TF) is spatiotemporally expressed around implanted electrodes. A.) Representative immunohistochemistry which presents transferrin expression at 24-hours, 1-week, and 6-weeks post implantation. **B.)** Non-cell type specific fluorescence intensity analysis which shows the average normalized fluorescence intensity of TF at the device interface paired with RNA expression Log2FC from our previous RNA-sequencing study (Bar Graph) . **C.)** Cell type specific analysis which presents the average normalized fluorescence intensity of TF from CC1+ (oligodendrocytes), Iba1+ (microglia), and NeuN+ (neurons) cells at the device interface. Line graphs are represented as mean intensity and error bars represent standard error. Dashed red line represents the area of tissue that was evaluated for RNA-sequencing. Horizontal brackets indicate significance of defined tissue regions relative to distal tissue (250μm from implant) and vertical brackets indicate significance between tissue at the device interface relative to contralateral tissue. Scale bar = 100 μm. P≤0.05* and P≤0.001**. Asterisks are color matched to the corresponding condition in each line graph. Bar graphs reproduced from reference [38] under CC BY 4.0 license.

the device injury. At 1-week post-implantation, Ptbp1 is generally elevated out to 100 µm from the device interface. Cell type-specific analysis revealed that Ptbp1 is significantly elevated within the astrocytic, microglial and oligodendrocyte populations. Astrocytes show greatly increased Ptbp1 expression directly at the device interface. Little to no Ptbp1 was detected within oligodendrocytes except at the 1-week timepoint when Ptbp1 was detected within a small number of CC1+ cells approximately 20 µm from the electrode. Microglial elevation of Ptbp1 expression was also found to be localized to a range of 10-20 µm from the device interface. At the 6-week time-point, nonspecific expression of Ptbp1 is significantly elevated out to 120 µm from the device injury.

3.2 NEUROFILAMENT HEAVY CHAIN (NEFH) AT THE DEVICE INTERFACE

In addition to the expected expression patterns of GFAP and the cellular proliferation associated protein Ptbp1, we also observed spatiotemporal changes in the expression of proteins associated with neuronal health and structure (Figure 3.4). Nefh, Plp1, and MBP are intrinsically important to the viability of neurons at the device interface[46]. Nefh, Plp1, and MBP expression were each found to be significantly disrupted locally at implanted devices. Our previous RNA-seq experiments showed that *Nefh* expression was significantly differentially expressed at 24-hours and 6-weeks post-implantation. Nefh was observed to be elevated at 24-hour post insertion out to ~100 µm from the device injury. At 1-week post implantation, we observed moderately elevated Nefh intensity from approximately 30-120 µm from the device interface. At 6-weeks post implantation, Nefh remains elevated directly at the interface (10-20 µm) and the structure of Nefh+ processes are tightly packed and reorganized around the indwelling electrode.

We also observed significantly elevated Nefh near the device injury relative to contralateral tissue at all timepoints. Our IHC data is generally aligned with our previous gene expression data as the fluorescence intensity is elevated at the same timepoints. In contrast to our transcriptional dataset, we also observed a modest, yet significant, elevation in Nefh intensity at the 1-week timepoint.

3.3 PROTEOLIPID PROTEIN-1 (PLP1) IS SPATIOTEMPORALLY EXPRESSED AT THE DEVICE INTERFACE

Plp1 is a structural protein which plays a major role in the makeup of the myelin sheath of axonal processes and is primarily expressed by oligodendrocytes. Our previous transcriptional data found that *Plp1* was differentially expressed 1- and 6-weeks within 100µm from implanted electrodes. At 24-hours post implantation, we observed Plp1 elevation directly at the device interface (10-20 µm), which is possibly driven in part due to extracellular Plp1 debris (Figure 3.4). At 1-week post implantation, we observed an increase in Plp1 intensity out to 120 µm from the implanted device. At 6-week post implantation, Plp1 remains elevated from 30-110 µm from the device injury. Relative to contralateral tissue, Plp1 is significantly increased directly at the device interface and decreased beyond 150 µm. Plp1 is also significantly elevated at 1- and 6-weeks post implantation relative to contralateral tissue. Our fluorescence intensity analysis of Plp1 in this study observed that protein expression appears to align with elevated protein intensity primarily at 1- and 6-weeks post implantation. Throughout the entire time course analyzed for this study, Plp1 appears to be initially disassociated with Nefh+ neuronal processes at the 24-hour timepoint and becomes gradually more organized and

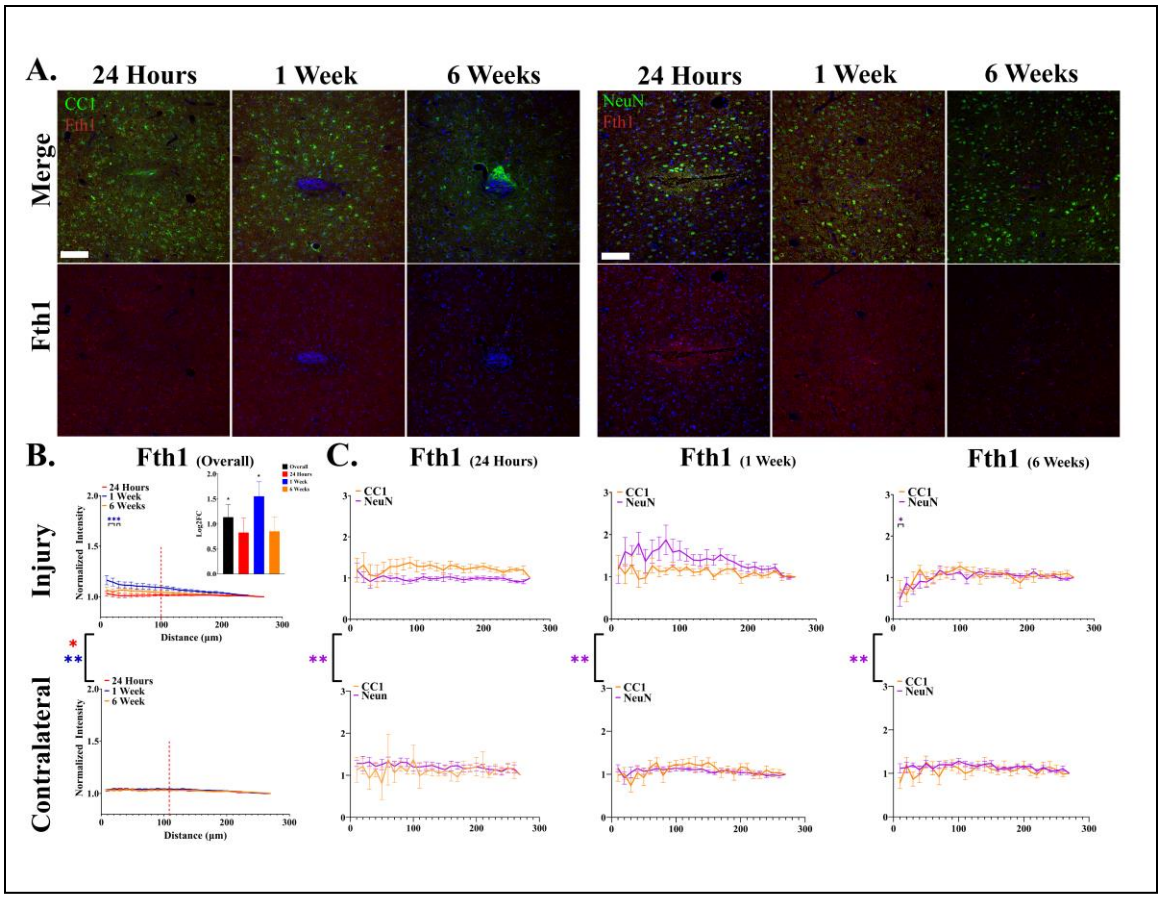

Figure 3.6: Ferritin Heavy Chain is spatiotemporally expressed around implanted electrodes. A.) Representative immunohistochemistry which presents Fth1 expression within neurons (NeuN), and oligodendrocytes (CC1) at 24-hours, 1-week, and 6-weeks post implantation. **B.)** Line graphs which present non-cell type specific intensity analysis of pooled Fth1 data from across all histology samples at the device interface paired with RNA expression Log2FC from our previous RNA-sequencing study (Bar Graph) . **C.)** Cell type specific analysis which presents the average normalized fluorescence intensity of Fth1 from CC1+ and NeuN+ cells at the device interface. Line graphs are represented as mean intensity and error bars represent standard error. Dashed red line represents the area of tissue that was evaluated for RNA-sequencing. Horizontal brackets indicate significance of defined tissue regions relative to distal tissue (250µm from implant) and vertical brackets indicate significance between tissue at the device interface relative to contralateral tissue. Scale bar = 100 µm. P≤0.05* and P≤0.001**. Asterisks are color matched to the corresponding condition in each line graph. Bar graphs reproduced from reference [38] under CC BY 4.0 license.

more strongly associated with Nefh+ processes by the 6-week timepoint.

3.4 MYELIN BASIC PROTEIN IS ELEVATED AT EARLY TIMEPOINTS

Protein expression of MBP is spatiotemporally altered at the device interface (Figure 3.2). Our previous gene expression data showed that MBP gene expression was significantly elevated at 6 weeks post-implantation. In this study, protein expression of MBP is not aligned with our gene expression results with MBP being the most elevated at 24 hours post implantation. At the 24-hour timepoint, we observed significantly elevated MBP intensity out to 70 μm from the device injury. Here, we have observed myelin which appears to be punctate and unassociated with neuronal processes. This is potentially indicative of MBP debris resulting from post-insertional myelin damage at the 24-hour timepoint. At 1-week post-implantation, MBP expression is significantly elevated 30 μm from the device tract with a reduced incidence of apparent myelin debris. At 6 weeks post-implantation, MBP debris is visibly apparent, but there was no significant difference in MBP intensity at the injury relative to distal tissue or at the device interface relative to contralateral tissue.

3.5 TRANSFERRIN IS SPATIOTEMPORALLY EXPRESSED IN NEURONS AND MICROGLIA AT THE DEVICE INTERFACE

Iron metabolism is essential for cellular populations in both healthy and diseased tissue. TF and Fth1 are key proteins involved in cellular iron metabolism and are spatiotemporally expressed in multiple cell types in the brain following device insertion. Our results indicate that transferrin is primarily present in neuronal populations at the device interface, but it is also present in oligodendrocytes and microglia (Figure 3.5). The

distribution and cell type-specificity at the device interface is spatiotemporally dynamic. Fluorescence intensity of transferrin at the device interface shares trends with our previous RNA-sequencing data. At 24 hours post-implantation, transferrin was found to be significantly elevated within 100 μm of the implanted device with signal contributions likely being from both intracellular and extracellular TF (Figure 3.1A). Cell type-specific interrogation revealed that microglia and neurons contain elevated levels of TF while oligodendrocyte-specific TF is relatively unchanged. At 1-week post-implantation, extracellular transferrin is present but diminished, and a large percentage of detected transferrin is localized within the cell bodies within 100 μm of implanted devices. Neuronal and microglial populations continue to contain elevated TF expression out to 100 μm while oligodendrocytes show elevated TF expression at approximately 50 μm from the device interface. At 6 weeks, there is very little exogenous transferrin and the overall intensity of detected transferrin remains elevated, but less so than in previous timepoints. At 6 weeks post-implantation, TF intensity is reduced relative to previous timepoints but remains significantly elevated. At the device interface, cell types which were evaluated for TF expression did not show significant changes at the device interface relative to the furthest bin analyzed. This result could possibly suggest that other cell types such as pericytes, NG2 glia, and oligodendrocyte progenitors, which we did not examine, are contributing to the global increase in TF intensity at the 6 week time-point.

3.6 FERRITIN EXPRESSION IS REDUCED IN NEURONS AT THE DEVICE INTERFACE 6-WEEKS POST IMPLANTATION

Ferritin is an iron binding protein that is comprised of light (Ftl) and heavy (Fth)

subunits and is present in all cell types as an important regulator of cellular metabolism[47,48]. We previously identified *Fth1* as differentially expressed 1-week post-implantation. In this study, we observed that detected Fth1 intensity aligns with our RNA-seq dataset (Figure 3.6). However, when we examined the spatiotemporal expression of Fth1 separately in neuronal and oligodendrocyte populations, our results indicated that Fth1 is dynamically expressed in neurons while Fth1 within oligodendrocytes remains unchanged throughout all timepoints. At 24-hours post-implantation, our results show that Fth1 intensity is relatively unchanged around the device interface with Fth1 showing higher enrichment in neurons than in oligodendrocytes. At 1-week post-implantation, we observed elevated Fth1 in neurons within 100 μm of the device interface while Fth1 within oligodendrocytes remains unchanged. At the 6-week timepoint, Fth1 expression remains slightly elevated, but we observed a marked decrease in neuronal Fth1 within 20 μm of the device interface while oligodendrocyte Fth1 remains unaltered.

4. DISCUSSION

This tissue response is a highly complex biological response that remains to be fully understood. Implantation of electrodes into the brain damages cortical vasculature, cellular populations, and neuronal processes[49]. This damage creates significant cellular debris which contains plasma proteins, lipid rich myelin debris, and cellular detritus which leads to the rapid proliferation of activated microglia and astrocytes, which then mobilize to clear pro-inflammatory cellular debris and gradually encapsulate implanted devices[16,17]. As time progresses, the remaining cellular populations redistribute

around indwelling devices in an apparent attempt to re-establish homeostasis. In a previous RNA-seq study, we identified hundreds of genes which are differentially expressed around implanted devices in the brain[38]. This study expands upon our previous work to determine whether our subset of differentially expressed genes share similar patterns of protein expression. With the exception of Ptbp1, GFAP, and MBP, protein expression aligns with transcriptional expression provided in our previous RNA-seq dataset. Nonetheless, each protein identified through RNA-seq was detectable at the device interface and was in some way disrupted by the presence of implanted electrodes. This suggests that even through protein expression will not always align with gene expression, it is possible to use RNA-seq to predict broad and cell-type specific changes of proteins involved in the tissue response to implanted devices. We have also provided new observations of Ptbp1 expression within activated glia surrounding electrodes, the spatiotemporal dynamics of neurite regeneration and remyelination, and the expression of proteins associated with iron metabolism in cell types involved at the device interface.

4.1 PTBP1 IS EXPRESSED WITHIN REACTIVE ASTROCYTES AND MICROGLIA

The role of astrocytes and microglia in the tissue response to implanted devices is an area of active inquiry. The behavior of these glia in the tissue response is complex and can exhibit either degenerative or protective phenotypes[30,50,51]. Ptbp1 is an alternative splicing RNA-binding protein involved in the regulation of cellular identity and proliferation; it is known to be expressed in both astrocytes and microglia[52–54]. Ptbp1 has been characterized as a pro-inflammatory oncogenic protein which is highly

expressed in fibrotic tissues and glioma[52,55–57]. Ptbp1 has been reported to play a key role in the differentiation of astrocytes during early development, with Ptbp1 expression being an established driver of astrocyte maturity[58,59]. Our RNA-seq dataset showed that *Ptbp1* is differentially expressed in tissues within 100 µm from implanted devices. Our histological analysis revealed that Ptbp1 is the most concentrated in cells directly at the interface relative to distal and contralateral tissues (Supplementary Figure 3). Specifically, Ptbp1 is enriched within activated glia which are known to proliferate around and or migrate to implanted electrodes. Cell type-specific protein intensity analysis identified that Ptbp1 is primarily expressed in astrocytes and microglia at 24-hours and 1-week post implantation, when we would expect to see the greatest inflammatory response. Ptbp1 has been previously reported to be a candidate for generating functional neurons in neurodegenerative disorders via reprogramming[60,61], but the suitability of Ptbp1 as a therapeutic target remains controversial [62,63]. Enrichment of Ptbp1 within microglia and astrocytes at early timepoints may point to Ptbp1 as a possible biomarker to identify reactive glia following device insertion or a therapeutic target to modulate inflammatory glial populations. The functions of Ptbp1 are not yet fully understood, but the upregulation of Ptbp1 at the transcriptional and protein level near implanted devices may suggest a functional role for this protein in activated glia.

4.2 NEURONAL STRUCTURE AND MYELIN INTEGRITY IS DISRUPTED BY IMPLANTED ELECTRODES

Our RNA-sequencing data had identified that neurofilament proteins, Nefh

specifically, is transcriptionally upregulated at 24 hours and 6 weeks post-implantation. Neurofilaments are useful biomarkers for brain injury and play key roles in neuronal structure, axonal transport, and ion channel function [46,64]. Following device insertion into the brain, axons are significantly disrupted by damage and subsequent remodeling at the device interface over time[16]. Damage to neuronal processes creates debris that is rich with neurofilaments and myelin components which are known activators of local microglia[65,66]. Axonal regeneration is a highly controlled process which is regulated, in part, by glial signaling[67–70]. In the inflammatory environment following device insertion, axonal regeneration can be hindered by microglial involvement and repellant signals presented by the astroglial scar[68,71,72]. In particular, Nefh deficient neurons in knockout mice show decreased outward rectification capabilities and decreased conduction velocities, which suggests that proper alignment of Nefh may play a role in neuronal signal generation[46]. In this study, we have evaluated changes in Nefh over time and our results suggest that Nefh protein expression is aligned with previous transcriptional dynamics. We attribute the elevated neurofilament at 24 hours to the noticeable damage and debris which is common around implanted electrodes. At 1- and 6-weeks post-implantation, Nefh remains elevated with a reduction in what we observed to be Nefh debris. The elevation of Nefh+ processes is localized to a range of approximately 50 – 130 μm from the device injury. However, the extent to which neuronal processes successfully regenerate around implanted cortical devices remains unknown. Even in otherwise healthy subjects, axonal regeneration is susceptible to failure following the diffuse axon injury created by indwelling electrodes[73,74]. Patterns

in disrupted axonal regeneration is characterized by aberrant and compacted neurofilament structures which are believed to disrupt axonal transport of essential proteins and organelles which can result in delayed neurodegeneration[73]. The temporal fluctuation of Nefh expression around implanted device may indicate neuronal repair immediately after device insertion. Nefh fluctuations may also indicate the need for further neurofilament production at later timepoints due to remodeling or further disturbance. Micromotion of implanted devices is one example of post-insertional disturbances which may necessitate further process remodeling and while additionally interfering with neuronal repair. Remodeling of neurofilaments at the device interface and any potential failures in axon regeneration and subsequent remyelination may contribute to detrimental changes in signal quality.

Healthy neuronal function is maintained in part by interfacial myelin sheaths which boost saltatory conduction of action potentials and provide essential trophic support to myelinated axons[75–79]. MBP and Plp1 are essential components of myelin structure which are primarily produced by oligodendrocytes to maintain or regenerate myelin following injury. The process of remyelination is complex and requires the presence of local oligodendrocyte progenitors and their subsequent differentiation. Our histological analysis found that MBP expression at the device interface is significantly elevated at the 24-hour and 1-week timepoint relative to distal and contralateral tissue. Plp1 expression is significantly elevated at all timepoints relative to distal and contralateral tissue. At the 24-hour timepoint, we attribute elevated MBP and Plp1 as myelin debris which is highly localized to the device injury and does not appear to be

associated with any contiguous neuronal process. Myelin debris in the extracellular space enhances the tissue response by activating glial populations and interferes with remyelination by inhibiting proliferation of oligodendrocyte progenitor cells[80–82]. Myelin debris is known to cause reactivity in microglial and astrocyte populations via the complement system which amplifies the tissue response to injury[66,80,83,84]. Myelin debris interacts with several microglial receptors (TLR4, CX3CR1, TREM2, MerTK, RXRa)[85], and the astrocytic receptor LRP1, which initiates phagocytotic behavior [80]. Myelin debris contains constituent proteins such as Nogo-A, Myelin Associated Glycoprotein, and chondroitin sulfate proteoglycans which have inhibitory effects on neuronal regeneration and remyelination[82,86,87]. At 1-week post-implantation, we observed a decline in myelin debris and a sustained elevation of MBP+ and Plp1+ processes relative to distal and contralateral tissue. This may indicate an increase in myelin thickness or abnormalities in myelin structure at the device interface. At the 6-week timepoint, Plp1 expression remains elevated while MBP is normal relative to distal and contralateral tissue. Disrupted remyelination and compromised myelin integrity has been shown to be an indicator of neuronal dysfunction and contributor to axonal degeneration[74,75,77,79]. While Nefh, MBP, and Plp1 at all upregulated around the device injury, we observe a lack of coherency between Nefh+ processes and Plp1+ processes: Nefh+ processes appear to be tightly re-organized around implanted devices with little to no apparent qualitative cohesion with Plp1. This is in contrast to expression patterns observed in contralateral tissue (Supplementary Figure 3.4, 3.5). Observed disorder between neuronal processes and myelin components may indicate the persistent

presence of inhibitory myelin debris and myelin structural disruptions, which are known drivers of neuronal regenerative failure. Following injury, neuronal survival relies on successful axonal regeneration and remyelination. Recent evidence has shown that neuronal processes facing implanted devices become truncated for at least 6-weeks post implantation[33]. The presence of deleterious myelin debris and disordered myelin structure at the device interface may contribute to observed neuronal degeneration via a combination of intrinsic inhibitory activity and trophic support deprivation, ultimately interfering with axonal regeneration.

4.3 IMPLANTED ELECTRODES DRIVE CHANGES IN ESSENTIAL IRON BINDING PROTEINS TF AND FTH1

The processes involved in glial activation, axonal regeneration, and remyelination each are energetically taxing on the affected cellular populations and require large amounts of energy. One mechanism that cellular populations in the brain utilize to meet these energy demands is iron metabolism. In this study, we observed the spatiotemporal dynamics of TF and Fth1 within neurons, microglia, and oligodendrocytes as a method to evaluate the dynamics of iron binding proteins following device insertion. The expression patterns of TF and Fth1 indicate that neurons, oligodendrocytes, and microglia are metabolically active following device insertion, and that neurons at the device interface become Fth1 deficient at the 6-week timepoint. We observed parallel trends in TF elevation within neurons and oligodendrocytes at 24-hours and 1-week, while Fth1 expression was only elevated within neuronal populations at the device interface. We also observed a persistent elevation of microglial TF at all timepoints relative to distal and

contralateral tissue. Iron metabolism is a highly regulated process in the brain and is essential for numerous cellular processes carried out by activated glia, remyelinating oligodendrocytes, proliferating cells, and regenerating neurons[88–91]. Implantation of electrode arrays in the brain damages vasculature and cellular populations, which creates an excess of iron in the extracellular environment which is sequestered by local cellular populations[92]. Free iron within cells needs to be utilized immediately or sequestered within iron binding proteins such as Fth1 and TF. Otherwise, it becomes a source of oxidative stress and a contributing factor of degeneration[93–96]. TF is a primary source of trafficked iron within cell types in the brain as their metabolic demands fluctuate and Fth1 is used as an indicator of high iron utilization as opposed to iron storage[47,48,97,98].

Immunofluorescent quantification at identified that TF and Fth1 are spatiotemporally expressed within microglia, neurons, and oligodendrocytes at the device interface relative to distal and contralateral tissues (Supplementary Figures 5,6). Microglia express high basal levels of TF in a homeostatic state and alter their metabolism during activation[99–101]. The persistent enrichment of TF within microglia may indicate the continued involvement of microglia in the tissue response beyond activation at acute timepoints. Neurons require iron for normal functions such as the production of neurotransmitters and successful regeneration of processes following injury. Neuronal iron homeostasis relies in part on glial mediated transport of iron and through interfacial myelin sheaths to axonal mitochondria[89] Increases in TF concentration within neurons and oligodendrocytes at device interface may reflect

elevated metabolic demand due to hyperexcitability and the initiation of regenerative processes, but may also indicate a susceptibility to oxidative stress[102–105]. Oligodendrocytes provide essential trophic support for neuronal function by maintaining myelin, which is used to secrete Fth1 and metabolic factors in addition to boosting axonal conductance[78,90]. Increases of neuronal and oligodendrocyte Fth1 may suggest a combination of heightened metabolic demand and the maintenance of neuronal trophic support. The decrease in neuronal Fth1 at the device interface at the 6-week timepoint may reflect a loss of glial mediated trophic support, general impairment of neuronal function, or a failure to successfully regenerate following damage to neuronal processes. Nonetheless, the altered expression of TF and Fth1 at the device interface indicate that there are lasting changes in iron metabolism within tissues at the device interface, which may provide additional context for loss of neuronal viability and glial activation over time.

5. CONCLUSIONS

The tissue response is a significant hurdle for seamless integration of implanted neural technologies. Understanding the tissue response to implanted devices is essential for the effective design and characterization of next-generation neural prostheses which exhibit improved biocompatibility. Here, we have shown that many of the proteins chosen for this study reflect the transcriptional changes observed in our previous RNA-sequencing study. Instances in which proteins did not align with prior transcriptional data may be explained by (1) secondary regulation of mRNA transcription, or (2) the presence of cell types at the device interface which contribute to protein expression which we did

not screen in this study. While it is well known that changes in changes in gene expression may not directly correlate to protein expression[39,40], we have found that exploratory RNA-sequencing can be used to predict and validate general fluctuations at the protein level in the context of implanted microelectrode arrays. Furthermore, we investigated the cell type-specificity of these proteins, and the results provide insight into which cell types may be contributing to the differential gene expression in our previous study. The results of this study also provide evidence for the expanded role of myelin associated proteins and cellular iron transport in the context of cortical implants. However, the mechanisms of the tissue response, the interplay between cell types, and their potential involvement in the failure of implanted electrodes require further study. The focus of the methodology in this study is limited to the interrogation of immunofluorescence at the overall tissue level and within cell bodies, but TF and Fth1 were unable to be identified in the processes of analyzed cell types. We also believe that it is important to consider that there are likely functional dynamics of the proteins identified in this study, such as Ptbp1, that have yet to be fully understood. The functional roles of proteins evaluated in this study, in particular, Ptbp1 and the myelin proteins, are greatly underserved. Recent reports have provided evidence that many of the genes which are differentially expressed at the device interface may be coincidentally involved with the progression of the tissue response to implanted electrodes[106]. While there were RNA-seq identified proteins that did not exactly spatiotemporally align with their transcriptional counterparts, we were able to use prior RNA-seq data to reliably predict device driven disruptions in these protein expression in general. Therefore, it is essential

that RNA-seq datasets of differentially expressed genes be further studied at the protein level so that the full scope of protein interactions, relationships between cellular density and protein level, and involvement in the tissue response can be considered in the cortical implant environment. In future studies it may also be useful to more thoroughly investigate the effects that the proteins analyzed in this study may have on specific pathways, such as those involved in neurodegeneration, inflammation, or the viability of cell types at the device interface. We believe that this study provides proof-of-concept evidence to motivate further RNA-seq driven immunohistological/protein assessments to investigate the mechanisms of the tissue response around implanted electrodes in the brain.

REFERENCES

[1] A.W. Laxton, D.F. Tang-Wai, M.P. McAndrews, D. Zumsteg, R. Wennberg, R. Keren, J. Wherrett, G. Naglie, C. Hamani, G.S. Smith, A.M. Lozano, A phase i trial of deep brain stimulation of memory circuits in Alzheimer's disease, Ann. Neurol. 68 (2010) 521–534. https://doi.org/10.1002/ana.22089.

[2] J. Kuhn, K. Hardenacke, D. Lenartz, T. Gruendler, M. Ullsperger, C. Bartsch, J.K. Mai, K. Zilles, A. Bauer, A. Matusch, R.J. Schulz, M. Noreik, C.P. Bührle, D. Maintz, C. Woopen, P. Häussermann, M. Hellmich, J. Klosterkötter, J. Wiltfang, M. Maarouf, H.J. Freund, V. Sturm, Deep brain stimulation of the nucleus basalis of Meynert in Alzheimer's dementia, Mol. Psychiatry. 20 (2015) 353–360. https://doi.org/10.1038/mp.2014.32.

[3] C.E. Bouton, A. Shaikhouni, N. V. Annetta, M.A. Bockbrader, D.A. Friedenberg, D.M. Nielson, G. Sharma, P.B. Sederberg, B.C. Glenn, W.J. Mysiw, A.G. Morgan, M. Deogaonkar, A.R. Rezai, Restoring cortical control of functional movement in a human with quadriplegia, Nature. 533 (2016) 247–250. https://doi.org/10.1038/nature17435.

[4] F.T. Sun, M.J. Morrell, R.E. Wharen, Responsive Cortical Stimulation for the Treatment of Epilepsy, Neurotherapeutics. 5 (2008) 68–74. https://doi.org/10.1016/j.nurt.2007.10.069.

[5] E.J. Quinn, Z. Blumenfeld, A. Velisar, M.M. Koop, L.A. Shreve, M.H. Trager, B.C. Hill, C. Kilbane, J.M. Henderson, H. Brontë-Stewart, Beta oscillations in freely moving Parkinson's subjects are attenuated during deep brain stimulation, Mov. Disord. 30 (2015) 1750–1758. https://doi.org/10.1002/mds.26376.

[6] P.J. Grahn, G.W. Mallory, O.U. Khurram, B.M. Berry, J.T. Hachmann, A.J. Bieber, K.E. Bennet, H.K. Min, S.Y. Chang, K.H. Lee, J.L. Lujan, A neurochemical closed-loop controller for deep brain stimulation: Toward individualized smart neuromodulation therapies, Front. Neurosci. 8 (2014) 169. https://doi.org/10.3389/fnins.2014.00169.

[7] A.L. Crowell, P. Riva-Posse, S.J. Garlow, H.S. Mayberg, Toward an Understanding of the Neural Circuitry of Major Depressive Disorder Through the Clinical Response to Deep Brain Stimulation of Different Anatomical Targets, Curr. Behav. Neurosci. Reports. 1 (2014) 55–63. https://doi.org/10.1007/s40473-014-0008-z.

[8] D.M. Whiting, N.D. Tomycz, J. Bailes, L. De Jonge, V. Lecoultre, B. Wilent, D. Alcindor, E.R. Prostko, B.C. Cheng, C. Angle, D. Cantella, B.B. Whiting, J.S. Mizes, K.W. Finnis, E. Ravussin, M.Y. Oh, Lateral hypothalamic area deep brain

stimulation for refractory obesity: A pilot study with preliminary data on safety, body weight, and energy metabolism: Clinical article, J. Neurosurg. 119 (2013) 56–63. https://doi.org/10.3171/2013.2.JNS12903.

[9] A.L. Ho, E.S. Sussman, A. V. Pendharkar, D.E. Azagury, C. Bohon, C.H. Halpern, Deep brain stimulation for obesity: Rationale and approach to trial design, Neurosurg. Focus. 38 (2015) E8. https://doi.org/10.3171/2015.3.FOCUS1538.

[10] D.R. Moore, R. V. Shannon, Beyond cochlear implants: Awakening the deafened brain, Nat. Neurosci. 12 (2009) 686–691. https://doi.org/10.1038/nn.2326.

[11] H.H. Lim, T. Lenarz, Auditory midbrain implant: Research and development towards a second clinical trial, Hear. Res. 322 (2015) 212–223. https://doi.org/10.1016/j.heares.2015.01.006.

[12] P.M. Lewis, H.M. Ackland, A.J. Lowery, J. V. Rosenfeld, Restoration of vision in blind individuals using bionic devices: A review with a focus on cortical visual prostheses, Brain Res. 1595 (2015) 51–73. https://doi.org/10.1016/j.brainres.2014.11.020.

[13] J. V. Smit, M.L.F. Janssen, H. Schulze, A. Jahanshahi, J.J. Van Overbeeke, Y. Temel, R.J. Stokroos, Deep brain stimulation in tinnitus: Current and future perspectives, Brain Res. 1608 (2015) 51–65. https://doi.org/10.1016/j.brainres.2015.02.050.

[14] J.L. Collinger, B. Wodlinger, J.E. Downey, W. Wang, E.C. Tyler-Kabara, D.J. Weber, A.J.C. McMorland, M. Velliste, M.L. Boninger, A.B. Schwartz, High-performance neuroprosthetic control by an individual with tetraplegia, Lancet. 381 (2013) 557–564. https://doi.org/10.1016/S0140-6736(12)61816-9.

[15] T. Aflalo, S. Kellis, C. Klaes, B. Lee, Y. Shi, K. Pejsa, K. Shanfield, S. Hayes-Jackson, M. Aisen, C. Heck, C. Liu, R.A. Andersen, Decoding motor imagery from the posterior parietal cortex of a tetraplegic human, Science (80-.). 348 (2015) 906–910. https://doi.org/10.1126/science.aaa5417.

[16] R. Biran, D.C. Martin, P.A. Tresco, Neuronal cell loss accompanies the brain tissue response to chronically implanted silicon microelectrode arrays, Exp. Neurol. 195 (2005) 115–126. https://doi.org/10.1016/j.expneurol.2005.04.020.

[17] R. Biran, D.C. Martin, P.A. Tresco, The brain tissue response to implanted silicon microelectrode arrays is increased when the device is tethered to the skull, J. Biomed. Mater. Res. - Part A. 82 (2007) 169–178. https://doi.org/10.1002/jbm.a.31138.

[18] C.H. Thompson, M.J. Zoratti, N.B. Langhals, E.K. Purcell, Regenerative Electrode Interfaces for Neural Prostheses, Tissue Eng. - Part B Rev. 22 (2016) 125–135. https://doi.org/10.1089/ten.teb.2015.0279.

[19] C.H. Thompson, T.E. Riggins, P.R. Patel, C.A. Chestek, W. Li, E. Purcell, Toward guiding principles for the design of biologically-integrated electrodes for the central nervous system, J. Neural Eng. 17 (2020) 021001. https://doi.org/10.1088/1741-2552/ab7030.

[20] X. Yang, T. Zhou, T.J. Zwang, G. Hong, Y. Zhao, R.D. Viveros, T.M. Fu, T. Gao, C.M. Lieber, Bioinspired neuron-like electronics, Nat. Mater. 18 (2019) 510–517. https://doi.org/10.1038/s41563-019-0292-9.

[21] L.J. Tang, M.H. Wang, H.C. Tian, X.Y. Kang, W. Hong, J.Q. Liu, Progress in research of flexible MEMS microelectrodes for neural interface, Micromachines. 8 (2017) 1–18. https://doi.org/10.3390/mi8090281.

[22] M.M. Maharbiz, R. Muller, E. Alon, J.M. Rabaey, J.M. Carmena, Reliable Next-Generation Cortical Interfaces for Chronic Brain-Machine Interfaces and Neuroscience, Proc. IEEE. 105 (2017) 73–82. https://doi.org/10.1109/JPROC.2016.2574938.

[23] J. Rivnay, H. Wang, L. Fenno, K. Deisseroth, G.G. Malliaras, Next-generation probes, particles, and proteins for neural interfacing, Sci. Adv. 3 (2017) e1601649. https://doi.org/10.1126/sciadv.1601649.

[24] N.J. Michelson, A.L. Vazquez, J.R. Eles, J.W. Salatino, E.K. Purcell, J.J. Williams, X.T. Cui, T.D.Y. Kozai, Multi-scale, multi-modal analysis uncovers complex relationship at the brain tissue-implant neural interface: New emphasis on the biological interface, J. Neural Eng. 15 (2018) 033001. https://doi.org/10.1088/1741-2552/aa9dae.

[25] N.F. Nolta, M.B. Christensen, P.D. Crane, J.L. Skousen, P.A. Tresco, BBB leakage, astrogliosis, and tissue loss correlate with silicon microelectrode array recording performance, Biomaterials. 53 (2015) 753–762. https://doi.org/10.1016/j.biomaterials.2015.02.081.

[26] C. Bennett, M. Samikkannu, F. Mohammed, W.D. Dietrich, S.M. Rajguru, A. Prasad, Blood brain barrier (BBB)-disruption in intracortical silicon microelectrode implants, Biomaterials. 164 (2018) 1–10. https://doi.org/10.1016/j.biomaterials.2018.02.036.

[27] D. Prodanov, J. Delbeke, Mechanical and biological interactions of implants with the brain and their impact on implant design, Front. Neurosci. 10 (2016).

https://doi.org/10.3389/fnins.2016.00011.

[28] H.C. Lee, F. Ejserholm, J. Gaire, S. Currlin, J. Schouenborg, L. Wallman, M. Bengtsson, K. Park, K.J. Otto, Histological evaluation of flexible neural implants; Flexibility limit for reducing the tissue response?, J. Neural Eng. 14 (2017) 036026. https://doi.org/10.1088/1741-2552/aa68f0.

[29] J. Thelin, H. Jörntell, E. Psouni, M. Garwicz, J. Schouenborg, N. Danielsen, C.E. Linsmeier, Implant size and fixation mode strongly influence tissue reactions in the CNS, PLoS One. 6 (2011) e16267. https://doi.org/10.1371/journal.pone.0016267.

[30] J.W. Salatino, K.A. Ludwig, T.D.Y. Kozai, E.K. Purcell, Glial responses to implanted electrodes in the brain, Nat. Biomed. Eng. 1 (2017) 862–877. https://doi.org/10.1038/s41551-017-0154-1.

[31] T.D.Y. Kozai, A.S. Jaquins-Gerstl, A.L. Vazquez, A.C. Michael, X.T. Cui, Brain tissue responses to neural implants impact signal sensitivity and intervention strategies, ACS Chem. Neurosci. 6 (2015) 48–67. https://doi.org/10.1021/cn500256e.

[32] K. Chen, S.M. Wellman, Y. Yaxiaer, J.R. Eles, T.D. Kozai, In vivo spatiotemporal patterns of oligodendrocyte and myelin damage at the neural electrode interface, Biomaterials. 268 (2021) 120526. https://doi.org/10.1016/j.biomaterials.2020.120526.

[33] B.A. Gregory, C.H. Thompson, J.W. Salatino, M.J. Railing, A.F. Zimmerman, B. Gupta, K. Williams, J.A. Beatty, C.L. Cox, E.K. Purcell, Structural and functional changes of pyramidal neurons at the site of an implanted microelectrode array in rat primary motor cortex, BioRxiv. (2022) 2022.09.15.507997. http://biorxiv.org/content/early/2022/09/17/2022.09.15.507997.abstract.

[34] S. Song, B. Regan, E.S. Ereifej, E.R. Chan, J.R. Capadona, Neuroinflammatory Gene Expression Analysis Reveals Pathways of Interest as Potential Targets to Improve the Recording Performance of Intracortical Microelectrodes, Cells. 11 (2022). https://doi.org/10.3390/cells11152348.

[35] K. Joseph, M. Kirsch, M. Johnston, C. Münkel, T. Stieglitz, C.A. Haas, U.G. Hofmann, Transcriptional characterization of the glial response due to chronic neural implantation of flexible microprobes, Biomaterials. 279 (2021) 121230. https://doi.org/10.1016/j.biomaterials.2021.121230.

[36] Q.A. Whitsitt, B. Patel, B. Hunt, E.K. Purcell, A Spatial Transcriptomics Study of the Brain-Electrode Interface in Rat Motor Cortex, BioRxiv. (2021)

2021.12.03.471147.
https://www.biorxiv.org/content/10.1101/2021.12.03.471147v1%0Ahttps://www.biorxiv.org/content/10.1101/2021.12.03.471147v1.abstract.

[37] Q.A. Whitsitt, B. Koo, M.E. Celik, B.M. Evans, J.D. Weiland, E.K. Purcell, Spatial Transcriptomics as a Novel Approach to Redefine Electrical Stimulation Safety, Front. Neurosci. 16 (2022) 1–17. https://doi.org/10.3389/fnins.2022.937923.

[38] C.H. Thompson, A. Saxena, N. Heelan, J. Salatino, E.K. Purcell, Spatiotemporal patterns of gene expression around implanted silicon electrode arrays, J. Neural Eng. 18 (2021). https://doi.org/10.1088/1741-2552/abf2e6.

[39] C. Buccitelli, M. Selbach, mRNAs, proteins and the emerging principles of gene expression control, Nat. Rev. Genet. 21 (2020) 630–644. https://doi.org/10.1038/s41576-020-0258-4.

[40] S. Haider, R. Pal, Integrated Analysis of Transcriptomic and Proteomic Data, (2013) 91–110.

[41] T.D.Y. Kozai, Z. Gugel, X. Li, P.J. Gilgunn, R. Khilwani, O.B. Ozdoganlar, G.K. Fedder, D.J. Weber, X.T. Cui, Chronic tissue response to carboxymethyl cellulose based dissolvable insertion needle for ultra-small neural probes, Biomaterials. 35 (2014) 9255–9268. https://doi.org/10.1016/j.biomaterials.2014.07.039.

[42] K. Zuiderveld, Contrast Limited Adaptive Histogram Equalization, in: Graph. Gems, Elsevier, 1994: pp. 474–485. https://doi.org/10.1016/b978-0-12-336156-1.50061-6.

[43] M.H. Chen, P.F. Yan, A Multiscaling Approach Based on Morphological Filtering, IEEE Trans. Pattern Anal. Mach. Intell. 11 (1989) 694–700. https://doi.org/10.1109/34.192464.

[44] Otsu, N., A threshold selection method from gray-level histograms, IEEE Trans. Syst. Man Cybern. 9 (1996) 62–66.

[45] J.W. Salatino, B.M. Winter, M.H. Drazin, E.K. Purcell, Functional remodeling of subtype-specific markers surrounding implanted neuroprostheses, J. Neurophysiol. 118 (2017) 194–202. https://doi.org/10.1152/jn.00162.2017.

[46] A. Yuan, M. V. Rao, Veeranna, R.A. Nixon, Neurofilaments and neurofilament proteins in health and disease, Cold Spring Harb. Perspect. Biol. 9 (2017). https://doi.org/10.1101/cshperspect.a018309.

[47] G.A. Salvador, Iron in neuronal function and dysfunction, BioFactors. 36 (2010) 103–110. https://doi.org/10.1002/biof.80.

[48] J.R. Connor, K.L. Boeshore, S.A. Benkovic, S.L. Menzies, Isoforms of ferritin have a specific cellular distribution in the brain, J. Neurosci. Res. 37 (1994) 461–465. https://doi.org/10.1002/jnr.490370405.

[49] S.M. Wellman, L. Li, Y. Yaxiaer, I. McNamara, T.D.Y. Kozai, Revealing spatial and temporal patterns of cell death, glial proliferation, and blood-brain barrier dysfunction around implanted intracortical neural interfaces, Front. Neurosci. 13 (2019) 1–17. https://doi.org/10.3389/fnins.2019.00493.

[50] C.T. Jiang, W.F. Wu, Y.H. Deng, J.W. Ge, Modulators of microglia activation and polarization in ischemic stroke (Review), Mol. Med. Rep. 21 (2020) 2006–2018. https://doi.org/10.3892/mmr.2020.11003.

[51] S.A. Liddelow, K.A. Guttenplan, L.E. Clarke, F.C. Bennett, C.J. Bohlen, L. Schirmer, M.L. Bennett, A.E. Münch, W.S. Chung, T.C. Peterson, D.K. Wilton, A. Frouin, B.A. Napier, N. Panicker, M. Kumar, M.S. Buckwalter, D.H. Rowitch, V.L. Dawson, T.M. Dawson, B. Stevens, B.A. Barres, Neurotoxic reactive astrocytes are induced by activated microglia, Nature. 541 (2017) 481–487. https://doi.org/10.1038/nature21029.

[52] V.N. Babenko, G.T. Shishkina, D.A. Lanshakov, E. V. Sukhareva, N.N. Dygalo, LPS Administration Impacts Glial Immune Programs by Alternative Splicing, Biomolecules. 12 (2022). https://doi.org/10.3390/biom12020277.

[53] P. van Bergeijk, U. Seneviratne, E. Aparicio-Prat, R. Stanton, S.A. Hasson, SRSF1 and PTBP1 Are trans -Acting Factors That Suppress the Formation of a CD33 Splicing Isoform Linked to Alzheimer's Disease Risk , Mol. Cell. Biol. 39 (2019). https://doi.org/10.1128/mcb.00568-18.

[54] J. Rexach, D. Geschwind, Selective Neuronal Vulnerability in Alzheimer's Disease: A Modern Holy Grail, Neuron. 107 (2020) 763–765. https://doi.org/10.1016/j.neuron.2020.08.018.

[55] T. Xu, W. Yan, Q. Wu, Q. Xu, J. Yuan, Y. Li, P. Li, H. Pan, C. Ni, MiR-326 Inhibits Inflammation and Promotes Autophagy in Silica-Induced Pulmonary Fibrosis through Targeting TNFSF14 and PTBP1, Chem. Res. Toxicol. 32 (2019) 2192–2203. https://doi.org/10.1021/acs.chemrestox.9b00194.

[56] A. Georgilis, S. Klotz, C.J. Hanley, N. Herranz, B. Weirich, B. Morancho, A.C. Leote, L. D'Artista, S. Gallage, M. Seehawer, T. Carroll, G. Dharmalingam, K.B. Wee, M. Mellone, J. Pombo, D. Heide, E. Guccione, J. Arribas, N.L. Barbosa-

Morais, M. Heikenwalder, G.J. Thomas, L. Zender, J. Gil, PTBP1-Mediated Alternative Splicing Regulates the Inflammatory Secretome and the Pro-tumorigenic Effects of Senescent Cells, Cancer Cell. 34 (2018) 85-102.e9. https://doi.org/10.1016/j.ccell.2018.06.007.

[57] H. Gong, A. Jiang, R. Jiang, Y. Wang, D. Zhang, Z. Wu, J. Xiao, PTBP1 as a Promising Predictor of Poor Prognosis by Regulating Cell Proliferation, Immunosuppression, and Drug Sensitivity in SARC, Oxid. Med. Cell. Longev. 2022 (2022). https://doi.org/10.1155/2022/5687238.

[58] J. Hu, H. Qian, Y. Xue, X.-D. Fu, PTB/nPTB: master regulators of neuronal fate in mammals, Biophys. Reports. 4 (2018) 204–214. https://doi.org/10.1007/s41048-018-0066-y.

[59] S. Dai, C. Wang, C. Zhang, L. Feng, W. Zhang, X. Zhou, Y. He, X. Xia, B. Chen, W. Song, PTB: Not just a polypyrimidine tract-binding protein, J. Cell. Physiol. 237 (2022) 2357–2373. https://doi.org/10.1002/jcp.30716.

[60] H. Qian, X. Kang, J. Hu, D. Zhang, Z. Liang, F. Meng, X. Zhang, Y. Xue, R. Maimon, S.F. Dowdy, N.K. Devaraj, Z. Zhou, W.C. Mobley, D.W. Cleveland, X.D. Fu, Reversing a model of Parkinson's disease with in situ converted nigral neurons, Nature. 582 (2020) 550–556. https://doi.org/10.1038/s41586-020-2388-4.

[61] M. Contardo, R. De Gioia, D. Gagliardi, G. Pietro Comi, L. Ottoboni, M. Nizzardo, S. Corti, Targeting PTB for Glia-to-Neuron Reprogramming In Vitro and In Vivo for Therapeutic Development in Neurological Diseases, Biomedicines. 10 (2022). https://doi.org/10.3390/biomedicines10020399.

[62] W. Chen, Q. Zhen, Q. Huang, S. Ma, M. Li, Repressing PTBP1 fails to convert reactive astrocytes to dopaminergic neurons in a 6-hydroxydopamine mouse model of Parkinson's disease, Elife. 11 (2022) 1–15. https://doi.org/10.7554/eLife.75636.

[63] T. Hoang, D.W. Kim, H. Appel, N.A. Pannullo, P. Leavey, M. Ozawa, S. Zheng, M. Yu, N.S. Peachey, S. Blackshaw, Genetic loss of function of Ptbp1 does not induce glia-to-neuron conversion in retina, Cell Rep. 39 (2022) 110849. https://doi.org/10.1016/j.celrep.2022.110849.

[64] C.H. Xia, E.A. Roberts, L.S. Her, X. Liu, D.S. Williams, D.W. Cleveland, L.S.B. Goldstein, Abnormal neurofilament transport caused by targeted disruption of neuronal kinesin heavy chain KIF5A, J. Cell Biol. 161 (2003) 55–66. https://doi.org/10.1083/jcb.200301026.

[65] T. Tanaka, M. Ueno, T. Yamashita, Engulfment of axon debris by microglia requires p38 MAPK activity, J. Biol. Chem. 284 (2009) 21626–21636.

https://doi.org/10.1074/jbc.M109.005603.

[66] T.J. Kopper, J.C. Gensel, Myelin as an inflammatory mediator: Myelin interactions with complement, macrophages, and microglia in spinal cord injury, J. Neurosci. Res. 96 (2018) 969–977. https://doi.org/10.1002/jnr.24114.

[67] S.L. Peterson, H.X. Nguyen, O.A. Mendez, A.J. Anderson, Complement Protein C3 Suppresses Axon Growth and Promotes Neuron Loss, Sci. Rep. 7 (2017) 1–13. https://doi.org/10.1038/s41598-017-11410-x.

[68] A.M. Tan, W. Zhang, J.M. Levine, NG2: A component of the glial scar that inhibits axon growth, J. Anat. 207 (2005) 717–725. https://doi.org/10.1111/j.1469-7580.2005.00452.x.

[69] G. Yiu, Z. He, Glial inhibition of CNS axon regeneration, Nat. Rev. Neurosci. 7 (2006) 617–627. https://doi.org/10.1038/nrn1956.

[70] D. Toy, U. Namgung, Role of Glial Cells in Axonal Regeneration, Exp. Neurobiol. 22 (2013) 68–76. https://doi.org/10.5607/en.2013.22.2.68.

[71] G.C. McConnell, H.D. Rees, A.I. Levey, C.A. Gutekunst, R.E. Gross, R. V. Bellamkonda, Implanted neural electrodes cause chronic, local inflammation that is correlated with local neurodegeneration, J. Neural Eng. 6 (2009). https://doi.org/10.1088/1741-2560/6/5/056003.

[72] D.O. Dias, C. Göritz, Fibrotic scarring following lesions to the central nervous system, Matrix Biol. 68–69 (2018) 561–570. https://doi.org/10.1016/j.matbio.2018.02.009.

[73] D.G. Siedler, M.I. Chuah, M.T.K. Kirkcaldie, J.C. Vickers, A.E. King, Diffuse axonal injury in brain trauma: Insights from alterations in neurofilaments, Front. Cell. Neurosci. 8 (2014) 1–10. https://doi.org/10.3389/fncel.2014.00429.

[74] J. Mu, M. Li, T. Wang, X. Li, M. Bai, G. Zhang, J. Kong, Myelin Damage in Diffuse Axonal Injury, Front. Neurosci. 13 (2019) 1–11. https://doi.org/10.3389/fnins.2019.00217.

[75] G.J. Duncan, T.J. Simkins, B. Emery, Neuron-Oligodendrocyte Interactions in the Structure and Integrity of Axons, Front. Cell Dev. Biol. 9 (2021). https://doi.org/10.3389/fcell.2021.653101.

[76] M. Simons, K.A. Nave, Oligodendrocytes: Myelination and axonal support, Cold Spring Harb. Perspect. Biol. 8 (2016) 1–16. https://doi.org/10.1101/cshperspect.a020479.

[77] Y. Lee, B.M. Morrison, Y. Li, S. Lengacher, M.H. Farah, P.N. Hoffman, Y. Liu, A. Tsingalia, L. Jin, P.W. Zhang, L. Pellerin, P.J. Magistretti, J.D. Rothstein, Oligodendroglia metabolically support axons and contribute to neurodegeneration, Nature. 487 (2012) 443–448. https://doi.org/10.1038/nature11314.

[78] C. Mukherjee, T. Kling, B. Russo, K. Miebach, E. Kess, M. Schifferer, L.D. Pedro, U. Weikert, M.K. Fard, N. Kannaiyan, M. Rossner, M.L. Aicher, S. Goebbels, K.A. Nave, E.M. Krämer-Albers, A. Schneider, M. Simons, Oligodendrocytes Provide Antioxidant Defense Function for Neurons by Secreting Ferritin Heavy Chain, Cell Metab. 32 (2020) 259-272.e10. https://doi.org/10.1016/j.cmet.2020.05.019.

[79] S.M. Wellman, K. Guzman, K.C. Stieger, L.E. Brink, S. Sridhar, M.T. Dubaniewicz, L. Li, F. Cambi, T.D.Y. Kozai, Cuprizone-induced oligodendrocyte loss and demyelination impairs recording performance of chronically implanted neural interfaces, Biomaterials. 239 (2020) 119842. https://doi.org/10.1016/j.biomaterials.2020.119842.

[80] G. Ponath, S. Ramanan, M. Mubarak, W. Housley, S. Lee, F.R. Sahinkaya, A. Vortmeyer, C.S. Raine, D. Pitt, Myelin phagocytosis by astrocytes after myelin damage promotes lesion pathology, Brain. 140 (2017) 399–413. https://doi.org/10.1093/brain/aww298.

[81] M.R. Kotter, W.W. Li, C. Zhao, R.J.M. Franklin, Myelin impairs CNS remyelination by inhibiting oligodendrocyte precursor cell differentiation, J. Neurosci. 26 (2006) 328–332. https://doi.org/10.1523/JNEUROSCI.2615-05.2006.

[82] H. Neumann, M.R. Kotter, R.J.M. Franklin, Debris clearance by microglia: An essential link between degeneration and regeneration, Brain. 132 (2009) 288–295. https://doi.org/10.1093/brain/awn109.

[83] C.L. Tatar, S. Appikatla, D.A. Bessert, A.S. Paintlia, I. Singh, R.P. Skoff, Increased Plp1 gene expression leads to massive microglial cell activation and inflammation throughout the brain, ASN Neuro. 2 (2010) 219–231. https://doi.org/10.1042/AN20100016.

[84] Q. Li, B.A. Barres, Microglia and macrophages in brain homeostasis and disease, Nat. Rev. Immunol. 18 (2018) 225–242. https://doi.org/10.1038/nri.2017.125.

[85] A. Lampron, A. Larochelle, N. Laflamme, P. Préfontaine, M.M. Plante, M.G. Sánchez, V. Wee Yong, P.K. Stys, M.È. Tremblay, S. Rivest, Inefficient clearance of myelin debris by microglia impairs remyelinating processes, J. Exp. Med. 212 (2015) 481–495. https://doi.org/10.1084/jem.20141656.

[86] J. Silver, M.E. Schwab, P.G. Popovich, Central nervous system regenerative failure: Role of oligodendrocytes, astrocytes, and microglia, Cold Spring Harb. Perspect. Biol. 7 (2015) a020602. https://doi.org/10.1101/cshperspect.a020602.

[87] J. Gruchot, V. Weyers, P. Göttle, M. Förster, D. Kremer, H.P. Hartung, P. Küry, The molecular basis for remyelination failure in multiple sclerosis, Cells. 8 (2019) 1–14. https://doi.org/10.3390/cells8080825.

[88] R.J. Ward, D.T. Dexter, R.R. Crichton, Iron, Neuroinflammation and Neurodegeneration, Int. J. Mol. Sci. 23 (2022) 1–18. https://doi.org/10.3390/ijms23137267.

[89] T. McElroy, R. Zeidan, L. Rathor, S. Han, R. Xiao, The role of mitochondria in the recovery of neurons after injury, Neural Regen. Res. 18 (2023) 317–318. https://doi.org/10.4103/1673-5374.343907.

[90] B. Todorich, J.M. Pasquini, C.I. Garcia, P.M. Paez, J.R. Connor, Oligodendrocytes and myelination: The role of iron, Glia. 57 (2009) 467–478. https://doi.org/10.1002/glia.20784.

[91] T. Moos, T.R. Nielsen, T. Skjørringe, E.H. Morgan, Iron trafficking inside the brain, J. Neurochem. 103 (2007) 1730–1740. https://doi.org/10.1111/j.1471-4159.2007.04976.x.

[92] G.M. Bishop, T.N. Dang, R. Dringen, S.R. Robinson, Accumulation of non-transferrin-bound iron by neurons, astrocytes, and microglia, Neurotox. Res. 19 (2011) 443–451. https://doi.org/10.1007/s12640-010-9195-x.

[93] C. Bennett, F. Mohammed, A. Álvarez-Ciara, M.A. Nguyen, W.D. Dietrich, S.M. Rajguru, W.J. Streit, A. Prasad, Neuroinflammation, oxidative stress, and blood-brain barrier (BBB) disruption in acute Utah electrode array implants and the effect of deferoxamine as an iron chelator on acute foreign body response, Biomaterials. 188 (2019) 144–159. https://doi.org/10.1016/j.biomaterials.2018.09.040.

[94] J.R. Connor, S.L. Menzies, Cellular management of iron in the brain, J. Neurol. Sci. 134 (1995) 33–44. https://doi.org/10.1016/0022-510X(95)00206-H.

[95] E.S. Ereifej, G.M. Rial, J.K. Hermann, C.S. Smith, S.M. Meade, J.M. Rayyan, K. Chen, H. Feng, J.R. Capadona, Implantation of neural probes in the brain elicits oxidative stress, Front. Bioeng. Biotechnol. 6 (2018). https://doi.org/10.3389/fbioe.2018.00009.

[96] P.J. Urrutia, N.P. Mena, M.T. Núñez, The interplay between iron accumulation, mitochondrial dysfunction, and inflammation during the execution step of neurodegenerative disorders, Front. Pharmacol. 5 MAR (2014) 1–12. https://doi.org/10.3389/fphar.2014.00038.

[97] D.F. Leitner, J.R. Connor, Functional roles of transferrin in the brain, Biochim. Biophys. Acta - Gen. Subj. 1820 (2012) 393–402. https://doi.org/10.1016/j.bbagen.2011.10.016.

[98] S. Levi, S.J. Yewdall, P.M. Harrison, P. Santambrogio, A. Cozzi, E. Rovida, A. Albertini, P. Arosio, Evidence that H- and L-chains have co-operative roles in the iron-uptake mechanism of human ferritin, Biochem. J. 288 (1992) 591–596. https://doi.org/10.1042/bj2880591.

[99] T.R. Carden, J. Correale, J.M. Pasquini, M.J. Pérez, Transferrin Enhances Microglial Phagocytic Capacity, Mol. Neurobiol. 56 (2019) 6324–6340. https://doi.org/10.1007/s12035-019-1519-0.

[100] I.C. Nnah, M. Wessling-Resnick, Brain Iron homeostasis: A focus on microglial Iron, Pharmaceuticals. 11 (2018). https://doi.org/10.3390/PH11040129.

[101] K. Borst, M. Schwabenland, M. Prinz, Microglia metabolism in health and disease, Neurochem. Int. 130 (2019) 104331. https://doi.org/10.1016/j.neuint.2018.11.006.

[102] D. Cantu, K. Walker, L. Andresen, A. Taylor-Weiner, D. Hampton, G. Tesco, C.G. Dulla, Traumatic Brain Injury Increases Cortical Glutamate Network Activity by Compromising GABAergic Control, Cereb. Cortex. 25 (2015) 2306–2320. https://doi.org/10.1093/cercor/bhu041.

[103] D.S. Alwis, E.B. Yan, M.C. Morganti-Kossmann, R. Rajan, Sensory Cortex Underpinnings of Traumatic Brain Injury Deficits, PLoS One. 7 (2012). https://doi.org/10.1371/journal.pone.0052169.

[104] S.F. Carron, D.S. Alwis, R. Rajan, Traumatic brain injury and neuronal functionality changes in sensory cortex, Front. Syst. Neurosci. 10 (2016) 1–17. https://doi.org/10.3389/fnsys.2016.00047.

[105] J.R. Eles, A.L. Vazquez, T.D.Y. Kozai, X.T. Cui, In vivo imaging of neuronal calcium during electrode implantation: Spatial and temporal mapping of damage and recovery, Biomaterials. 174 (2018) 79–94. https://doi.org/10.1016/j.biomaterials.2018.04.043.

[106] M.G. Moore, C.H. Thompson, M.A. Reimers, E.K. Purcell, Differential Co-Expression Analysis of RNA-Seq Data Reveals Novel Potential Biomarkers of

Device-Tissue Interaction, Proc. Annu. Int. Conf. IEEE Eng. Med. Biol. Soc. EMBS. 2022-July (2022) 3072–3076. https://doi.org/10.1109/EMBC48229.2022.9871437.

CHAPTER 4 | SPATIOTEMPORAL GENE EXPRESSION WITH SINGLE-CELL RESOLUTION AROUND POLYIMIDE CORTICAL ELECTRODES OF VARYING DIMENSIONS

1. INTRODUCTION

Implantable electrodes arrays can interface with the central nervous system to record from and stimulate neural tissues to treat neurological disease and injury[1]–[14]. However, the tissue response to implanted electrodes can limit their functional longevity[15]–[18]. In recent years, many next-generation electrodes have been developed with unique design strategies with the goal to attenuate or circumvent the cortical tissue response[19], [20]. These next-generation devices delivered some success in reducing the degree of neuronal loss and gliosis, driven by subcellular features and softer materials which result in reduced bending stiffness [21]–[23]. In recent years, some researchers in the field have moved to evaluate the tissue response using transcriptomics methods. In recent years, new RNA-sequencing datasets which identify hundreds of differentially expressed genes have deepened the understandings of the tissue response beyond prior characterizations[24]–[26]. These studies provided vast datasets which provided new spatiotemporal data regarding the tissue response, yet the cell-type specific expression of these genes remains unclear. However, previous transcriptomics studies of the tissue response did not have single-cell resolution which left significant questions regarding which cells or cell types were driving mRNA expression results. Due to the lack of studies which directly compare the tissue response, at the single cell level, and this study seeks to fill that gap in knowledge while exploring the effects of varying

electrode materials and dimensions.

In this study, we utilized new technologies in multiplexed error robust in-situ hybridization (MERFISH) to assess a panel of 100 RNA-seq identified genes at the spatiotemporal level with single cell resolution around implanted silicon and polyimide probes of sub- (10um) and supra- (100um) cellular scale. Initial obsevations from this ongoing study revealed the spatiotemporal patterns of gene expression associated with neuronal function, myelination, cellular stress, glial activation, and cellular metabolism around implanted devices. We have also identified 16 unique cellular subtypes, based on transcriptional profiles, around polyimide devices which add important context for the nature of neuronal and glial responses to indwelling electrodes.

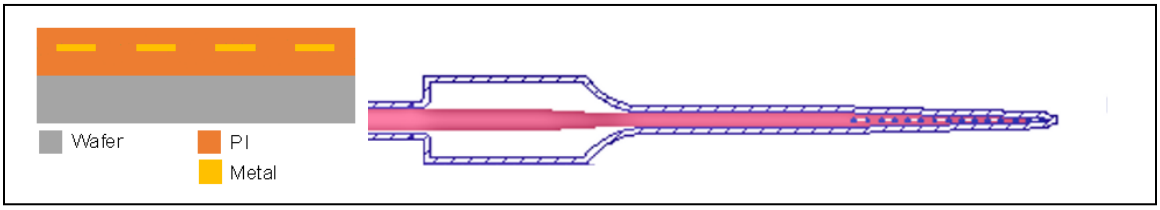

Figure 4.1: Overview of polyimide device construction. Polyimide devices were fabricated layer-by-layer first with a foundation 4.5um polyimide layer. 100/50/100 nm of Au/Pt/Au was vapor deposited. Lastly, an additional 4.5um polyimide layer was spun coated prior to etching of devices.

2. METHODS

2.1 POLYIMIDE ELECTRODE PREPARATION

To examine device related effects on the tissue response, polyimide devices of 10um x 10um and 100um x 10um were custom fabricated to match the features of standard Michigan style probes (16-channel A1 x 16-3mm, 10um thick, 703um^2 site size 100um spacing, Neuronexus Technologies) (Figure 4.1). Polyimide devices were epoxy mounted to plastic faux omnetics connectors and were subsequently measured under light

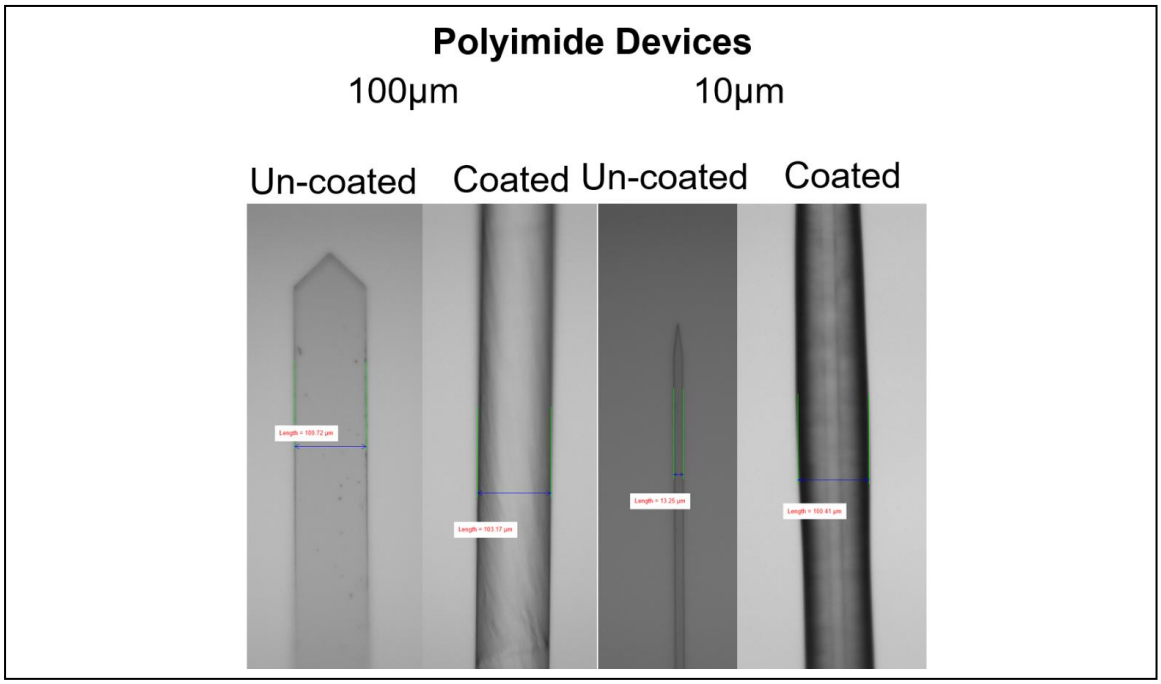

Figure 4.2: Representative microscope images of polyimide device measurements before and after coating. Microscope images were also used to verify the uniformity of PEG 4000 coatings.

microscopy (Figure 4.2) to verify device dimensions. The assembled devices were then ethylene oxide sterilized. Prior to surgical implantation, polyimide and silicon microelectrodes of all dimensions were reinforced with polyethylene glycol (PEG) M.W 4000 to prevent buckling of polyimide devices. PEG4000 was initially heated to 120°C and then allowed to cool to 70°C and devices were dip-coated to a target thickness. To control for any potential PEG 4000 mediated effects on the tissue response, all devices were coated with PEG 4000. To control for any device insertion mediated effects on the tissue response, all devices were coated with PEG4000 to a total post-coating width of approximately 100-105 um.

2.2 SURIGAL IMPLANTATION OF ELECTRODES

One nonfunctional polyimide device of each size was stereotaxically implanted

bilaterally in the motor cortex (M1) of male Sprague-Dawley rats (aged 12-14 weeks). Animals were isoflurane-anesthetized and a craniotomy was performed over M1 (+3.0 mm Anterior, +/- 2.5 mm mediolateral from Bregma), dura was resected, and one electrode of each dimension (same material) was stereotaxically inserted in each hemisphere to a depth of 1.8mm from the cortical surface. PEG coated devices were rapidly inserted into M1 to maintain structure before coating was able to dissolve. A dental cement head-cap was used to secure the bilateral implants to two stainless steel bone screws. Bupivacaine and Neosporin were applied topically to the area around the incision to minimize discomfort and infection risk. Meloxicam was administered via injection for post-operative pain management. Devices remained implanted in M1 for the duration of a designated time-point (6 Weeks). All surgical procedures described were approved by the Michigan State University Animal Care and Use Committee.

2.3 TISSUE EXTRACTION AND PREPARATION

At the terminal time-point, animals were deeply anesthetized, decapitated, and the brain was removed. Extracted brains were immediately cryopreserved by OCT embedding in dry ice cooled 2-methylbutane. Brains were cryosectioned to a thickness of 10µm and mounted on Superfrost ^{tm} Plus slides for later histological applications. An additional 10 sections were stored for RNA integrity analysis, which consistently yielded RIN values above 8. A single tissue section from each animal per condition-timepoint (three sections) was placed on a Xenium ^{tm} (10x Genomics) slide from an average depth of 800µm from the cortical surface and stored at -80°C for downstream in-situ hybridization following delivery to the University of Michigan advanced genomics

research core facility.

Gene Panel									
Apod	C1qc	Ctsb	Dusp1	Grn	Lss	Ncan	Olig2	Slc32a1	Stxbp1
Apoe	C3	Ctsl	Dynll1	Hcn2	Mag	Ncdn	Picalm	Slc44a1	Syn1
Aqp4	Camk2a	Ctss	Fth1	Il6	Map4	Nefh	Plp1	Slc6a17	Tf
Arc	Camta1	Cttn	Ftl1	Itgam	Map4k4	Nefl	Ptbp1	Slc7a11	Tln1
Bak1	Chil1	Cx3cr1	Gad1	Kalrn	Mbp	Nefm	Ptn	Snap25	Tlr2
Best1	Cltb	Cxcl2	Gfap	Kif5a	Megf10	Nes	Ptprz1	Sod1	Tlr4
Brinp1	Cnksr2	Cyfip2	Glul	Kif5b	Mertk	Npc2	Serping1	Sod2	Tnf
Bsn	Cox6b1	Dlg4	Gpnmb	Kif5c	Mmp2	Nptxr	Shank2	Sparc	Tnfrsf1a
C1qa	Csf1r	Dock8	Gria1	Lcn2	Mmp9	Nrgn	Slc17a7	Sparcl1	Trem2
C1qb	Cspg4	Dst	Grin1	Lgmn	Mog	Olig1	Slc1a2	Stx1a	Vim

Table 4.1: List of the 100 genes included in the custom xenium gene panel used for this study.

2.4 IN-SITU XENIUM ANALYSIS

Processing of tissue for imaging and analysis was performed as described in the vendor's protocol datasheet. Fresh frozen tissue was incubated at 37^{o}C for 1 minute and subsequently fixed in chilled 70% methanol for 30 minutes at room temperature. Fixed tissue sections were then rinsed in PBS then permeabilized in a 1% SDS solution for 2 minutes at room temperature. Slides were rinsed once again before being fixed in chilled 70% methanol for 1 hour. Sections were them immersed in probe hybridization mix (10x Genomics) which included the gene panel and incubated at 50^{o}C for 16-24 hours. Probe hybridization mix was then removed and all tissue sections were immediately rinsed with PBS-T three times for 1 minute each. PBST was removed and tissue sections were incubated in ligation mix (10x genomics) for 2 hours at 37^{o}C. Prior to amplification, ligation buffer was removed and the tissue was rinsed in PBS-T 3 times for 1 minute each. Following this rinse step, the tissue was then incubated in amplification buffer (10x

Genomics) for 2 hours at 30°C. Tissue was then rinsed in TE buffer 3 times for 1 minute each prior to autofluorescence quenching using 10x genomics reducing agents and autofluorescence mix. Post-quenching, tissue was incubated in nuclear staining buffer (10x Genomics) for 1 minute and rinsed 3 times for one minute each prior to imaging on a Xenium analyzer (10x Genomics).

2.5 CUSTOM GENE PANEL

For this study, we chose a panel of 100 RNA-seq identified genes which are associated with astrocytes, microglia, neurons, and oligodendrocytes. We also chose genes that are widely expressed and associated with biological processes such as innate immune response, cellular metabolism, cellular proliferation, and oxidative stress (Table 4.1). These genes were all found to be differentially expressed in tissue surrounding implanted devices in previous transcriptomic studies[24], [25].

2.6 IMMUNOFLUORESCENCE AND IMAGING

Following Xenium analysis of slides, each slide was rinsed, quenched, and subsequently prepared for immunofluorescence. Tissue sections were hydrated in PBS, and blocked with 10% normal donkey serum for one hour and subsequently incubated with primary antibodies (rabbit anti-NeuN (Abcam AB177487) , mouse anti-Olig2 (MilliporeSigma ZMS1019), chicken anti-Gfap (Abcam AB4674)). Following primary incubation, samples were rinsed three times in PBS for 10 minutes and secondary antibodies (alexa-fluor 488 (Thermo-Fisher) 1:400, alexa-fluor 594 1:400 Thermo-Fisher) were applied for two hours. Slides were rinsed an additional two times for 10

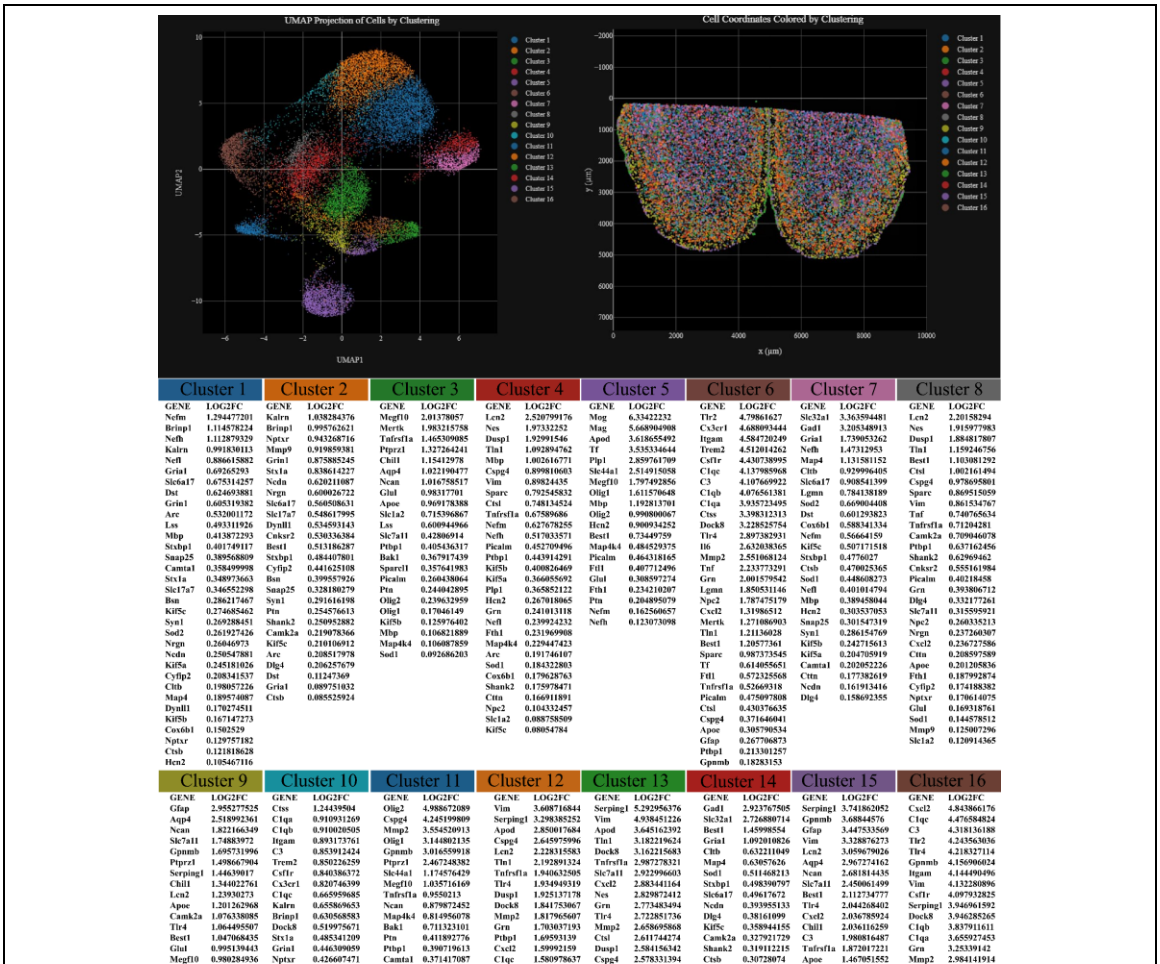

Cluster 1		Cluster 2		Cluster 3		Cluster 4		Cluster 5		Cluster 6		Cluster 7		Cluster 8	
GENE	LOG2FC	GENE	LOG2FC	GENE	LOG2FC	GENE	LOG2FC	GENE	LOG2FC	GENE	LOG2FC	GENE	LOG2FC	GENE	LOG2FC
Nefm	1.294477201	Kalrn	1.038284376	Megf10	2.01378057	Lcn2	2.520799176	Mog	6.33422232	Tlr2	4.79861627	Slc32a1	3.363594481	Lcn2	2.20158294
Brinp1	1.114578224	Brinp1	0.995762621	Mertk	1.983215758	Nes	1.97332252	Mag	5.668904908	Cx3cr1	4.688093444	Gad1	3.205348913	Nes	1.915977983
Nefh	1.112879329	Nptxr	0.943268716	Tnfrsf1a	1.465309085	Dusp1	1.929915546	Apod	3.618655492	Itgam	4.584720249	Gria1	1.739053262	Dusp1	1.884817807
Kalrn	0.991830113	Mmp9	0.919859381	Ptprz1	1.327264241	Tln1	1.092894762	Tf	3.535336644	Trem2	4.512014262	Nefh	1.47312953	Tln1	1.159246756
Nefl	0.886615882	Grin1	0.875885245	Chil1	1.15412978	Mbp	1.002616771	Plp1	2.859761709	Csf1r	4.430738995	Map4	1.131581152	Best1	1.103081292
Gria1	0.69265293	Stx1a	0.838614227	Aqp4	1.022190477	Cspg4	0.899810603	Slc44a1	2.514915058	C1qc	4.137985968	Cltb	0.929996405	Ctsl	1.002161494
Slc6a17	0.675314257	Ncdn	0.620211087	Ncan	1.016758517	Vim	0.89824435	Megf10	1.797492856	C3	4.107669922	Slc6a17	0.908541399	Cspg4	0.978695801
Dst	0.624693881	Nrgn	0.600026722	Glul	0.98317701	Sparc	0.792545832	Olig1	1.611578648	C1qb	4.076561381	Lgmn	0.784138189	Sparc	0.869515059
Grin1	0.605319382	Slc6a17	0.560508631	Apoe	0.969178388	Ctsl	0.748134524	Mbp	1.192813701	C1qa	3.935723495	Sod2	0.669004408	Vim	0.861534767
Arc	0.532001172	Slc17a7	0.548617995	Slc1a2	0.715396867	Tnfrsf1a	0.67589686	Olig2	0.990800067	Ctss	3.398312313	Dst	0.601293823	Tnf	0.740765634
Lss	0.493311926	Dynll1	0.534593143	Lss	0.600944966	Nefm	0.627678255	Hcn2	0.900934252	Dock8	3.228525754	Cox6b1	0.588341334	Tnfrsf1a	0.71204281
Mbp	0.413872293	Cnksr2	0.530336384	Slc7a11	0.42806914	Nefh	0.517033571	Best1	0.73449759	Tlr4	2.897382931	Nefm	0.56664159	Camk2a	0.709046078
Stxbp1	0.401749117	Best1	0.513186287	Ptbp1	0.405436317	Picalm	0.452709496	Map4k4	0.484529375	Il6	2.632038365	Kif5c	0.507171518	Ptbp1	0.637162456
Snap25	0.389568809	Stxbp1	0.484407801	Bak1	0.367917439	Ptbp1	0.443914291	Picalm	0.464318165	Mmp2	2.551068124	Stxbp1	0.4776027	Shank2	0.62969462
Camta1	0.358499998	Cyfip2	0.441625108	Sparcl1	0.357641983	Kif5b	0.400826469	Ftl1	0.407712496	Tnf	2.233773291	Ctsb	0.470025365	Cnksr2	0.555161984
Stx1a	0.348973663	Bsn	0.399557926	Picalm	0.260438064	Kif5a	0.366055692	Glul	0.308597274	Grn	2.001579542	Sod1	0.448608273	Picalm	0.40218458
Slc17a7	0.346552298	Snap25	0.328180279	Apoe	0.244042895	Plp1	0.365852122	Fth1	0.234210207	Lgmn	1.850853146	Ndfl	0.401014794	Grn	0.393806712
Bsn	0.286217467	Syn1	0.291616198	Olig2	0.239632959	Hcn2	0.267018065	Ptn	0.204895079	Npc2	1.787475179	Mbp	0.389458044	Dlg4	0.332177261
Kif5c	0.274685462	Ptn	0.254576613	Olig1	0.17046149	Grn	0.241013118	Nefm	0.162560657	Cxcl2	1.31986512	Hcn2	0.303537053	Slc7a11	0.315595921
Syn1	0.269288451	Shank2	0.250952882	Kif5b	0.125976402	Nefl	0.239924232	Nefh	0.123073098	Mertk	1.271086903	Snap25	0.301547319	Npc2	0.260335213
Sod2	0.261927426	Camk2a	0.219078366	Mbp	0.106821889	Fth1	0.231969908			Tln1	1.21136028	Syn1	0.286154769	Nrgn	0.237260307
Nrgn	0.26046973	Kif5c	0.219106912	Map4k4	0.106087859	Map4k4	0.229447423			Best1	1.20577361	Kif5b	0.242715613	Cxcl2	0.236727586
Ncdn	0.250547881	Arc	0.208517978	Sod1	0.092686203	Arc	0.191746107			Sparc	0.987373545	Kif5a	0.204705919	Cttn	0.208597589
Kif5a	0.245181026	Dlg4	0.206257679			Sod1	0.184322803			Tf	0.614055651	Camta1	0.202052226	Apoe	0.201205836
Cyfip2	0.208341537	Dst	0.11247369			Cox6b1	0.179628763			Ftl1	0.572325568	Cttn	0.177382619	Fth1	0.187992874
Cltb	0.198057226	Gria1	0.089751032			Shank2	0.175978471			Tnfrsf1a	0.52669318	Ncdn	0.161913416	Cyfip2	0.174188382
Map4	0.189574087	Ctsb	0.085525924			Cttn	0.166911891			Picalm	0.475097808	Dlg4	0.158692355	Nptxr	0.170614075
Dynll1	0.170274511					Npc2	0.104332457			Ctsl	0.430376635			Glul	0.169318761
Kif5b	0.167147273					Slc1a2	0.088758509			Cspg4	0.371646041			Sod1	0.144578512
Cox6b1	0.1502529					Kif5c	0.08054784			Apoe	0.305790534			Mmp9	0.125007296
Nptxr	0.129757182									Gfap	0.267706873			Slc1a2	0.120914365
Ctsb	0.121818628									Ptbp1	0.213301257				
Hcn2	0.105467116									Gpnmb	0.18283153				

Cluster 9		Cluster 10		Cluster 11		Cluster 12		Cluster 13		Cluster 14		Cluster 15		Cluster 16	
GENE	LOG2FC	GENE	LOG2FC	GENE	LOG2FC	GENE	LOG2FC	GENE	LOG2FC	GENE	LOG2FC	GENE	LOG2FC	GENE	LOG2FC
Gfap	2.955277525	Ctss	1.24439504	Olig2	4.988672089	Vim	3.608716844	Serping1	5.292956376	Gad1	2.923767505	Serping1	3.741862052	Cxcl2	4.843866176
Aqp4	2.518992361	C1qa	0.910931269	Cspg4	4.245199809	Serping1	3.298385252	Vim	4.938451226	Slc32a1	2.726880714	Gpnmb	3.68844576	C1qc	4.476584824
Ncan	1.822166349	C1qb	0.910020505	Mmp2	3.554520913	Apod	2.850017684	Apod	3.645162392	Best1	1.45998554	Gfap	3.447533569	C3	4.318136188
Slc7a11	1.74883972	Itgam	0.893173761	Olig1	3.144802135	Cspg4	2.645975996	Tln1	3.182219624	Gria1	1.092010826	Vim	3.328876273	Tlr2	4.243563036
Gpnmb	1.695731996	C3	0.853912424	Gpnmb	3.016559918	Lcn2	2.228315583	Dock8	3.162215683	Cltb	0.632211049	Lcn2	3.059679026	Tlr4	4.218327114
Ptprz1	1.498667904	Trem2	0.850226259	Ptprz1	2.467248382	Tln1	2.192891324	Tnfrsf1a	2.987278321	Aqp4	0.63057626	Aqp4	2.967274162	Gpnmb	4.156906024
Serping1	1.44639017	Csf1r	0.840386372	Slc44a1	1.174576429	Tnfrsf1a	1.940632505	Slc7a11	2.922996603	Snd1	0.511468213	Slc7a11	2.458061499	Itgam	4.144490496
Chil1	1.34402761	Cx3cr1	0.820746399	Megf10	1.035716169	Tln1	1.934949319	Cxcl2	2.883441164	Stxbp1	0.498390797	Slc7a11	2.458061499	Vim	4.132280896
Lcn2	1.23930273	C1qc	0.665959685	Tnfrsf1a	0.9550213	Dusp1	1.925137178	Nes	2.829872412	Slc6a17	0.49617672	Best1	2.112734777	Csf1r	4.097932825
Apoe	1.201262968	Kalrn	0.655869653	Ncan	0.879872452	Dock8	1.841753067	Grn	2.773483494	Ncdn	0.393955133	Tlr4	2.044268402	Serping1	3.946961592
Camk2a	1.076338085	Brinp1	0.630568583	Map4k4	0.814956078	Mmp2	1.817965607	Tlr4	2.722851736	Dlg4	0.38161099	Cxcl2	2.036785924	Dock8	3.946285265
Tlr4	1.064495507	Dock8	0.519975671	Bak1	0.711323101	Grn	1.783037193	Mmp2	2.658695868	Kif5c	0.358944155	C1qb	2.036116259	C1qb	3.837911611
Best1	1.047068435	Stx1a	0.485341209	Ptn	0.411892776	Ptbp1	1.65953139	Ctsl	2.611744274	Camk2a	0.327921729	C3	1.980816487	C1qa	3.655927453
Glul	0.995139443	Gria1	0.446309059	Ptbp1	0.390719613	Cxcl2	1.59992159	Dusp1	2.584156342	Shank2	0.319112215	Tnfrsf1a	1.872017221	Grn	3.25339142
Megf10	0.980284936	Nptxr	0.426607471	Camta1	0.371417087	C1qc	1.580978637	Cspg4	2.578331394	Ctsb	0.30728074	Apoe	1.467051552	Mmp2	2.984141914
Tnfrsf1a	0.936142945	Npc2	0.414033903	Cttn	0.307320791	Sparc	1.560896745	Ptbp1	2.49176157	Sod2	0.289044667	Ptbp1	1.418958303	Ctss	2.912799759
Mertk	0.925033939	Best1	0.403045345	Best1	0.275144623	Nes	1.541990544	Sparc	2.263102452	Lgmn	0.258663228	Npc2	1.322195886	Apoe	2.748803721
Slc1a2	0.789961759	Slc6a17	0.387176471	Apoe	0.275040422	Slc7a11	1.520052338	Bak1	1.979504203	Dst	0.25581181	Ptprz1	1.3087357	Trem2	2.64689712
Ptbp1	0.761056312	Slc17a7	0.34193055	Ftl1	0.270705156	Gpnmb	1.241876956	Lcn2	1.941097328	Cox6b1	0.251211235	Sparc	1.180812016	Tln1	2.645232551
Sparcl1	0.71584831	Nrgn	0.326658182	Tlr4	0.236299564	Picalm	1.157404524	Gpnmb	1.771296452	Cyfip2	0.247426418	Tln1	1.119703778	Best1	2.565044655
Npc2	0.695953327	Lgmn	0.319275957	Dst	0.19805821	Ctsl	1.110065599	Picalm	1.762001269	Syn1	0.221555888	Mertk	1.086356588	Tnfrsf1a	2.428590475
Sparc	0.644585972	Stxbp1	0.282265504	Tln1	0.193634901	Apoe	0.940063701	Apoe	1.651113675	Cttn	0.190751787	Ftl1	1.066031136	Tnf	2.393246023
Tln1	0.603254542	Il6	0.26421764	Camk2a	0.191511426	Bak1	0.915742899	Npc2	1.486723903	Snap25	0.173718499	Nes	1.050525198	Lgmn	2.355272272
Vim	0.521854573	Tlr2	0.262703651	Gfap	0.166689631	Npc2	0.867202077	C1qc	1.475813767	Gria1	0.146929949	Apod	0.993870771	Slc7a11	2.332805692
Cxcl2	0.513098378	Bsn	0.246225842	Shank2	0.134280048	Slc7a11	0.865676115	Ptn	1.468115658			Ctsl	0.908017187	Lcn2	2.258295867
Map4k4	0.48807451	Syn1	0.209411049			C1qa	0.782779857	Tnf	1.442246762			Gfap	0.898320981	Nes	2.096425941
Tnf	0.348919213	Ncdn	0.207166409			Ftl1	0.776768093	Ftl1	1.323096882			Dock8	0.886845867	Il6	2.063182534
Ftl1	0.301255299	Dynll1	0.199716217			C1qb	0.768159522	Cttn	1.280775239			C1qa	0.847643255	Npc2	2.013355055
Shank2	0.281465844	Cyfip2	0.195835258			Ptn	0.704864841	Ctsb	1.239037462			Bak1	0.843411887	Cx3cr1	1.942168557
Nes	0.274994751	Snap25	0.186743833			Gfap	0.633602744	Map4k4	0.962028789			Itgam	0.826639901	Ftl1	1.935350279
Bak1	0.261814355	Cnksr2	0.183903736			Aqp4	0.589158841	Lgmn	0.927021619			Map4k4	0.815562071	Tf	1.903910189
Ctsl	0.237444382	Arc	0.160003519			Tnf	0.588492419	Csf1r	0.866304041			Sparcl1	0.786117344	Gfap	1.777769461
Olig1	0.156487036	Dst	0.14301632			Map4k4	0.558256779	Best1	0.86202218			Lss	0.760460374	Sparc	1.698541814
		Kif5c	0.137797177			Tlr2	0.54799116	Sod1	0.861597068			C1qc	0.676967233	Ptbp1	1.617140829
		Ctsb	0.117330521			Cttn	0.446230111	Slc44a1	0.84430901			C1qb	0.656755574	Ctsl	1.507022049
		Gria1	0.111434476			Mertk	0.439341792	Gfap	0.833936129			Csf1r	0.654875895	Apoe	1.446549648
						Ctsb	0.42737297	Tlr2	0.809280718			Slc44a1	0.644800268	Ctsb	1.420519075
						Il6	0.412147365	Il6	0.727846084			Megf10	0.618588519	Bak1	1.275732889
						Ctss	0.40436843	C1qa	0.710010887			Ctsb	0.584737137	Ptn	1.014888968
						Sparcl1	0.371925338	Fth1	0.602511677			Glul	0.552083837	Picalm	0.896839863
						Glul	0.336923408	C3	0.552504764			Tlr2	0.543415254	Mertk	0.746702508
						Tf	0.299092688	Tf	0.521064089			Plp1	0.476816219	Dusp1	0.654314113
						Fth1	0.262097621	Glul	0.505694578			Slc1a2	0.461342903	Slc44a1	0.639978553
						Sod1	0.246094389	C1qb	0.45174337			Ctss	0.344539138	Aqp4	0.581472271
						Slc44a1	0.241644797	Megf10	0.393062865			Lgmn	0.25910193	Cspg4	0.523556633
								Mertk	0.389353961					Map4k4	0.513817126
								Sparcl1	0.366464918						
								Camta1	0.281909036						
								Kif5b	0.238780569						

Figure 4.3: Differential gene expression by cluster. UMAP projections of clusters and spatial organization of identified clusters overlaid on the analyzed tissue section containing one 10um polyimide device (left) and one 100um polyimide device (right). Each cell cluster contains a set of differentially expressed genes which is listed (below). Log2FC values belonging to each cluster were identified as statistically significant (Benjamini-Hochenberg test) $P \leq 0.05$.

minutes and nuclei were counterstained with 1ug/ml Hoechst. Images were acquired using an Nikon A1 inverted confocal microscope with a x20 PlanFluor dry objective (0.5 NA) at a resolution of 1024×1024 pixels. A slide of tissue sections for each animal was used as a 'no-primary' control to validate the absence of autofluorescence and non-specific binding of antibodies.

2.7 XENIUM ANALYSIS AND STATISTICAL METHODS

Xenium in-situ analysis and statistical methods for image processing, puncta detection, decoding, quality scoring, cell segmentation, clustering, and differential gene expression were performed as described in [27], [28].

3. RESULTS

At the time this dissertation was compiled, data collection and analysis were still underway and these results are preliminary in nature. In this study, we have identified broad spatial expression of 100 genes around implanted polyimide devices with single cell resolution. Our results identified elevated expression of genes associated with inflammation, the complement system, glial activation, and cellular remodeling around both 100um and 10um devices. We also observed relatively lower levels of gene expression for key transcripts associated with myelination and neuronal function around both devices. While both devices express biomarkers of the tissue response, the gene expression of tissue response related genes is reduced around sub-cellular devices relative to supra-cellular devices. We also observed that there are increased numbers of reactive and inflammatory cell types around 100 um polyimide devices. We have identified 16 unique clusters of cells which represent distinct phenotypes of astrocytes, microglia,

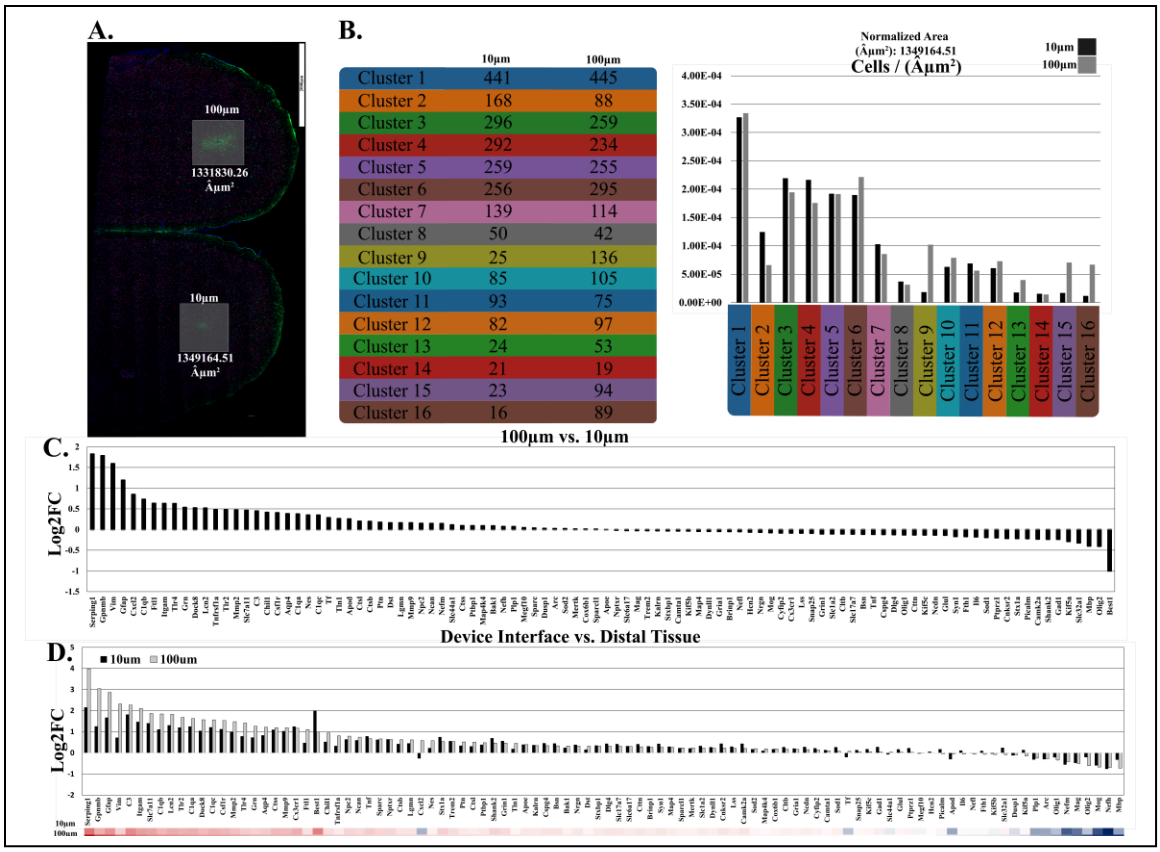

Figure 4.4: Spatial analysis of cell clusters and differentially expressed genes around implanted silicon electrodes. A.) confocal image of brain section analyzed in this study. Gray squares indicate region of interest used to quantify cell counts and transcript number from within each region. B.) Table of counted cells from each cluster from within each region of interest and bar graph of cellular density sorted by cluster and device condition. Cell counts were normalized to the larger ROI. C.) Bar graph of Log2FC from the region of interest around the 100um polyimide device relative to interfacial tissue around the contralateral 10um polyimide device. D.) Bar graph and heat map of Log2FC values of each polyimide device relative to distal tissue (posterior from implant region of interest).

neurons, and oligodendrocytes at the device interface (Figure 4.3). Based on the top differentially expressed genes from each cluster and the complementary immunofluorescence we have identified each cluster as likely belonging to a specific cell type: reactive glia (Clusters 9, 12, 13, 15, & 16), modulatory glia (Clusters 3, 4, 6, 8, & 10), oligodendrocytes / OPCs (Clusters 5 & 11), excitatory neurons (clusters 1 &2), and

Cell Count

	10µm Area (Âµm^2): 1349164.51	100µm Area (Âµm^2): 1331830.26
Cluster 9	25	136
Cluster 12	82	97
Cluster 13	24	53
Cluster 15	23	94
Cluster 16	16	89

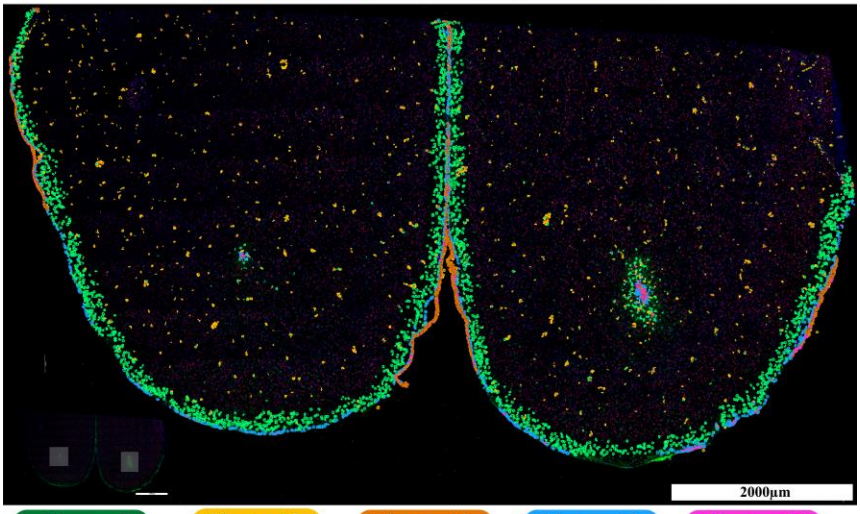

Cluster 9		Cluster 12		Cluster 13		Cluster 15		Cluster 16	
GENE	LOG2FC	GENE	LOG2FC	GENE	LOG2FC	GENE	LOG2FC	GENE	LOG2FC
Gfap	2.955277525	Vim	3.608716844	Serping1	5.292956376	Serping1	3.741862052	Cxcl2	4.843866176
Aqp4	2.518992361	Serping1	3.298385252	Vim	4.938451226	Gpnmb	3.68844576	C1qc	4.476584824
Ncan	1.822166349	Apod	2.850017684	Apod	3.645162392	Gfap	3.447533569	C3	4.318136188
Slc7a11	1.74883972	Cspg4	2.645975996	Tln1	3.182219624	Vim	3.328876273	Tlr2	4.243563036
Gpnmb	1.695731996	Lcn2	2.228315583	Dock8	3.162215683	Lcn2	3.059679026	Tlr4	4.218327114
Ptprz1	1.498667904	Tln1	2.192891324	Tnfrsf1a	2.987278321	Aqp4	2.967274162	Gpnmb	4.156906024
Serping1	1.44639017	Tnfrsf1a	1.940632505	Slc7a11	2.922996603	Ncan	2.681814435	Itgam	4.144490496
Chil1	1.344022761	Tlr4	1.934949319	Cxcl2	2.883441164	Slc7a11	2.450061499	Vim	4.132280896
Lcn2	1.23930273	Dusp1	1.925137178	Nes	2.829872412	Best1	2.112734777	Csf1r	4.097932825
Apoe	1.201262968	Dock8	1.841753067	Grn	2.773483494	Tlr4	2.044268402	Serping1	3.946961592
Camk2a	1.076338085	Mmp2	1.817965607	Tlr4	2.722851736	Cxcl2	2.036785924	Dock8	3.946285265
Tlr4	1.064495507	Grn	1.703037193	Mmp2	2.658695868	Chil1	2.036116259	C1qb	3.837911611
Best1	1.047068435	Ptbp1	1.69593139	Ctsl	2.611744274	C3	1.980816487	C1qa	3.655927453
Glul	0.995139443	Cxcl2	1.59992159	Dusp1	2.584156342	Tnfrsf1a	1.872017221	Grn	3.25339142
Megf10	0.980284936	C1qc	1.580978637	Cspg4	2.578331394	Apoe	1.467051552	Mmp2	2.984141914
Tnfrsf1a	0.936142945	Sparc	1.560896745	Ptbp1	2.49176157	Ptbp1	1.418958303	Ctss	2.912799759
Mertk	0.925033939	Nes	1.541990544	Sparc	2.263102452	Npc2	1.322195886	Apod	2.748803721
Slc1a2	0.789961759	Slc7a11	1.520052338	Bak1	1.979504203	Ptprz1	1.3087357	Trem2	2.64689712
Ptbp1	0.761056312	Gpnmb	1.241876956	Lcn2	1.941097328	Sparc	1.180812016	Tln1	2.645232551
Sparcl1	0.71584831	Picalm	1.157404524	Gpnmb	1.771296452	Tln1	1.119703778	Best1	2.565044655
Npc2	0.695953327	Ctsl	1.110065599	Picalm	1.762001269	Mertk	1.086356588	Tnfrsf1a	2.428590475

Figure 4.5: Representative figures of cell clusters organized by cell type and spatial organization around implanted polyimide probes. Clusters which express genes associated with reactive glia are tightly organized around implanted electrode. Tables above each confocal image represent cell count by cluster from within an approximately equal region of interest around each device injury. Minimized confocal images represent the region of interest that was used to quantify cell counts by cluster. Log2FC values belonging to each cluster were identified as statistically significant (Benjamini-Hochenberg test) $P \leq 0.05$.

inhibitory neurons (clusters 7 &14).

3.1 SPATIOTEMPORAL PATTERNS OF GENE EXPRESSION AROUND POLYIMIDE ELECTRODES

After identifying the gene expression within each cluster of cells, we then drew regions of interest (ROI) around each implant site (Figure 4.4A). From within each ROI, we found that the spatial distribution of clusters differed between large and small polyimide devices (Figure 4.4B). Clusters 6, 9, 10, 12, 15, and 16 were increased and clusters 2, 3, 4, 7, and 11 were decreased around 100um polyimide devices. A cursory comparison of the transcript count number around approximately equal ROIs around both polyimide devices found that there was an increase in Log2FC of genes associated with glial activation, fibrosis, and oxidative stress around 100um polyimide devices. Likewise, we found that genes positively associated with neuronal function, myelination, and oligodendrocyte progenitors were increased near 10um devices relative to 100um devices (Figure 4.4C). We then drew additional ROIs around distal tissue posterior to each polyimide implant and calculated to Log2FC of tissue around each polyimide device relative to distal tissue (Figure 4.4D). When compared to distal tissue, gene expression around both devices identified increased expression in genes associated with reactive gliosis, oxidative stress, innate immune response, and cellular proliferation. We also found that most genes associated with neuronal function, myelination, and oligodendrocyte differentiation were less affected around both 10- and 100um devices. However, nearly all tissue response associated genes tested in this panel were expressed less around 10um polyimide devices. *Cxcl2*, *Tf*, *Slc44a1, Apod, Fth1*, *Slc32a1,* and *Kif5a*

were found to be inversely expressed around 10um polyimide electrodes compared to 100um devices. However, to conclusively determine the true effect of device size on gene expression around implanted electrodes, additional samples need to be included in this analysis for effective calculations of Log2FC around polyimide devices.

3.1.1 REACTIVE GLIA AT THE DEVICE INTERFACE RESEMBLES GLIA LIMITANS

It is often observed that reactive astrocytes and microglia progressively encapsulate implanted devices over time. The results of this study have identified five clusters of likely astrocytes, microglia, and progenitor cells which are observed to be localized to the device interface, within vasculature, and within the glia limitans (Figure 4.4A). Clusters 13, 15, and 16 lie directly in the center of the implant site and express genes that are associated with reactive microglia and astrocytes. Cluster 13 expressed genes that are associated with an activated microglial phenotype (*Serping1, Vim, Apod, Tln1, and Dock8*). Cluster 16 is spatially located alongside cells within cluster 13, yet appears to belong to a different phenotype of reactive microglia that expresses genes associated with the innate immune response and the complement system (*Cxcl2, C1qa, C1qb, C1qc, C3, Itgam, Csf1r*). Cluster 16 is spatially localized just beyond clusters 13 and 16 at the device interface. Cluster 16 expresses genes associated with activated astrocytes (*Serping1, Gpnmb, Gfap, Lcn2, Chil1, C3*). Cluster 9 lies just beyond the immediate device interface and shares gene expression patterns with clusters 15 and 13 (*Serping1, Gpnmb, Gfap, Lcn2, Chil1, C3*) with reduced magnitude. Cluster 12 is present at the device interface, but is also distributed around vasculature which is unrelated to the

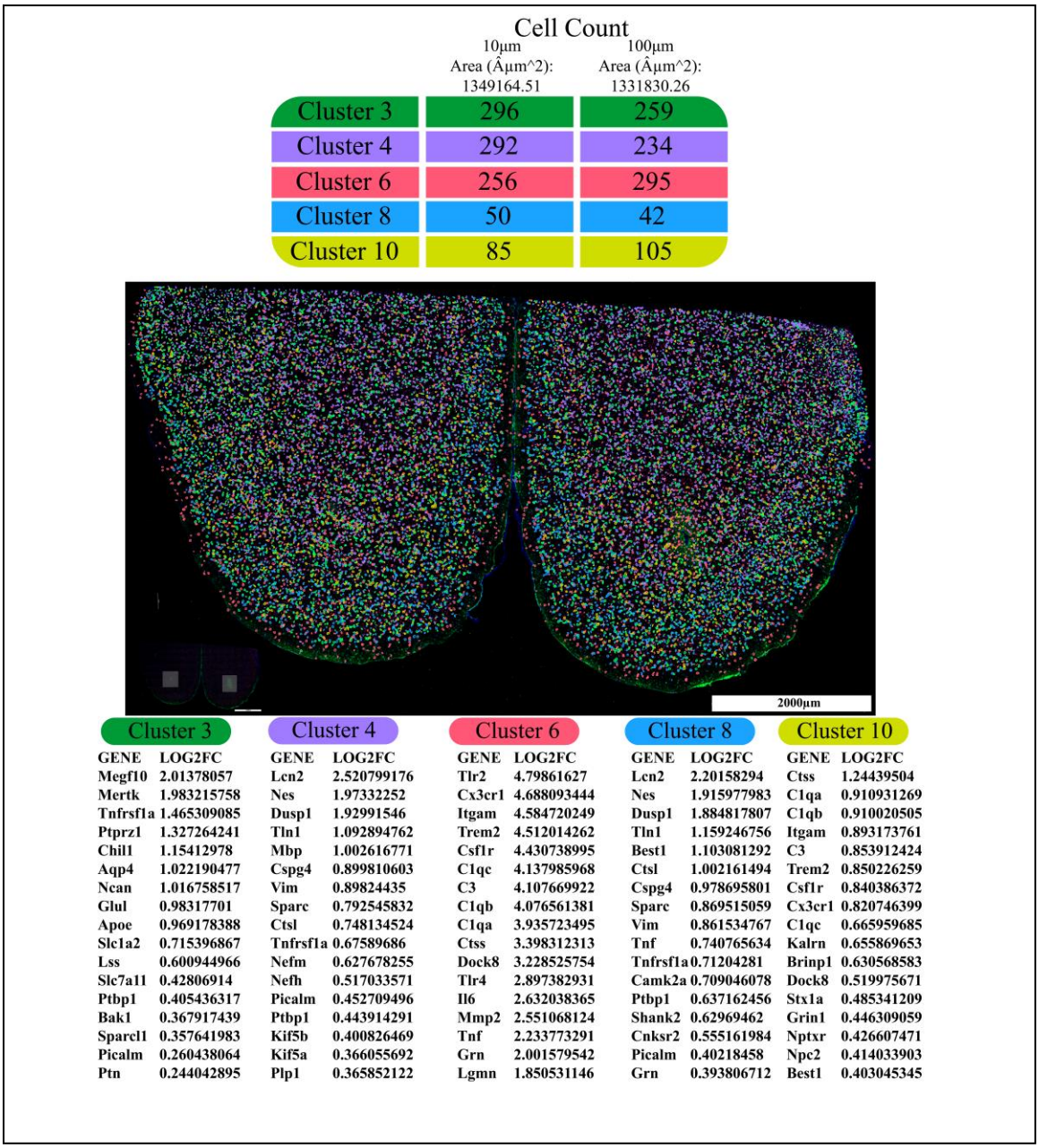

Figure 4.6: Clusters that express genes associated with reactive / modulatory glia which are diffusely organized around implanted devices. Tables above each confocal image represent cell count by cluster from within an approximately equal region of interest around each device injury. Minimized confocal 2images represent the region of interest that was used to quantify cell counts by cluster. Log2FC values belonging to each cluster were identified as statistically significant (Benjamini-Hochenberg test) $P \leq 0.05$.

device interface itself. Each of these clusters are not only present at the device interface, but are highly localized to the glia limitans which acts as a boundary between the meninges and neural parenchyma[25]. Quantification of cluster specific cells identified that the density of each cluster is elevated around supra-cellular polyimide devices relative to sub-cellular polyimide devices.

3.1.2 REACTIVE AND MODULATORY GLIA ARE CONCENTRATED AROUND REACTIVE GLIA AT THE DEVICE INTERFACE

Beyond the reactive glial center of the device interface, we identified five distinct clusters of glia which appear to be interspersed within the reactive glial scar as well as throughout the entire tissue section (Figure 4.6). Cells identified within cluster 3 were observed to primarily express genes *Megf10, Mertk, Tnfrsf1a, Ptprz1, Chil1, Aqp4,* and *Ncan*. Cluster 4 cells express *Lcn2, Nes, Dusp1, Tln1, Mbp,* and Cspg4). Cluster 6 highly expresses inflammation associated genes such as *Tlr2, Cx3cr1, Itgam, Trem2, Csf1r, C1qa, C1qb, C1qc,* and *C3*. Gene expression within cluster 8 is similar to cluster 4 in expression of *Lcn2, Nes, Duskp1,* and *Tln1*. However, cluster 8 expresses genes such as *Sparc, Vim, Tnf, Shank2, Cnksr2,* and *Grn*. Cluster 10 expresses genes that appear to be similar to those of cluster 6 (*Tlr2, Cx3cr1, Itgam, Trem2, Csf1r, C1qa, C1qb, C1qc, and C3*), however cluster 10 uniquely contains *Kalrn, Brinp1, Stx1a, Grin1, Nptxr,* and *Npc2*. Based on observations between define cell clusters and immunofluorescence imaging, clusters 4 and 8 do not align with stained NeuN+ or Olig2+ nuclei. These clusters only appear to align with GFAP+ nuclei as well as other hoechst+ nuclei. Cluster 6 cells appear to be localized to Hoechst+ nuclei throughout the tissue section and proximal to

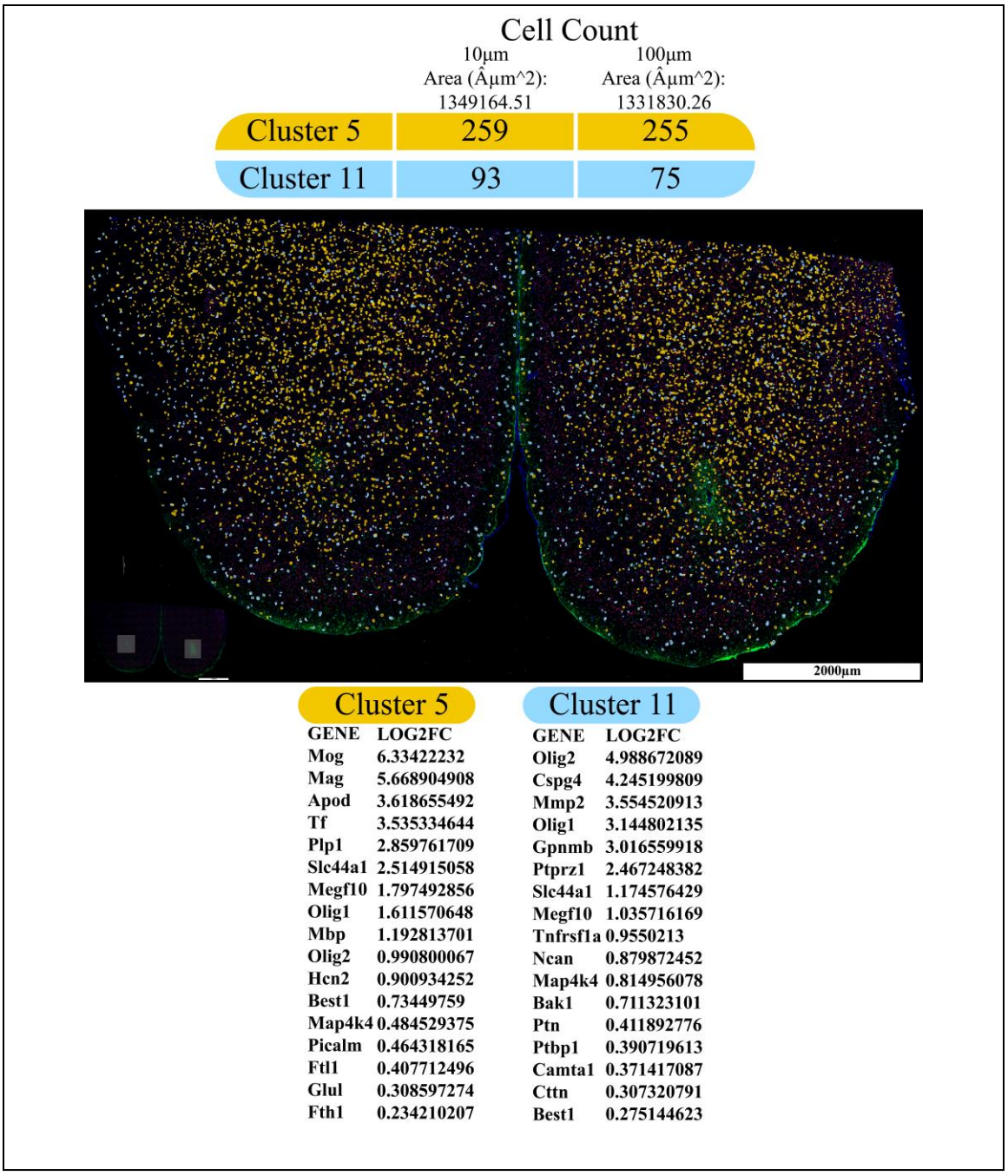

Cluster 5	
GENE	LOG2FC
Mog	6.33422232
Mag	5.668904908
Apod	3.618655492
Tf	3.535334644
Plp1	2.859761709
Slc44a1	2.514915058
Megf10	1.797492856
Olig1	1.611570648
Mbp	1.192813701
Olig2	0.990800067
Hcn2	0.900934252
Best1	0.73449759
Map4k4	0.484529375
Picalm	0.464318165
Ftl1	0.407712496
Glul	0.308597274
Fth1	0.234210207

Cluster 11	
GENE	LOG2FC
Olig2	4.988672089
Cspg4	4.245199809
Mmp2	3.554520913
Olig1	3.144802135
Gpnmb	3.016559918
Ptprz1	2.467248382
Slc44a1	1.174576429
Megf10	1.035716169
Tnfrsf1a	0.9550213
Ncan	0.879872452
Map4k4	0.814956078
Bak1	0.711323101
Ptn	0.411892776
Ptbp1	0.390719613
Camta1	0.371417087
Cttn	0.307320791
Best1	0.275144623

Figure 4.7: Clusters which express genes associated with Oligodendrocytes and OPCs. Tables above each confocal image represent cell count by cluster from within an approximately equal region of interest around each device injury. Minimized confocal images represent the region of interest that was used to quantify cell counts by cluster. Log2FC values belonging to each cluster were identified as statistically significant (Benjamini-Hochenberg test) $P \leq 0.05$.

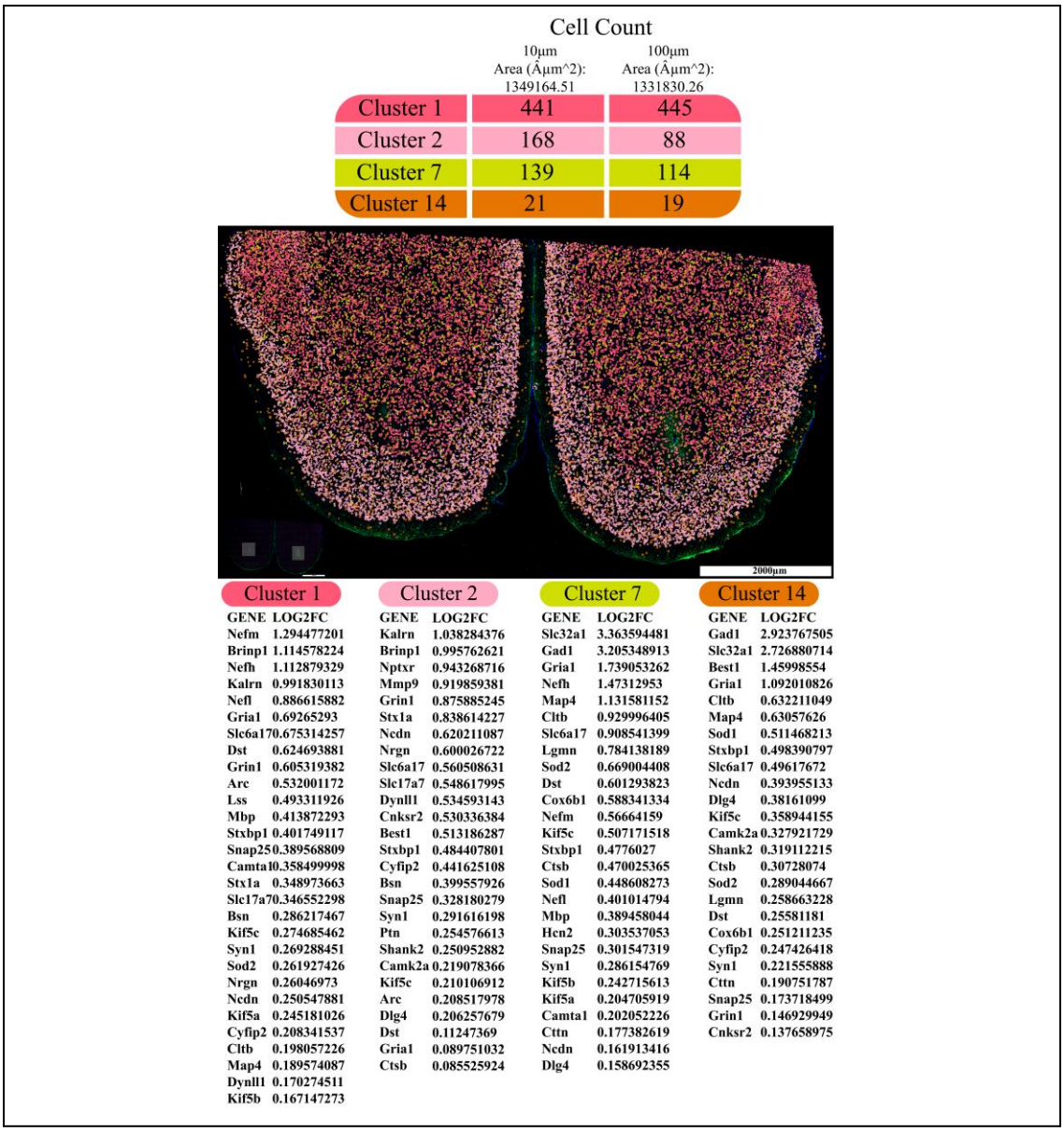

Figure 4.8: Spatial distributions of cellular clusters associated with inhibitory and excitatory neurons around implanted polyimide devices. Clusters of cells associated with neuronal phenotypes are reduced around 100um polyimide devices relative to 10um devices. Tables above each confocal image represent cell count by cluster from within an approximately equal region of interest around each device injury. Minimized confocal images represent the region of interest that was used to quantify cell counts by cluster. Log2FC values belonging to each cluster were identified as statistically significant (Benjamini-Hochenberg test) $P \leq 0.05$.

NeuN+ positive cells. Cluster 10, however appears to be almost entirely localized to NeuN+ cells and hoechst+ cells near neuronal nuclei.

3.1.3 OLIGODENDROCYTES AND OLIGODENDROCYTE PROGENITORS ARE REDUCED AROUND 100µm POLYIMIDE DEVICES

This study also identified two clusters (clusters 5 & 11) of cells which express genes associated with oligodendrocyte lineage (Figure 4.7). Cluster 5 expresses genes associated with mature and myelinating oligodendrocytes (*Olig1, Olig2, Mog, Mbp, Plp1, Slc44a1, Hcn2, Apod*). We also observed expression of iron metabolism genes Tf, Fth1, and Ftl1 within cluster 5 cells. The second cluster expresses genes associated with both OPCs and mature oligodendrocytes (*Cspg4, Olig1, Olig2, Ptprz1, Slc44a1*). Within this sample of tissue, cells which express high levels of pro-myelinating genes were qualitatively more closely located around 10um polyimide devices and more distant from 100um devices. However, counting of cells belonging to clusters 5 & 11 suggested negligible losses of cluster 5 and a greater reduction in cluster 11 cells around 100um polyimide devices.

3.1.4 NEURONAL POPULATIONS ARE REDUCED AROUND 100µm POLYIMIDE DEVICES

The results of this study indicated 4 distinct clusters of cells which express genes associated with excitatory, and inhibitory neurons and are highly associated with NeuN+ nuclei (Figure 4.8). Clusters 1 & 2 identified cells which highly express genes associated with excitatory neurons (*Slc17a7*) as well as pan neuronal genes associated with axonal transport (*Kif5a, Kif5b, Kif5c, Dynll1*), synaptic transmission (*Dlg4, Bsn, Snap25, Syn1,*

Stxbp1, Ncdn, Stx1a, Nrgn, Slc6a17, Grin1, Gria1, Camk2a, Nptxr), cytoskeletal structure (*Nefh, Nefm, Nefl, Dst, Map4*), and dendritic spine maintenance (*Kalrn, Cyfip2, Shank2*). Clusters 7 & 14 identified cells express genes associated with inhibitory neurons (*Slc31a1, Gad1,* as well as pan neuronal genes associated with axonal transport (*Kif5a, Kif5b, Kif5c, Dynll1*), synaptic transmission (*Dlg4, Bsn, Snap25, Syn1, Stxbp1, Ncdn, Stx1a, Nrgn, Slc6a17, Grin1, Gria1, Camk2a*), cytoskeletal structure (*Nefh, Nefm, Nefl, Dst, Map4*), and dendritic spine maintenance (*Kalrn, Cyfip2, Shank2*). We also observed Mmp9 expression within some excitatory neurons as well as Sod2 within inhibitory neurons throughout the tissue section and at the device interface. When directly comparing these clusters at the device interface, we observed that there were fewer neurons around larger polyimide devices at the 6-week timepoint.

4. DISCUSSION

Understanding the tissue response to indwelling electrodes is essential to improving the functional longevity and improving the biocompatibility of neural prostheses. Here in this study, we have provided some of the first transcriptional analyses of the tissue response to implanted electrodes with single cell resolution which have produced promising preliminary results. We have also utilized new transcriptionally identified biomarkers of the tissue response to directly compare implanted electrodes of supra- and sub-cellular dimensions. Prior to the onset of spatial transcriptomics around implanted electrodes, the understanding of the tissue response was primarily limited to observations of histological analysis. In this study, we can see a first glimpse of cellular organization by phenotype directly paired with immunofluorescence of key cell types at

the device interface.

4.1 REACTIVE GLIA AT THE DEVICE INTERFACE

In this study, we identified 5 clusters (Clusters 9, 12, 13, 15, & 16) of cellular phenotypes which are heavily concentrated around the core of the electrode injury. These clusters are concentrated at the device injury and express genes associated inflammatory microglia and astrocytes. The genes expressed are linked to fibrosis, glial activation, cellular proliferation, and synaptic pruning. The genes *Serping1*, *Gfap*, *Vim*, *C3*, *Lcn2*, *Chil1*, and *C1q*, which are associated with neurotoxic astrocyte activation, are present together in clusters 9 and 15. Genes associated with disease / damage associated microglia are high expressed within clusters 12, 13, and 16. We observed high expression of pro-phagocytic genes (*Dock8*, *C3*, *C1qa*, *C1qb*, *C1qc*, *Itgam*, *Tlr2*, *Tlr4*, and *Gpnmb*) which have been previously associated with synaptic pruning and neurodegeneration [29]–[33]. Due to the high relative expression of *Gfap* in these clusters, we are considering them to be astrocytic. These astrocyte clusters both express *Ncan* (Cspg3); which is both a secreted and transmembrane chondroitin sulfate proteoglycan which can act as an inhibitory cue for neuronal processes[34]. The expression of Ncan and neurotoxic markers within these cell clusters at the boundary of the glial scar may influence the retention of local neuronal populations and their processes.

We observed *Cspg4* (NG2) and *Nes* expressing cells (cluster 12) organized around the device injury and within neurovascular units which we may represent pericytes. Cspg4 is a membrane bound chondroitin sulfate proteoglycan expressed by pericytes, OPCs, and microglia which can modulate the inflammatory glial response and

inhibit axonal growth[35], [36]. The coincidence of this cluster at the device injury and vascular units may indicate neurovascular remodeling at the device interface, but may also have implications in the inflammatory environment. Non-pericyte *Cspg4* glia generally differentiate into oligodendrocytes in healthy cortical tissue, however, *Cspg4* glia can differentiate into reactive astrocytes in inflammatory conditions[37]. It may be possible that within the environment of the inflammatory glial scar that non-pericyte Cspg4 expressing glia may be more likely to differentiate into reactive astrocytes at the device interface potentially, further inhibiting axonal regeneration.

These cellular clusters are also organized throughout the glia limitans and appear to be similarly organized around implanted electrodes. The glia limitans' primary purpose in the brain is to create a boundary between cortical tissue and pia mater within the subarachnoid space. In addition to glial activation and inflammation, implanted electrodes are believed to create a steric blockade within cortical tissue which local cells recognize as a foreign body. Based on the cluster specific stratification within the glia limitans and the device injury, it may be possible that that one function of the reactive glia around implanted devices is to create an expansion of the glia limitans to protect surviving cortical tissues. Nonetheless, the number of cells belonging to clusters 9, 12, 13, 15, & 16 are reduced around the subcellular device relative to the supracellular polyimide implant which indicates a reduced inflammatory and neurotoxic device footprint of smaller devices.

4.2 MODULATORY GLIA AT THE DEVICE INTERFACE

Our results in this study identified 5 additional clusters (Clusters 3, 4, 6, 8, & 10)

of cells which do not appear to be spatially aggregated with the glial scar at the device interface. These clusters are diffusely organized throughout the section and express less neurotoxic or inflammatory markers than those tightly packed at the device interface. Based upon the gene expression profiles and histological overlap of these clusters, we have identified them as likely belonging to astrocytes and microglia. Cluster 3 appears to belong to a less reactive or homeostatic astrocyte phenotype. This cluster is largely coincident with GFAP+ histology and expresses relatively less *Gfap* than other astrocyte populations in the glial limitans and glial scar. Cluster 3 astrocytes differ from clusters 9 & 15 astrocytes in that they express less inflammatory genes and instead more heavily express genes associated with neuroprotective and homeostatic genes (*Megf10*, *Mertk*, *Ptprz1*, *Glul*, *Slc1a2*, *Sparcl1*, *Picalm*, and *Ptn*). Astrocytic driven synaptic pruning is mediated in part by the Megf10 and Mertk pathway[38]. Astrocytic expression of *Glul* (glutamate synthetase) and *Slc1a2* is essential for the astrocytic regulation of glutamate concentration within neuronal populations and within synapses[39]. Sparcl1 and Sparc regulate neuroligin – neurexin interactions are also expressed by homeostatic astrocytes, which suggests these genes play a role in the proper maintenance of synapses and dendritic spines[39]. Expression of *Picalm* is associated with clathrin mediated endocytosis and regulates autophagy, as well as clearance of cellular debris such as tau from the extracellular space[40]. Astrocytes in this cluster also appear to express *Ptn*, which is a secreted neurotrophic growth factor that also negatively regulates inflammatory glial[41], [42]. Clusters 4 & 8 appear coincident with astrocytes and pericytes which are proximal to NeuN+ histology. These clusters differ from cluster 3 in

that they primarily express *Lcn2*, *Nes*, and *Dusp1* from our panel of selected genes. Lcn2 is dominantly characterized by its role in neurodegeneration and neuronal cell death in inflammatory conditions[43]. However, Lcn2 also has roles in iron metabolism as Lcn2 can bind iron in an inflammation independent manner to regulate cellular oxidative stress[44]. *Dusp1* suppression is used as a biomarker for inflammation and oxidative stress as it may act to negatively regulate *Tlr2* and *Tlr4* expression. These clusters express relatively high Dusp1 and less *Tlr2* and *Tlr4* which may provide indication that these clusters are assuming a more homeostatic phenotype compared to the other reactive clusters. Nestin is an intermediate filament which can act as a co-polymer with Gfap and is upregulated in neurotrophic reactive astrocytes[45], [46]. As these 'modulatory cells' are not entirely a part of the reactive glial core and express different gene profiles from those of the glial scar, it may be possible that they are representative of cells which play a different role in the tissue response.

Clusters 6 & 10 appear to be coincident with perineuronal glia and express similar genes to those of reactive microglia at the device interface. However, while these cells are somewhat elevated at the device interface, they appear diffusely throughout the cortex as well and express relatively high Cx3cr1, which is known to be upregulated in homeostatic satellite microglia which play a neuroprotective role[47]–[49]. Both of these clusters express a mixture of genes involved in the complement system (*C3, C1qa, C1qb, C1qc*) as well as phagocytosis (*Itgam* and *Dock8*). These genes are also upregulated in neurotoxic reactive microglia, and they also play an essential role in clearing debris from the extracellular space and modulating synaptic structures[50], [51]. As these clusters of

cells are not entirely a part of the reactive glial core and express different gene profiles from those of the glial scar, it may be possible that they are representative of cells which play a different role in the tissue response. However, whether these cells represent reactive glia or not is unclear.

4.3 OLIGODENDROCYTES AT THE DEVICE INTERFACE

We also identified two clusters that appear to be associated with oligodendrocytes (Cluster 5) and OPCs (Cluster11). Cluster 5 is strongly coincident with Olig2+ immunofluorescence and expresses genes associated with myelinating oligodendrocytes (*Mog*, *Mag*, *Olig1*, *Olig2*, *Apod*, *Plp1*, and *Mbp*). This cluster also expresses genes associated with the regulation of myelin length (*Hcn2*)[52] and remyelination (*Slc44a1*)[53]. Hcn2 is also expressed by neurons and plays a key role in modulating neuronal firing rate[54] and neurons near implanted devices have shown reductions in sag amplitude and increased spike frequency adaptation[55]. The number of cluster 5 myelinating oligodendrocytes is relatively unchanged around 10um polyimide devices compared to 100um polyimide devices. However, cells belonging to cluster 11 express genes associated with the differentiation of OPCs to mature oligodendrocytes (*Cspg4*, *Olig2*, *Ptprz1*, *Gpnmb*). These cells are reduced around 100um devices. *Ptprz1* and *Gpnmb* are both expressed by OPCs with *Ptprz1* being implicated in the maintenance of the OPC phenotype[56][57]. As this preliminary observation shows slight reduction in OPC-type cells around larger polyimide devices, this may imply that remyelination and replenishment of oligodendrocyte populations is impacted around devices with a larger footprint.

5. CONCLUSIONS

The promising preliminary data collected from this study illustrate single-cell resolution transcriptomics surrounding implanted electrodes for the first time. We identified 16 clusters of distinct cellular phenotypes which provided new information about the dynamics of the tissue response to devices of sub- and supra-cellular dimensions. However, the observations are preliminary and data collection is ongoing. In addition to further analyzing the data from our 6-week polyimide devices, we still have yet to include data from polyimide device at 1-week post-implantation as well as 1- and 6-week silicon device tissue.

REFERENCES

[1] A. W. Laxton *et al.*, "A phase i trial of deep brain stimulation of memory circuits in Alzheimer's disease," *Ann. Neurol.*, vol. 68, no. 4, pp. 521–534, Oct. 2010, doi: 10.1002/ana.22089.

[2] J. Kuhn *et al.*, "Deep brain stimulation of the nucleus basalis of Meynert in Alzheimer's dementia," *Mol. Psychiatry*, vol. 20, no. 3, pp. 353–360, Mar. 2015, doi: 10.1038/mp.2014.32.

[3] F. T. Sun, M. J. Morrell, and R. E. Wharen, "Responsive Cortical Stimulation for the Treatment of Epilepsy," *Neurotherapeutics*, vol. 5, no. 1, pp. 68–74, Jan. 2008, doi: 10.1016/j.nurt.2007.10.069.

[4] E. J. Quinn *et al.*, "Beta oscillations in freely moving Parkinson's subjects are attenuated during deep brain stimulation," *Mov. Disord.*, vol. 30, no. 13, pp. 1750–1758, Nov. 2015, doi: 10.1002/mds.26376.

[5] P. J. Grahn *et al.*, "A neurochemical closed-loop controller for deep brain stimulation: Toward individualized smart neuromodulation therapies," *Front. Neurosci.*, vol. 8, no. 8 JUN, p. 169, Jun. 2014, doi: 10.3389/fnins.2014.00169.

[6] A. L. Crowell, P. Riva-Posse, S. J. Garlow, and H. S. Mayberg, "Toward an Understanding of the Neural Circuitry of Major Depressive Disorder Through the Clinical Response to Deep Brain Stimulation of Different Anatomical Targets," *Curr. Behav. Neurosci. Reports*, vol. 1, no. 2, pp. 55–63, Jun. 2014, doi: 10.1007/s40473-014-0008-z.

[7] D. M. Whiting *et al.*, "Lateral hypothalamic area deep brain stimulation for refractory obesity: A pilot study with preliminary data on safety, body weight, and energy metabolism: Clinical article," *J. Neurosurg.*, vol. 119, no. 1, pp. 56–63, Jul. 2013, doi: 10.3171/2013.2.JNS12903.

[8] A. L. Ho, E. S. Sussman, A. V. Pendharkar, D. E. Azagury, C. Bohon, and C. H. Halpern, "Deep brain stimulation for obesity: Rationale and approach to trial design," *Neurosurg. Focus*, vol. 38, no. 6, p. E8, Jun. 2015, doi: 10.3171/2015.3.FOCUS1538.

[9] D. R. Moore and R. V. Shannon, "Beyond cochlear implants: Awakening the deafened brain," *Nat. Neurosci.*, vol. 12, no. 6, pp. 686–691, Jun. 2009, doi: 10.1038/nn.2326.

[10] H. H. Lim and T. Lenarz, "Auditory midbrain implant: Research and development towards a second clinical trial," *Hear. Res.*, vol. 322, no. 1, pp. 212–223, Apr. 2015, doi: 10.1016/j.heares.2015.01.006.

[11] P. M. Lewis, H. M. Ackland, A. J. Lowery, and J. V. Rosenfeld, "Restoration of vision in blind individuals using bionic devices: A review with a focus on cortical

visual prostheses," *Brain Res.*, vol. 1595, pp. 51–73, Jan. 2015, doi: 10.1016/j.brainres.2014.11.020.

[12] J. V. Smit, "Exploring deep brain stimulation as a treatment for tinnitus," Maastricht University, 2018. doi: 10.26481/dis.20180921js.

[13] J. L. Collinger *et al.*, "High-performance neuroprosthetic control by an individual with tetraplegia," *Lancet*, vol. 381, no. 9866, pp. 557–564, Feb. 2013, doi: 10.1016/S0140-6736(12)61816-9.

[14] T. Aflalo *et al.*, "Decoding motor imagery from the posterior parietal cortex of a tetraplegic human," *Science (80-.).*, vol. 348, no. 6237, pp. 906–910, May 2015, doi: 10.1126/science.aaa5417.

[15] R. Biran, D. C. Martin, and P. A. Tresco, "The brain tissue response to implanted silicon microelectrode arrays is increased when the device is tethered to the skull," *J. Biomed. Mater. Res. - Part A*, vol. 82, no. 1, pp. 169–178, Jul. 2007, doi: 10.1002/jbm.a.31138.

[16] R. Biran, D. C. Martin, and P. A. Tresco, "Neuronal cell loss accompanies the brain tissue response to chronically implanted silicon microelectrode arrays," *Exp. Neurol.*, vol. 195, no. 1, pp. 115–126, Sep. 2005, doi: 10.1016/j.expneurol.2005.04.020.

[17] N. J. Michelson *et al.*, "Multi-scale, multi-modal analysis uncovers complex relationship at the brain tissue-implant neural interface: New emphasis on the biological interface," *J. Neural Eng.*, vol. 15, no. 3, p. 033001, Jun. 2018, doi: 10.1088/1741-2552/aa9dae.

[18] T. D. Y. Kozai, A. S. Jaquins-Gerstl, A. L. Vazquez, A. C. Michael, and X. T. Cui, "Brain tissue responses to neural implants impact signal sensitivity and intervention strategies," *ACS Chem. Neurosci.*, vol. 6, no. 1, pp. 48–67, Jan. 2015, doi: 10.1021/cn500256e.

[19] C. H. Thompson, T. E. Riggins, P. R. Patel, C. A. Chestek, W. Li, and E. Purcell, "Toward guiding principles for the design of biologically-integrated electrodes for the central nervous system," *J. Neural Eng.*, vol. 17, no. 2, p. 021001, Mar. 2020, doi: 10.1088/1741-2552/ab7030.

[20] X. Yang *et al.*, "Bioinspired neuron-like electronics," *Nat. Mater.*, vol. 18, no. 5, pp. 510–517, May 2019, doi: 10.1038/s41563-019-0292-9.

[21] A. M. Stiller *et al.*, "A meta-analysis of intracortical device stiffness and its correlation with histological outcomes," *Micromachines*, vol. 9, no. 9, p. 443, Sep. 2018, doi: 10.3390/mi9090443.

[22] H. C. Lee *et al.*, "Histological evaluation of flexible neural implants; Flexibility limit for reducing the tissue response?," *J. Neural Eng.*, vol. 14, no. 3, p. 036026,

Jun. 2017, doi: 10.1088/1741-2552/aa68f0.

[23] Z. J. Du *et al.*, “Ultrasoft microwire neural electrodes improve chronic tissue integration,” *Acta Biomater.*, vol. 53, pp. 46–58, 2017, doi: 10.1016/j.actbio.2017.02.010.

[24] C. H. Thompson, A. Saxena, N. Heelan, J. Salatino, and E. K. Purcell, “Spatiotemporal patterns of gene expression around implanted silicon electrode arrays,” *J. Neural Eng.*, vol. 18, no. 4, 2021, doi: 10.1088/1741-2552/abf2e6.

[25] Q. A. Whitsitt, B. Patel, B. Hunt, and E. K. Purcell, “A Spatial Transcriptomics Study of the Brain-Electrode Interface in Rat Motor Cortex,” *bioRxiv*, p. 2021.12.03.471147, 2021, [Online]. Available: https://www.biorxiv.org/content/10.1101/2021.12.03.471147v1%0Ahttps://www.biorxiv.org/content/10.1101/2021.12.03.471147v1.abstract

[26] Q. A. Whitsitt, B. Koo, M. E. Celik, B. M. Evans, J. D. Weiland, and E. K. Purcell, “Spatial Transcriptomics as a Novel Approach to Redefine Electrical Stimulation Safety,” *Front. Neurosci.*, vol. 16, no. July, pp. 1–17, 2022, doi: 10.3389/fnins.2022.937923.

[27] “Cell Ranger’s Gene Expression Algorithm - Official 10x Genomics Support.”

[28] A. Janesick *et al.*, “High resolution mapping of the breast cancer tumor microenvironment using integrated single cell, spatial and in situ analysis of FFPE tissue,” *bioRxiv*, p. 2022.10.06.510405, 2022, [Online]. Available: https://www.biorxiv.org/content/10.1101/2022.10.06.510405v1%0Ahttps://www.biorxiv.org/content/10.1101/2022.10.06.510405v1.abstract

[29] H. W. Bedell, N. J. Schaub, J. R. Capadona, and E. S. Ereifej, “Differential expression of genes involved in the acute innate immune response to intracortical microelectrodes,” *Acta Biomater.*, vol. 102, no. xxxx, pp. 205–219, Jan. 2020, doi: 10.1016/j.actbio.2019.11.017.

[30] S. Song, B. Regan, E. S. Ereifej, E. R. Chan, and J. R. Capadona, “Neuroinflammatory Gene Expression Analysis Reveals Pathways of Interest as Potential Targets to Improve the Recording Performance of Intracortical Microelectrodes,” *Cells*, vol. 11, no. 15, 2022, doi: 10.3390/cells11152348.

[31] J. Presumey, A. R. Bialas, and M. C. Carroll, “Complement System in Neural Synapse Elimination in Development and Disease,” in *Advances in Immunology*, 1st ed., vol. 135, Elsevier Inc., 2017, pp. 53–79. doi: 10.1016/bs.ai.2017.06.004.

[32] K. Namekata, X. Guo, A. Kimura, N. Arai, C. Harada, and T. Harada, “DOCK8 is expressed in microglia, and it regulates microglial activity during neurodegeneration in murine disease models,” *J. Biol. Chem.*, vol. 294, no. 36, pp. 13421–13433, 2019, doi: 10.1074/jbc.RA119.007645.

[33] M. L. Neal, A. M. Boyle, K. M. Budge, F. F. Safadi, and J. R. Richardson, “The glycoprotein GPNMB attenuates astrocyte inflammatory responses through the CD44 receptor,” *J. Neuroinflammation*, vol. 15, no. 1, pp. 1–14, 2018, doi: 10.1186/s12974-018-1100-1.

[34] M. K. E. Schäfer and I. Tegeder, “NG2/CSPG4 and progranulin in the posttraumatic glial scar,” *Matrix Biol.*, vol. 68–69, pp. 571–588, 2018, doi: 10.1016/j.matbio.2017.10.002.

[35] Q. Gao, J. Lu, Y. Huo, N. Baby, E. A. Ling, and S. T. Dheen, “NG2, a member of chondroitin sulfate proteoglycans family mediates the inflammatory response of activated microglia,” *Neuroscience*, vol. 165, no. 2, pp. 386–394, 2010, doi: 10.1016/j.neuroscience.2009.10.022.

[36] X. Du, Z. Zhang, H. Zhou, and J. Zhou, “Differential Modulators of NG2-Glia Differentiation into Neurons and Glia and Their Crosstalk,” *Cell. Mol. Neurobiol.*, vol. 41, no. 1, pp. 1–15, 2021, doi: 10.1007/s10571-020-00843-0.

[37] P. Honsa *et al.*, “Generation of reactive astrocytes from NG2 cells is regulated by sonic hedgehog,” *Glia*, vol. 64, no. 9, pp. 1518–1531, 2016, doi: 10.1002/glia.23019.

[38] W. S. Chung *et al.*, “Astrocytes mediate synapse elimination through MEGF10 and MERTK pathways,” *Nature*, vol. 504, no. 7480, pp. 394–400, 2013, doi: 10.1038/nature12776.

[39] K. S. Wardlaw and G. E. Hardingham, “Long-term plasticity of astrocytic phenotypes and their control by neurons in health and disease,” *Essays Biochem.*, vol. 67, no. 1, pp. 39–47, 2023, doi: 10.1042/EBC20220090.

[40] K. Sung and M. Jimenez-Sanchez, “Autophagy in Astrocytes and its Implications in Neurodegeneration,” *J. Mol. Biol.*, vol. 432, no. 8, pp. 2605–2621, 2020, doi: 10.1016/j.jmb.2019.12.041.

[41] M. Linnerbauer *et al.*, “Astrocyte-Derived Pleiotrophin Mitigates Late-Stage Autoimmune CNS Inflammation,” *Front. Immunol.*, vol. 12, no. January, pp. 1–14, 2022, doi: 10.3389/fimmu.2021.800128.

[42] A. M. Nikolakopoulou *et al.*, “Pericyte loss leads to circulatory failure and pleiotrophin depletion causing neuron loss,” *Nat. Neurosci.*, vol. 22, no. 7, pp. 1089–1098, 2019, doi: 10.1038/s41593-019-0434-z.

[43] F. Bi *et al.*, “Reactive astrocytes secrete lcn2 to promote neuron death,” *Proc. Natl. Acad. Sci. U. S. A.*, vol. 110, no. 10, pp. 4069–4074, 2013, doi: 10.1073/pnas.1218497110.

[44] A. C. Ferreira, N. Sousa, J. M. Bessa, J. C. Sousa, and F. Marques, “Metabolism and adult neurogenesis: Towards an understanding of the role of lipocalin-2 and

iron-related oxidative stress," *Neurosci. Biobehav. Rev.*, vol. 95, no. April, pp. 73–84, 2018, doi: 10.1016/j.neubiorev.2018.09.014.

[45] S. A. Liddelow *et al.*, "Neurotoxic reactive astrocytes are induced by activated microglia," *Nature*, vol. 541, no. 7638, pp. 481–487, 2017, doi: 10.1038/nature21029.

[46] M. Potokar, M. Morita, G. Wiche, and J. Jorgačevski, "The Diversity of Intermediate Filaments in Astrocytes," *Cells*, vol. 9, no. 7, 2020, doi: 10.3390/cells9071604.

[47] A. Lampron *et al.*, "Inefficient clearance of myelin debris by microglia impairs remyelinating processes," *J. Exp. Med.*, vol. 212, no. 4, pp. 481–495, 2015, doi: 10.1084/jem.20141656.

[48] P. Chen, W. Zhao, Y. Guo, J. Xu, and M. Yin, "CX3CL1 / CX3CR1 in Alzheimer ' s Disease : A Target for Neuroprotection," vol. 2016, 2016.

[49] T. Mizuno, J. Kawanokuchi, K. Numata, and A. Suzumura, "Production and neuroprotective functions of fractalkine in the central nervous system," *Brain Res.*, vol. 979, no. 1–2, pp. 65–70, 2003, doi: 10.1016/S0006-8993(03)02867-1.

[50] B. Stevens *et al.*, "The Classical Complement Cascade Mediates CNS Synapse Elimination," *Cell*, vol. 131, no. 6, pp. 1164–1178, 2007, doi: 10.1016/j.cell.2007.10.036.

[51] M. K. Zabel and W. M. Kirsch, "From development to dysfunction: Microglia and the complement cascade in CNS homeostasis," *Ageing Res. Rev.*, vol. 12, no. 3, pp. 749–756, Jun. 2013, doi: 10.1016/j.arr.2013.02.001.

[52] M. Swire, P. Assinck, P. A. McNaughton, D. A. Lyons, C. Ffrench-Constant, and M. R. Livesey, "Oligodendrocyte hcn2 channels regulate myelin sheath length," *J. Neurosci.*, vol. 41, no. 38, pp. 7954–7964, 2021, doi: 10.1523/JNEUROSCI.2463-20.2021.

[53] E. Traiffort, S. O'Regan, and M. Ruat, "The choline transporter-like family SLC44: Properties and roles in human diseases," *Mol. Aspects Med.*, vol. 34, no. 2–3, pp. 646–654, 2013, doi: 10.1016/j.mam.2012.10.011.

[54] C. S. Chan, R. Shigemoto, J. N. Mercer, and D. J. Surmeier, "HCN2 and HCN1 channels govern the regularity of autonomous pacemaking and synaptic resetting in globus pallidus neurons," *J. Neurosci.*, vol. 24, no. 44, pp. 9921–9932, 2004, doi: 10.1523/JNEUROSCI.2162-04.2004.

[55] B. A. Gregory *et al.*, "Structural and functional changes of deep layer pyramidal neurons surrounding microelectrode arrays implanted in rat motor cortex," *Acta Biomater.*, vol. 168, pp. 429–439, 2023, doi: 10.1016/j.actbio.2023.07.027.

[56] M. N. Murthy, C. Blauwendraat, S. Guelfi, J. Hardy, P. A. Lewis, and D. Trabzuni,

"Increased brain expression of GPNMB is associated with genome wide significant risk for Parkinson's disease on chromosome 7p15.3," *Neurogenetics*, vol. 18, no. 3, pp. 121–133, 2017, doi: 10.1007/s10048-017-0514-8.

[57] H. Tanaka *et al.*, "The potential of GPNMB as novel neuroprotective factor in amyotrophic lateral sclerosis," *Sci. Rep.*, vol. 2, pp. 1–11, 2012, doi: 10.1038/srep00573.

CHAPTER 5 | CONCLUSIONS AND FUTURE WORK

This dissertation expands basic science understandings of the tissue response to implanted electrodes. The contents of this dissertation have covered the first full transcriptome sequencing of tissue around implanted silicon electrode arrays, which identified hundreds of potential biomarkers for further investigation. We have also identified that RNA-seq identified genes can be used to guide future studies of protein expression at the device interface. Finally, this dissertation provided the first observations, with single-cell resolution, into the cellular dynamics of the tissue response from a panel of 100 RNA-seq identified genes. 16 unique phenotypes of cellular clusters that are discretely organized around implanted electrodes were identified which include reactive glia, modulatory glia, neurons, and oligodendrocytes. However, there is still significant work left to be done before the tissue response is fully understood. While there is a much better understanding of the gene expression and potential pathways involved, there is still a need to interrogate discrete molecular mechanisms of the biomarkers that have been covered in this body of work as well as those that are being conducted by other groups in parallel. This future work will be essential in the field of neural prosthetics for two primary reasons: (1) there is a need for new methods to benchmark the biological integration of implanted electrodes and assess electrode safety, and (2) the ability to directly link functional electrode outcomes with well characterized biological outcomes. This dissertation has discussed many next-generation devices that have utilized design-based strategies to reduce the tissue response to indwelling electrodes, which can introduce new challenges in electrode fabrication, long-term device

stability, and the reproducibility between devices. However, it can be difficult to assess the performance of novel electrode technologies without a thorough understanding of biological responses to implanted devices. The contents of this dissertation provide the foundations for 'biology-based' strategies in which the mechanisms of the tissue response at both the transcriptional and protein level can be considered during electrode design. By understanding the tissue response to implanted devices, new therapeutics and intervention strategies can be developed to treat aspects of the tissue response which are currently unable to be solved by device design alone. In understanding these mechanisms, and the true impact that they might have on the tissue response as well as signal fidelity around implanted devices we may be able to create neural prostheses which are fully integrated with their surrounding biology.